PHYSICAL PROPERTIES OF VANADIUM DIOXIDE NANOPARTICLES: APPLICATION AS 1-D NANOBELTS ROOM TEMPERATURE FOR HYDROGEN GAS SENSING

By

ALINE SIMO

Dissertation

Submitted in partial fulfillment of the requirements for the degree of

DOCTOR OF PHILOSOPHY

In the Department of Physics, University of the Western Cape

December 2013

Supervisor: Prof Malik Maaza

Materials Research Department, iThemba LABS-NRF

Co-Supervisor: Prof Reginaldt Madjoe

Department of Physics, University of the Western Cape

ABSTRACT:

Transition metal oxides magneli phases present crystallographic shear structure which is of great interest in multiple applications because of their wide range of valence, which is exhibited by the transition metals. The latter affect chemical and physical properties of the oxides. Amongst them we have nanostructures VO_2 system of V and O components which are studied including chemical and physical reactions based on non-equilibrium thermodynamics. Due to their structural classes of corundum, rocksalt, wurtzite, spinel, perovskite, rutile, and layer structure, these oxides are generally used as catalytic materials which are prepared by common methods under mild conditions presenting distortion or defects in the case of VO_2. Existence of an intermediate phase is proved using an x-ray thermodiffraction experiment providing structural information as the nanoparticles are heated. Potential application as gas sensing device has been the first time obtained due to the high surface to volume ratio, and good crystallinity, purity of the material and presence of suitable nucleating defects sites due to its n-type semiconductor behavior. In addition, annealing effect on nanostructures VO_2 nanobelts shows a preferential gas reductant of Ar comparing to the N_2 gas. Also, the hysteresis loop shows that there is strong size dependence to annealing treatment on our samples. This is of great interest in the need of obtaining high stable and durable material for Mott insulator transistor and Gas sensor device at room temperature.

KEYWORDS:

Semiconductor-Transition Metal Oxide-Nanostructures-Phase change transformations thermodynamics-Vanadium Oxides-Sol-gel Synthesis (hydrothermal, Spin Coating, Annealing)-Facile route Synthesis-X-Ray Diffraction-Scanning Electron Microscopy-HRTEM- DSC- Application as gas sensing device (Gas sensors-Principle-Selectivity H_2 gas)–Time dependent effect (XRD-SEM-XPS) -Sensor device Infrared Sensor (Optical Properties of VO_2 imbedded in polymer-Facile route synthesis-High Infrared Sensor)-Current-Voltage Description- Mott insulator material

DECLARATION:

I, the undersigned, hereby declare that the work contained in this Ph.D. thesis is my original work, that it has not been previously submitted for any degree or examination in any other university, and that all the sources I have used or quoted have been clearly indicated and acknowledged by complete references.

Aline Simo

Signature: ……………………………………………………

Date: …………………………………………………………

"I can do all things through Christ who strengthen me"

Philippians 4: 13

ACKNOWLEDGEMENTS:

TABLE OF CONTENTS:

Pages

UNIVERSITY *of the*
WESTERN CAPE

LIST OF TABLES

UNIVERSITY *of the*
WESTERN CAPE

LIST OF FIGURES

CHAPTER ONE:

INTRODUCTION, PROBLEM STATEMENT & OBJECTIVES

1.1 Introduction

Most of the properties of solids, which present basic results in Physics and Chemistry of solids, depend on the overall structure i.e. chemical composition, arrangement of the atoms and size of the solids in one, two or three dimensions. Hence the synthesis of materials and/or devices with new properties by manipulation control of their structure on the atomic level has become an emerging interdisciplinary field based on solid state physics, chemistry, biology and materials science [1]. The development of new types of ultrafast switches operating in the RF microwave and sensors is based on the use of a class of materials undergoing fast, reversible phase transformation from semi conducting state to metallic one. An example of such a material is vanadium dioxide VO_2 whose energy band gap varies relatively slightly under the influence of external pressure or magnetic field. This may serve the purpose of tuning into the resonance of one-phonon interband transition [2]. Numerous kinds of gases are emitted from various sources into our living space or outdoors. Many of them are hazardous to human beings and the environment (air pollutant). They are present at very low concentration requiring extremely good sensing characteristics for their monitoring [3]. Solving challenges for hydrogen carrier is highly demanded. Technological difficulties of hydrogen production, distribution, storage and provision of the necessary infrastructure, at a competitive cost, require a major concerted even global effort. Apart from pure technological development, the introduction of new technologies to the market necessitates an appreciation of the non-technical barriers which, if not fully addressed, may hinder or delay the market deployment of the new technologies. These issues refer to:

- Overcoming the regulatory barriers to widespread hydrogen use

- Understanding the different safety issues associated with hydrogen compared to today's fuels and developing strategies for managing these
- Understanding and analyzing societal issues.

Hydrogen opens up access to a broad range of primary energy sources, including fossil fuels, nuclear energy and, increasingly, renewable energy sources (e.g. wind, solar, ocean, and biomass), thus enhancing energy security through increased diversity. Hydrogen and electricity also allow interoperability and flexibility in balancing centralized and decentralized power, based on managed, intelligent grids, and power for remote locations (e.g. island and mountain sites), air quality and health improvement for Greenhouse gas reduction. Hydrogen can be produced from carbon-free or carbon-neutral energy sources or from fossil fuels with carbon dioxide capture and storage (sequestration). Thus, the use of hydrogen could eventually eliminate greenhouse gas emissions from the energy sector. Regarding the economical competiveness, the development and sales of energy systems are major components of wealth creation, from automobiles to complete power stations, creating substantial employment and export opportunities, especially for the industrialized nations.

1.2 Statement of the Problem

Hydrogen has been widely used in many industrial applications, and in the public domain as would be expected for an energy carrier. Normally, in these commercial and industrial environments, only well-trained personnel come into contact with hydrogen. Due to the continuous increase of hydrogen uses as an energy carrier, contact with laypersons demands different fail-safe routines and technologies. Introduction of hydrogen as an energy carrier therefore requires research efforts in the field of safety. Only a small number of hydrogen and fuel cell systems and components required for the hydrogen economy are in operation today. Consequently, only limited data is available on the operational and safety aspects of these new technologies and research are required to understand hydrogen's behavior as a fuel for both vehicles and stationary applications, and to support the development of technologies for the

detection and safe management of unscheduled hydrogen releases or incidents involving hydrogen systems. VO_2 based solid state gas sensors represent a novel powerful detection with high exquisite selectivity of hydrogen, fast response, recovery, and potential for integration of addressable arrays on a massive scale [4]. The great interest of industrial and scientific world on solid state gas sensors come from their numerous advantages like small sizes, possibility of on-line operation due to bench production, low cost. We believe that the high efficiency of our sensor needs prior understanding of the interplay between Metal-insulator transition and multiferroic domains. In contrast to 2D crystalline nanobeams, 1D geometric materials result in emergence of several possible families of ferroelastic domains in nanoplates, allowing strain controlled transitions in the presence of geometrical frustration [5]. The nanoplatelets possess planar surface which is required for most applications such as sensors, optical modulation, and electromechanics. In the case of lower temperature M1 phase, large surface breaks into orientational domains. This latter arise due to the presence of multiple energy equivalent orientations which reduce symmetry on cooling through the transition point and only one way is realized at each point in the sample volume.

1.3 Objectives and outline of the thesis

One of the objectives of this research was to successfully synthesize nanoparticles VO_2 (M) directly through a soft chemistry process where we used metal alkoxide V_2O_5 as starting precursor. This latter follows hydrolysis and condensation steps which depend on the electronegativity of the metal atom and allow no breaking of weak bonds such as Wan Der Waals, hydrogen and hydrophobic interactions with low temperature processing. Secondly, we successfully reproduce nanobelts shape–VO_2, which are very promising for sensors applications due to their faces exposed to the gas environment in a likely manner and their size which is to produce a complete depletion of carriers inside the belt. Additionally, we quantify the coexistence of differents phases present in our sample as we follow the metal-insulator transition by applying x-ray

thermodiffraction synchrotron radiation. In accordance to our finding, a more pronounced mixture phase M2 was obtained revealing a further strengthening of V-V bonds with a direct opening effect of the band gap structure describing VO_2 as a band insulator. Tselev et al. [5] showed that M2 phase can coexist in the M1 stable low-temperature phase which can be stabilized by application of an external stress along $<110>_R$ direction. This suggests that in pure unconstrained VO_2 under ambient pressure, the M2 phase correspond to a local minimum or to a saddle point of the free energy and become an absolute minimum due to a perturbation. The displacements of the atoms which are associated with the breaking of the symmetry were described through the Ginzburg-Landau theory expansion of the free energy. The simplest example of a structural phase transition occurs when the distortions may be described by a single normal mode; the amplitude of the distortion is then given by the order parameter. The M2 phase according to Pouget et al. [6] was interpreted as alternative phase of pure VO_2 whose free energy is slightly higher than the one of M1 phase. This observation was observed in our nanoplatelet VO_2 (M). Additionally we explore the strong size effect function of the external temperature stress inducing a decrease into the hysteresis loop upon heating and cycling through Differential Scanning Calorimetry. This latter technique was mostly used due to the accurate information obtained concerning crystallization time and temperature, percent of crystallinity of our nanoplatelet, heat of fusion and reactions and purity of our material. Also, we present X-Ray Diffraction and Raman characterizations techniques respectively to have coherent reflected intensities which give the random direction of distribution of the crystallite and phase identification of the sample and Stokes vibration frequencies characteristic of existing elements presents in the material. Here, we propose a new thermodynamic model depending on the length and size of the nanobelts showing that the size of the particles have strong correlation effect on the phase transition which would be a significant contribution to nanoscale materials physics. One of the direct applications of this technology was found to be gas sensor device High hydrogen gas sensing capabilities within ppm level which was demonstrated for the first time to be highly selective

comparing to other gases such as: CO and CO_2, reproducible even at 50 deg. C which confirms the good operation of our device in dry air at room temperature where the conduction response is mainly associated with the electronic surface interaction with H_2 molecules. The adsorption of the H_2 molecules is well described via the power law of the gas concentration $R \sim P_{H2}^{-n}$ [7]. Possible mechanism can be present during sensor mechanism [8] reduction or oxidation of the sample, anion exchange by a gaseous species either bonding to the bare surface or bonding to a previously adsorbed species. This latter is due to the presence of defects which are possible sites for surface atoms. In our case the open junction grain can be considered in that regard. Lastly, we probed the transport properties of the VO_2 thick films by measuring the I-V characteristics in the voltage interval -1V to 1V which average over 15 times of I-V scans in each spot and grid measureament. The I-V behavior observed, originate from the soliton tunneling conductivity of the material. The metal insulator transition in VO_2 nanocrystals is described through the existence of a negative coefficient temperature at high current level. This mechanism prevents the device from thermal runaway and breakdown. Non stoichiometry defects present in VO_2 such as oxygen vacancies serve as localized traps required for the I-V behavior of VO_2. The decrease of the band gap with increase of free carrier concentration become significant just below the transition temperature Tc according to the quadratic equation: $Eg(T) \sim E0 - A (kBT)^2$.

An overview of the literature is given in chapter 2 as well as a more details regarding the physical properties of VO_2 such as electronic, electrical, optical and magnetic properties and its chemical properties are highlighted. Chapter 3 focus on the methods of growth of VO_2 followed by a decription of hydrothermal process synthesis used to obtain high quality VO_2 with no impurities under optimal conditions of pressure P~20 MPa and T~240 ^{o} C for two days using Stainless steel Teflon autoclave 3.5cm × 5.5 cm sizes. Chapter 4 presents an overview of gas sensing background and current literature on vanadium oxides gas sensing properties. Chapter 5 discussed all the experimental results obtained in 5 subsections 4.1, 4.2, 4.3, 4.4, and 4.5. Chapter 6 contains a summary

of the work presented in this thesis as well as the outlook for future work. Finally we present some characterizations techniques used in the framework of our experiment as an Appendix.

1.4 References

[1] Gleiter, H.; *Acta Mater.* 48, 2000, 1-29.

[2] Lozovik, Y.E.; Merkulova, S.P.; Ovchinnikov, I.V.; *Physics Letters A* 282, 2001, 407-414.

[3] Yamazoe, N.; Sakai, G.; and Shimanoe, K.; *Catalysis Surveys from Asia*, 7(1), April 2003

[4] Huang, X. J.; Choi Y.K.; *Sensors and Actuators B* 122, 2007, 659-671

[5] Tselev, A.; Strelcov,E.; Luk`yanchunck, I.A.; Budai,J.D.; Tischler, J.Z.; Ivanov, I.N.; Jones, K.; Proksch,R.; Kalinin,S.V.; and Kolmakov, A.;*Nano Lett.* 10, 2010, 2003-2011

[6] Pouget, J.P.; and Launois, H.; *Colloque C4, supplement au no 10, Tome 37*, Octobre 1976, C4-49

[7] Barsan, N.; Weimar, U.; *Journal of Electroceramics, 7*, 2001, 143-167.

[8] Morrison, S.R.; *Sensors and Actuators* 2, 1982, 329-341.
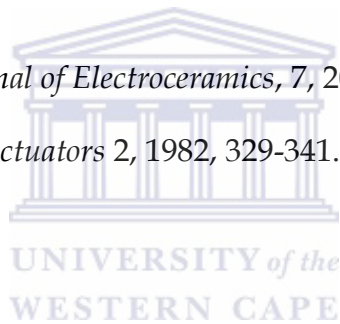
CHAPTER TWO:

VO$_2$, PHYSICAL-CHEMICAL PROPERTIES

2.1 Overview

2.1.1 Introduction

Transition elements are formed by the electron filling of the 3d, 4d and 5d shells with a position between the s-block and the p block elements in the periodic table. Their properties are transitional between reactive metallic elements of the s-block forming ionic compound and elements of the p-block that are largely covalent [1]. The addition of the electrons to the penultimate shell expanding it from 8 to 18 electrons normally characterizes these d-elements which give rise to many physical and chemical properties. They present good conductivity of electricity and heat with a metallic lustre, hardness, strength and ductility and they are able to form alloys with other metals such as element in transportation (automotive, aviation and aerospace where aviation and space flight are considered). Amongst transition elements, Vanadium (chemical symbol V) is a relatively rare metal that occurs naturally in about 65 different minerals and fossil fuel deposits. It is typically produced in limited quantities either from steel smelter slag, from the flue dusts of heavy oil or as a byproduct of uranium mining. Roughly 60,000 tons of contained vanadium was produced globally in 2011 and 97% of that production came from South Africa. Vanadium is usually introduced as a metal capable of beautiful color changes when it passes through its various oxidation states due to the d-d electronic transition, charge transfer spectra and from defects in the solid [2]. Vanadium has an unparalleled tendency to form coordination compounds with Lewis bases i.e (groups that`s able to donate an electron pair. Those groups are called ligands.). The ability to form complexes is in contrast to the s-block and p-block elements. This is due to the fact that they have small, highly charged ions and have vacant low energy orbitals to accept lone pairs of electrons donated by other groups or ligands. See table 2.1.

Table 2.1: Electronic structure of Vanadium [1]

Element	Electronic structure		Oxidation states*
Vanadium	**V**	**[Ar]3d34s2**	(-I)(O)(I)(II)III **IV** V
Nobium	**Nb**	**[Kr]4d35s2**	(-I)(O)(I)(II)III (IV) **V**
Tantalum	**Ta**	**[Xe]4f145d36s2**	(-I)(O)(I)(II)III (IV) **V**

*The most important oxidation states (generally the most abundant and stable) are shown in bold. Other well-characterized but less important states are shown in normal type. Oxidation states that are unstable (or in doubt) are given in parentheses. The tendency to form single ionic compounds decreases as the oxidation state increases. The oxidation state (+IV) is the most stable and exist in a wide range of compounds both as solid and in solution. * The V^{3+} ion has a d^2 configuration occupying the t_{2g} orbitals i.edxy, dxz and dyz.*

2.1.2 Vanadium Oxides

Several Magneli phases exhibit a metal insulator transition phase (V_nO_{2n-1}) among which VO_2 (340K) and V_2O_3 (150 K) are the most studied. The reduction process is observed as: $V_2O_5 \rightarrow V_3O_4 \rightarrow V_4O_9 \rightarrow V_6O_{13} \rightarrow VO_2$ [3]. It was observed that in the vanadium oxides, the superimposed electrical and magnetic properties changes are accompanied by a latent heat and also by a reduction in crystal symmetry with discontinuous volume expansion on cooling through the transition temperature. The magnitude of semiconductor–metal transition is sensitive to the crystallinity and stoichiometry and presents a complexity of the phase diagram. The V_2O_5 compound is amphoteric but mainly acidic and it is generally used as metal alkoxide precursor to produce VO_2. It dissolves slightly in water giving a pale yellow acidic solution and readily in NaOH forming colourless solutions with a wide range of vanadate ions. The ions formed depend on the pH: various isopolyvanadates at intermediate pH and orthovanadate at high pH. Some reactions of V_2O_5 can be detailed as follows:

$$V_2O_5 + NaOH \text{ --------------various vanadates} \qquad Eq.2.1$$

$$V_2O_5 + H_2O_2 \text{ --------------peroxovanadates} \qquad Eq.2.2$$

$$V_2O_5 + Cl_2 \text{ -------------VOCl}_3 \qquad Eq.2.3$$

$$V_2O_5 + SO_2 \text{ --------------VO}_2 + SO_3 \qquad Eq.2.4$$

$$V_2O_5 + H_2 \text{ --------------VO}_2 + V_2O_3 \qquad Eq.2.5$$
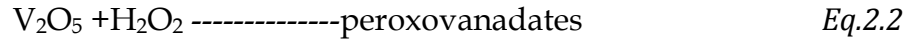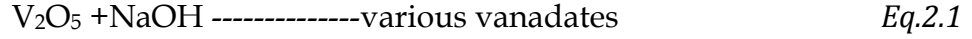
V_2O_5 consists of distorted trigonalbipyramids of VO_5 units sharing edges with other units to form zigzag double chains which derived by crystallographic shear translations with high degrees of distortion leading to the formation of layered crystal structure. See figure 2.1. The ability to reversibly lose or gain oxygen when heated is of great interest as a catalytic activity.
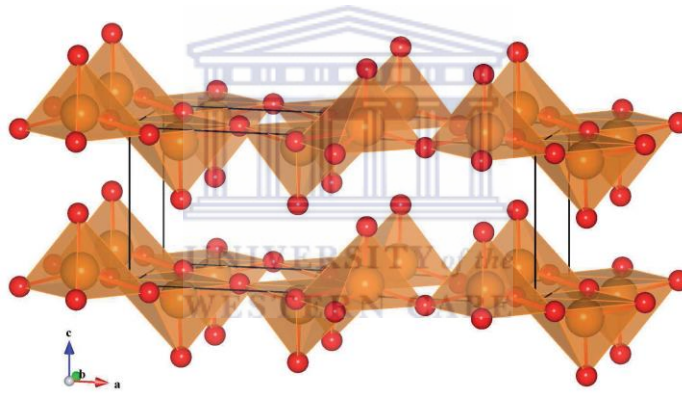
Figure 2.1: Crystal structure of V_2O_5 with the polyhedra (VO_5 square pyramid units), V is shown as orange and O as red spheres [4]

2.1.3 Ionic bonding and elastic properties

The information of stability of given vanadium oxide phase is described by the energy of formation per atom E_f with respect to the elements as:

$$E_f(V_xO_y) = \frac{E(V_xO_y) - (xE(V) + \frac{1}{2}yE(O_2))}{x + y} \qquad Eq.2.6$$

Hence the total energies of bcc vanadium and O can be calculated. See table 2.2

Table 2.2: vanadium valency oxygen content and energy of formation E_f for each phase as well as volume per atom V [4].

	VO	V_2O_3	VO_2	V_6O_{13}	V_4O_9	V_3O_7	V_2O_5
Valency	2	3	4	4.333	4.5	4.667	5
Oxygen content	0.5	0.6	0.667	0.684	0.692	0.7	0.714
Ef (eV/atom)	-1.778	-2.636	-2.770	-2.794	-2.766	-2.773	-2.733
V ($\mathring{A}^3$/atom)	9.169	9.687	9.897	11.545	11.858	11.838	13.051
B (GPa)	243.6	253.8	248.5	208.1	197.3	202.3	173.5
C_{44} (GPa) (i)	-88.6	165.2	155.1	74.7	78.6	75.5	40.2
B/C_{44}		1.54	1.60	2.79	2.51	2.68	4.32
B (GPa)	243.6	221.7	226.6	166.7	103.7	158.0	86.6
C_{44} (GPa) (ii)	-88.6	153.3	127.8	75.9	66.3	63.2	25.3
B/C_{44}		1.45	1.77	2.20	1.57	2.50	3.42

V represents the volume of the vanadium oxide, B is the bulk modulus and C_{44} is the elastic constant. B/C_{44} is function of vanadium valency and is used to measure the plasticity of the material. The large ratios value obtained show that vanadium oxides have lubricating properties. The elastic properties and decohesion energies are generally based on the electronic structure. In general vanadium oxides are characterized by ionic bonding due to the charge transfer from vanadium to oxygen. In VO_2 (P4mnm High symmetry), small regions are present with low electron density between the ions or rather between the V-O polyhedral. This implies relatively strong bonding. See figure 2.2.
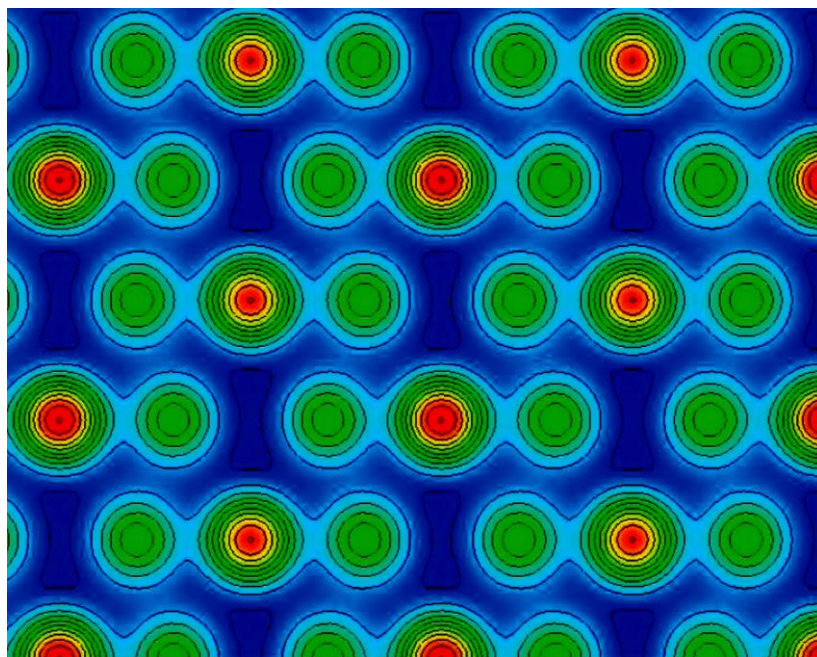
Figure 2.2: Ionic bonding due to charge transfer ions between Vanadium and Oxygen [4]

2.1.4   Vanadium Dioxide

VO_2 has attracted tremendous interest over almost half a century and is a benchmark problem of solid state chemistry because of its near room temperature metal semiconductor phase transition [5]. It presents a d^1 configuration in an oxidized form of the metal vanadium [6] where oxygen reacts with vanadium to form VO_2. The atoms form crystals that look like long rectangular boxes. The crystallography structure consists of vanadium atoms that line up along the four edges of the box in regularly spaced rows. A single crystal of VO_2 can have many of these boxes which line up side by side, and the crystals conduct electricity like a wire as long as they are kept warm. While other materials exhibit a similar electronic property, VO_2 is unique in that the change occurs at a relatively fast speed in less than a trillionth of a second. In recent years, scientists have put these quirky properties to work. VO_2 is a nonmagnetic, strongly correlated material which undergoes a reversible phase transition between a monoclinic insulator and a rutile metal, at a critical temperature T_c of 340K [7-9]. The

structure can be explained by pure Mott phase transition with Peierls electron-lattice distortion giving ultrafast transformation of the semiconducting monoclinic VO_2 to metallic rutile structure. Daniel P et al. [7] observed a corrobative existence for the two phase combination in VO_2 by using RMC simulation (See figure 2.3). This shows that the two dimensional histogram with the most probable positions of Vanadium cations in the a-c plane where V are spherical for T>340K and dramatic splitting are observed at T<340K. At 340 K, there is an intermediate shape distinct from the two regimes at either side.
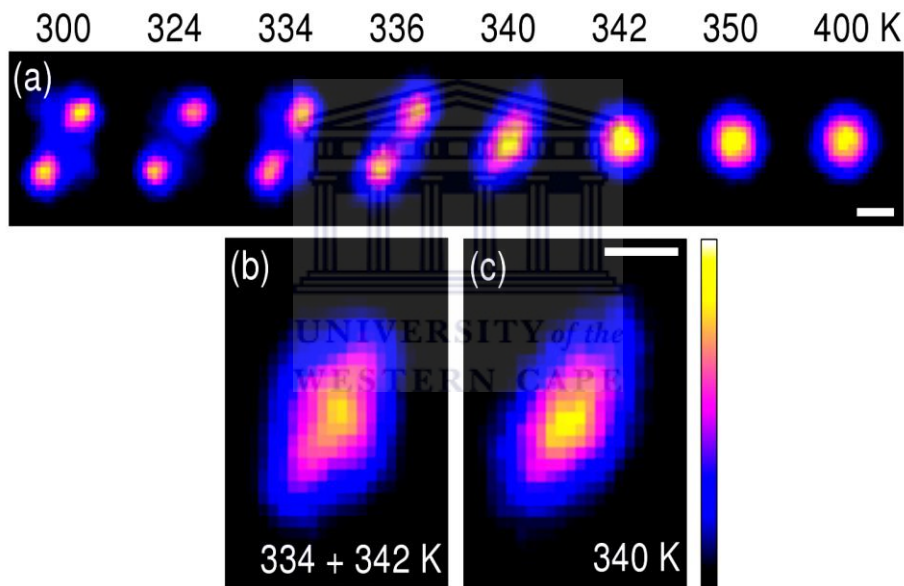
Figure 2.3: Probability of Vanadium atoms observed at T<,>, = 340K [7]

Generally electrons experience strong Coulombic repulsion because of their spatial confinement in the orbitals. The interplay of the d electrons internal degree of freedom, spin, charge and orbital moment make the material very sensitive to the small changes in external parameters such as temperature, pressure or doping. VO_2 has a blue-black colour metal oxide with high melting point of 1967 °C and a density of 4340 kg m^{-3}. It possesses a formula weight of 82.94 with a percentage of 38.58 in Oxygen and 61.42 in

Vanadium [10]. See table 2.3 below presenting crystal structures for some transitions metal oxide.

Table 2.3: Crystal Structural Classes of Some Common Transition Metal Oxides [11]

Sc_2O_3c s	TiO r* Ti_2O_3 cr TiO_2 t,a,b	VO r V_2O_3cr VO_2 t* V_2O_5 or	Cr_2O_3 cr CrO_2 t CrO_3 or	MnO r Mn_3O_4sp* Mn_2O_3cs* MnO_2 t* and others	FeO r Fe_2O_3cs, sp Fe_3O_4sp	CoO r Co_3O_4s p	NiO r	CuO s Cu_2O c	ZnO w
Y_2O_3cs	ZrO r ZrO_2m, tet	NbO_2 t* Nb_2O_5 mt	MoO_2 m (t*) MoO_3 l(or)	TcO_2 m, (t) Tc_2O_7 or	RuO_2 t	Rh_2O_3c r* RhO_2 t	Pd O s	Ag_2 O c	CdO r
La_2O_3 mt	HfO_2 m	TaO_2 t Ta_2O_5 or	WO_2 (m,t*) WO_3 m	ReO_2 m, (t) ReO_3 cub (perosvkite), Re_2O_7 or	OsO_2 t OsO_4 m	IrO_2 t	Pt_3 O_4 cub PtO_2 t		HgO or and others

r=rocksalt, c=interpenetrating cristobalite, l=layer, mt=multiple modifications, s=PtS structure, w=wurtzite, f=fluoride, tet=tetragonal, *= distorted or defective, t=rutile, cr= corundum, m= monoclinic, or=orthorhombic, a= anatase, sp= spinel, cub=cubic, b=brookite, cs=C structure

2.1.5   Solid state structure: crystallography, Lattice parameters.

VO_2 structure consists generally of six metals vanadium atoms coordinate and three oxygen atoms coordinate where all the bonds lengths are the same and all the oxygen

angles around the metal, u=0.293 and c/a=2u [11] (u is the coordinate of the metal with the oxygen at the origin.) are 90 °C in the rutile. The tetragonal lattice P4mnm presents regular VO_6 octahedron with slight elongation along its 4-fold axis with four (two) distances dv-o = 1.90 Å (1.95 Å) and a closed packed hexagonal lattice giving vanadium atom into close distance. Each vanadium atoms are located on (000) and (1/2 1/2 1/2) and is surrounded by 6 atoms of O (oxygen octahedron). Spacing in the tetragonal phase above the transition temperature suggests metal-metal bonding, and the conditions for a transition from cation clustering to the formation of narrow cation sub-latticed bands were argued and shown to be satisfied by VO_2 [12-13]. The Low-temperature VO_2 has the monoclinic ($P2_1/c$) structure. See Fig. 2.4. A striking feature of this monoclinic phase is the presence of cation-cation pairs along the $a_m = 2c_r$, axis with alternation of V-V separations which are 2.65 and 3.12 Å in place of the regular 2.87 Å. The oxygen are located at ± (u, u, 0) and ± (1/2+u, 1/2 –u, 1/2) [13]. Three distances are present for dv-o each in the range 1.76 - 1.87 Å and 2.01 - 2.05 Å, respectively and angles ($\widehat{OVO}$) vary between 78° and 99° [14]. Heckingbottom and Linett [15] were the first to emphasize the second significant feature of the low-temperature structure which represents the antiferroelectric distortion, coinciding with the displacement of cation from the center of its interstice toward one or more anions characteristic of a ferroelectric type distortion, giving one shortest vanadium oxygen (V-O) separation R= 1.76 Å perpendicular to the c axis. The two bridging oxygens O between paired vanadium ions have R= 1.86, and 1.87 Å. The other three cation-anion distances are R = 2.01, 2.03, and 2.05Å.
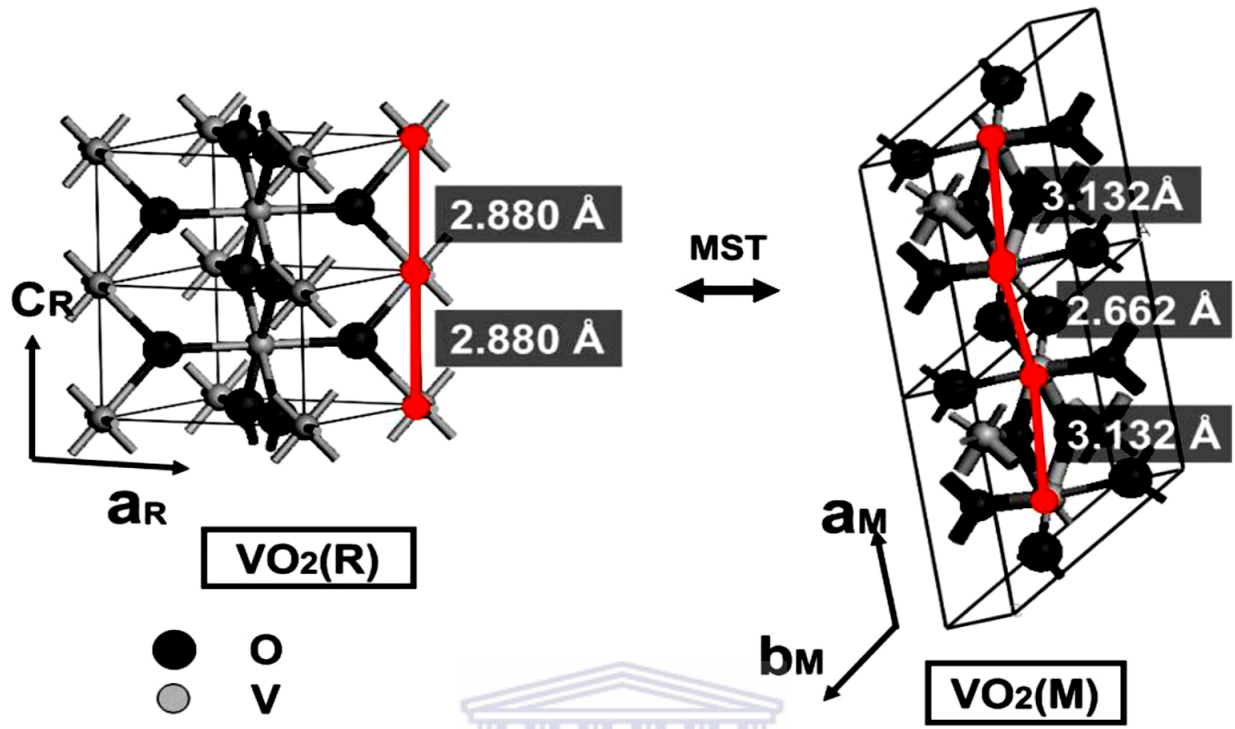
Figure 2.4: Geometry of vanadium: Prototypical Structure VO_2 [16]
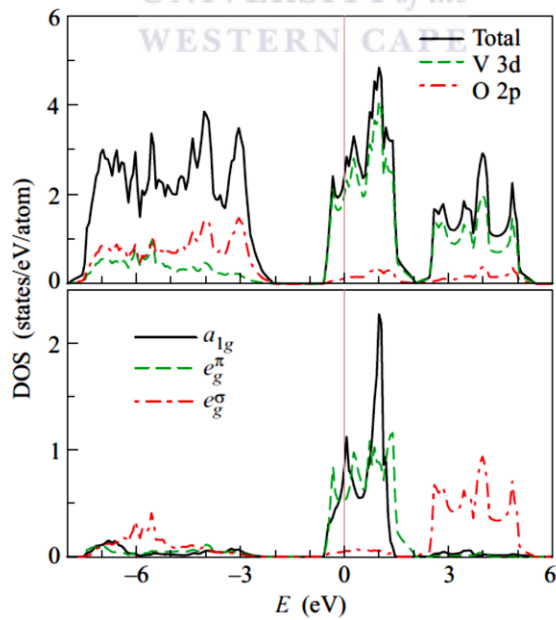
Figure 2.5: LDA density of states of vanadium atoms V 3d and O 2p doses [17]

Belozerov et al. [17] calculated the electronic structure of VO_2 showing that the states crossing the Fermi level are of vanadium t_{2g} symmetry spreading from -0.5 to 2 eV and they are separated by a gap of 1.4 eV from occupied bonding states of O 2p and V e_g^σ character. The DOSes for vanadium atoms presented at the bottom panel of figure 2.5 shows that the a_{1g} state is more narrow than π one and has one dimensional like shape. The electron belonging to a_{1g} state presents jumping to the same orbital on the nearest neighbor atom with largest hopping and smaller probability of the electron to hop to another chains. The hoppings are described through energy splittings between peaks and the remaining structure gives the asymmetry of density of states and its broadening while the structure of the π hoppings is uniform with 3 dimensional shape of density of states.

According to Nihoul et al. [18], all the VO_2 structures are based on a bcc oxygen lattice with some vacancies for the A and B structures. The stoichiometry VO_2 is obtained by only the filling of 1/6 of the sites by vanadium atoms and the association of the three octahedral sublattices is obtained by the translations of the oxygen lattice vectors: [1/2,0,0]x, [0,1/2,0]y, [0,0,1/2]z. The vanadium atoms were obtained through the ordering model of Static Concentration Waves (SCW) which calculates the occupancy probabilities of each site as Fourier series on the reciprocal space vectors [19]. The possible structures correspond to the negativity of the configuration energy variation. In the case of vanadium atoms, two sublattices can be occupied while the other one is completely vacant or one is occupied while the two others are vacant. In the case of VO_2 R where $n_x=n_y \neq 0$, and $n_z = 0$, we have two successive orderings introducing wave vectors k=½, ½, 0 and k =1/2, - 1/2, 0 giving a site of occupation of:

$$n_x(R) = \frac{1}{4} + \frac{1}{4}exp[i2\pi x] + \frac{1}{4}\{exp[i\pi(x + y)] + exp[i\pi(x - y)]\} \qquad Eq.2.7$$

$$n_y(R) = \frac{1}{4} - \frac{1}{4}exp[i2\pi x] + \frac{1}{4}\{-exp[i\pi(x + y)] + exp[i\pi(x - y)]\} \qquad Eq.2.8$$

$$n_z(R) = 0 \qquad Eq.2.9$$

X and y are the oxygen coordinates of an atom. In the case of (001) plane of rutile, all x and y are integers and for n_x= 0, x+y is odd while n_y= 0 for all x and y. The rutile structure is obtained for three successive orderings described as: $\left(V_{1/4}\,\square_{3/4}\right)_{x'}$ $\left(V_{1/4}\,\square_{3/4}\right)_{y'}$, $(\square)_z$ O where $\square$ stands for a vacancy. It corresponds to a large decrease in energy. In the case of the second possibility, n_x= n_y= 0, and $n_z \neq 0$, the dominant wave vector according to Leroux [20] is given as: k = 1/3 [1,-1, 2] which leads to a decrease in energy and a site occupation of:

$$n_x(R) = n_y(R) = 0 \qquad\qquad Eq.\,2.10$$

$$n_z(R) = \frac{2}{3} - \frac{2}{3}\left[\frac{cos2\pi(x - y + 2z)}{3}\right] \qquad\qquad Eq.\,2.11$$

Which means that the vacancies are located on every third (1,-1, 2) plane when x-y+2z=3p, p is an integer. The minimization of energy for other VO_2 is given for a wave vector such that k=H/n, where H is the reciprocal lattice vector and n = 2, 3 or 4. The minimization obtained is k = 1/3 [1, 1, 2] which restores a tetragonal symmetry giving: $V_{4/9}\,\square_{5/9}$ O, i.e V_4O_9 and VO_2(A) where one oxygen is not stable. Here VO_2 (A) is also $\left(V_{4/9}\,\square_{5/9}\right)\left(O_{8/9}\,\square_{1/9}\right)$ different from VO_2 (B). Both structures present a decrease in energy smaller than for VO_2 (R). Another wave vector which generates other ordering is given by: k'= 1/9 [219] where one oxygen atom is not stable. Hence a vacancy will be created at that site resulting in VO_2 (B). Hiroyuki Horiuchi et al [21] describe the interatomic distances of the oxygen atoms on the shared faces and edges of VO_6 octahedra which are generally smaller than those of the oxygen atoms at the shared corners while the V-O distances of oxygen atoms on the shared corners are smaller than those of the oxygen atoms on the shared faces and edges. These interatomic distances are clear for V_7O_{13}. The O-V-O angles of oxygen atoms on the shared faces and edges of VO_6 octahedra are generally smaller than those of oxygen atoms at the shared corners. The mean V-O and O-O distances for VO_6 octahedra of V_nO_{2n-1} are listed in the table 2.4.

Table 2.4: Interatomic distances and angles of the mean V-O and O-O distances [21]

		V_2O_3	V_3O_5	V_4O_7	V_5O_9	V_6O_{11}	V_7O_{13}	IVO_2	$II\ VO_2$
Mean of V-O (Å)	OCT1 OCT2 OCT3 OCT4	2.010	1.999 2.018	1.9777 1.974	1.969 1.969 1.951	1.964 1.967 1.955	1.964 1.959 1.942 1.947		
								1.937	1.925
Mean of O-O	OCT1 OCT2 OCT3 OCT4	2.832	2.794 2.849	2.765 2.786	2.752 2.776 2.762	2.743 2.774 2.762	2.744 2.757 2.743 2.753		
								2.728	2.721
Svo	OCT1 OCT2 OCT3 OCT4	2.2	5.6 2.1	5.8 3.2	6.2 4.2 1.0	6.9 4.5 2.2	6.9 5.0 2.5 1.2		
								5.9	0.3
Soo	OCT1 OCT2 OCT3 OCT4	3.9	5.9 4.1	5.4 3.4	5.2 3.5 2.9	5.4 3.8 2.8	5.1 3.5 2.8 2.8		
								3.0	3.1
Sovo	OCT1 OCT2 OCT3 OCT3 OCT4	6.6	11.7 5.2	11.5 5.4	11.4 6.7 3.5	11.7 6.6 3.9	11.7 6.5 4.3 3.5		
								6.8	4.0

The mean values for the pairs of the octahedra are classified under OCT1 for V1and V2, OCT2 for V3 and V4, OCT3 for V5 and V6, and OCT4 for V7 and V8. The mean values V-O and O-O distances are much smaller in VO_2 than any other phases. It was noted that the arrangements of oxygen atoms for VO_2 are denser comparing to V_2O_3. This can be explained as the size of the octahedra is affected by the strong V-V interactions across the shared faces and edges especially in OCT1 and OCT2 which affect also the octahedral configuration of oxygen atom around vanadium atoms. This effect is expressed by s_{oo}, s_{vo} and s_{ovo} by the following equations:

$$S_{oo} = \frac{100}{\bar{A}} \left[\frac{\sum_{i=1}^{12}(A_i - \bar{A})^2}{11} \right]^{1/2} \qquad\qquad Eq.\,2.12$$

$$S_{oo} = \frac{100}{\bar{B}} \left[\frac{\sum_{i=1}^{6}(B_i - \bar{B})^2}{5} \right]^{1/2} \qquad\qquad Eq.\,2.13$$

$$S_{oo} = \frac{100}{90} \left[\frac{\sum_{i=1}^{12}(C_i - 90)^2}{11} \right]^{1/2} \qquad\qquad Eq.\,2.14$$

Where A_i, B_i and C_i are the O-O, V-O, distances and O-V-O angles in each octahedra, $\bar{A}$ and $\bar{B}$ are the mean values and the summations in the equations are calculated for all combinations. s_{oo} (distortion from regular oxygen octahedra), s_{vo} and s_{ovo} (consider distortion and displacement of vanadium atoms form the centers of the oxygen octahedra) represent the standard deviations of the distances of O-O and V-O and angles O-V-O for each octahedron. The change of s_{oo} becomes slightly smaller and those of s_{vo} and s_{ovo} become greater for the phase with larger n values. Smaller expansion and distortion of oxygen octahedra with great displacement of vanadium atoms from the center of octahedra are observed for wide structure V_6O_{11} or V_7O_{13}. But we observed greater expansion and distortion for narrow structure V_3O_5 or V_4O_7 with smaller displacement of vanadium atoms. The displacement of vanadium is small for high temperature VO_2. However low temperature VO_2 presents great displacement of vanadium atoms though the distortion of vanadium of octahedra is small. Alder and

Brooks [22] show that the absence of electron correlation accounts for a first order transition giving a quantitative relationship between the T_t and the energy gap. See figure 2.6.

$$E_{g0}/KT_t = 8.10 \hspace{4cm} Eq.\,2.15$$
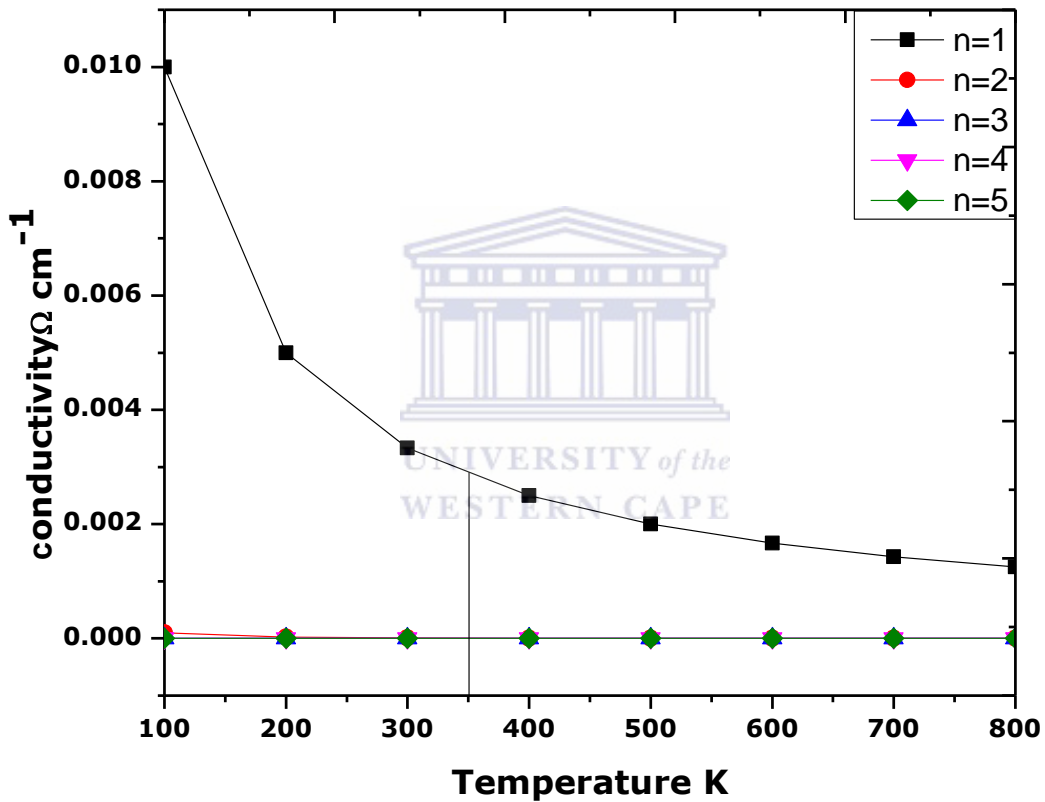
Figure 2.6: Conductivity versus temperature

However this is too large relative to T_t= 341K eliminating cation clustering as driven mechanism responsible of the transition. Several theories have been used to predict the conductivity dependence temperature. Here we plotted $\sigma \sim 1/T^n$ with 1<n<5. We can see that the curves display the same data between 100 and 800K. Only n_1 cannot be fitted with any straight line. Hence no single activation energy is present. The curves $T^{-1/2}$,

$T^{-1/3}$, $T^{-1/4}$ give good fit to straight lines with two segments. Temperature dependence on narrow band gap semi-conductor factors are thermal expansion and interactions of phonon-electron which can be calculated by the EPP (Empirical Pseudopotential Parameters) using Varshni`s equation:

$$E_g(T) = E_0 - \frac{\alpha T^2}{\beta + T} \qquad\qquad Eq.\,2.16$$

α, β are fitting parameters constants, characteristic of a given material which predicts quadratic temperature dependence at low temperature. However the phonon contribution to the energy shift coincides with the equation:

$$E_g(T) = E_B - a_B \left[1 + \frac{2}{exp(\theta/T) - 1} \right] \qquad\qquad Eq.\,2.17$$

Where E_B and a_B are constants and θ describes the average phonon frequency and the energy threshold decreases linearly by a term proportional to an average Bose Eistein statistical factor for phonon emission and absorption. KP O`Donnell et al. [23] advocate a new equation as a direct replacement of Varshni equation using the vibronic model of Huang and Rhys to derive expressions for the thermodynamics functions as:

$$E_g(T) = E_g(0) - S\langle \hbar\omega \rangle \left[coth\left(\frac{\langle \hbar\omega \rangle}{2kT} \right) - 1 \right] \qquad\qquad Eq.\,2.18$$

S is a dimensionless coupling constant, $\langle \hbar\omega \rangle$ phonon energy, $E_g(0)$ is the band gap at zero temperature. The entropy and enthalpy of formation electron hole pairs can be obtained considering that the standard Gibbs energy is identified to the band gap energy [24-25] giving:

$$E_g(T) = \Delta E_{CV} \qquad\qquad Eq.\,2.19$$

$$\Delta S_{CV} = -\frac{d}{dT}\Delta E_{CV} = \frac{S\langle \hbar\omega \rangle^2}{2k}\left(\frac{csch(\langle \hbar\omega \rangle)/2kT}{T} \right)^2 \qquad\qquad Eq.\,2.20$$

For high temperature:

22

$$\Delta S_{CV} \qquad \rightarrow \qquad -2Sk \qquad\qquad Eq.2.21$$

(Si: Eg=1.17 eV), S =1.49,$\langle\hbar\omega\rangle = 25.5$ Mev. The temperature dependent electron-phonon interactions determine effectively semiconductor band gaps for the band gap reflect the bond energy. An increase in temperature induces changes in chemical bonding as electrons are promoted from valence band to conduction band. The lattice phonons are generally small energies and are excited in large numbers at moderated temperature. The lattice contribution expression is given as:

$$\Delta E_{g(lattice)} = -\left[\frac{\partial E_g}{\partial p}\right]_v . B\frac{\Delta V(T)}{V_0} \qquad\qquad Eq.2.22$$

$$B\frac{\Delta V(T)}{V_0} = \gamma\frac{\bar{E}}{V} \qquad\qquad Eq.2.23$$

Which is the mean thermal energy of the sample depending on the bulk modulus B, and lattice volume V_0 and $\Delta V(T)$. For a single effective mode, the mean thermal energy is given by:

$$\bar{E} = \hbar\omega_0[n(\omega_0 T) + 1/2] \qquad\qquad Eq.2.24$$

(Lattice dependence temperature)

The high temperature tetragonal rutile structure presents$O^{-2}$with three coplanar bear neighbor cations and the anion $p_\pi$orbitals are directed perpendicular to the plane. The electrostatic Madelung energy E_M for the effective charge ions is observed to stabilize the O^{2-} : 2p orbitals relative to V^{4+}: 3d orbitals even after ionization of the cation and electron affinity of the anion which reduce the stabilization energy. Figure 2.8 a) presents energy levels for ionic V^{4+} and O^{2-} with crystal field splittings of the 3d band and 2p levels. The $3d^1$ energies of V^{4+} are split into two less stable twofold degenerate states of e_g symmetry and more stable threefold degenerate states of t_{2g} symmetry. The two e_g orbitals are split into two d_σ orbitals and the three t_{2g} orbitals into $d\pi$ orbital which mix with the anion p_π and $d_{//}$ orbital parallel along the c_r axis. 3d electrons in

23

oxides are generally itinerant, or localized, depending on the strength of the interaction which is the transfer energy, giving by:

$$\left(\Psi_i, \mathcal{H}\Psi_j\right) \approx \varepsilon\left(\Psi_i, \Psi_j\right)$$ $Eq.\,2.25$

Where $\mathcal{H}$ is the perturbation of the potential at Rj due to the presence of a near neighbor cation at Ri and ε is the electron energy.

2.1.6 Theoretical models for correlated metals and Mott insulators in d-electrons systems

The transition metal ion constructed via atomic orbitals is presented as eigenstates under spherical potential. When the solid is formed, the atomic orbital forms bands due to the periodic potential of atoms. The bandwidth is basically determined from the overlap of two d orbitals on two adjacent transition metals each and the overlap comes from the tunneling of two adjacent so-called virtual bound states of d orbitals. Due to the small radius of the wave function, compared to the lattice constant in crystals, d-electron systems have in general smaller overlap and hence smaller bandwidths than alkaline metals. The overlap is often determined by indirect transfer between d orbitals through ligand p orbitals. This means that the bandwidth is determined by the hybridization of the d wave function at a transition metal atom and the p wave function at the adjacent ligand atom if the ligand atoms make bridges between two transition-metal atoms. Because of this indirect transfer through ligand atomic orbitals, the d bandwidth becomes in general even narrower. Another origin of the relatively narrow bandwidth in transition-metal compounds is that 4s and 4p bands are pushed well above the d band, where screening effects by 4s and 4pelectrons do not work well. This makes the interaction relatively larger than the bandwidth. In any case, because of the narrow bandwidth, the tight-binding models constructed from atomic Wannier orbitals provide a good starting point. The fivefold degeneracy of the 3d orbital (L=2: Lz =2, 1, 0, 1, 2) with a total of tenfold degeneracy including spins, is lifted by the anisotropic crystal field. In transition-metal compounds, a transition-metal atom is surrounded by ligand atoms to help in the formation of a solid through the increase in cohesive energy

by covalent bonds of the two species. Because the ligand atoms have a strong tendency towards negative valence, the crystal field of electrons in the direction of the ligand atom is higher than in other directions. When a transition-metal atom is surrounded by ligand atoms with an octahedron configuration, the e_g orbital has anisotropy with larger amplitude in the direction of the principle axes, namely, toward neighboring ligand atoms. The basis of these orbitals may be expanded by $d_{x^2-y^2}$ and $d_{3z^2-r^2}$ orbitals. See figure 2.7 b). On the other hand, the t_{2g} orbital has anisotropy with larger amplitude of the wave function toward the other directions and it is represented by the dxy, dyz, and dzx orbitals. For tetrahedral surroundings of ligand ions, e_g orbitals lie lower than t_{2g} which is in contrast to cubic symmetry or octahedron structure. Only a few bands (formed from 3d orbitals from compounds such as Ti, V, and Cr) are occupied by electrons per atom. Therefore the t_{2g} orbital (more precisely, the t_{2g} band under the periodic potential) is the relevant band for low-energy excitations in the case of the above mentioned octahedron structure because the Fermi level crosses bands mainly formed by t_{2g} orbitals. By contrast, in transition-metal compounds with heavy transition metal elements such as Cu and Ni, the t_{2g} band is fully occupied far below the Fermi level, and low-energy excitations are expressed within the e_g band, which is formed mainly from e_g atomic orbitals. In the case where t_{2g} or e_g orbitals are filled partially, this generally leads again to degeneracy of the ground state, which frequently induces the Jahn-Teller effect to lift the degeneracy [26]. The interaction of *dxz* and *dyz* orbitals with the *pz* orbitals of oxygen ions leads to the formation of coordination (donor–acceptor) πbands, hence, the formation of π and π* bands by bonding and antibonding molecular orbitals in the macroscopic crystal. The π* band formed by antibonding π* orbitals is almost empty inthe monoclinic phase (at room temperature), being separated from the nearest filled band by a gap of 0.7 eV. The orbital of the vanadium ion is in the plane of the oxygen octahedron's base and does not form bonds with oxygen ion orbitals due to the zero overlap integral with them [14]. However, due to the overlap of this orbital with a similar orbital of the vanadium atom at the center of the neighboring octahedron's base, an additional $3d_{||}$ band split in the low temperature (monoclinic)

phase into two subbands appears in the vanadium dioxide energy spectrum. The bottom subband is almost completely occupied by electrons; the upper subband separated from the bottom one by a gap of 2.5 eV is almost empty and it is also well above (~2.3 eV) the Fermi level. [27]
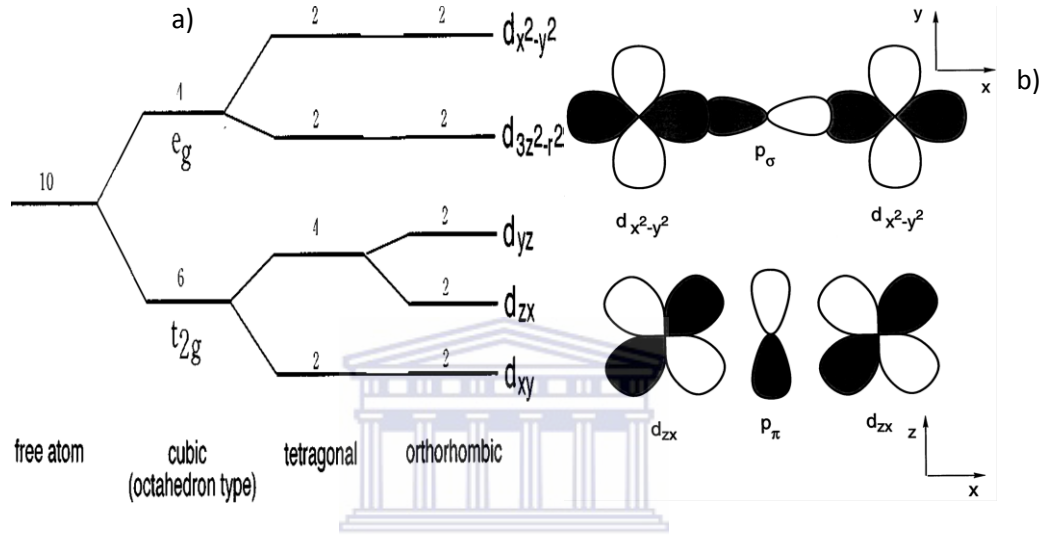
Figure 2.7 Crystal field splitting of VO_2 a) and atomic orbitals of VO_2 b) [26]

In the R phase, the t_{2g} levels in the octahedral crystal field are further split into $d_{//}$ and Π^* levels in the R phase, comprising the electronic states near the Fermi level of the metallic state. Here, the $d_{//}$ orbitals are rather nonbonding, while the Π^* orbitals are strongly hybridized with the O 2p, state and hence lie higher than the $d_{//}$ level. In the insulating M1 phase, the pairing of the V atoms along the c_R axis promotes the 3d-2p hybridization and upshifts the Π^* band off the Fermi level, as well as causing bonding-antibonding splitting of the $d_{//}$ band as shown in the right panel of figure 2.8.
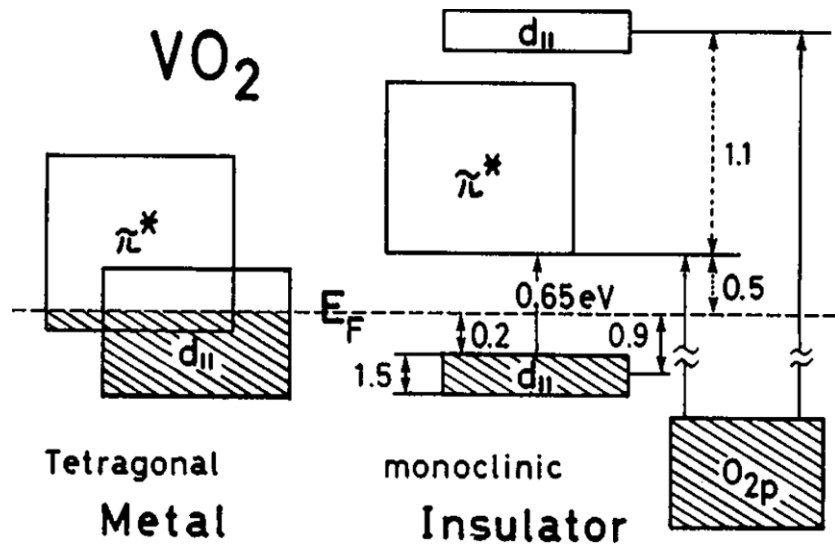
Figure 2.8: Electron band structure for tetragonal and monoclinic VO_2 [27]
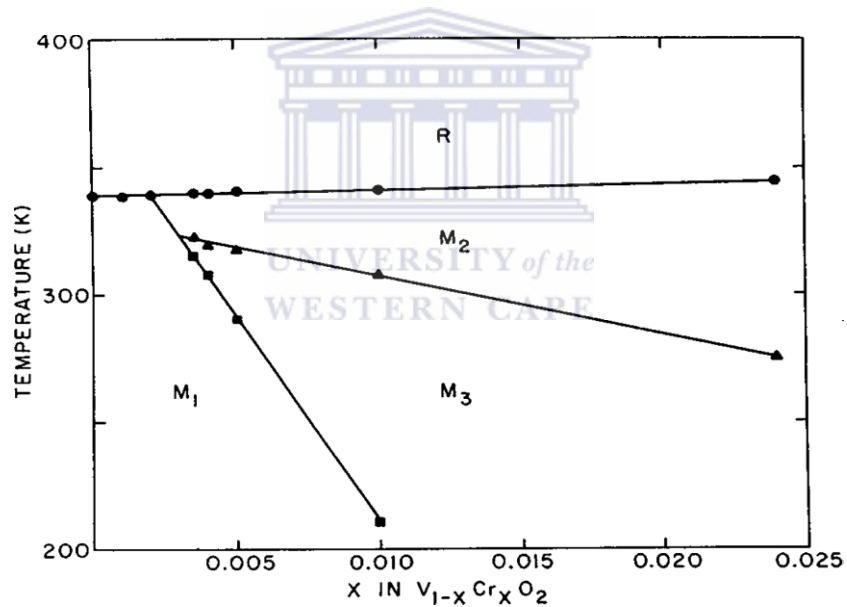
Figure 2.9: T-x phase diagram for $V_{1-x}Cr_xO_2$ according to Marezio [28]

The T-x phase diagram for $V_{1-x}Cr_xO_2$ is presented in Fig. 2.9. Two other distinct phases emerge, the insulating monoclinic M2 and the triclinic T phase, in addition to the aforementioned metallic R and insulating (nonmagnetic) M1 phases. Uniaxial pressure also gives rise to the M2 and T phases and leads to a similar phase diagram [29]. The exact mechanism by which the T and M2 can stabilize, was possible more directly by

applying a uniaxial stress in the (110) $_R$ direction. They observed that the M2 and M3 phases are alternative phases which under a critical stress Sc ~100-300 bars appear small that the free energy are extremely close to M1 at temperatures below the metallic rutile phase in pure VO_2. The M2 phase represents two kinds of V. Thus it is clear that these V chains in M2 are Mott-Hubbard insulators.

2.1.7   Metal-Insulator transition (MIT)

2.1.7.1   MIT Models

Oxides of the 3d transition series can be classified as they are metallic at all temperatures (TiO), semiconducting at all temperatures (NiO) or undergoing semiconductor ↔metal phase transition on heating through a critical temperature [30]. Further, it seems probable owing to the smallness of the splitting effected by the lower symmetry components of the anion field that two or more partially overlapping d-subbands are involved in the conduction for T >Tt.

Metal-semiconductor phase transition can be described through different models:

- Antiferromagnetic state on cooling where the antiferromagnetic state of the material becomes metallic according to band theory where the exchange field associated with the long range magnetic order splits the half-filled band into a filled and empty subband separated by a gap providing Tt to be T_N due to the vanishing of the intercationic exchange splitting.

- Reduction in crystal symmetry where Goodenough attributed the non-metallic nature of the oxides is due to the existence of homopolar bonds between d-electrons on neighbouring cation pairs where the cations are displaced from their positions they occupied at T>Tt. The transition was classified as cooperative. This is interpreted as an increase in number of the cations per primitive cell on entering the displaced lower symmetry phase where the partially filled band is split into two subbands separated by a gap: the lower regarded as the bonding band and the upper band the antibonding band. The transformation of the structure through a

finite temperature with concomitant collapse of the bonding–antibonding gap shows that the low temperature phase is regarded as distorted for the high temperature. The stability of the distorted structure requires a decrease in electronic energy on entering this phase to dominate the strain energy which is in quadratic form in the distorsion.

- Coulomb correlations between carriers are used to describe the nonmetallic ground states of metal-insulator transition. Frölich [31] demonstrated that the coulomb correlations were responsible of the establishment of Mott insulating ground state which turns the thermal ionization of the localized electrons into delocalized band states which leads to a cooperative process. For through screening effects, the ionization energy 2I become dependent on the existing degree of ionization the gap between the localized many electron states and the conductive continuum of band states decreases with excitation across it. As T→Tt, the gap decreases avalanches until at T = Tt and the screening provided by the already ionized electrons reduces the potential energy associated with the intracationic Coulomb repulsion U to a value comparable with the magnitude of the one- electron bandwidth W. I vanish (or becomes exceedingly small) and the population of the band states increases catastrophically, leading to a first-order phase transition into the metallic state. The second type of coulomb correlations can be explained as the establishment of the excitonic phase which involves the creation of a charge density wave coupling to the lattice causing therein instability and a resulting divergence in the static dielectric constant. These ideas conceived originally by Knox and Kohn [32-33] and developed by Jerome et al. [34] who demonstrate, in particular, the much less drastic (continuous) quenching of the electrical conductivity which is associated with this second-order phase transition. The excitonic phase is characterized either by an anti-ferromagnetic order or, in the case of strong carrier-phonon coupling by a lattice distortion; the realization of this latter possibility can change the order of the transition from second to first [35-36].

2.1.7.2   Density Functional Theory

Various microscopic properties of solids have been calculated using the Density Functional Theory (DFT) allowing the computation of the total energy giving in terms of the functional of the density as:

$$\Gamma[\rho(r)] = T[\rho(r)] + \int V_{ext}(r)\rho(r)d^3r + 1/2 \int \frac{\rho(r)\rho(r`)}{|r - r`|} d^3(r)d^3(r`) + E_{xc}\ [\rho(r)]\ Eq.\,2.26$$

The kinetic energy of the non-interacting system represents the first term, the potential energy of the crystal plus the Hartree contribution to the Coulomb interaction between the charges is the second term and the rest is the exchange and correlation energy term. The minimization of the Kohn-Sham equations which has the form of the one particle Schrödinger equations with a potential is given as:

$$V_{KS}(r) = V_{ext}(r) + \int \frac{\rho(r`)}{|r - r`|} d^3(r`) + \frac{\delta E_{xc}}{\delta \rho}[\rho(r)] \qquad Eq.\,2.27$$

The static mean field of the electrons serving as a reference system yielding the correct ground state density is described where:

$$\rho(r) = \sum_i f(\varepsilon_i)|\Psi_i(r)|^2 \qquad Eq.\,2.28$$

Where $f(\varepsilon_i)$ is the Fermi function. However, the DFT is only applicable in non-interacting single particle systems for many body interacting system. Neville Mott presented a real space picture of the strongly correlated materials at low temperature as a collection of localized electrons bound to atoms with open shells. The excited configurations are scattered via internal degree of freedom (orbital angular momentum and spin) which propagate through a crystal incoherently and broaden to form bands called lower and upper Hubbard bands [37]. According to the band theory, if the density of states vanishes then the system should have even number of electrons per unit cell and thus have completely filled bands. On the other hand, an odd number of electrons per unit cell give partially filled bands and thus a metal. Three subgroups

describe the insulator behavior (which is understood as interaction of single electrons with the electrostatic field of the ions in the crystal). Its interaction with the ions and the electron can be defined by an effective single particle Hamiltonian in the periodic potential of the ion: Bloch-Wilson insulator; For Pearls insulator, the electron-ion interaction produces lattice distortion that changes the periodicity of the crystal which in turn affects the electron transport. Anderson insulators are those in which the insulating behavior is produced by the interaction of independent electron with random lattice defects. The other main type of an insulator is the Mott insulator in which band theory and hence independent electron assumption fails. Mott insulators are characterized by correlated many-electron phenomenon and Coulomb interaction between the charge carriers. Mott insulators are generally classified as Mott-Hubbard, Charge Transfer (CT) and Mott-Heisenberg insulators. Strongly correlated materials, described by a simple Hamiltonian approach take into account few relevant degrees of freedom typically the valence electron orbitals near the Fermi level. The Hubbard Hamiltonian model is required to describe the electrons with spin directions σ ↑or ↓ moving with between localized states at lattices sites i and j. The kinetic energy and interaction energy are characterized by the hopping term t_{ij} and the local Coulomb energy U of repulsion. These terms compete due to the mobility of the electrons or the repulsion of the electrons each other localized on atomic different sites. The properties of a strongly correlated material describe by Hubbard model are function of the ratio U/W where W represents the bandwidth determined by the hopping t_{ij}.

$$H = \sum_{ij,\sigma} t_{ij} c_{i\sigma}^{\dagger} c_{j\sigma} + U \sum_i n_{i\uparrow} n_{i\downarrow;} \qquad\qquad Eq.\,2.29$$

Where the density of the electrons at site i with spin σ is given by:

$$n_{i\sigma;} = c_{i\sigma}^{\dagger} c_{i\sigma} \qquad\qquad Eq.\,2.30$$

The quantum spin liquids (without breaking of symmetries) are generally observed in Mott insulators with ground state not smoothly connected to the band insulator. The

excitations of spins are fractional (spinons) with superconductivity in Mott insulators and non-Fermi liquid phenomena in correlated d electrons metals. The Anderson impurity model yielding the exact local Green function for local one-electron photoemission spectrum in DMFT is given by:

$$H_{AIM} = H_{atom} + \sum_{v,\sigma} \varepsilon_v^{medium} + n_{v,\sigma}^{medium} + \sum_{v,\sigma} V_v c_{0,\sigma}^\dagger a_{v,\sigma}^{medium} + h.c \qquad Eq.\,2.31$$

Which describe the lattice`s site atomic degrees of freedom (first term), the remaining degrees of freedom are treated as a medium of electrons with energy levels ε_v^{medium}. Electrons hope in and out of the atomic site with the hybridization V_v energy of atomic $c_{0,\sigma}$ and the medium electron $a_{v,\sigma}^{medium}$. The hybridization function $\Delta(\omega)$ capturing the ability of an electron to enter or leave an atom on a time scale $1/\omega$ is given by:

$$\Delta(\omega) = \sum_v \frac{|V_v|^2}{\omega - \varepsilon_v^{medium}} \qquad Eq.\,2.32$$

Hence by introducing the local Green function of the correlated orbital, the DMFT provides an explicit approximation for E_{xc}:

$$\Gamma[\rho(r), G] = T[\rho(r), G]$$
$$+ \int V_{ext}(r)\rho(r)d^3r + 1/2 \int \frac{\rho(r)\rho(r`)}{|r - r`|} d^3(r)d^3(r`) + E_{xc} \; [\rho(r), G] \quad Eq.\,2.33$$

Where T [ρ,G] is the kinetic energy of a system with given density ρ (r) and local Green function G which gives the probability amplitude required to create an electron with spin up and down at site i at a time τ` and destroy it at the same time τ is given by:

$$G_{i\sigma}(\tau - \tau`) \equiv -\langle c_{i\sigma}(\tau)c_{i\sigma}^\dagger(\tau`)\rangle \qquad Eq.\,2.34$$

The Density of States (DOS) of electrons is generally given according to the local Coulomb interaction between them. When the electrons are entirely independent the DOS describe a free electron model having the form of a half ellipse with the level of Fermi located in the middle of the band. See figure 2.10 a). The weak correlated regime

presents weak potential U where electrons are considered as quasiparticles but the density of States still behaves as free electrons. See figure 2.10 b).
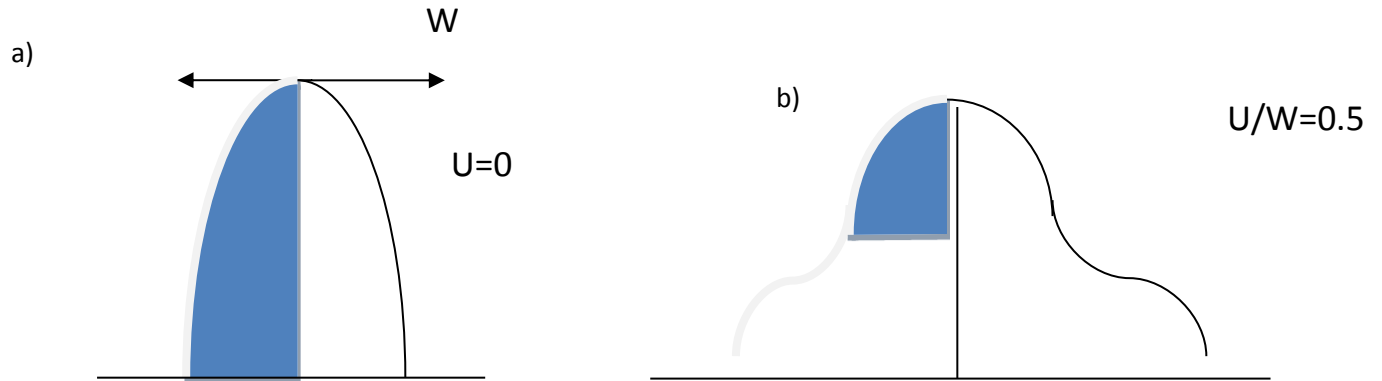
Figure 2.10: Free electron model a) and weak correlated regime b) [37].

In strongly correlated metals, the spectrum exhibits a characteristic three peaks structure : the Hubbards bands originating from local atomic excitations, and broadening by hopping electrons away the atom and quasi particle peak near the Fermi level. See figure 2.11.
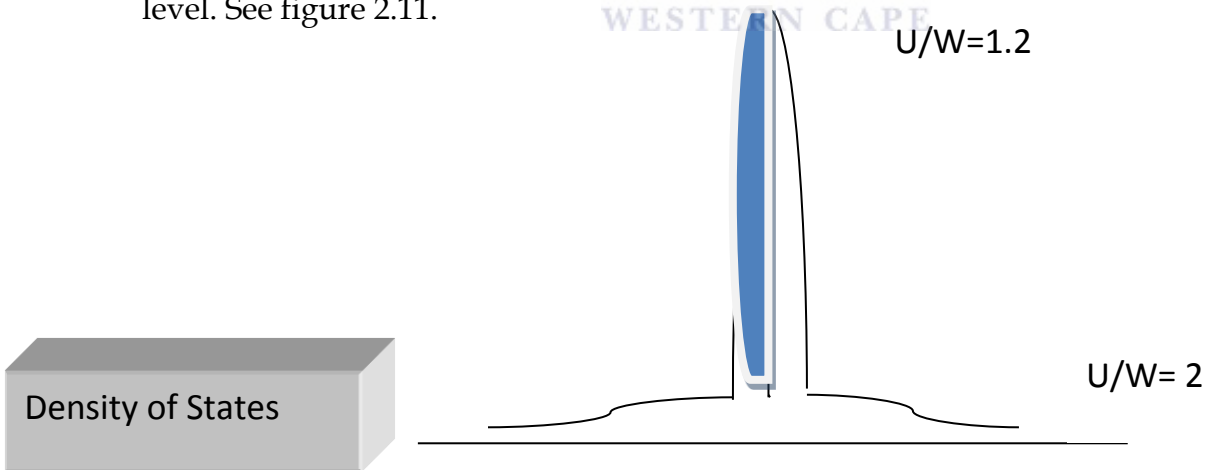
Figure 2.11: Strongly correlated material [37].
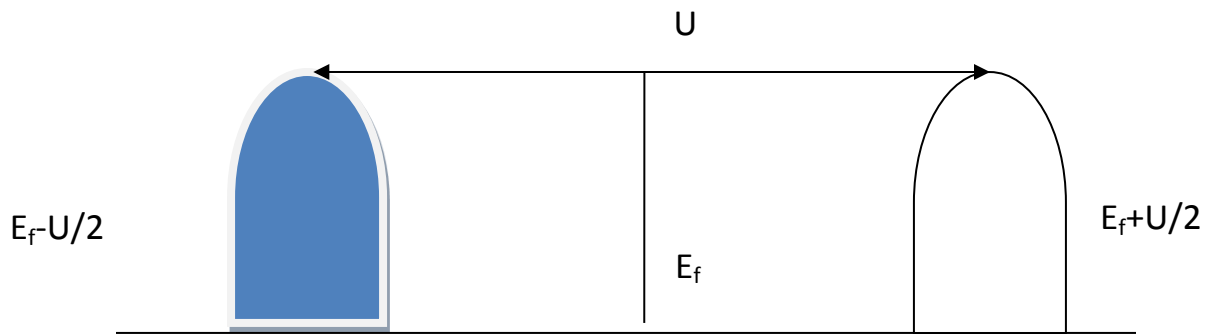
Figure 2.12: Mott insulator states [37].

The fourth state figure 2.12 describes the Mott-insulator transition when the electron interactions are sufficiently strong to cause the quasi particles peak to vanish as the spectral weight of the low frequency peak is transferred to the high frequency Hubbard bands. Phase change in correlated electron system is utilized in Mott field-effect transistor (Mott FET). Mott phase transition present in correlated electron materials can be triggered under applied field electric or by photo and thermal excitations for potential optical switches. It has been explored for the first time in cuprate oxide channel materials and VO_2 who attracted much attention recently due to the sharp transition metal-insulator with approximately five orders in single crystals. Experimental challenges with correlated electron oxide Mott FETs include fundamental understanding of gate oxide-functional oxide interfaces and local band structure changes in the presence of electric fields [38]. Understanding the electronic arrest mechanisms while de-coupling from structural Peierls distortions is of interest. A schematic phase diagram of a Mott insulator diagram is obtained. See figure 2.13.
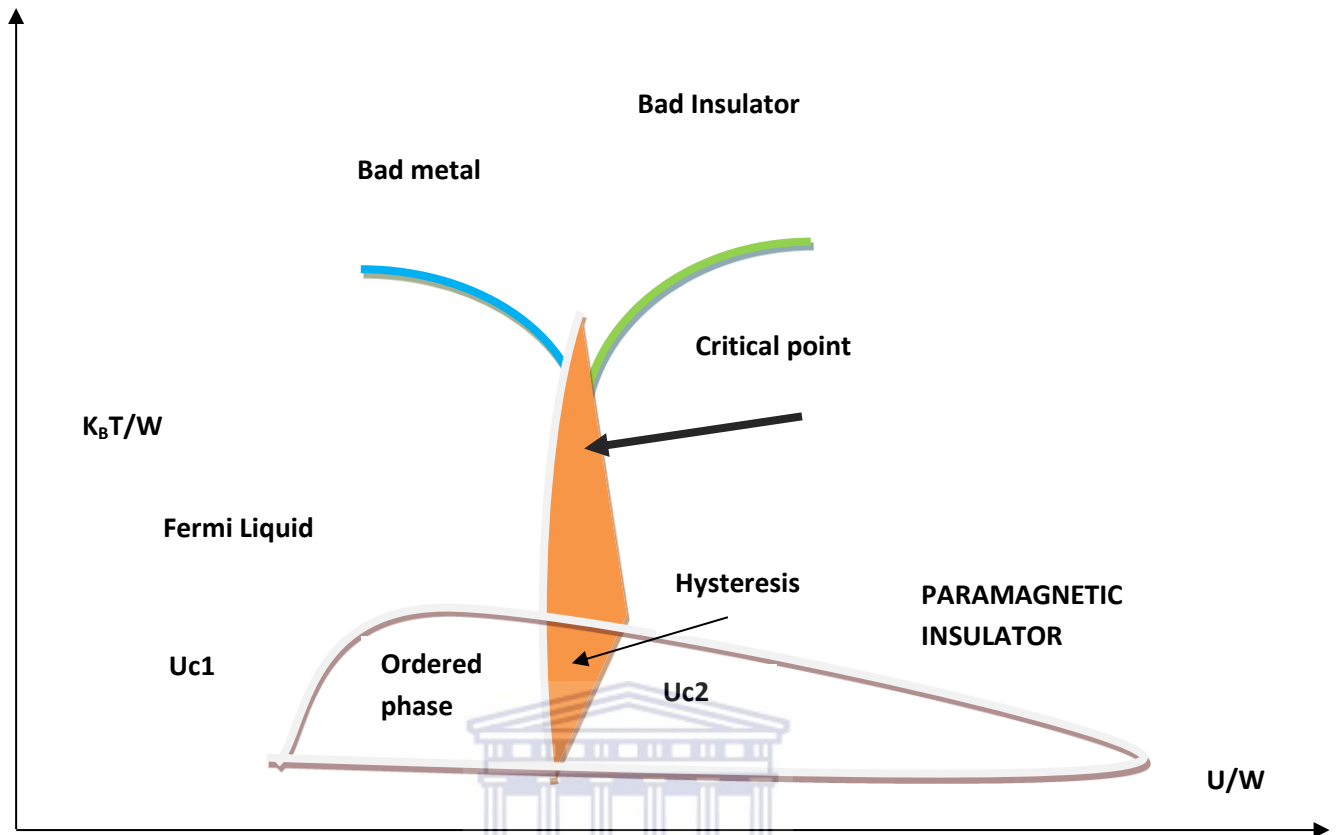
Figure 2.13: Mott insulator phase diagram [38].

At low temperature the material has long range order according to the solution of the DMFT. The type of ordering is material and model dependent. The presence of hysteresis is due to the two distinct paramagnetic solutions bounded by the lines U_{c1} and $U_{c2.}$ In equilibrium, a first transition order phase presents the cross of the two paramagnetic solutions. This first order transition terminates at a second order critical point where the material behaves with different crossover regimes which indicate the change in the material properties. The first regime presents the change from a Fermi liquid to a bad metal where the resistivity is anomalously large, while the second regime presents the properties of a bad insulator where the resistivity decreases as temperature increases.

2.1.7.3 Case of VO₂

The reduction of symmetry in VO_2 was described as a non collinear pairing up of cations which are equally spaced in the metallic phase along the c axis. It appears as an ideal candidate of distorted material with a paramagnetic susceptibility at low temperature. According to Frohlich model, Coulomb correlations cause a localization of d electrons on the body centered tetragonal lattice; the lowering in energy is achieved by electrons on successive c-axis cations which adopt antiparallel spins–pair wise antiferromagnetic order; the distortion of the lattice resulting in the formation of cation pairs is due to the cation valency and to the reduction in screening of the cation-anion interaction upon localization; the increase in overlap of the wave functions of the localized electron result from the displacement leading to pair wise delocalization of d-electrons into a homopolar bond. It was hence concluded that the transition in VO_2 is an excitonic phase change of first order according to the strong electron-lattice interaction [39]. This latter was described through the local density approximation across the metal-insulator transition describing the monoclinic structure as a distorted ground state and an almost open gap to charge excitations which doubles the cell size through V-V pairing and brings the number of structural degrees of freedom to 13. The metal – insulator transition in VO_2 was accounted to the strengthening of the vanadium d-d bonds which reorganize their state near the Fermi level hence denoting VO_2 as a band insulator. However the strong relation of VO_2 with the Mott insulator V_2O_3 with consideration of the spin excitations below the charge excitation gap of 0.6eV similar to singlet to triplet on vanadium dimers or deeply bound triplet excitons described VO_2 states according to Mott-Hubbard model. Grinolds et al. [40] used a four dimensional ultrafast electron microscopy of phase transitions describing through the imaging and diffraction the metal-insulator phase transition of VO_2 which is described as a correlation assisted Peierls transition or a renormalized Peierls insulator at low energies and a Mott-Hubbard insulator at high energy. They observed that the transition occurs

as a result of nonthermal excitation and that both the electron and optical pulses must be coincident.

2.1.7.4 Phase Transition Thermodynamic

We consider a binary system V-O which can exchange energy and matter with the environment. Considering the pressure is kept fixed, we denote the specific enthalpy ζ and the energy flux $\tilde{\omega}$. The principle of conservation of the energy gives:

$$\frac{\partial \zeta}{\partial t} = -\bar{\nabla}.\tilde{\omega} \; in \; Q \subset \mathbb{r}^3,$$

$$Eq. 2.35$$

Q represents the space confinement. For each component with concentration c_i and flux density $\bar{J_i}$ (i=1, 2). The conservation of mass without chemical reactions is given as:

$$\frac{\partial c_i}{\partial t} = -\bar{\nabla}.\bar{J_i}$$

$$Eq. 2.36$$

Let denote the S the specific entropy, T the absolute temperature and μ_1, μ_2 the chemicals potentials reactions of the two components of the system. The non-equilibrium thermodynamic system assumes the validity of Gibbs formula defines as:

$$dS = \frac{d\zeta}{T} - \frac{\mu_1}{T} dc_1 - \frac{\mu_2}{T} dc_2 \; for \; \zeta > 0, c_i \in [0,1]$$

$$Eq. 2.37$$

Hence : $\qquad \frac{\partial S}{\partial \zeta} = \frac{1}{T}, \frac{\partial S}{\partial c_i} = -\frac{\mu_i}{T} (i = 1,2), c_1 + c_2 = 1, \qquad \bar{J_1} + \bar{J_2} = \bar{0}$ $\qquad Eq. 2.38$

The entropy balance equation is given by:

$$\frac{\partial S}{\partial t} = -\frac{\bar{\nabla}.\tilde{\omega}}{T} + \frac{\mu.\bar{\nabla}.\bar{J}}{T} = -\bar{\nabla}.\bar{J_S} + \sigma ,$$

$$Eq. 2.39$$

Where the entropy flux is given by:

$$\bar{J_S} = \frac{\bar{\omega} - \mu\bar{J}}{T}$$

$$Eq. 2.40$$

And the entropy production rate is:

$$\sigma = \bar{\omega}.\nabla\frac{1}{T} - \bar{J}.\nabla\frac{\mu}{T} \qquad\qquad Eq.\,2.41$$

The second principle of thermodynamic is generally described by the Clausius-Duhem inequality where the irreversible process is satisfied for σ>0 and for a reversible process σ = 0. These equations are valid for a homogeneous system (solid, liquid or gaseous).

$$\sigma = \sum_{i=1}^{2} \bar{J}_i\,\bar{X}_i \qquad\qquad Eq.\,2.42$$

This equation describes a typical thermodynamic non-equilibrium system with two states of variables $\frac{1}{T}$ and $-\frac{\mu}{T}$. By introducing the Onsager reciprocity relations, through a symmetrical L (u) positive tensor, we have:

$$L(u) = \{L_{ij}(u)\} \qquad\qquad Eq.\,2.43$$

$$\begin{pmatrix} \bar{\omega} \\ \bar{J} \end{pmatrix} = \begin{pmatrix} L_{11} & L_{12} \\ L_{21} & L_{22} \end{pmatrix} \begin{pmatrix} \nabla\dfrac{1}{T} \\ -\nabla\dfrac{\mu}{T} \end{pmatrix}, L_{21} = L_{12} \qquad\qquad Eq.\,2.44$$

For heterogeneous systems let take as an example α and β, we consider two neighboring zones separating by a curve I. A first order phase transition takes place with the discontinuity of ζ and c across the surface with the jump conditions satisfied by:

$$c: n_t = \overline{[J]}.\overline{n_x} \qquad\qquad Eq.\,2.45$$

$$\zeta: n_t = [\bar{\omega}].\overline{n_x} \qquad\qquad Eq.\,2.46$$

The above equations are available on the interphase between the two phases denotes S where $\bar{n}_x$ and n_t $normal\ to\ S\ in\ the\ space\ and\ time.$ According to the free Gibbs formula, S=S (ζ, c), we denote his conjugate function S* (1/T, μ/T), we have:

$$dS* = \zeta d\frac{1}{T} - cd\frac{\mu}{T} \qquad\qquad Eq.\,2.47$$

On the physical interphase,

$$S\ dS^* = 0 \qquad\qquad Eq.2.48$$

$$\zeta d\frac{1}{T} - cd\frac{\mu}{T} = 0 \Leftrightarrow \frac{\zeta}{c} = \frac{d\left(\frac{\mu}{T}\right)}{d\left(\frac{1}{T}\right)} = \mu - T\frac{d\mu}{dT} \qquad Eq.\,2.49$$

Remark that $-\frac{\mu}{T} \to \pm\infty\ respectively\ for\ c \to 0\ ou\ 1$. The transition temperature can be obtained between the transition temperatures of the pure components. In the case of VO_2 the presence of an intermediate temperature denotes eutectic point or tricritical point with the competition of two solid phases with distinct crystal structures. See figure 2.14.
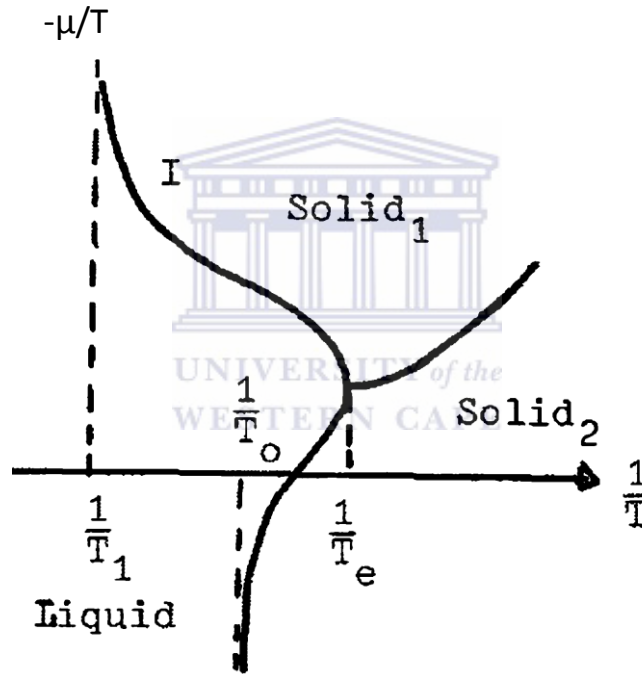
Figure 2.14: Competition between two solid phases [33].

Considering the contribution of electrons and lattices during the phase transition near the metal to insulator transition for Fermi statistics, the entropy is given as:

$$TS = kT\sum\left[nlog\left(\frac{1}{n} - 1\right) - \log(1 - n)\right] \qquad Eq.\,2.50$$

This is valid over all electron states. At low temperature, in the case of semisonductor,

$$TS = kT\left[\frac{5}{2}(N + P) + N\frac{E_C - E_F}{kT} + P\frac{E_F - E_V}{kT}\right] \qquad Eq.\,2.51$$

N and P represent the number of electron and holes per mole. In the case of metallic state, N= nV = 3.38 10^{-17}electrons /mole. In this section the value of entropy is negligible compared to the latent heat = 1kcal/mole.

The contribution of lattice thermodynamic is approximated through bose statistics such that:

$$TS = kT \int_0^{\infty} \sigma(\omega)d\omega \left[nlog\left(1 + \frac{1}{n}\right) + log(1 + n)\right] \qquad Eq. 2.52$$

It was showed that a 20% change in the lattice entropy would account for the entire latent heat while the electronic entropy contribution (460 cal/mol) is less than half of the latent heat (1020 cal/mol) which is not enough to cover the whole transition phase of the semiconductor VO_2 [41].

2.1.8 Vanadium Dioxide phases

The lattice symmetry is the driven force of the competition between several phases where the metallic phase lattice of vanadium oxide can 'fold' in different ways while cooling, so what people observed was different types of its folding [42]. Amongst the different phases of vanadium oxides, we have VO_2 (B) which is a metastable monoclinic form of vanadium dioxide with a space group C2/m and a crystal structure isotopic with $Na_{0.20}TiO_2$. It can be used as active materials into the aqueous Lithium Ion Batteries with high energy density of the nanostructures 74.9 mAhg^{-1}and better cycling behavior in mild aqueous electrolyte [43-44].VO_2 (B) represents the more promising candidate anode material for aqueous Li-ion battery on the basis of proper electrode potential and tunnel structure with intercalation and deintercalation in reversible Li-ion battery. Depending of its morphology, it is possible to make an ideal host for small molecules or ions which allow the realization of region-dependent surface reactivity. Also the strong mechanical structure can sustain water soakage for a long period of time in the cycling process. VO_2 (A) is the metastable tetragonal structure which can be transformed to rutile structure in an irreversible manner via annealing process [13, 45]. The self-assembly of nanostructures gives properties as coupling effect and synergistic effect.

The growth direction is generally determined by relative stocking rate at various crystal faces. The longest bond (V-O) generally gives a short crystallinity with slowest growth direction while the shortest bond along [010] gives high crystallinity with a faster growth direction. A striking feature of the monoclinic phase VO_2 (M) is the presence of cation-cation pairs along the $a_m = 2c_r$ axis which alternate with V-V separations being 2.65 and 3.12 Å in place of the regular 2.87 Å spacing in the tetragonal phase just above the tricritical temperature. The different polymorphic structures of VO_2 with lattice parameters are given in the table 2.5.

Table 2.5 Polymorphic structures of VO_2 [45]

Polymorphic structures / space group	A	B	C	β °
VO_2(M) / $P2_1/c$	0.576	0.542	0.538	122.6
VO_2(B)/ C_2/m	1.203	0.369	0.642	106.6
VO_2(R)/ $P4_2/mnm$	0.455	0.455	0.288	
VO_2(A)/ $P4_2/nmc$	0.844	0.844	0.768	

2.1.9 Phase Diagram of VO_2

V-O system equilibrium solid phase at 0.1 MPa hydrostatic pressures is given below presenting the different atomic percentage of vanadium and oxygen. It is a binary two-component system which summarizes the effect of temperature on the binary phase vanadium and oxygen. VO_2 presents tetragonal β and monoclinic α phases above and below 67 deg C with a melting temperature of 1542 deg C with 61.42 at% of vanadium and 38.58 at% of oxygen. The crystals structure and lattices parameters are listed in the table below showing the lattice parameters, phases and atomic percentage of oxygen for

different vanadium phases. According to Gibbs phase diagram rule, the degrees of freedom are given by:

$$F = C - P + 2 , \qquad\qquad Eq.\,2.53$$

Where C is the number of components and P is the number of phases. For P fixe:

$$F = C - P + 1 \qquad\qquad Eq.\,2.54$$

For F = 0, at most three coexisting phases for one single eutectic or peritectic temperature. The Hume-Rothery Rules for substitutional solution which describes the crystal structures of the two components are the same to form a continuous series of solids solutions. The internal free Gibbs energy of formation of the oxide VO_2 can be described by the reaction: [46]

$$V+O_2 \text{ (g, 1atm)} \qquad\longrightarrow\qquad VO_2 \qquad\qquad Eq.\,2.55$$

Where the relative partial free energies of oxygen is given by:

$$\Delta G_f^0(VO) = \frac{RT}{2}\int_0^1 lnp_{O2}\,dC \qquad\qquad Eq.\,2.56$$

Here R is the gas constant; P_{O2} is the oxygen and vanadium function of C and T which represents the equilibrium pressure over the oxide. The description of the oxygen in equilibrium with metals, where extensive dissolution of oxygen takes place, is given by a more generalized Sieverts equation as below:

$$lnp = f(C) + 2lng(C) + \frac{h(C)}{T} \qquad\qquad Eq.\,2.57$$

Where f(C) and g(C) result from the thermal and configurationally entropy; h(C) is the relative partial enthalpy of the gas dissolution and g (C) is generally given by:

$$g(C) = \frac{C}{\varepsilon - C} \qquad\qquad Eq.\,2.58$$

Where ε is correlated to the stoichiometry. For a bcc structure, ε=3 rather 1 for a fcc structure. the best combination of determining the α phase and the α+β are best described in the light of the integral constraint and pressure continuity at the phase boundary α and α+β. Vasil`eva and Seregin [47] report in polynomial form the isotherms of the relative free Gibbs energies:

$$ln\, p_\alpha = 20.48 + 2ln\frac{C}{C_{\frac{\alpha}{\alpha+\beta}}} - \frac{10.15 \times 10^4}{T} \qquad\qquad Eq.\, 2.59$$

Where p is in atmosphere, C is the O/V ratio, $C_{\frac{\alpha}{\alpha+\beta}}$ is the O/V ratio at the phase boundary and T is in K. The equilibrium pressures over the two phases α+β can be extracted:

$$ln\, p_{\alpha+\beta} = 20.48 - \frac{11.62 \times 10^4}{T} \qquad\qquad Eq.\, 2.60$$

The composition temperature relationships of the phase boundaries can be expressed as:

$$C_i = aT^2 + bT + c \qquad\qquad Eq.\, 2.61$$

The p-C-T relationship has been studied in many V-O systems V_4O, VO and V. The VO_2 system can be deduced describing the thermodynamic of the oxide [46].

The dissolution of the oxygen in the vanadium metal is given through the Sieverts law:

$$½\ O_{2(gas)} \qquad\longrightarrow\qquad O\ diss\ (\alpha V) \qquad\qquad Eq.\, 2.62$$
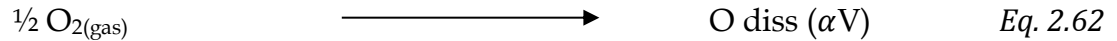
The evaluation of the $\Delta G_f^0(VO_2)$ can be deduce from the one of $\Delta G_f^0(VO)$ knowing that the only difference will be the factor ½ bacause the vanadium dioxide requires one atom of O_2 to be formed rather ½ to form vanadium monoxide.

$$\Delta G_f^0(VO_2) = 2\left(-431.8 + 0.089T\ \frac{kJ}{mol}\right) \qquad\qquad Eq.\, 2.63$$
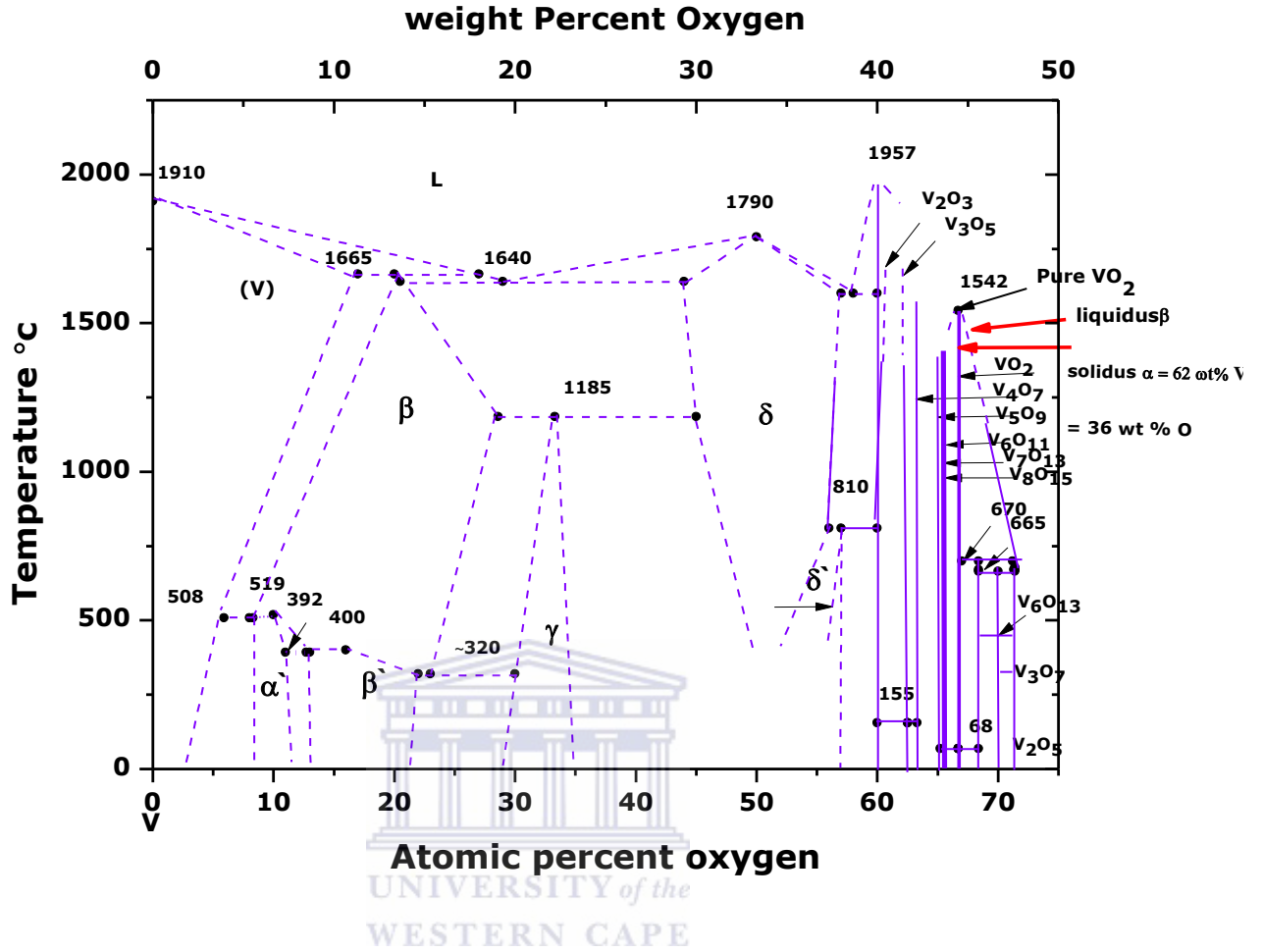
Figure 2.15: V-O Phase Diagram at 0.1 MPa [46, 48]

The high temperature heat capacity and enthalpy of phases in the V-O system as shown in figure 2.15, is given corresponding to V_2O_4 [49].

$$C_p(\alpha - V_2O_4) = 3R\left[\left\{D\left(\frac{258}{T}\right)\right\} + 2E\left(\frac{394}{T}\right) + 3E(709T)\right] \qquad Eq.\,2.64$$

$$H(T) - H^0(298.15K) = 125.14T - 37313, \qquad 298 < T < 345K \; for \; V_2O_4(\alpha) \qquad Eq.\,2.65$$

$$H(T) - H^0(298.15K) = 149.37T + 7.11 \times 10^{-3}\,T^2 + 33.01 \times 10^5 T^{-1} - 47509,$$
$$345 < T < 1818K \qquad\qquad\qquad\qquad\qquad Eq.\,2.66$$

$$H(T) - H^0(298.15K) = 213.38T - 24727, \qquad 1818l < T < 1900K \; for \; V_2O_4(l) \qquad Eq.\,2.67$$

2.1.10   Doping effects

VO$_2$ semiconductor transition n-type is too high for many practical applications and so doping lower the transition temperature to make the material suitable for many important applications. For example the substitution of V atoms by W large induces distortion of the structure with breaking of the homopolar bond V^{4+}-V^{4+} to form V^{3+}-W^{6+}and V^{3+}-V^{4+}and promotion of transition [50] is not the first time physicists have lowered the transition temperature of VO$_2$ by adding other materials a technique known as "doping. But Natelson said hydrogen doping is unique in that it is completely reversible [51]. To remove the hydrogen, the material simply has to be baked in an oven at moderate temperature. On the applied side, there may be a number of applications for this, like ultrasensitive hydrogen sensors. But the more immediate payoff will likely be in helping us to better understand the physics involved in the VO$_2$ phase transition. Additionally, Andreev et al [52] studied the temperature dependence of the electrical conductivity of H$_x$VO$_2$ thin films showing that the electrical conductivity increase with the increase in hydrogen content x and a decrease in the temperature according to the equation:

$$log(\sigma) \sim \frac{1}{T} \qquad\qquad Eq.\,2.68$$

And they assume that the electrical conduction in heavily doped vanadium dioxide is provided by hoping of small radius polarons. This is in accordance with Redfield`s results [53] showing that the Cr doped Vanadium dioxide presents a rutile structure at high temperature while at low temperature it is orthorhombic with monoclinic symmetry. This is in accordance with Marezio et al [28]. The transition temperature takes place in a lower temperature due to the exact ionization state of Cr ions in the crystal (Cr^{+3}). The effect of high ionicity was demonstrated to reduce the number of carriers for example in V-Cr-V or V-Ti-V bands and to reduce the extension of the overlap of the a$_{1g}$ wave functions along the vanadium atom chains. Contrarily the effect of doping can be opposite according to the concentration of the dopant. It has been observed in TiO$_2$ doped VO$_2$ that the transition region is broaden showing a mechanical

effect due to the coexistence of both phases. Hence TiO_2 inhibits the distortion of VO_2 phase which has an effect of hydrostatic pressure causing the increase of the transition temperature. Permanent erasable holographic storage on VO_2 thin films utilizes change in optical properties of the material when it passes through the transition. This application relies on the coexistence of both phases at a single temperature which is due to mechanical strains. Another application relying on the transient temperature profile is electron beam recording medium. Some materials present large temperature effects on VO_2: Tungsten dopant W, followed by Molybdenum Mo, then Ta and Niobium. According to [54], the dynamics range changes quickly for a low doping level and the transition temperature T_t moves slightly while for x~ 0.02 it is possible to get T_t at -30 ^{o} C giving the best range for passive solar building applications.

Table 2.6: Transition Temperature vs composition for doped VO_2 [12].

M	$\dfrac{dT_t}{dx}(\dfrac{K}{at}.\% M)$	x for T_t= 310K	σ/σ_0 at T_t
Ta	-5 to -10		
Nb	~ -8	0.04	< 10
Mo	-12	0.025	100+
W	-21	~0.014	100
	~-28	~0.010	

2.2 Physical Properties of vanadium dioxide

2.2.1 Electronic properties

Current technological revolution influenced by the semi-conductors, present enormous advances in electronics and computer science via the best understanding of the properties of semi-conductor. They have great impact on the electronic structure of the solids. The identity of constituents' atoms gives explanation and prediction of the properties of the semi-conductor. VO_2 are materials which belong to the family of smart materials that react to temperature variations, electric or magnetics field and or pressure with narrow electron bands. Their ability to be electrons strongly correlated systems

allows the fabrication of microelectronics systems showing that the phase transition is size dependent. Phase transitions are often associated with large changes in the electrical, optical and magnetic properties [55]. The Metal Insulator Transition is generally affected by the grain size, the defects, the minor stoichiometry inclusions and the substrate temperature. Competition among phases is generally obtained through light illuminations which initiate the phase transition at moderate intensity or drive large optical nonlinearities. It was pointed out that lower vanadium oxides and titanium behave like metals. Transition metals at the Neel temperature were reported for Ti_2O_3, VO, V_2O_3 and VO_2 showing the electrical conductivity measurement due to the existence of a conduction band of t_{2g} orbitals. Typical conductivity curve shown in figure 2.16 presents transition temperatures from conductivity measurements spread out over a range of temperature. Above the temperature transition, the metallic state shows positive temperature coefficient of resistance typical of metal. TiO was found to be a metal over the whole temperature range while for V_2O_3 and VO; the transitions were very abrupt with no measureable time and temperature dependence. In the case of TiO and VO which are rock salt structures, the connection between each cation and its twelve nearest neighbor is due to the overlapping of the t_{2g}orbitals which are partially filled bands in the metallic state. The band is split into two set of bands: one set spin up and one set for spin down. In the case of VO each set of bands contain three lower states per atom which are full and three higher states per atom which are empty. Hence VO is an insulator below transition temperature. In TiO the lower bands are only two thirds filled so TiO shows no transition to an insulator but VO_2 is much more complicated for reasons of the structure and because the transition in conductivity occurs even though the t_{2g} orbitals are partially filled. A more general point of view has been suggested by Anderson and is based on the observation that antiferromagnets which involve indirect exchange are insulators. Two processes in competition are suggested: the correlation effect which tends to localize the d electrons and which is aided by setting the cation spins in an antiferromagnetic alignment and the tendency of electrons to delocalize themselves by spreading into a band and thereby gaining kinetic energy. These two

processes are fairly energetic which are indicated by the conductivity change of a factor 10^6 in VO and V_2O_3 at the phase transition. VO_2 oxide`s electrical transition is accompanied only by a crystallographic distortion from body-centred tetragonal (T > Tt) to monoclinic (T < Tt) symmetry; the reduction in symmetry derives from a noncolinear pairing up of cations which for T >Tt, are equally spaced along the tetragonal c axis. It is paramagnetic for T >Tt, exhibiting for T <Tt, a temperature-independent susceptibility which increases at T, to a temperature-dependent value deriving from itinerant (conduction) electrons of low mobility candidate for the distortion model provided the existence of a paramagnetic susceptibility . In this connection there are two possibilities, namely Van Vleck (high frequency) paramagnetism deriving from (a) the component of electronic angular momentum perpendicular to the axis of the cation pairs, and (b) a departure in spherical symmetry of the anions due to possible covalency effects or to polarization by the cation field. The magnitudes of these contributions must, of course, be sufficient to dominate the diamagnetism of the system.
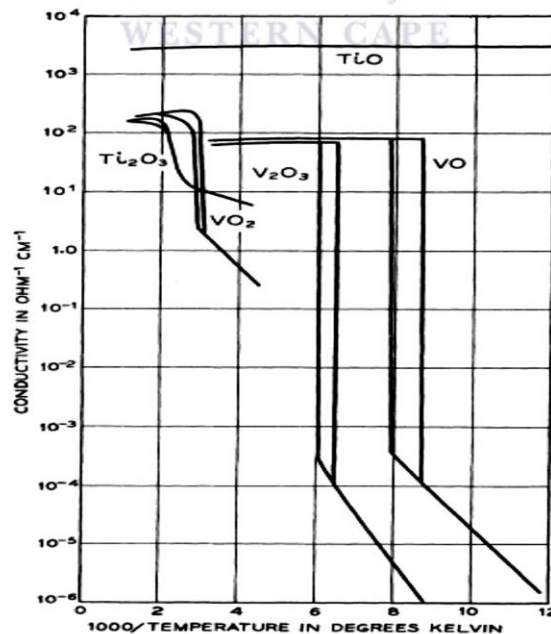
Figure 2.16: Conductivity change of vanadium dioxide and titanium function of reciprocal temperature [55].

2.2.2 Optical Properties

Optical methods are emerging as primary probe of correlations [56]. The infrared properties in the VO₂ films are consistent with a 0.5 eV gap in the insulating phase and a Drude like feature in the metallic regime. During the metal-semiconductor transition, the gaps filled gradually taking strength from various high energy electronic excitations and present an isosbestic point in the optical conductivity. See figure 2.17. The isosbestic point at a frequency of 11,500±125cm⁻¹is defined as the location of equal conductivity for all spectra obtained at different temperatures [58].
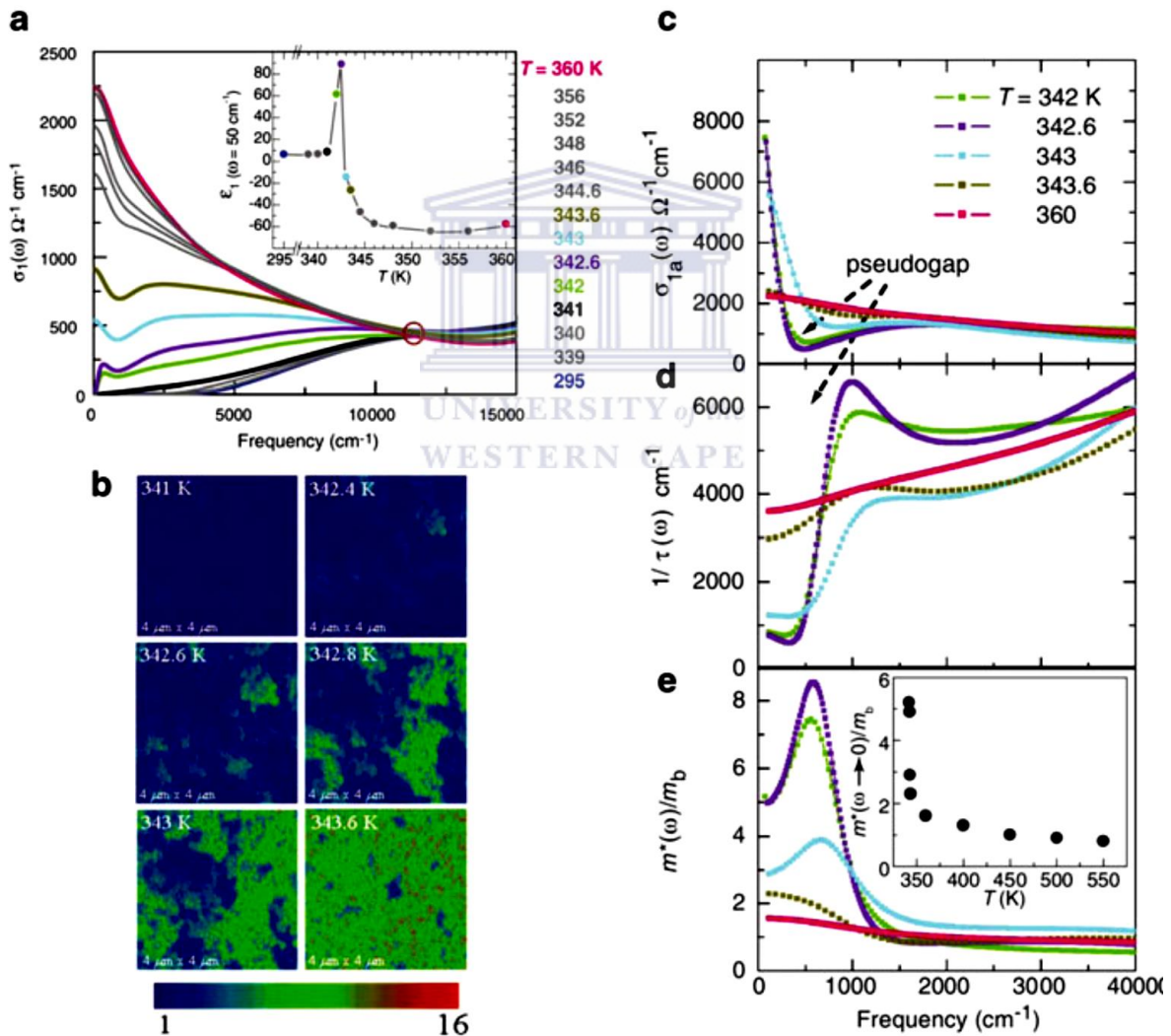
Figure 2.17: (a) Optical conductivity of VO₂ as a function of frequency for various temperatures. (b) Images of near-field scanning amplitude over a 4 mm area showing

the insulating and metallic domain structure and how it develops through the transition regime. (c) Optical conductivity of the metallic domains extracted from a modified effective medium analysis. (d, e) The relaxation rate and effective mass vs. temperature [57].

The importance of electron correlation is shown with the divergence of the effective carrier mass and a pseudo-gap like structure in the relaxation rate which is a signature of the Mott transition. The changes in optical constants during phase transition was described through the Maxwell`s electromagnetic theory through the expression:

$$\frac{n^2 - 1}{n^2 - 2} \frac{3\varepsilon_0}{N} = \frac{\alpha\rho}{M},$$

$$Eq.\, 2.69$$

Where M is the molecular weight, ρ is the density, α is the polarizability, n is the refractive index N and ε_0 are the Avogadro`s number and vaccum permittivity respectively. This formula show that the refractive index increases with ion accumulation density and ion polarisability. The polarization occurs when d $_{v-o}$ is less than the sum of the radii V^{4+} ion and O^{2-}. However, in the case of VO_2 at high temperature above Tt, $[VO_6]$ becomes tetragonal in structure and dv-o equals 0.194nm, very close to R v-o. Therefore, the polarizability of monoclinic VO_2 is larger than that of tetragonal rutile VO_2. As the ion accumulation density is similar for these two different structures, the refractive index of VO_2 decreases when VO_2 changes from monoclinic structure at low temperature to tetragonal rutile structure at high temperature due to the thermally induced phase transition [59]. Nanoparticles present a strong surface–plasmon resonance which dominated the optical response that is absent in the bulk. The resonance is due to collective oscillation of the electron plasma which can directly couple to light in a dielectrically confined geometry. The large absorption coefficient at the surface plasmon frequency can be calculated from the classical Mie theory formula for the polarisability of a spherical particle for particles sizes much smaller than wavelength of light. In the absence of damping the polarisability diverges when the real part of the dielectric constant equals -2ε_m where ε_m is the dielectric constant of the

surrounding medium. This singularity which relaxed in the presence of damping can be observed only when the nanoparticles are in the metallic phase in which the real part of the dielectric constant is negative. In that regard, Nano-photonics Au-VO₂ obtained onto Corning glass substrates with an average films thickness of 160 ± 3 nm was synthesized by the Off-axis XeCl pulsed laser ablation configuration [60-61]. A nonlinear optical phenomenon observed experimentally in noble metal nanocomposites was successfully elucidated by percolation phenomena, power law or universal critical exponents and renormalization theory which is strongly induced by the local electric field within the metallic nanoparticles. The nano-gold surface plasmon wavelength approximately 648 nm below Tc presents a shift to 603 nm above Tc towards the blue region. This confirms the tunability of the surface plasmon frequency via an external temperature stimulus. Hans W. Verleur et al. [62] studied the jump in the resistivity versus temperature in VO₂ crystals. They show that the optical properties occur with few degrees of the transition temperature and that the optical properties are relatively insensitive to temperature well above or well below. Recently, Maaza et al. [63] reports on the ultrafast optical limiting in the IR regime of pulse laser deposited VO₂ nanostructures more specifically at 1.064 µm. They described that the reversible optical transition would be translated as a significant reversible modulation in the refractive index dielectric constants where the temperature dependence of the standard real and imaginary parts can be expressed as:

$$(n(w,T) + jk(w,T))^2 = e_\infty + e_1(w,T) + e_2(w,T) + e_3(w,T) \qquad Eq.\,2.70$$

$$e_1(w,T) = [(e_s - e_\infty)w_t^2]/[w_t{}^2 - jwG_0] \qquad Eq.\,2.71$$

$$e_2(w,T) = \sum_{j=1}^{n} \left[[f_j w_{0j}^2] \Big/ [w_{0j}^2 - w^2 + jwg_i] \right] \qquad Eq.\,2.72$$

$$e_3(w,T) = w_p^2[-w^2 + jw_d] \qquad Eq.\,2.73$$

While $\varepsilon_\infty + \varepsilon_1(\omega,T) + \varepsilon_2(\omega,T)$ is the Lorenz component describing the semiconducting state, $\varepsilon_3(\omega,T)$ is the Drude part; the driving component of the metallic state. The temperature, T, and frequency ω dependence of the real part of the refractive index, n(ω,T), is

determined by the dominant physical processes. The limit dielectric constants $\varepsilon(0)$ and $\varepsilon(\infty)$ for bulk VO_2 are 43 and 10.0 in the dielectricregime, respectively, and 18.3 and 9.0 in the metallic regime. In the near infrared, $\varepsilon(\omega)$ has values of approximately 8.64 and 5.7 inthe dielectric and metallic states respectively. By considering not only the dominant physical processes but also higher order processes, impurities and defects, the temperature dependance of refractive index was giving according to Lorentz-Lorenz formula:

$$\left[\left[n^2((T,w)-1)\right] \Big/ \left[n^2(T,w)+2\right] \right] = r(T) + \frac{\alpha_\rho(r,T)}{3e_0 \, Eq} \qquad Eq. \, 2.74$$

ρ =N/V represents the number density of oscillators per unit volume, α_ρ is the polarisability. The refractive index derivative was described with the contribution of two factors such as the thermal expansion with changes in volume and another factor is the temperature change versus polarisability. The negative value of dn/dT in the VIS and IR spectral regions shows that volume expansion is the dominant factor of optical phase change.
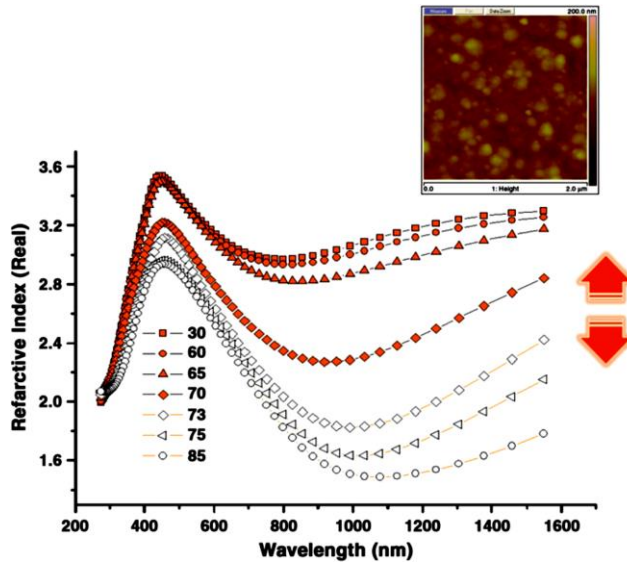
Figure 2.18: Thermal modulation of the real part of the refractive index n(ω,T) of the pulsed laser deposited ~400 nm coating of VO_2 onto quartz glass substrate deduced

fromellipsometry investigations at 5 different temperatures; T=30, 60, 65, 70, 73, 75 and 85 °C. The inset figure shows a typical atomic force microscopy surface topography of the thickest film i.e. 1204±1 nm.[63]

The very large modulation of the refractive index with temperature see figure 2.18, shows that VO₂ allows a natural optical limiting response. This was confirmed with the log-log variation of the optical transmission versus the laser input energy where the optical emission of VO₂ coating efficiency was shown to be thickness dependence with 1204 nm which presents the most operational size within the standard laser damage protection regulations. See figure 2.19. In addition to the solid state aspect of VO₂, the unique broad spectral modulation of VO₂ over all NIR to the FIR spectrum makes VO₂ a good optical limiter material.
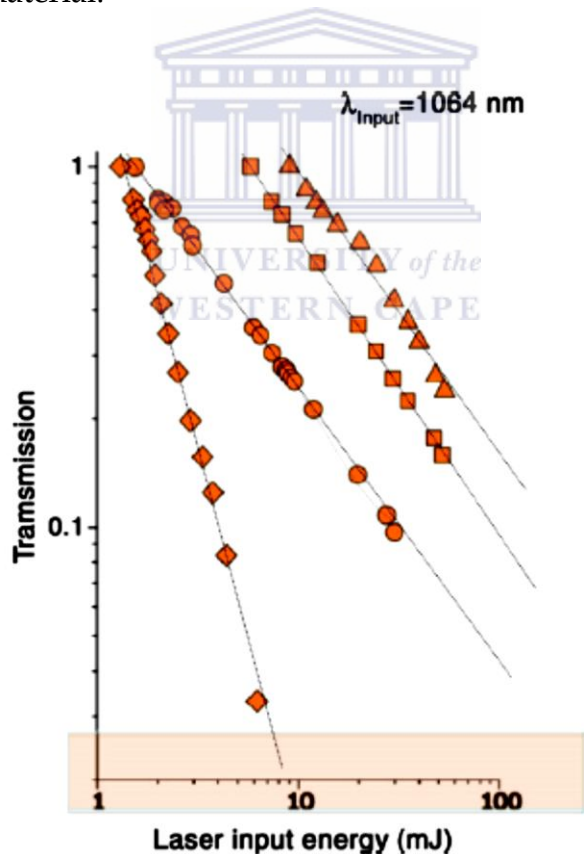
Figure 2.19: Log-log optical transmission /laser input energy of 4 different pulsed laser deposited VO₂ nanocoatings onto quartz-substrate with different thicknesses.[63]

Cavalleri et al. [64] demonstrate that the photon-induced phase transition can with analogy to chemical substitution favor relaxation of the system into a competing state. They used time resolved spectroscopy probing new physical pathways of VO_2 phase transition and they observed a prompt drop in the transmission of the sample immediately after laser excitation which was interpreted as the effects of holes created in the valence band of d symmetry of vanadium while electrons are promoted to the conduction band, formed by orbitals of mixed p-d character and therefore less evident at the V L edges. These V L edges are more sensitive to the holes of purely d symmetry than to electrons in the conduction band. According to Lysenko et al. [65], the alteration of the material induced by light was as fast as the laser pulse duration ~100 fs depending on the pump power. The observed phase transition was associated with the optical interband transition with a competitive process between thermal and pure light induced intermediate exciton state possible in insulator phase. Ultrafast optical spectroscopy is of particular interest to interrogate a metastable phase wich may only exist for a few ns before thermal fluctuations drive the system back toward the true groundstate.

Table 2.7: Basic properties of VO_2 [66]

	Valence 3d electron (number)	crystal structure	Tc (K)	Transport T<Tc	Magnetic T<Tc	Optical Band gap
V_2O_5	$V^{5+}(3d^0)$	Orthorhombic layered		n-type		~2eV
V_6O_{13}	$2V^{5+} + 4V^{4+}$ $(3d^{0.66})$	Monoclinic layered	145	p-type	Antiferromagnetic $T_N=55K$	?
VO_2	$V^{4+} (3d^1)$	TiO_2 T>Tc Monoclinic	340	n-type	Non magnetic	~0.7eV
V_2O_3	$V^{3+}(3d^2)$	Al_2O_3 T>Tc Hexagonal	168	n-type	Antiferromagnetic $T_N= 168$ K	~0.2eV

Litao Kang et al. observed that the finite size effects play a very important role in the energy band structure and subsequent shift of absorption edges [66]. Additionally the morphology of the grains affects the optical properties which were observed through a dependence of the increase of porosity with decrease of absorption coefficient, refractive index and extinction coefficient. P J Hood et al. [67] studied the dielectric mixture phenomena in VO_2 in the high temperature phase at millimeter–wave frequencies through phase transition. The Bruggeman mixture relationship was used to relate the dielectric properties of the insulating matrix, the grains in the conductive state, and the volume fraction of the film in the conductive state to the dielectric properties of the mixture. It was expressed as:

$$(1 - \varphi)(\epsilon_2 - \epsilon_1)/(\epsilon_2 - \varepsilon) = (\epsilon_1/\epsilon)^{1/2} \qquad Eq.\,2.75$$

φ is the volume fraction of the conductive phase, ϵ_1, ϵ_2, ϵ are complex dielectric constants of the matrix, conductive phase, and mixture respectively. They observed strong resonance of the matrix permittivity at very high volume fractions of the conductive phase; the sensitivity of the matrix permittivity at the resonance to small increase in the matrix conductivity and the insensitivity of the conductivity to increase in the matrix conductivity. The dependence of the permittivity on film thickness was attributed to the increase in grain boundary width with decrease in conductivity width. The effect of dielectric properties on device performance is dependent upon the device design and function which is strongly correlated to the film stoichiometry, microstructure, crystalline orientation and stress. The optimal performance in most microwave devices is obtained with materials having the greatest change in resistivity between two states.

2.2.3   Magnetic properties

VO_2 phase transition was discovered to be based upon a free energy expression function of the amplitude of the lattice distortion and the magnetic local moment. The localized magnetic moments are understood as a consequence of electron-electron correlations with existence of well-developed local moments in low temperature,

exhibiting a Curie-like susceptibility [68]. VO_2 metallic phase is paramagnetic with Pauli-like susceptibility decreasing with increasing temperature while the insulating phase presents vanishing of the susceptibility. This is in accordance with Junfeng Liu et al. [69] who measured the magnetization of the as-prepared $VO_2(B)$ with a superconducting quantum interference device magnetometer and they showed that the materials are paramagnetic nanobelts. In the other hand, the electronic–lattice mechanism would imply a normal Pauli susceptibility in the metallic phase a diamagnetic behavior in the insulating one. The susceptibility calculation has been performed for both the d// and π* bands yielding $\chi_{total}= \chi// + \chi^*$ where numerically they obtained for VO_2:

$$X_{total}(340K) = 4.30 *10^{-4} \text{ emu/mole} \qquad Eq.2.76$$

$$X_{total}(900K) = 3.74 *10^{-4} \text{ emu/mole} \qquad Eq.2.77$$

They accounted qualitatively the discontinuous increase of χ at the transition and for its temperature dependence while $\frac{\partial^2 \mathcal{F}}{\partial \mu^2}$ was accounting for the mutual electrostatic interaction. $\frac{\partial^2 \mathcal{F}}{\partial \mu^2}$ was given as the variability of total free energy for a statistical distribution including thermal fluctuations such that:

$$\Delta^2 \mathcal{F} = \Delta \mathcal{F} + \frac{K_B T}{\frac{\partial^2 \mathcal{F}}{\partial \mu^2}} \frac{\partial^2}{\partial \mu^2}(\Delta \mathcal{F}) \qquad Eq.2.78$$

2. 3 Applications of VO_2

The phase transformation detector using VO_2 as sensitive material has been shown to have high sensitivity coupled with good responsivity, speed of response and highly flexible performances parameters. It shows to operate in a quasi-photoconductive mode and to be thermally self-regulating which require a constant current bias supply. It relies in the conversion of temperature change in the detector material to an electrical signal. The VO_2-device proposed was entirely isothermal in operation, and makes use of

the change in resistivity which occurs at a metal-semiconductor phase transition. While several transition metal oxides exists which exhibit such a phase transition, the material appearing to have the best chance of making a practical detector at the present time was demonstrated to be VO_2 [70]. Electric field-induced transitions are typically explored with Mott FET; additionally nanoscale thermal switches with Mott materials could also be of substantial interest. Possible sub-ns switching speeds in ultra-thin device elements in the vicinity of room temperature is obtained with nanoscale two terminal VO_2switches and is of great interest to Mott memory. Such correlated materials can be seen as 'threshold materials' wherein the conducting state can be rapidly switched by a slight external perturbation leading to potential applications in electron devices [38]. Nanoscale data storage, switching and photonics technologies rely on switchable modification of the electrical and optical properties. Because they are scale down, a deeper understanding of entangled structural and vibrational properties are essential to tailor the functionality of phase changing materials, of particular interest are surfaces swing to their pronounced contribution at the nanoscale. Also the effects of strained VO_2 in specific orientations grains favor the nucleation of the grains and change structure to monoclinic. In the nanoparticles prompt formation of the metallic state results in the appearance of surface plasmon. Narrow band gap semi-conductor are most sensitive detectors for the mid-infrared range (3-20 µm) representing the most sensitive detectors for the near-IR range (750-2500) nm [71]. They possess broad spectral sensitivity up to the cutoff wavelength with high quantum efficiency which are generally use in IR light generation and detection with the tenability of the band gap structure using the temperature. This latter is dependent of individual energy bands and interbands electronic transition yielding information about electron-phonon interactions. Thermally decoupled electric field in VO_2 has great applications for integration in nanoscale electronic devices such as Mott field transistors [72].VO_2 belongs to the family of smart materials that react to temperature variations, electric or magnetic field and/or pressure variations. That property of smart material is due to its first order transition phase at around 340 K [54, 73-74]. Additionally practical

applications in technology can be obtained: switching devices, thermal relays and energy management, sensors and actuators, electrochromic and photochromic memories, high speed solid state displays, modulation, polarization, and control functions, plasmonic response in the near infrared communications wavelengths, ferroelasticity. Dielectric confinement and particle shape affect the change in optical properties across the room temperature. Ultrafast transition first-order characterized by several orders of magnitude change in optical transmittance and conductivity. These effects induce attractive materials from Mott field effect transistors to thermochromic coatings and optical waveguides. Ivan P. Parkin et al. [75] proposed vanadium dioxide thin films coated on glass for use as an intelligent window coating that can change one or more of its properties in response to some external stimulus. Here the optical properties are changed with temperature and the intelligent thermochromic window become more reflective at infrared wavelengths at elevated temperature. This behavior is highly applicable to climates where there are extreme changes in temperature over the year for example central and northern Europe, Japan, United States and Canada which present hot summer and cold winter. Valmalette et al. [76] proposed for the first time VO_2 composites imbedded in a transparent polymer and study its artificial solar radiation using a Beer Lambert model. It was observed that the efficiency of thermochromic behavior depends on the anisotropic space distribution of the pigments and their mean size. The most recent and successful thermochromic composites VO_2 polymer was obtained by Litao Kang et al. [66] who provide an effective process to control the thermochromsim through polymer degradation rate with variation of the annealing conditions and they confirmed that the state of the grain boundaries influences the semi- conductor transition. VO_2 has been employed as a bolometer in the non-hysteretic part of the resistance temperature characteristics [77]. The bolometer sensor performance was theoretically evaluated using a valid mathematical model required to fully describe the major and minor hysteresis loops. The Preisach model was widely accepted as a suitable tool to describe hysteresis phenomena. Considering VO_2 material composed of microcrystals which individually exhibit sharp hysteretic

transition, the classical model described the Preisach model as a sum of simple relay operators weighted by a statistical distribution function $\mu(T_\alpha, T_\beta)$ giving the resistance of the material as:

$$R(t) = \iint \hat{\gamma} T_\alpha T_\beta T(t) \ \mu(T_\alpha, T_\beta) dT_\alpha dT_\beta \qquad\qquad Eq.\, 2.79$$

The distribution function is equal to zero for the insulator and equal to 1 for semiconductor.

Figure 2.20: Preisach triangle adapted for VO₂ thermal hysteresis [77].

The Preisach model generally rely on the wiping out and congruency properties represented by a set of piecewise monotonic excitations. See figure 2.20. Jing Du et al. [78] used the compatibility difference of inorganic salts with polyvinylpyrrolidone (PVP) to introduce phase separation and obtain films with large microroughness. The obtained films were simply prepared and exhibited excellent optical performance. Doping was also applied in this deposition process. By tungsten doping, they successfully lowered down the SMT temperature down to 25.4 1ºC. Moreover, emissivity of films is lowered 0.20 for monoclinic and 0.33 for rutile phase for a VO₂-

based film with Zn/V=0.1 and W/V=0.01. The sample shows the SMT temperature of 43.4 1C, T_{lum} of 30.0%, and ΔT_{sol} of 8.82%.

2.4 References

[1] Lee J.D.; *Concise Inorganic Chemistry*-4th Ed.; Loughborough University of Technology, printed by Chapman and Hall, 2-6 Boundary Row, London SE1 8HNPart four, 1991.

[2] Rehder, D.; *BioMetals,* 5, 1992, 3-12.

[3] Ningyi, Y.; Jinhua, L.; Chenglu, L; *P.D Dernier, Bell Laboratories, Mat. Res. Bull.*, 9, 1974, 955-964.

[4] Reeswinkel, T.; *Self-lubricious tool coatings for ecological metal cutting*. Materials Chemistry Dissertation, 16 (2012).

[5] Whittaker, L.; ChernoJaye; Fu, Z.; Fischer, D.A.; and Banerjee, S.; *J. Am. Chem Soc.*, 131, 2009, 8884–8894

[6] Wei, J.; Ji, H.; Guo, W.; Nevidomskyy, A.H.; Natelson, D.; *Nnano*.2012.70.

[7] Schoemaker, D.P.; PhD. Thesis, *Understanding atomic disorder in polar and magnetic oxides* 2010.

[8] Korotin, M.A.; Skorikov, N.A.; and Anisimov, V.I.; *cond-mat.str-el,* 2003.

[9] Greenberg, C.B.; *Thin Solid Films*, 110, 1983, 73-82.

[10] Macintyre, J.E.; Ed. in Dictionary of inorganic compounds, volumes 1-3, Chapman & Hall, London, UK, 1992-R.T. Sanderson in Chemical Periodicity, Reinhold, New York, USA, 1960.

[11] Guelfucci, M.F.; *Journal of Physics and Chemistry of Solids* 62, 2001, 1961-1966.

[12] Goodenough, J.B.; *Journal of Solid State Chemistry*, 3, 1971, 490-500.

[13] Ramanathan, S.; *Thin Film Metal-Oxides Fundamentals and Applications in Electronics and Energy*, Springer Science+Business Media, LLC 2010

[14] Hermann K.; and Witko, M.; *Oxide Surfaces,* D.P. Woodruff, editor 136 © Elsevier Science B. V. All rights reserved, 2001.

[15] Heckingbottom, R.; and Linett, J.W.; *Nature* 194, 1962, 678

[16] Li, Y.; Ji, S.; Gao, Y.; Hongjie Luo, H.; & Kanehira, M.; *Sci. Rep.*; 3, 2013, 1370.

[17] Belozerov, A.S.; Poteryaev, A.I.; Anisimov, V.I.; ZhETF, P.v.; 93(2), 2011, 73-77.

[18] Nihoul, G.; Leroux, Ch.; Madigou, V.; Durak, J.; *Solid State Ionics* 117, 1999, 105-112.

[19] Pokrovskii, B.I.; and A.G. Khachaturyan, A.G.; *J. Solid State Chem*. 61, 1986, 137.

[20] Leroux, C.; Nihoul, G.; Tendeloo, G.V.; *Physical Review B*, 57, 1998, 9.

[21] Horiuchi, H.; Morimoto, N.; and Tokonami, M.; *Journal of Solid State Chemistry* 17, 1976, 407-424.

[22] Alder, D.; and Brooks, H.; *Phys. Review*, 155 (3), 1967, 826-840.

[23] O`Donnel K.P.; and Chen, X.; *Appl. Phys Lett*. 58, 1991, 25.

[24] Huang, K.; and Rhys, A.; *Proc R Soc. A* 277, 1964, 312.

[25] Thurmond, C.D.; *J Electrochem.Soc*.122, 1975, 1133.

[26] Shin, S.; Suga, S.; Tanigushi, M.; Fujisawa, M.; Kanzaki, H.; Fujimori, A.; Daimon, H.; Ueda, Y.; Kosuge, K.; Kachi, S.; *Phys B*, 41, 1990, 8.

[27] Ilinskiy, A.V.; Kvashenkina, O.E.; and Shadrin, E.B.; *Semiconductors*, 46 (9), 2012, 1171–1185.

[28] Marezio, M.; McWhan, D.B.; Remeika, J.P.; and Dernier, P.D.; *Phys Rev B*, 5, 1972, 7.

[29] Pouget, J.P.; and Launois, H.; *Journal de Physique Colloque C4*, 10*(37)*, 1976, C4-49.

[30] Hyland, G.J.; *Journal of Solid State Chemistry,* 2, 1970, 318-331.

[31] Frohlich, H.; *Quantum Theory of Atoms, Molecules and the Solid State*, P.-0. Lowdin, Ed., Academic Press Inc., N.Y., 1966, pp. 465-468.

[32] Knox, R. S.; *Solid State Phys. Suppi*. 5(100), 1963, 119.

[33] Kohn, W.; Tomizuka, C.T.; and Emrick, R.M.; *Physics of Solids at High Pressures*, Eds., Academic Press Inc., N.Y., 1965, 561-566.

[34] Jerome, D.; Rice, T.M.; and Kohn, W.; *Phys. Rev*. 158, 1967, 462.

[35] Cloizeaux, J.D.; *J. Phys. Chem. Solids* 26, 1965, 259.

[36] Halperin and Rice, T.M.; *Rev. Mod. Phys*. 40, 1968, 755.

[37] Cherian, J.; *Mott metal insulators transitions*, April 7 2010; http://www.physics.fsu.edu

[38] Imada, M.; Fujimori, A.; Tokura, Y.; *Metal Insulator Transitions Reviews of Modern Physics*, 70 (4), 1998.

[39] Wentzcovitch, R.M.; *Physical Review Letters*, 72 (21), 1994.

[40] Grinolds, M.S.; Lobastov, V.A.; Weissenrieder, J.; and Zewail, A.H.; *PNAS*, 103 (49), 2006, 18427-18431.

[41] Ladd, L.A.; Technical Report No. HP-26, Technical Report No. ARPA-, *Electrical and Optical properties of high quality crystalline V_2O_4 near the semiconductor metal transition temperature*, Division of Engineering and Applied Physics Harvard University Cambridge, Massachusetts, 1971.

[42] Tselev, A.; Luk'yanchuk, I.A.; Ivanov, I.N.; Budai, J.D.; Tischler, J.Z.; Strelcov, E.; Kolmakov, A.; Kalinin, S.V.; *Nano Letters*, 10 (11), 2010.

[43] Zhang, S.; Li, Y.; Wu, C.; Zheng, F.; and Xie, Y.; *J. Phys. Chem. C* 13, 2009, 113, 15058-15067.

[44] Chao, Z.K.; Meng, C.D.; You, L.Z.; *TransferrousMet.Soc. China* 16, 2006, 517-521.

[45] Wang, Y.L.; Li, M.C.; Zhao, L.C.; *Surface Coating technology* , 201(15), 2007, 6772-6776.

[46] Kim, Y.S.; *Journal of Alloys and Compounds* 312, 2000, 86–93.

[47] Vasil'eva, I.A.; Seregin, A.N.; Khim. Z.F.; *Russ. J. Phys. Chem.* 57(7), 1983, 987.

[48] Wriedt, H.A.; *Bulletin of Alloy Phase Diagrams,* 10 (3), 1989.

[49] Matsui, T.; Naito, K.; *Netsu. Sokutei*, 15 (1), 1988, 27-41.

[50] Cao, C.; Gao, Y.; and Luo, H.; J. *Phys. Chem. C,* 112, 2008, 18810-18814.

[51] Wei, J.; Ji, H.; Guo, W.; Nevidomskyy, A.H.; & Natelson, D.; *Nature Nanotechnology* 7, 2012, 357–362

[52] Andreev, V.N.; Klimov, V.A.; and Kompan, M.E.; *Fizika Tverdogo Tela*, 54 (3), 2012, 562–56

[53] Redfield D.; and Balberg, I.; RCA Laboratories, Princeton NJ 08540, Final Report June 1972, US Department of the Navy Office of Naval Research Washington, DC 20390

[54] Jorgenson G.V.; and Lee, J.C.; *Solar Energy Materials* 14, 1986, 205-214.

[55] Rini, M.; Cavalleri, A.; Schoenlein, R.W.; Lopez R.; Feldman, L.C.; Richard F. H.; F.R.; Jr H.; Boatner, L.A.; and Haynes, T.E.; *Optics Letters* 30, 2005, 5.

[56] Basov, D.N.; Averitt, R.D; Marel, D.V.D.; Dressel, M.; Haule, K.; *cond-mat.str-el*, 12 , arXiv:1106.2309 v1, 2011.

[57] Musfeldt, J.L.; Wu J.; et al. (eds.), *Functional Metal Oxide Nanostructures*, Springer Series in Materials Science 149, Springer Science+Business Media, DOI 10.1007/978-1-4419-9931-3_5, LLC 2012.

[58] Qazilbash, M.M.; Brehm, M.; Chae, B.-G.; Ho, P.C.; Andreev, G.O.; Kim, B.-J.; Yun, S.J.; Balatsky, A.V.; Maple, M.B.; Keilmann, F.; Kim, H.-T.; Basov, D.N.; *Science* 318, 2007, 1750.

[59] Lu, S.; Hou, L.; Gan, F.; *Journal of Materials Science* 28 (2169), 1993, 2177.

[60] Maaza, M.; Nemraoui, O.; Sella, C.; Beye, A.C.; Barak, B.B.; *Optics Communications* 254, 2005, 188–195.

[61] Maaza, M.; O Nemraoui,O.; Sella, C.; and Beye, A.C.; *Gold Bulletin* 38, 2005, 3.

[62] Verleur, H.W.; Barker, A.S.; Jr; and Berglund, C.N.; *Phys. Review* 3, 1968,172.

[63] Maaza, M.; Hamidi, D.; Simo, A.; Kerdja, T.; Chaudhary, A.K.; Kana, J.B.K.; *Optics Communications* 285, 2012, 1190–1193.

[64] Cavalleri, A.; Chong, H.H.W.; Fourmaux, S.; Glover, T.E.; Heimannn, P.A.; Kieffer, J.C.; Padmore, H.A.; Schoenlein, R.W.; *Phys. Review Lett.*, 95, 2005, 067405.

[65] Lysenko, S.; Rua, A.J.;Vikhnin, V.; Jimenez, J.; Fernandez, F.; Liu, H.; *Applied Surface Science* 252,2006, 5512–5515.

[66] Kang, L.; Gao, Y.; Zhang, Z.; Du, J.; Cao, C.; Chen, Z.; and Luo, H.; *J.Phys.Chem. C* 20120, 114, 1901-1911.

[67] Hood, P.J.; and DeNatale, J.F.; *J. Appl. Phys.* 70 (1) 1991.

[68] Hugon, P.L.; and Paquet, D.; *ColloqueC5*, 6 (41) 1980, page C5-67.

[69] Liu, J.; Li, Q.; Wang, T.; Yu D.; and Li, Y.; *Angew. Chem*. 116, 2004, 5158-5162.

[70] Scott, R. S.; Fredericks, G.E.; *Infrared Physics*. 16, 1976, pp. 619-626.

[71] Zogg H.; and Arnold, M.; *Opto-Electronics Review* 14 (1), 2006, 33-36.

[72] Whitaker, L.; Zhang, H.; Banerjee, S.; *Journal of Materials Chemistry,* 19, 2009, 2968-2974.

[73] http://www-als.lbl.gov/ Berkeley Lab.

[74] Moffat, C.; Wigstein, A.; *FOI-R-1684-SE*, 22 (7), 2005, 1746-1748.

[75] Parkin, I.P.; and Manning, T.D.; *Journal of Chemical Education,* 83 (3), 2006.

[76] Valmalette, J.C.; Gavarri, J.R.; *Solar Energy Materials and Solar Cells* 33, 1994, 135-144.

[77] Almeida, L.A.L.; Lima, A.M.N.; Neff, H.F.; and Freire, R.C.S.*; IEEE Transactions on Instrumentation and Measurement*, 50(4), 2001.

[78] Du, J.; Gao, Y.; Chen, Z.; Kang, L.; Zhang, Z.; Luo, H.; *Solar Energy Materials & Solar Cells* 110, 2013, 1–7.
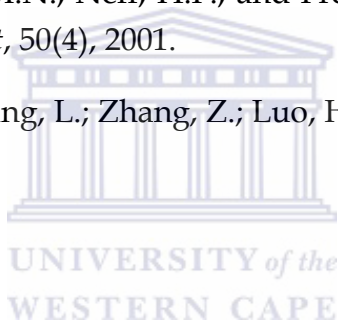
CHAPTER THREE:

SOL-GEL METHOD –HYDROTHERMOLYSIS

3.1 Experimental Procedure VO$_2$ growth techniques

The differents types of process for making nanoclusters, nanolayers, and nanofilms, as well as methods for nanoprofiling to make nanoscale features can be summarized as seen in figure 3.1.
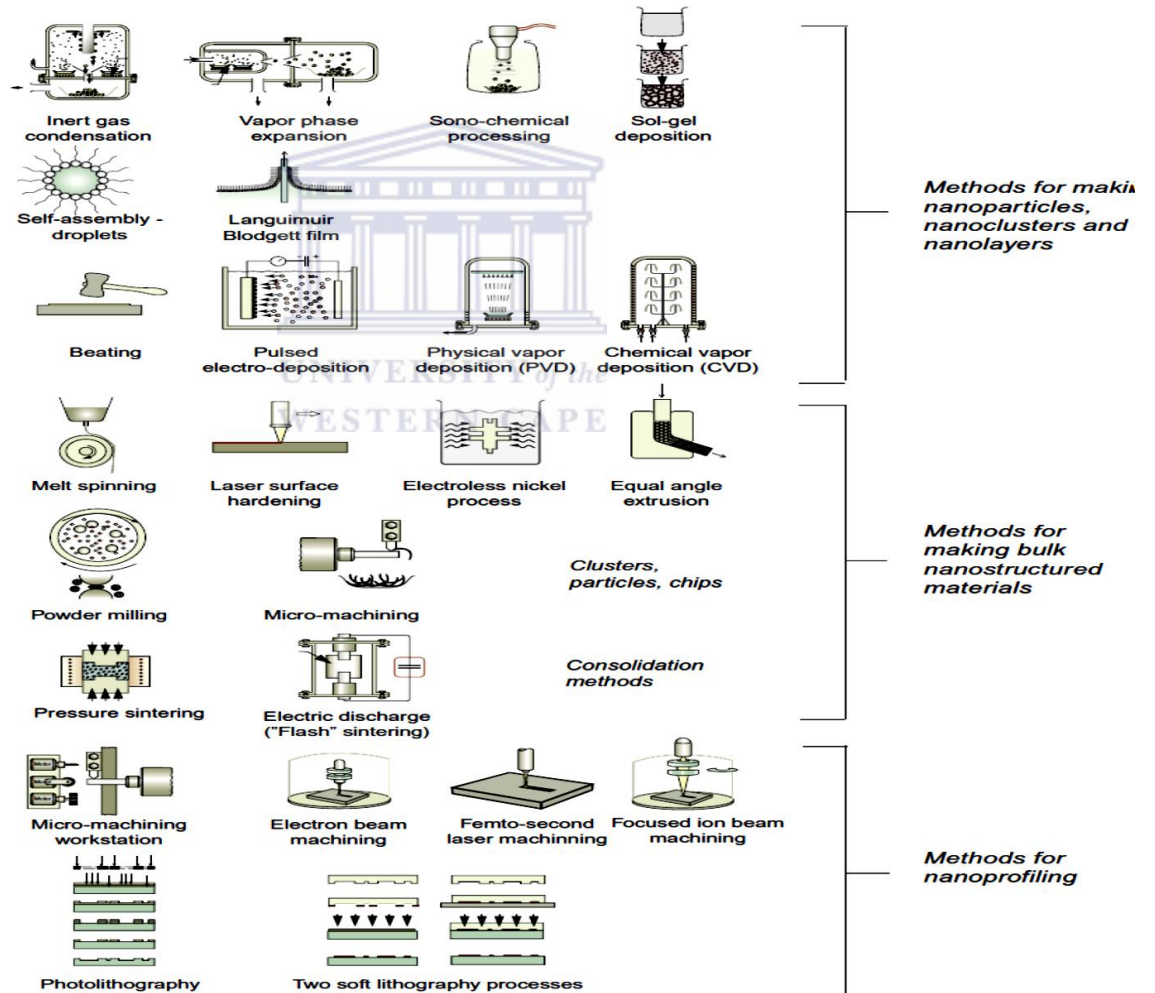
Figure 3.1: Possible synthesis methods used for bulk nanostructures materials [1].

VO_2 nanostructures can be prepared by several methods: Ion implantation in a silica matrix; Sputtering; Chemical vapor Deposition; Pulsed Laser Deposition; Sol gel method /hydrothermolysis. The level of control achieved over the dimensions and stoichiometry of VO_2 nanostructures is due to the challenge to stabilize and maintain the right oxidation state for several energetic minima with high or lower oxidation states which are easily accessible.

3.1.1 PLD (Pulsed Laser Deposition)

Pulsed Laser Deposition gained great attention in depositing materials with complex stoichiometry. It is a comparatively recent entry into the world of thin film coating and is especially suited for oxide growth. It was developed as a deposition technique for oxide superconductor in the late 1980s and was first used for VO_2 deposition by Singh in 1993 with the ablation of a metallic vanadium target in ultrahigh vacuum deposition chamber with Ar and O_2 (10:1) atmosphere of 100 mTorr. [2-3].
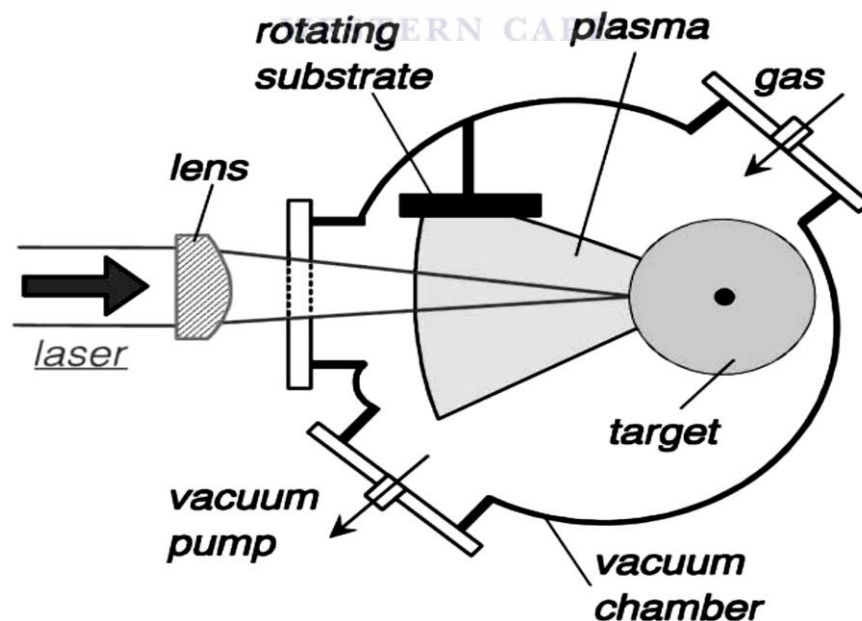
Figure 3.2: PLD deposition process [2].

The absorption energy of the laser by the target is converted to electronic excitation and thermal, chemical and mechanical energy resulting in evaporation, ablation, plasma formation and exfoliation. PLD synthesis is generally manipulated in ultra-high vacuum or in the background of a gas such as oxygen or argon which are preferred for the obtention of metal-oxide. See figure 3.2. Generally PLD relies on a photon interaction which creates an ejected plume of material from any target whose distance from the substrate is placed in a short distance. It is considered that the ejection of the material occur due to the rapid explosion with superheating. The principle of pulsed laser deposition is a very complex physical phenomenon which do not involve the physical process of the laser ablation in the impact of the high power pulsed radiation, but also the plasma plume with high energetic species and transfer of the ablated material through the plasma plume unto the heated substrate surface. PLD consist in four processes:

1) laser radiation and interaction with the target

2) Dynamic of the ablation materials

3) Deposition of the ablation materials with the substrate

4) Nucleation and growth of a thin film on the substrate surface

Nucleation-and-growth of crystalline films depends on many factors such as the density, energy, ionization degree, and the type of the condensing material, as well as the temperature and the physico-chemical properties of the substrate. The two main thermodynamic parameters for the growth mechanism are the substrate temperature T and the supersaturation Dm. They can be related by the following equation:

$$D_m = kT ln \left({R}/{R_e} \right) \qquad\qquad Eq.\ 3.1$$

Where k is the Boltzmann constant, R is the actual deposition rate, and Re is the equilibrium value at the temperature T. The nucleation is dependent on the interfacial energies between the three phases present: substrate, the condensing material and the vapor. The deposition rate and the substrate temperature influence the critical size of

the nucleus. The crystalline film growth depends on the surface mobility of the adatom (vapour atoms). Normally, the adatom will diffuse through several atomic distances before sticking to a stable position within the newly formed film. The surface temperature of the substrate determines the adatom's surface diffusion ability. Hence, high temperature favours rapid and defect free crystal growth, whereas low temperature or large supersaturation crystal growth may be overwhelmed by energetic particle impingement, resulting in disordered or even amorphous structures. Metev and Veiko [4] that N, the mean thickness at which the growing, thin and discontinuous film reaches continuity is given by the formula:

$$N = \frac{A\left(\frac{1}{R}\right)1}{3} exp\left(-1/T\right) \qquad Eq.3.2$$

Where R is the deposition rate (supersaturation related) and T is the temperature of the substrate and A is a constant related to the materials.

3.1.2   CVD (Chemical Vapor Deposition)

The Chemical Vapor Deposition (CVD) consists to bring into contacts a reactant gas mixture with the surfaces to be coated. Several authors have used this method to grow desired VO_2 on a particular substrate [5]. The main advantages of this process are [6]: 1) Scaling up of production to industrial level; and (2) Appreciable control over growth of desired (diameter, length and position) which is more important for electronic applications. The CVD can be categorized depending on the energy sources: plasma-enhanced CVD (PECVD), thermal CVD, etc. The wafer is exposed to one or more volatile precursors which react and or decompose on the substrate and make the desired deposit. The precursors are heated in UHV in a crucible to sufficient high temperature and the molecules evaporate and leave the surface to condense on a substrate as a thin film. Generally the temperature is used as a source of atoms or molecular beam and the source is a solid which is heated or fluids (for instance in a Knudsen cell) where the atoms possess thermal energies which correspond to 0.1eV. See

figure 3.3. The first deposition technique used for VO_2 thin films appears to have been CVD and after half a century it is still used extensively.
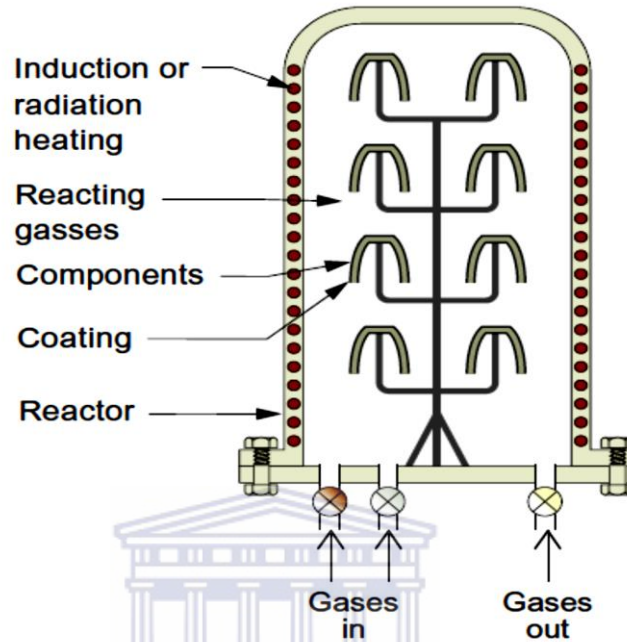
Figure 3.3: Chemical vapor deposition CVD. Reaction of gases in the chamber causing deposition of the reaction product as a layer that can be of nano thickness [1].

Koide and Takei had grown for the first time in 1966 single crystals of VO_2 by CVD [7]. One year later they introduced fumes of vanadium oxychloride carried by N_2 into the growth chamber which was then hydrolysed on the surface of rutile substrates to give epitaxial VO_2 films. In 1968 MacChesney et al. [8] used CO_2 transporting $VOCl_3$, and then applied annealing treatment between 500 ^{o} C and 550 ^{o} C under appropriate oxygen pressure. These researchers were the first to elucidate the phase diagram for the O-V system. Additionally, the electric field can be associated to the CVD to assist the deposition. See figure 3.4.
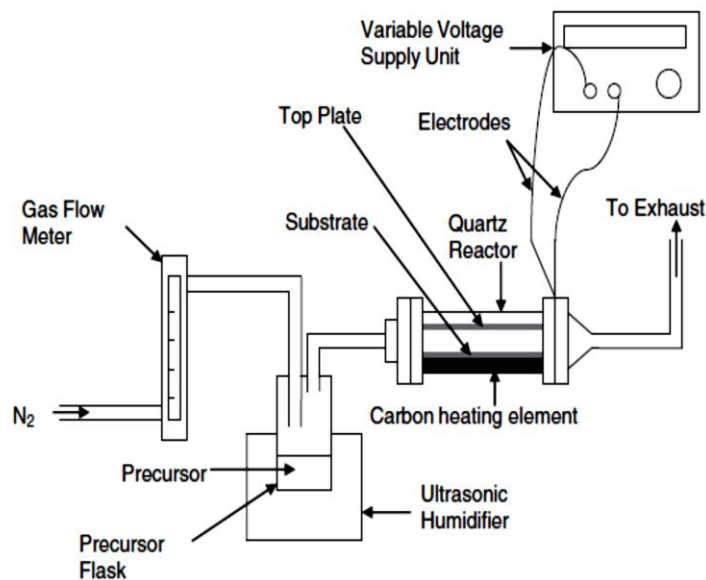
Figure 3.4: Diagram illustrating the set-up of electric field assisted chemical vapor deposition [7].

3.1.3 Sputtering Radio frequency

Physical technique based on the atoms /ions that hit on a target, with high enough energy, where transfer of energy and impulse towards the target atoms take place. Ions are implanted into the material and partially resputtered. Particles at the surface leave the surface as soon as the binding energy of the target is overcome. There are three common dioxide sputtering arrangements utilizing DC discharge, Capacitative RF discharge or Capacitative RF discharge plus planar magnetron. RF operates at lower pressure and lower sputtering gas pressure producing higher deposition rates and sputtering of an insulated target becomes possible while the RF discharge plus a planar magnetron feature a magnetically assisted argon-ion discharge in which a permanent magnet defines lines of magnetic flux perpendicular to the applied electric field from the RF source. The magnetic field concentrates the plasma and intensifies it in the space above the target by trapping electrons near the target surface. RF reactive inverted cylindrical magnetron sputtering (ICMS) was reported for the first time by J.B Kana Kana et al. [9-10] giving polycrystalline structure of single phase monoclinic VO_2

without the presence of any vanadium oxide phases. See figure 3.5. Annealing effect on VO$_2$ thin films deposited by RF ICMS were also studied in detail by J B Kana Kana (2010) [11] towards higher temperature with tunability of the transition temperature at higher substrate temperature and a sizeable variation of ~10 ºC with increasing substrate temperature. It was shown that for VO$_2$ films thickness less or equal to 50 nm, the semiconductor phase exhibits lower visible transmittance than its metallic phase. The higher the substrate temperature, the lower the transmittance in the visible light region with approximately 35% at λ=700 nm for 600 º C while the ones at 450 º C, 500 ºC and 550 ºC present a transmittance of 45%.
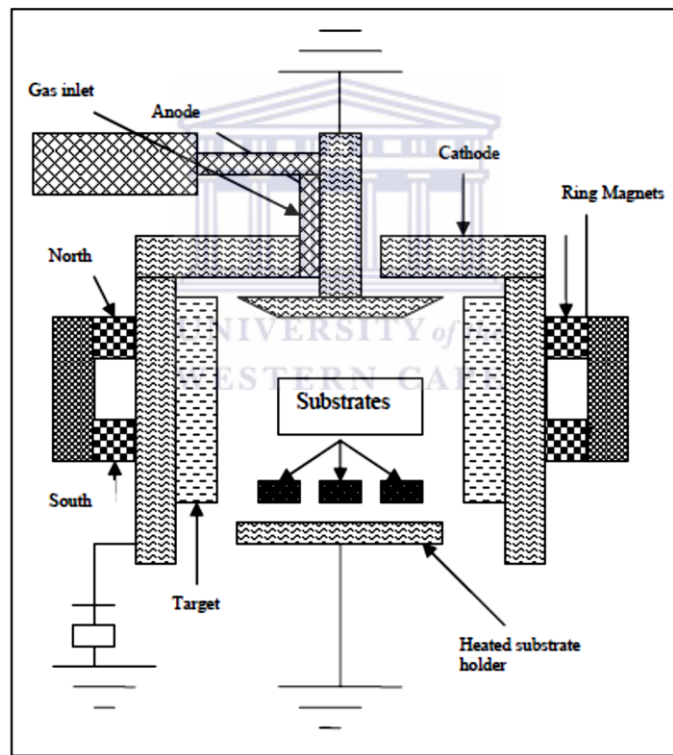
Figure 3.5: RF ICMS sputter gun, the cylindrical ring vanadium metal target with the circular magnet enclosed behind the target. The anode and cathode are perpendicular to each other and the substrates lie perpendicular to the target. [11]

This was explained by the fact that the high temperature influences the sticking factor of the sputtered particles to the substrate surface, implying a slight increase of the

deposition rate. By considering the low energy model, the sputtering yield Y(E) is given as:

$$Y(E) = 0.3 \frac{M_i M}{(M_i + M)^2} \alpha \left(\frac{M}{Mi}\right) \frac{E_0}{U_0}$$

Eq. 3.3

Where Mi and M are atomic masses of incident of the incident ion and target atom respectively; $\alpha\left(\frac{M}{Mi}\right)$ is a function varying from 0.5 to 1.5, E_0 is the energy of the ion and U_0 is the surface binding energy of the target atom. [12].

3.1.4 Dual ion Beam Sputtering

The deposition consists to tune independently the deposition parameter such as: pressure, ion current and energy. Here there is no plasma contamination on the films due to the fact that the plasma generation zone and substrate zone are far apart. It consists of two ion Radio Frequencies ion sources where the first impinges on the target and the second directly against the substrate to make assisted depositions [13].
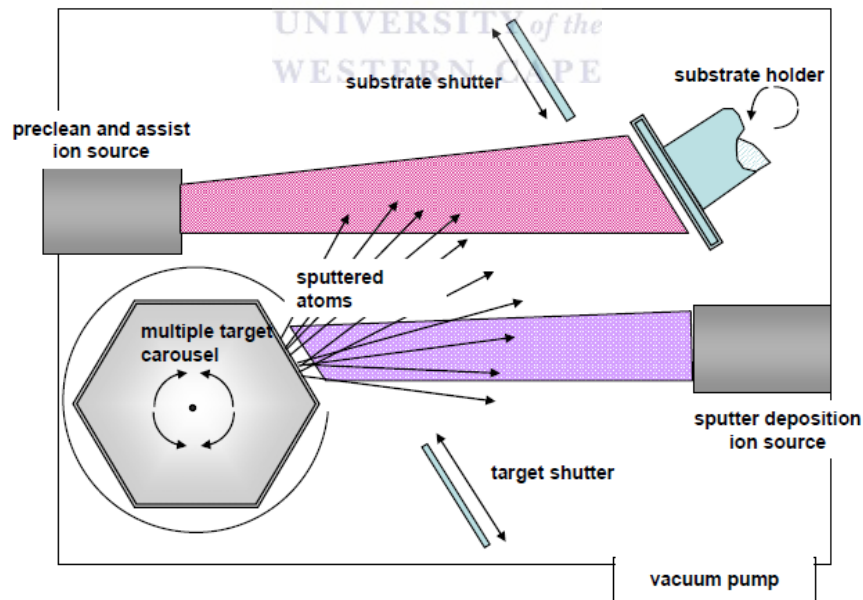
Figure 3.6: Dual Ion Beam Sputtering scheme [13].

The deposition gun is at 45 ^{o} oriented with respect to the target and the target is 45 ^{o} with respect to the substrate. See figure 3.6. The film uniformity is improved by rotating the substrate around its normal axis. In both the ion guns, neutral or reactive gases are used. Zintu et al. [14] synthesized microbolometric VO_2 with DIBS technique presenting the possibility to tune independently each deposition parameter such as: deposition pressure, ion current, and energy. They found that all the vanadium oxides can be obtained by DIBS from a vanadium pentoxide target, but the one desirable to produce microbolometer device is VO_2 which presents a sensitive behavior with a thermal capacity resistivity of -3.0% K^{-1} with 1 Ωcm resistivity, having the desirable sheet resistance with a thickness of about 2000 Å and a detectivity up to 10^8 cm $H_Z^{1/2}/W$, and a response time of few milliseconds.

3.1.5 Spray pyrolysis

The spray pyrolysis technique is a deposition technique where the reactants for the film are deposited unto a target substrate under heating forming the desired film on the surface. See figure 3.7.
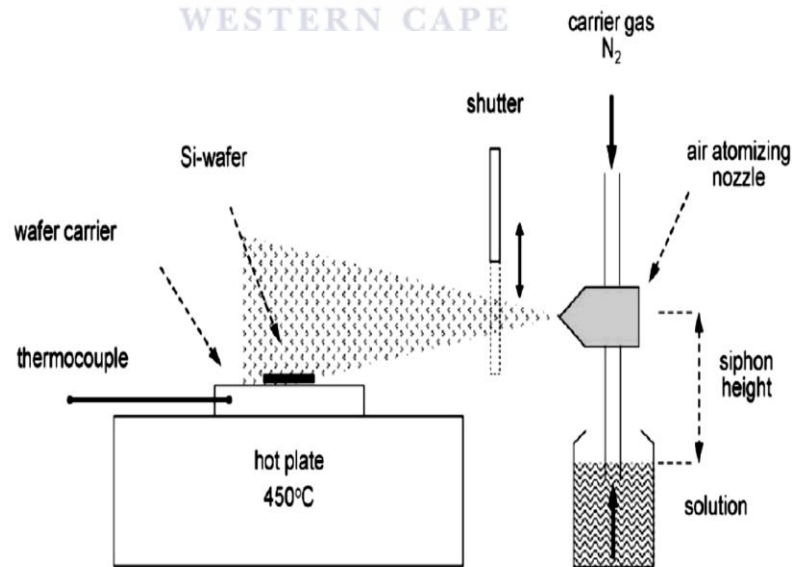
Figure 3.7: Spray pyrolysis deposition technique film [15].

Typical spray pyrolysis equipment consists of an atomizer, precursor solution, substrate heater and temperature controller. The first patents concerning spray pyrolysis date back from 1950s where the solution is atomized to droplets which are passed by means of a carrier gas flow through diffusion dryer then the thermolysis reactor, and finally a calcination furnace. Droplets impact on the substrate surface spread into a disk shaped structure and undergo thermal decomposition. The shape and size of the disk depends on the momentum and volume of the droplet, as well as the substrate temperature. Consequently, the film is usually composed of overlapping disks of metal salt being converted to oxide on the heated substrate [16]. Various applications of spray pyrolysis involve solar cell applications, metal-oxide sensors, metal oxide coatings, oxide fuel cells. The first synthesis of vanadium dioxide obtained by spray pyrolysis was done by Mwakikunga et al. [17]. They used vanadium trichloride in an aqueous solution of 0.085 M ammonium meta-vanadate under an argon carrier gas of 11 ml mn^{-1} and a function temperature above 600 $^{\circ}$ C with a system pressure of 4-10 Ncm^{-2}. They observed that the change of the oxygen to vanadium ratio sensitively affects the transition temperature of vanadium dioxide in the vicinity of 1.93 or 2.05, bringing the transition temperature to room temperature. Hence impregnating VO$_2$ with dopants is not the only route to reduce the transition temperature which apparently comes at the expense of the switching quality and transmittance or reflectance contrast.

3.1.6 Spray drying process

Earliest descriptions date from 1860 with the first patented design recorded in 1872. The basic idea of spray drying is the production of highly dispersed powders from a fluid feed by evaporating the solvent. This is achieved by mixing a heated gas with an atomized (sprayed) fluid of high surface-to-mass ratio droplets, ideally of equal size, within a vessel (drying chamber), causing the solvent to evaporate uniformly and quickly through direct contact [18].The dry particles are continuously discharged from the drying chamber and recovered from the drying media using a cyclone. See figure 3.8.
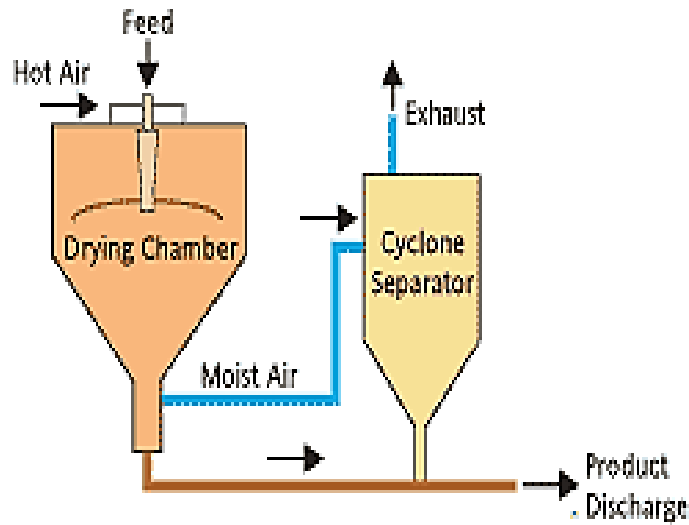
Figure 3.8: Spray drying system consisting of a dryer and cyclone for product recovery [18]

The spray drying process relies on the atomization which include centrifugal, nozzle, pneumatic and sonic process. The droplet size is dependent of a given energy spent for breaking down the liquid into fragments that is increasing the overall surface of the liquid. The spray drying process is energy intensive. It follows that optimization of the setup efficiency is required to reduce the energy consumption per kilogram dry material. The efficiency of the drying process is then given as:

$$\eta = (T_{in} - T_{out})/(T_{in} - T_{amb}) \qquad Eq.\,3.4$$

Where T_{in} is the inlet air temperature, T_{out} is the outlet air temperature and T_{amb} is the ambient air temperature. The higher the air temperature the lower the outlet temperature, the better the efficiency [19]. He et al. [20] recently fabricated thermochromic VO_2/mica pigments using spray-drying process with a rotating sprinkler at the top of a spray-dryer vessel and subsequent annealing at high temperature for 90min under static atmosphere of argon. Several others methods have been used to synthesize VO_2 such as high flux electron beam radiation [21], polymer assisted deposition [22] and ozone based atomic layer deposition [23-24].To obtain VO_2, one of the most unstable oxides, controlled conditions are required. In the following

chapter we present an easy method of synthesis with low cost at low temperature of fabrication with optimized conditions: sol-gel method synthesis that we used to design our materials at the nanoscale dimension.

3.2 Sol-gel chemistry background

The use of soft chemistry processes in solid state chemistry has increased dramatically during the past decade. These processes include intercalation, deintercalation, ion exchange, and mild thermal decomposition, among others [25]. More recently there has been a desire to build structures with open crystalline lattices or expandable layer structures that can undergo redox reactions and therefore be used in electrochemical devices such as batteries, displays and sensors. Such structures are unlikely to be thermally stable under traditional high temperature solid state conditions, so new low-temperature approaches need to be found. One of these is mild hydrothermal synthesis, defined as reactions occurring between 100 and 200°C under autogenous pressure. A number of conditions are critical in determining what solid phases, if any, are formed. These include the pH of the reaction medium, its temperature (and therefore the pressure), and the cations in solution.

VO_2 nanobelts hydrothermally synthesized formed the backbone of this dissertation. Hence we review salient features of sol-gel hydrothermolysis in this section. Generally they are prepared from a solution containing appropriate precursor compounds. They allow non-breaking of weak bonds as Wan Der Waals, hydrogen, hydrophobic, hydrophilic interactions. Sol-gel chemistry plays an important role during growth of molecules [26]. The sol-gel process is generally used at low temperature presenting various advantages for the powderless processing of ceramics, advanced materials design or synthesis of organic-inorganic compounds.

3.2.1 Hydrothermal synthesis genesis-importance and key parameters

The term hydrothermal is from a purely geological origin which was used for the first time by the British geologist, Sir Roderick Murchison (1792–1871), to describe the action of water at elevated temperature and pressure in bringing about changes in the earth's

crust, and leading to the formation of various rocks and minerals [27]. Hydrothermal research had its origin in Europe, and later spread its activity to North America during the early 20th century. The hydrothermal research in Asia began in the 1920s in Japan. Today, Japan has emerged as a leader in this field of research with the USA. However, the hydrothermal research is becoming quite popular in several other countries, particularly in the last three decades. The countries engaged in hydrothermal research are listed below in alphabetical order: Australia, Belgium, Brazil, Bulgaria, Chile, China, Canada, Denmark, France, Germany, Holland, Italy, India, Japan, Korea, Norway, Poland, Russia, Switzerland, Spain, Sweden, Taiwan, UK, Ukraine, and USA. Amongst these countries, over 50% of the hydrothermal research is going on in Japan, USA, and China. Figure 3.9 shows the countries actively engaged in hydrothermal research and figure 3.10 presents the world`s largest autoclave used in Japan.
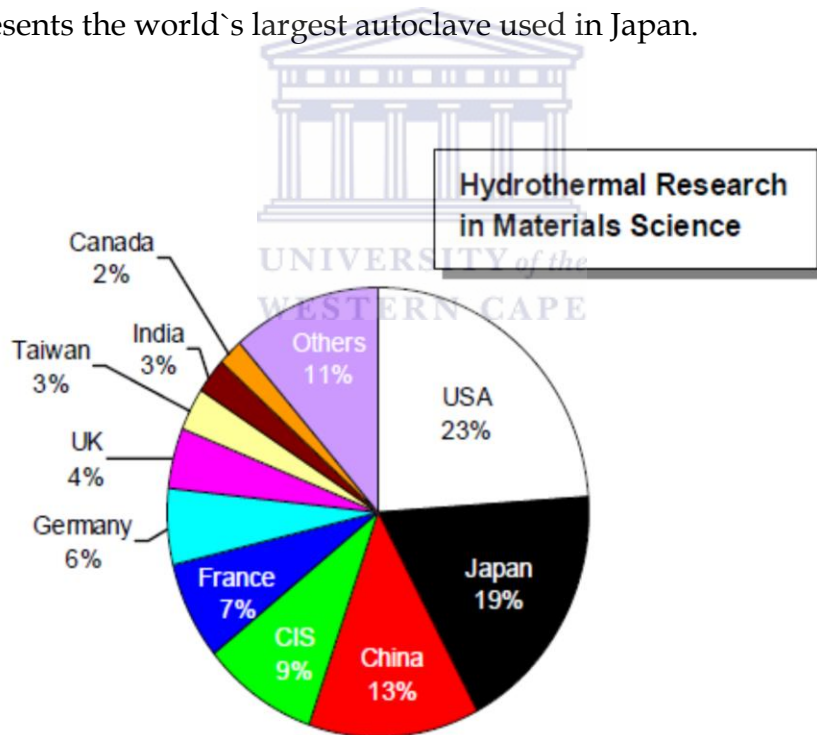
Figure 3.9: Number of papers published in hydrothermal synthesis statistics [27].

Figure 3.10: Growth of quartz crystals in the world`s largest autoclave Japan with >50% production in the world. [27]

In the last decade, the hydrothermal technique has offered several new advantages like homogeneous precipitation using metal chelates under hydrothermal conditions, decomposition of hazardous and/or refractory chemical substances, monomerization of high polymers like polyethylene terephthalate, and a host of other environmental engineering and chemical engineering issues dealing with recycling of rubbers and plastics (instead of burning). Similarly, it is used to remove caffeine and other food-related compounds selectively. It offers several advantages such as: obtention of difficult compounds possible through the closed system method, obtention of low temperature phases materials for example α-quart and synthesis of metastable compounds. Additionally it has been discovered that hydrothermal technique produces homogeneous precipitation, facilitates the decomposition of hazardous and /or refractory systems, monomerization of high polymer. The period from the late 1930s to 1940s is referred to as the "golden period" in the hydrothermal research, not only because of the enhanced research activity, but also because of the many new discoveries

with reference to autoclave designs and other important technological materials. The cheapest and safest solvent used for hydrothermal experiment is water. It can act as a mineralizer or catalyst under high pressure-temperature conditions.

3.2.2 Experimental procedure

The sol-gel method is a wet chemical process generally used for the fabrication of materials typically metal oxide starting of a chemical solution which contains colloidal precursors such as metal alkoxides and metal chlorides. The metal-oxide is formed through the connection of metals centers with oxo or hydroxo bridges which generate metal oxo or hydroxo polymers in solution: M-O-M or M-OH-M. The sol-gel process allows the fine control of the products and chemical composition. The metal Insulator-phase transition obtained through the hydrothermal synthesis is due to the hydrothermal reduction and the exfoliation of bulk layered V_2O_5 by aliphatic alcohols and ketones into the VO_2 (M) structures. In general, the sol-gel process consists of:

i) Preparation of a homogeneous solution either by dissolution of metal-organic precursors in an organic solvent that is miscible with water, or bydissolution of inorganic salts in water; ii) conversion of the homogeneoussolution into a sol bytreatment with a suitable reagent (generally water with or without any acid/base); iii) aging; iv) shaping; v) and thermal treatment/sintering. The first step in a sol-gel reaction leads to the formation of an inorganic polymer by hydrolysis and condensation reactions: the transformation of the molecular precursor into a highly crosslinked solid.

Hydrolysis leads to a sol, a dispersion of colloidal particles in a liquid, and furthercondensation results in a gel, an interconnected, rigid and porous inorganicnetwork enclosing a continuous liquid phase. This transformation is called thesol-gel transition. There are two possibilities to dry the gels. Upon removal ofthe pore liquid under hypercritical conditions, the network does not collapseand aerogels are produced. When the gel is dried under ambient conditions, shrinkage of the pores occurs, yielding a xerogel. Contrarily to others system of synthesis, the highly attractive features of the sol-gel process is the possibility to shape the material into any desired

shapes. See figure 3.11. The morphology and size depend on the reaction time and the concentration of the added structure directing agent.

Solution

Aerogel

Gel

Sol

Drying

Xerogel

Precipitation

Heating

Casting=sintering

Spin or dip
coating

Spining

Uniform
powders

Ceramic glass

Fibers
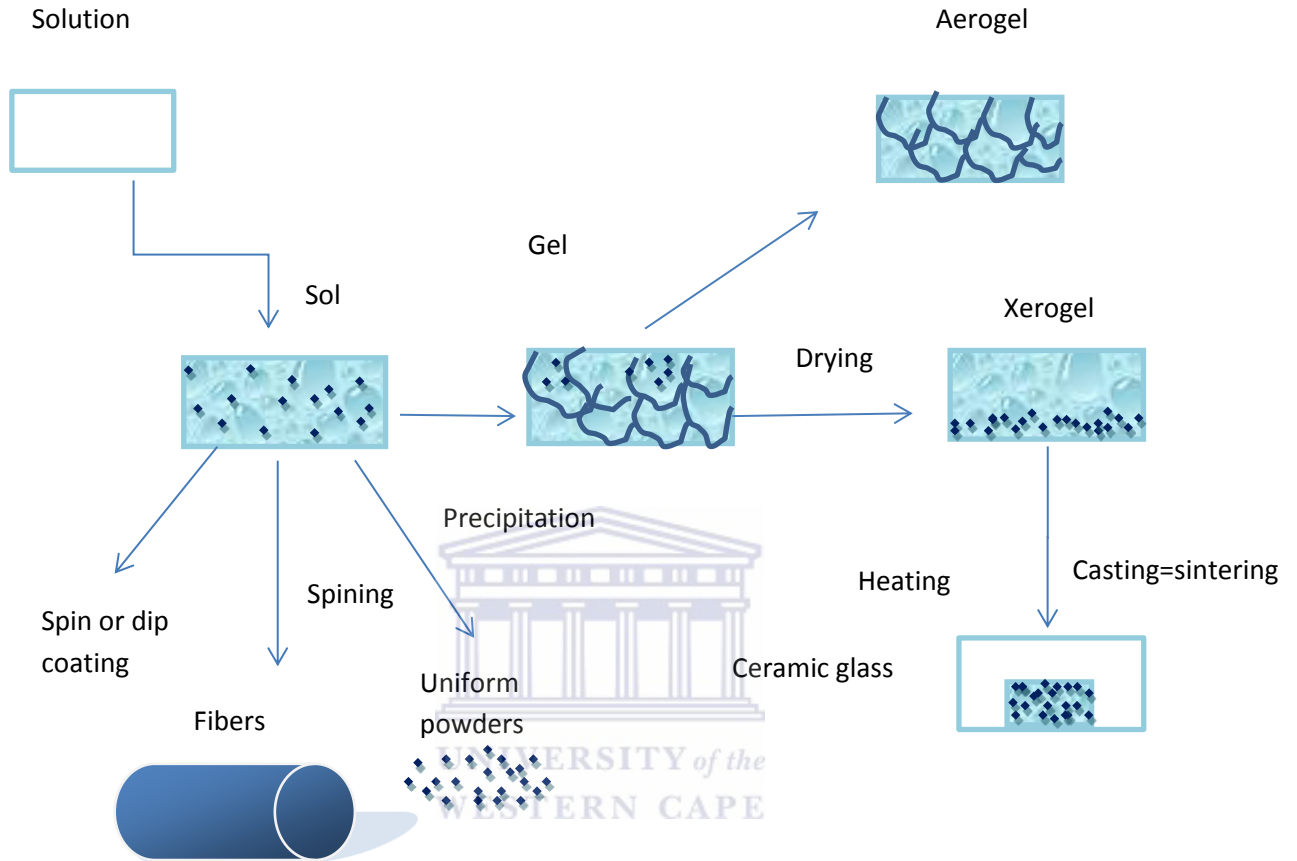
Figure 3.11: Various steps in the sol-gel process to control the final morphology [28].

During the sol gel conversion of metal alkoxides, two main reactions take place: [28-29]: Hydrolysis and condensation (See scheme below). During hydrolysis, the alkoxide groups (-OR) are replaced via the nucleophilic attack of the oxygen atom of a water molecule under release of alcohol and the formation of a metal hydroxide. Condensation reactions between two hydroxylated metal species leads to M-O-M bonds under release of water (oxolation), whereas the reaction between a hydroxide and an alkoxide leads to M-O-M bonds under release of an alcohol (alkoxolation).

- Hydrolysis where the water is split into two parts: OH⁻ and H⁺

$$\equiv M - OR + H_2O \rightarrow \equiv M - OH + ROH \qquad Eq.\ 3.5$$
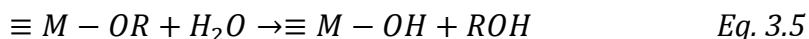
- Condensation – Polymerization (oxolation and alkoxolation)

$$\equiv M - OH + HO - M \equiv \rightarrow \equiv M - O - M \equiv + H_2O \qquad Eq.\ 3.6$$

$$\equiv M - OR + HO - M \equiv \rightarrow \equiv M - O - M \equiv + ROH \qquad Eq.\ 3.7$$
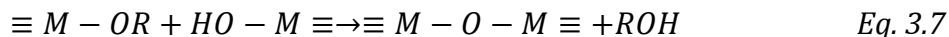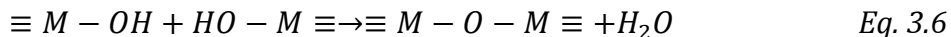
The chemical reactivity of metal alkoxides towards hydrolysis and condensation depends mainly on the electronegativity of the metal atom, its ability to increase the coordination number, the steric hindrance of the alkoxy group, and on the molecular structure of the metal alkoxides (monomeric or oligomeric). The amount of added water in the hydrolysis step and how the water is added, determines, whether the alkoxides are completely hydrolyzed or not and which oligomeric intermediate species are formed. Additional parameters are the polarity, the dipole moment, and the acidity of the solvent. The oxygen for the formation of the oxidic compound is supplied by the water molecules.
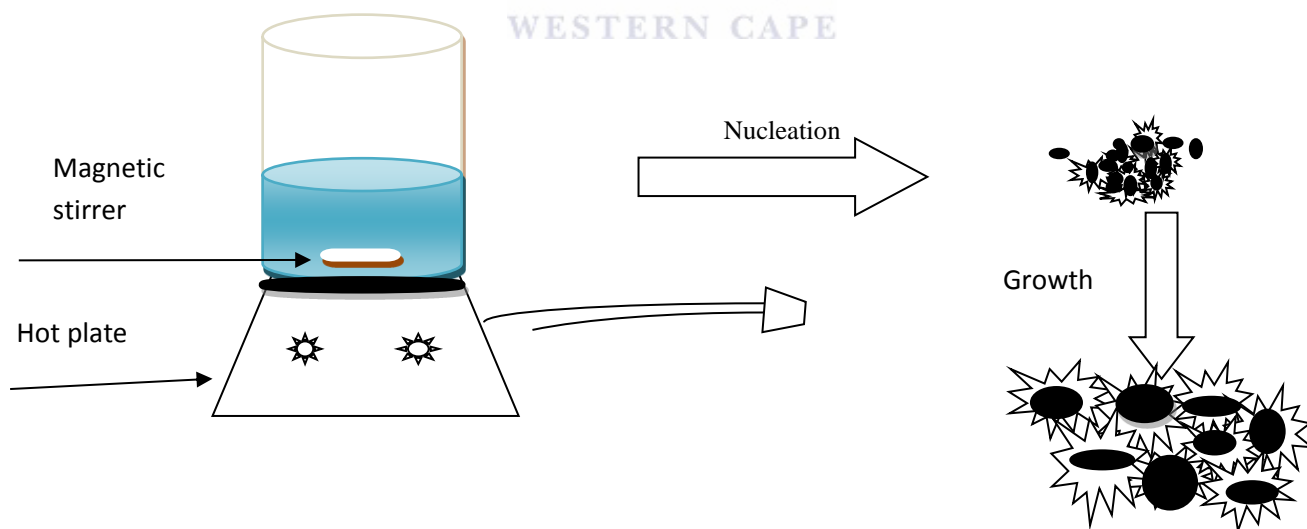
Figure 3.12: Experimental setup and reaction scheme for the hot injection process [30].

The injection of the precursor induces high degree of supersaturation which results in a short burst of nucleation. This latter signifies that the concentration of the precursor

decreases abruptly in the solution. The drop in temperature due to the injection of cold reactants and low concentration of unreacted remaining precursor prevent any further nucleation events. Hence the temperature is applied for the next step characterized by the slow growth of the nuclei to larger nanoparticles as shown in figure 3.12.Vanadium oxides can also be obtained via the hydrolysis and condensation of vanadium alkoxides $VO(OR)_3$. When hydrolyzed with an excess of water, these alkoxides give fully hydroxylated precursors $VO(OH)_3$ and condensation leads to $V_2O_5.nH_2O$ gels similar to those formed from aqueous solutions. This is no more the case when hydrolysis is performed with a small amount of water (h=H_2O/V~1), amorphous oxopolymers $[VO(OH)x(OR)_{3-x}]_n$ rather than layered oxides gels are formed [31].

3.2.3 Why Nanobelts?

Since the discovery of semiconducting oxide nanobelts in 2001 [32], nanobelts (NBs) have been demonstrated as the fundamental building blocks for fabricating various nanosized devices such as field-effect transistors [33-34], ultrasensitive gas sensors [35]. Additionally to our current study, various nanobelts materials have been prepared for specific purposes [36]. Guodong Wei et al. reported 3C-SiC ultrathin nanobelts which can be used as field emitting materials with low turn on field of 3.2 V/µm. it has been shown that the optical response is strongly correlated to the quatum confinement of the nanobelt due to the closest thickness of the nanobelt to the atomic Bohr radius of the bulk. When the nanobelt thickness approaches the effective Bohr radius, the electronholepair gets spatially confined, namely electron-hole confinement. The calculation has been constructed in one dimensional thickness model according to a rectangular infinite well potential:

$$E(q_x) = \frac{\hbar^2 q_x^2}{2m^*} + \frac{\hbar^2}{2m^*}\left[\left(\frac{\pi}{L_y}\right)^2 + \left(\frac{\pi}{L_z}\right)^2\right] \qquad Eq.\,3.8$$

h is the constant of Planck, m*=0.195 m_e is the reduced mass of the exciton.

SnO$_2$ nanobelt have been reported as field effect transistor and intrinsic response to hydrogen sensor [37] which is due to the unicity of the belt nanostructures presenting high surface to volume ratio with intrinsic surface chemistry and tunable composition. It has been shown that the quasi 1D nanomaterials present high sensitivity due to their large active surface and their lateral dimension is comparable to the width of the surface space charge region [38]. Cheng et al. demonstrated that the nanobelts materials have hydrogen sensing capabilities with a significantly enhanced reaction time and high sensitivity at room temperature. Nanocrystals of semi-conducting oxide materials can be applied for short wavelength optical devices and exitonic devices operating at room temperature. They generally contribute to the confinement of the excitons [39].The nanobelts (ultralongbeltlike or ribbonlike) nanostructures could be an ideal system for fully understanding dimensionally confined transport phenomena in functional oxides and building functional devices along individual nanobelts [32]. Lingzhi et al. [40] synthesized Cl doped-CdSe nanobelts which were constructed as nano-FETs, and Schottky Diodes which can also be used as photodetectors with fast response speed. Zakharova et al.[41] prepared V$_3$O$_7$.H$_2$O nanobelts through hydrothermal process which works as growing seed for V$_2$O$_5$ nanobelt upon annealing temperature up to 350 $^{\circ}$C in air. Their potential application was shown to be correlated to the high specific energy density, high working voltage and long life cycles. Nanobelts are very promising for sensors due to the fact that their faces exposed to the gas environment are always the same and the size is likely to produce a complete depletion of carriers inside the belt [42]. The sol gel method is proved to be efficient for the synthesis of VO$_2$ micro-nanostructures and is proved to be efficient economically and easy to scale up in industrial production with the absence of reductant and vacuum conditions. Liu et al. [43] prepared VO$_2$ (B) nanobelts starting from V$_2$O$_5$ involving hydrothermal process at 180 deg C for 24h which were transfer into a 50 ml stainless steel autoclave. While 1 D structures generally allow formation of domain walls perpendicular to the longitudinal axis which thus can be completely strain-relaxed or under uniform strain, the 2D nature of the platelets generates multiple domain variants and hence geometric frustration

between different domain orientations additionally 2D systems domain structures are easily accessible for local microscopic observations. The preservation of the nanobelt structure and lateral size at high temperature and upon cooling back to room temperature force the material to break into ferroelastic domains along length spanning the whole width to accommodate the change of the lattice geometry. The domains are self-organized into quasi periodic structures minimizing the elastic energy of the nanoplatelet [44].

3.2.4   Sol-gel method Approach

The preparation of 1D nanomaterial can be prepared by bottom-up approach or top-down approach. Comparatively to the top down approach which use fully developed semiconductor industry technology, with long preparation time and elevated costs, the bottom–up approach consists to assemble building block at molecular level which gives better crystallinity and purity with smaller diameter, lowering production cost. Sol-gel method techniques are generally applied in different ways: spray coating where the colloidal dispersion is sprayed unto the substrate using a spray gun which is generally moved across the substrate; drop coating technique which is used by depositing the colloidal dispersion on the surface substrate by using the microinjector or the micropipette; finally another way of depositing sol-gel precursor is by spin coating of the pre-processed metal-oxide onto the substrate whereby the thickness of the deposited gel layer can be controlled by varying the revolution rate.
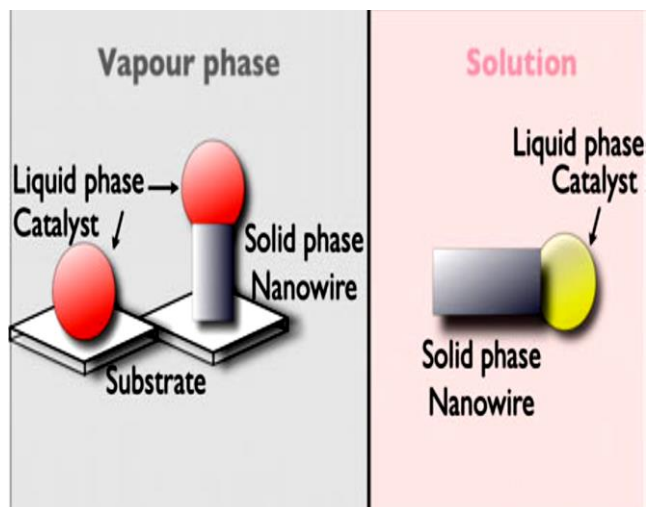
Figure 3.13: Schematic representation of vapor-liquid-solid growth and solution-liquid-solid growth mechanism [45].

The solution based-growth relies on two methods: template assisted (sol-gel) and template-free methods. Regarding the template assisted method; hydrothermal growth is well known for material synthesis. It has been proposed since 1970s [20] for the production of nanocrystalline materials. See figure 3.13. In our case, we use it as template assisted method where the crystallization happens at high temperature 240° C in aqueous solutions at high vapor pressures (>1atm). The crystal growth is habitually performed in an apparatus consisting of a steel pressure vessel (autoclave) in which an aqueous mixture of soluble metal salt of the precursor material is supplied. Several oxides have been synthesized using wet chemical hydrothermal approach [46-49]. The Common method for sol-gel synthesis is described below. See figure 3.14.
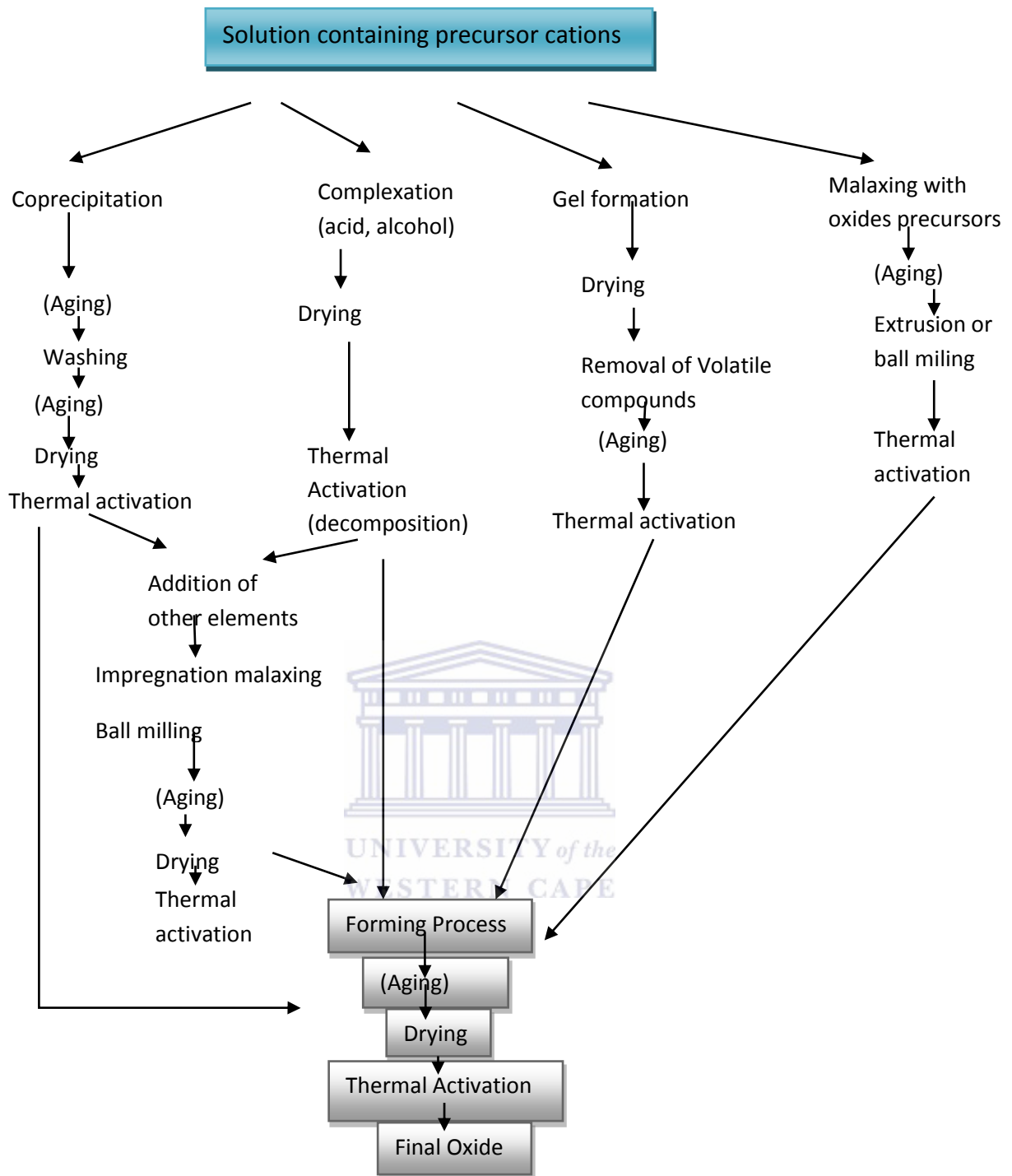
Figure 3.14: Common methods for the preparation of mixed oxides [50].

3.3 Polarity of the water versus dielectric constant and density

The solubility of non-polar species increases while ionic and non-polar compounds decrease. This result in a drop of polarity of the water with increase of molecular mobility due to the decrease in solvent viscosity η. See table 3.1. Drastic changes in hydration come from the decrease in dielectric constant ε and density ρ. See figure 3.15,

figure 3.16 and figure 3.17. The ambient values are ρ_a= 0.997g.cm^{-3}, ε_a= 78.3, η = 0.890mPa s. The saturation pressure vapor is low for temperature below 150-200 $^\circ$ C and rise sharply above 200 $^\circ$ C according to figure 3.15. This is due to hydrogen bonding.

Table 3.1: Values of. ε_r, ρ (g.cm^{-3}) and η (mPa s) of water at high temperatures and high Pressures [51].

p/MPa	Parameter	200	250	300	350	400	450
10	ε_r	35.1	27.4	20.4	1.2	1.2	1.1
	ρ	0.871	0.806	0.715	0.045	0.038	0.034
	η	0.136	0.108	0.087	0.022	0.025	0.027
20		35.3	28.0	21.2	14.1	1.6	1.4
		0.878	0.816	0.733	0.600	0.101	0.079
		0.139	0.110	0.091	0.070	0.026	0.028
30		35.9	28.4	22.0	15.7	5.9	2.1
		0.885	0.826	0.751	0.646	0.357	0.148
		0.141	0.113	0.094	0.076	0.044	0.031
40		36.3	28.9	22.6	16.7	10.5	3.8
		0.891	0.835	0.765	0.672	0.523	0.271
		0.114	0.115	0.097	0.080	0.062	0.039
50		36.6	29.3	23.1	17.6	12.2	6.6
		0.897	0.843	0.777	0.693	0.278	0.402
		0.146	0.118	0.099	0.083	0.068	0.051
60		37.0	29.7	23.6	18.2	13.3	8.5
		0.903	0.850	0.788	0.711	0.612	0.480
		0.148	0.120	0.101	0.086	0.073	0.059
70		37.3	30.0	24.0	18.8	14.2	9.9
		0.909	0.857	0.798	0.726	0.638	0.528
		0.150	0.122	0.104	0.089	0.077	0.065
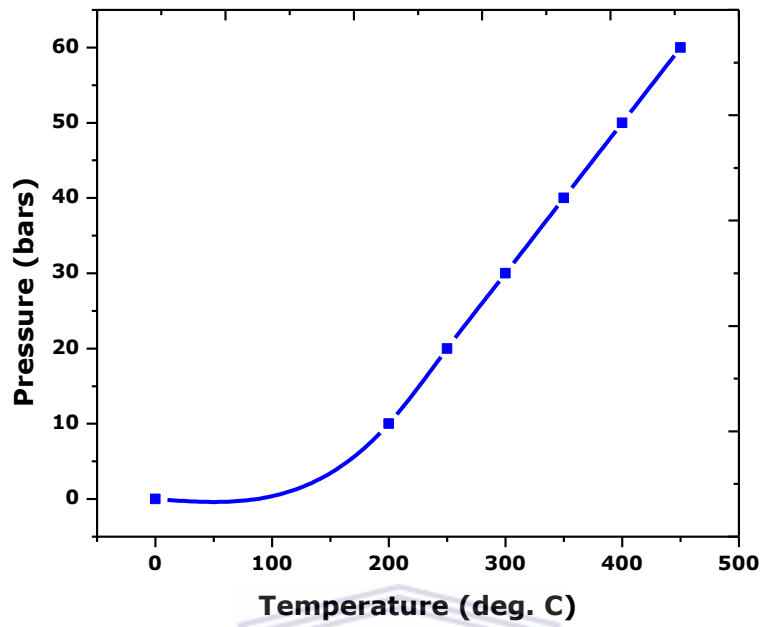
Figure 3.15: Temperature dependence of saturation vapor pressure
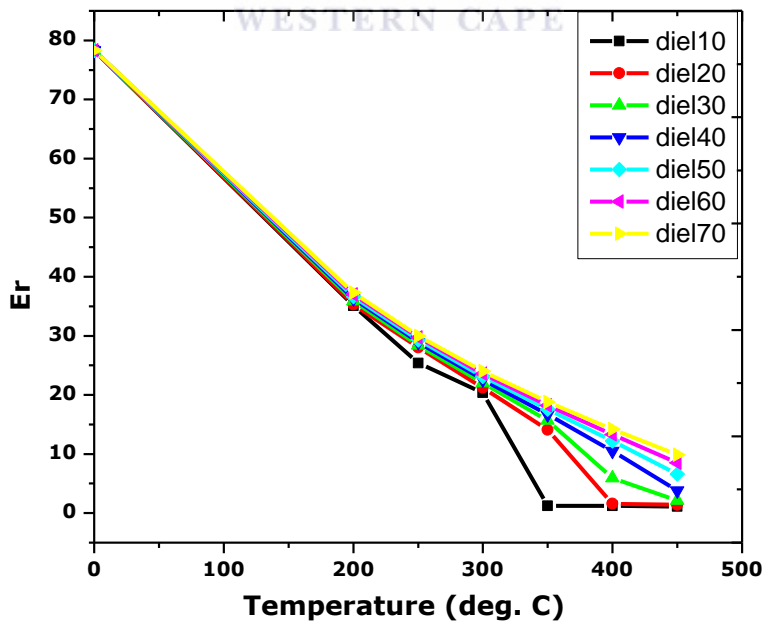
Figure 3.16: Temperature dependence of dielectric constant

89
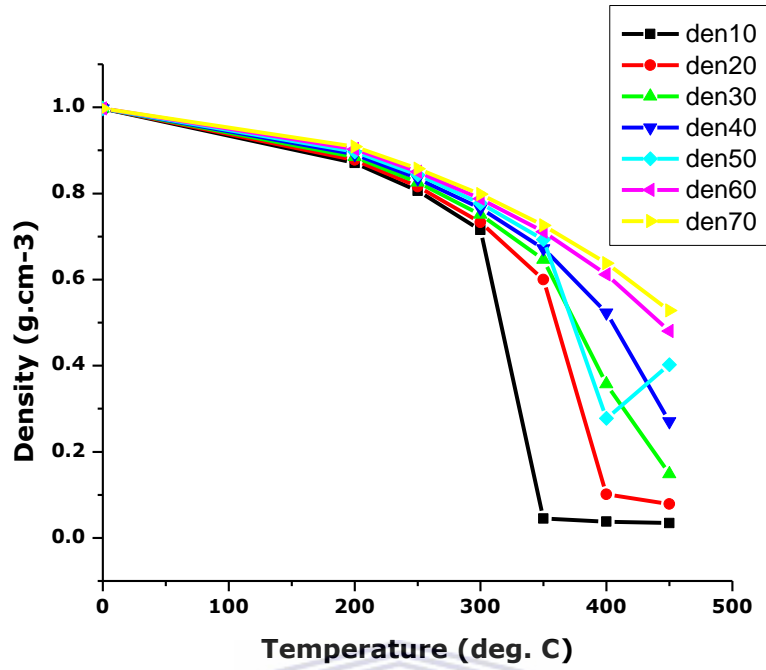
Figure 3.17: Temperature dependence of density of water
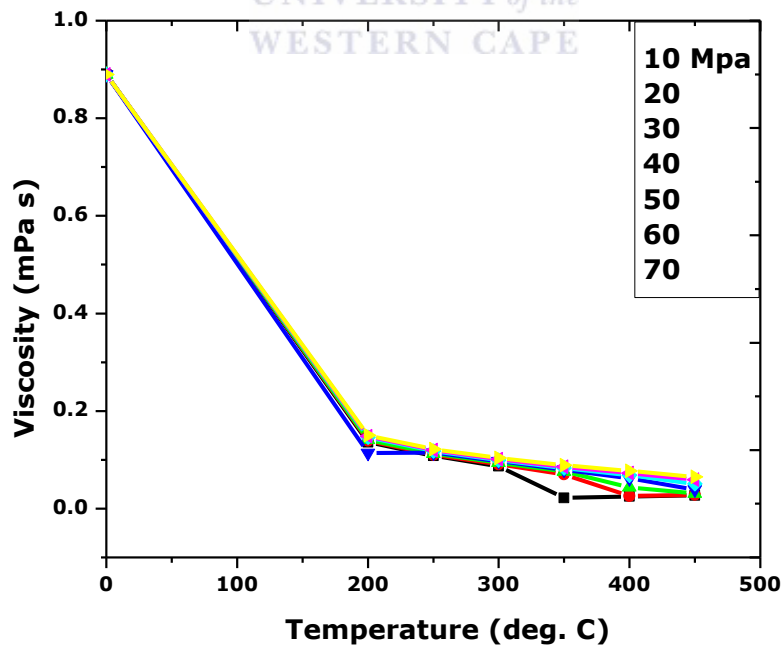
Figure 3.18: Temperature dependence of water viscosity

In our case we use a temperature of 230-240 °C which gives an approximate pressure of 20 MPa. Hence the behavior of the dielectric, viscosity and density of water in those conditions are expressed as seen in figure 3.18, figure 3.19 and figure 3.20.
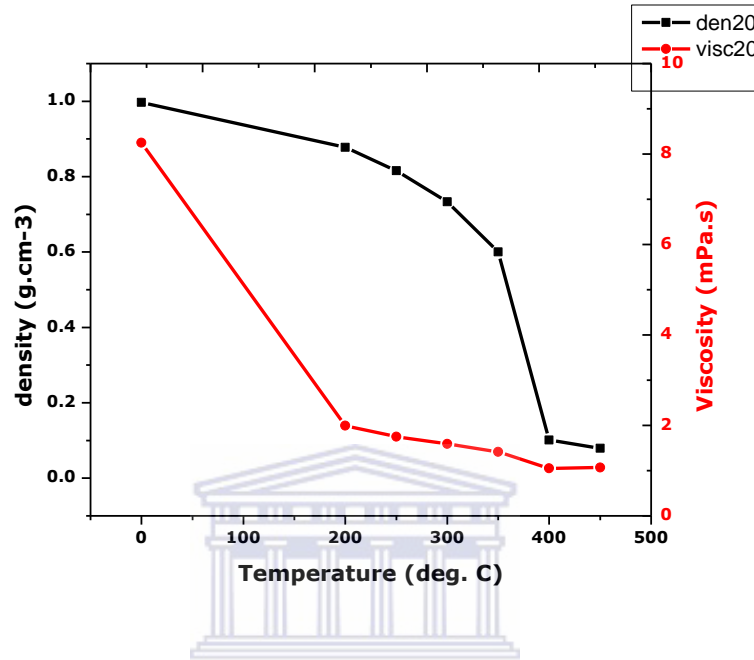
Figure 3.19: Temperature dependence of density and viscosity at 20Mpa.
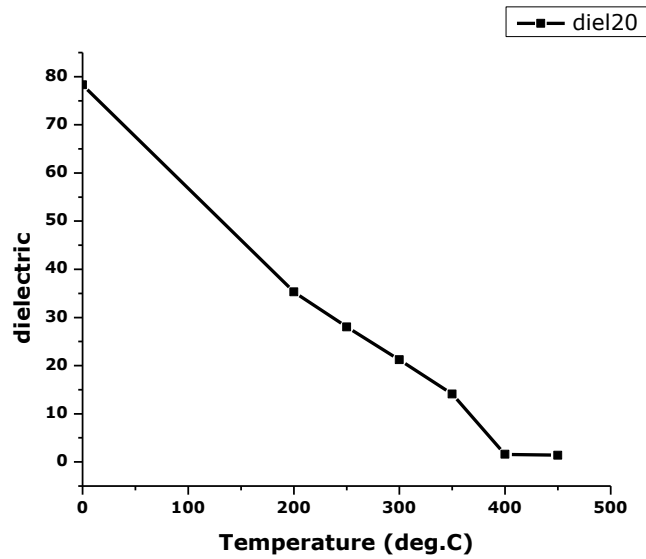
Figure 3.20: Temperature dependence dielectric constant at 20 MPa.

Solvothermal processes were used to speed chemical reactions that were performed in a closed reaction vessel at temperatures higher than the boiling point of the solvent employed (240°C). Solvothermal processes are mainly defined by chemical parameters such as the nature of the reagents and of the solvents, and by thermodynamical factors, in particular temperature and/or pressure. For higher temperatures above boiling points, we use autoclaves, a kind of Teflon cups containers which provide protection against corrosion. The use of Teflon in a closed reactor has the advantage of improving the reproducibility by excluding the influence of the surrounding environment. The Teflon cups were used not only for solvothermal conditions or for high reactions temperatures but also to prevent the evaporation of low-boiling organic compounds that need to be present in the reaction vessel to drive the nanoparticle formation to completion. The hydrothermal conditions generally for an aqueous medium correspond to temperatures and pressures higher than 100 ° C and 1 bar respectively. Such conditions allow modification of the chemistry of cations in solution, favoring the formation of metastable structures, more complex, of lower symmetry involving smaller enthalpy and entropy changes [52]. Hydrothermal solutions are known for their low dielectric constants, and electrolytes completely dissociated under normal conditions forming ion pairs or complexes of small electrostatic charge; then the increase of temperature decreases the viscosity of the water leading to an increased mobility of dissolved species compared with normal conditions; finally the advantage of hydrothermal process is the ionicity product of the water which increases strongly with the temperature as:

$$log K_e = -\left(\frac{3018}{T}\right) - 3.55 \qquad\qquad Eq.\,3.9$$

3.4 Thermodynamic kinetics of Vanadium dioxide precipitation synthesized by hydrothermal synthesis

The formation of VO_2 (precipitation) can be explained by using the kinetics aspect of the condensation mechanisms which present four steps:
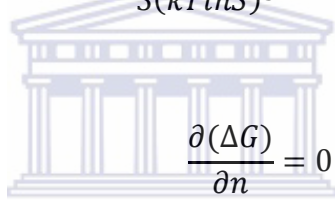
- Formation of the zero charge precursors able to condense and form a solid phase. It can take place through the addition of a base, thermohydrolysis or the thermal decomposition of a base.

- Creation of nuclei through condensation of zero-charge precursor which is function of the precursor concentration. Beyond a critical concentration C_{min}, the concentration rate increases abruptly and polynuclear entities are formed in an explosive manner. The nucleation process is a rapid kinetic phenomenon because the order of reaction is higher than the precursor concentration. The free enthalpy of nucleation is given by:

$$\Delta G = -nkTln\,S + n^{\frac{2}{3}}(36\pi v^2)^{\frac{1}{3}}\gamma \qquad\qquad Eq.3.10$$

$$n^* = \frac{32\pi\gamma^3 v^2}{3(kTlnS)^3} \qquad\qquad Eq.3.11$$

This is given by:

$$\frac{\partial(\Delta G)}{\partial n} = 0 \qquad\qquad Eq.3.12$$

$S = c_L/c_S$ is the supersaturation ratio of the solution with c_L is the concentration of the precursor in solution and c_S is the solubility of the solid phase. γ is the surface tension which is usually positive for a supersaturated solution. v is the molecular volume of the n precursors. See figure 3.21.

- The growth of nuclei which follow the chemical mechanism as nucleation is of first and second order. Generally the number and particle size of the particles are linked to the relative nucleation and growth rates. Particles of homogeneous size obtained require a greater nucleation rate than the rate at which the precursor is generated. Hence the nucleation rate is very brief and decoupled from the growth phase whereas in a low rate nucleation, the nucleation and growth are simultaneous giving large particle size distribution. See figure 3.22.

- Finally we have the aging of particles in suspension which lead to various possible modifications of the primary particles after their growth where we

observe Otswald ripening and possible aggregation. Aging take place over a very large time scale (hours, days and months) which allow the system to tend towards or to reach stability. See figure 3.23.
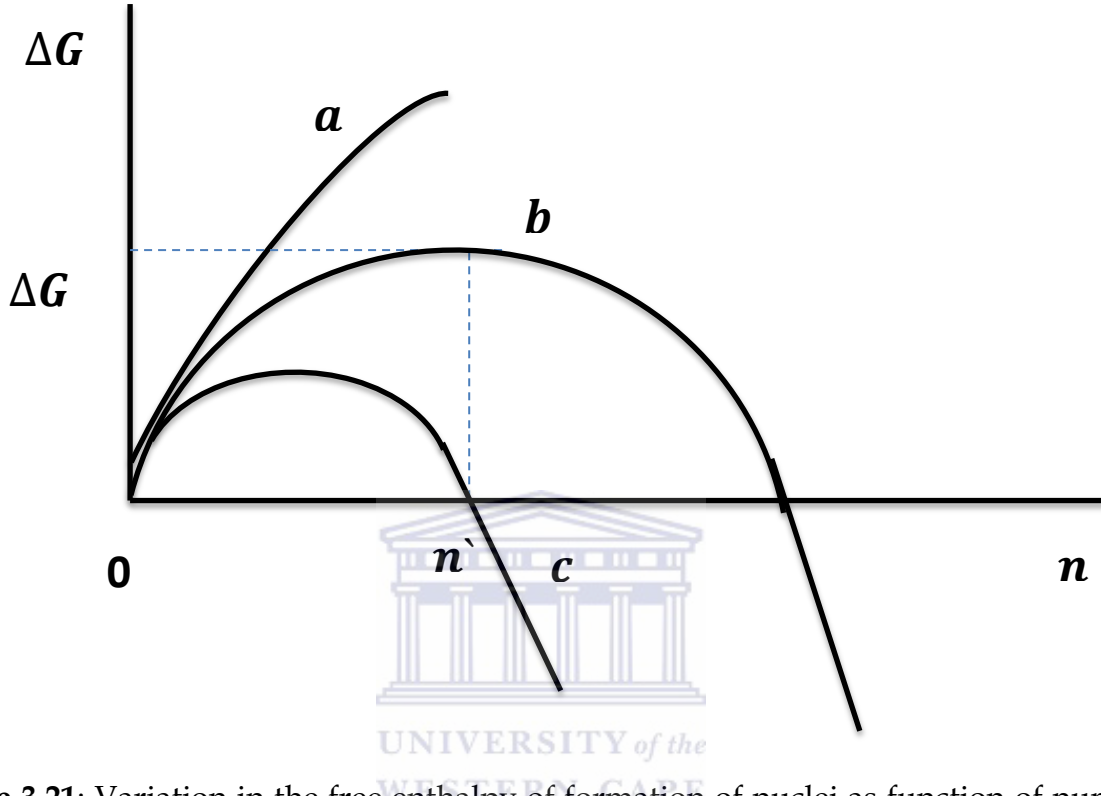
Figure 3.21: Variation in the free enthalpy of formation of nuclei as function of number of precursor's molecules n. a is for a solution that is non -supersaturated S<1, and b and c are for supersaturated solution $S_c > S_b$. [52].
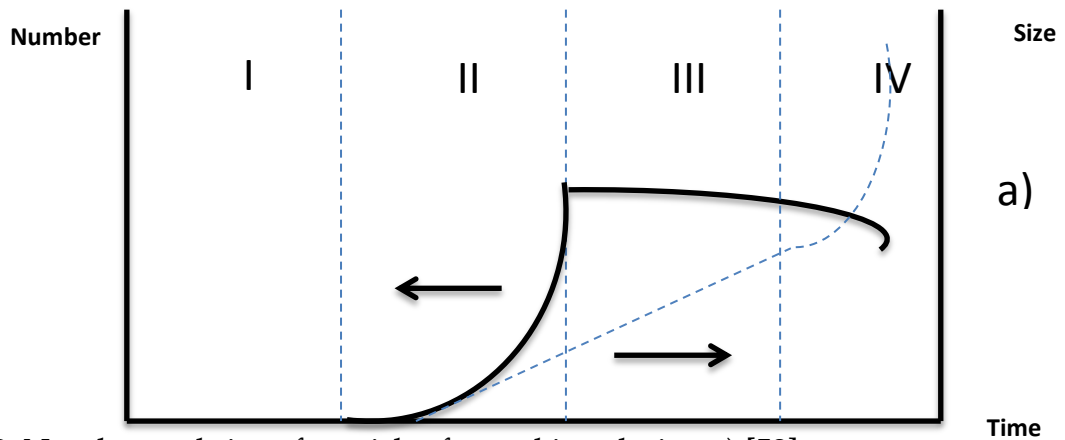
Figure 3.22: Number and size of particles formed in solution a) [52]

The condensation rate is zero for C<Cmin and infinite for C ≥ Cmax, Cs is the solubility of the solid phase [52].

Concentration
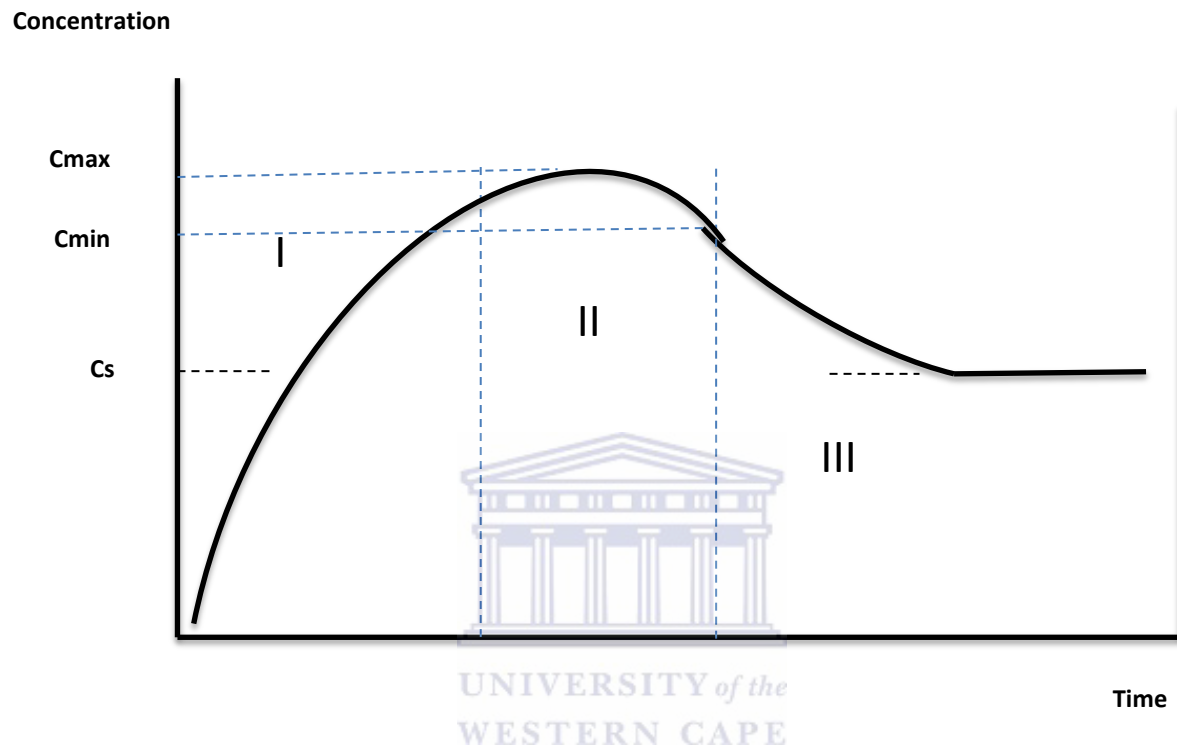
Figure 3.23: Number and size of particles formed in the solution C during precipitation b) [52].

3.5 References

[1] Ashby, M.F.; Ferreira, J.P.; Schodek, D.L.; *Nanomaterials, Nanotechnologies and Design*, Elsevier Ltd , Butterworth-Heinemann, 30 Corporate Drive, Suite 400, Burlington, MA 01803, USA, Linacre House, Jordan Hill, Oxford OX2 8DP, UK, 2009.

[2] Nag, J.; and Jr, H.R.F.; *J. Phys. Condens. Matter* 20, 2008, 264016. 14pp.

[3] Shoning, M.J.; Mourzina, Y.G.; Schubert, J.; Zander, W.; Legin, A.; Vlasov, Y.G.; Luth, H.; *Sensors and Actuators B* 78, 2001, 273-278.

[4] http://titan.physx.u-szeged.hu/~lamilab/plden.htm.

[5] Cao, J.; Ertekin, E.; Srinivasan, V.; Fan, W.; Huang, S.; Zheng, H.; Yim, J.W.L.; Khanal, D.R.; Ogletree, D.F.; Grossman, J.C.; and Wu, J.; *Nature Nanotechnology*, 4, 2009, 732.

[6] Kuchibhatla, S.V.N.T.; Karakoti, A.S.; *Progress in Materials Science* 52, 2007, 699–913.

[7] Koide, S.; and Takei, H.; *J. Phys. Soc. Japan* 22, 1967, 946-7.

[8] MacChesney, J. B.; Potter, J. F.; and Guggenheim, H. J.; *J Electrochem. Soc*. 115, 1968, 52-5.

[9] Kana, J.B.K.; Ndjaka, J.M.; Ngom, B.D.; Nemraoui, O.; Fasasi, A.Y.; Nemutudi, R.; Gibaud, A.; Knoesen, D.; Maaza, M.; *Thin Solid Films* 2009, doi:10.1016/ .jtsf.2009.11.074

[10] Kana, J.B.K.; Ndjaka, J.M.; Ateba, P.O.; Ngom, B.D.; Manyala, N.; Nemraoui, O.; Beye, A.C.; Maaza, M., *Applied Surface Science* 254, 2008, 3959-3963.

[11] Kana, J.B.K.; Ndjaka, J.M.; Ngom, B.D.; Fasasi, A.Y.; Nemraoui, O.; Nemutudi, R.; Knoesen, D.; Maaza, M.; *Optical Materials* 32, 2010, 739-742.

[12] Martin, J.P.; *Journal of Materials Science* 21, 1986, 1-25.

[13] http://www.iiti.ac.in/DIBSD/about_DIBSD_facility.htm

[14] Zintu, D.; Tosone, G.; Mercuri, A.; *Infrared Physics and Technology*, 43, 2002, 245-250

[15] Tischner, A., Maier, T.; Stepper, C.; Kock, A.; *Sen. Actuat. B-Chem*, 134, 2008, 796-802

[16] Perednis, D.; PhD. Thesis, Swiss Federal Institute of Technology Zurich, 2003.

[17] Mwakikunga, B.W.; Haddad, E.S.; Maaza, M.; *Optical Materials* 29, 2007, 481-487

[18] http://www.eurotherm.com/industries/life-sciences/applications/spray-drying

[19] Niro, G.; "A Primer on Spray Drying Chemical Engineering, November 2009. [Online]. Available at www.che.com

[20] He, P.; Huang, W.X.; Yan, J.Z.; Zhi, M.Y.; Cai, J-H.; Luo, R.-R.; *Materials Research Bulletin* 46, 2011, 966–969

[21] Lin, L.B.; Lu, T.C.; Liu, Q.; Lu, Y.; Feng, X.D.; *Surface and Coatings Technology* 158, 2002, 530-533

[22] Du, J.; Gao, Y.; Luo, H.; Zhang, Z.; Kang, L.; Chen, Z.; *Sol. Energy Mater. Sol.Cells* 2011.

[23] Rampelberg, G.; Schaekers, M.; Martens, M.K.; Xie, Q.; Deduytsche, D.; Schutter, B.D.; Blasco, N.; Kittl, J.; and Detavernier, C.; *Applied Physics Letters* 98, 2011, 162902.

[24] Dagur, P.; Mane, A.U.; Shivashankar, S.A.; *Journal of Crystal Growth* 275, 2005, e1223–e1228.

[25] Whittingham, M.S.; *Current Opinion in Solid State and Materials Science*, 1(2), 1996, 227–232.

[26] Livage, J.; Beteille, F.; Roux, C.; Chatry, M.; and Davidson, P.; *Acta mater*. 46(3), 1998 743-750.

[27] Byrappa, K.; and Yoshimura, M.; *Handbook of Hydrothermal Technology, A Technology for Crystal Growth and Materials Processing*, Noyes Publications Park Ridge, New Jersey, U.S.A.William Andrew Publishing, LLCNorwich, New York, U.S.A., 2001.

[28] www.solgel methods .com, 2011.

[29] Niederberger, M.; Pinna, N.; *Metal Oxide Nanoparticles in Organic Solvents: Synthesis, Formation, Assembly and Application*, Springer-Verlag London Limited 2009.

[30] Jia, C.-J.; and Schüth, F.; Phys.Chem.Chem.Phys., 13, 2011, 2457-2487.

[31] Guzman, G.; Beteille, F.; Morineau, R.; and Livage, J.; *Eur. J. Solid State Inorg. Chem.*, 32, 1995, 851.

[32] Pan, Z.W.; Dai, Z. R.; Wang, Z.L.; *Science* 291(5510), 2001, 1947-9.

[33] Cheng, Y.; Xiong, P.; Fields, L.; Zheng, J.; Yang, R.; Wang, Z.; *Appl. Phys. Lett*. 89, 2006, 093114.

[34] Ding, Y.; and Wang, Z.L.; *Micron* 40, 2009, 335–342.

[35] Sadek, A.Z.; Choopun, S.; Wlodarski, W.; Ippolito, S.J.; Zadeh, K.K.; *IEEE Sens.* J. 7, 2007, 919.

[36] Wei, G.; Qin, W.; Kim, R.; Sun, J.; Zhu, P.; Wang, G.; Wang, L.; Zhang, D.; Zheng, K.; *Chemical Physics Letters* 461, 2008, 242–245.

[37] Cheng, Y.; Yang, R.; Zheng, J.-P.; Wang, Z.L.; Xiong, P.; *Materials Chemistry and Physics* 137, 2012, 372-380.

[38] Lilach, Y.; Zhang, J.P.; Moskovits, M.; Kolmakov, A.; *Nano Lett.* 5, 2005, 2019-2022.

[39] Bando, K.; Sawabe, T.; Asaka, K.; Masumoto, Y.; *Journal of Luminescence* 108, 2004, 385–388.

[40] Lingzhi, D.; Lei, Y.; *Materials Letters* 106, 2013, 100–103.

[41] Zakharova, G.S.; Volkov, V.L.; Täschner, C.; Hellmann, I.; Leonhardt, A.; Klingeler, R.; Büchner, B.; *Solid State Communications* 149, 2009, 814-817.

[42] Comini, E.; Faglia, G.; and Sberveglieri, G.; Pan Z.; and Wang, Z.L.; *Applied Physics Letters* 81(10), 2002.

[43] Liu, X.; Xie, G.; Huang, C.; Xu , Q.; Zhang , Y.; Luo,Y.; *Materials Letters* 62, 2008, 1878–1880.

[44] Tselev, A.; Vincent Meunier, V.; Strelcov, E.; Shelton, W.A.; Jr; Igor A Luk`yanchuck, I.A.; Jones, K.; Proksch, R.; Kolmakov, A.; and Kalinin S.V.; [ACS]*NANO* 4, www.acsnano.org.

[45] Baratto, C.; Comini, E.; Faglia, G.; Sberveglieri, G.; Fleischer, M.; and M. Lehmann, M.; (eds.), *Solid State Gas Sensors – Industrial Application, Springer Series on Chemical Sensors and Biosensors* 11, 2012, 53–78.

[46] Liu, B.; Zeng, H.C.; *Am Chem Soc* 125, 2003, 4430-4431.

[47] Cao, M.H.; Wang, Y.H.; Guo, C.X.; Qi, Y.J.; Hu, C.W.; Wang, E.B.; *J Nanosci Nanotechnol* 4, 2004, 824–828.

[48] Zhou, K.B.; Wang, X.; Sun, X.M.; Peng, Q.; Li, Y.D.;*J Catal* 229, 2005, 206–212.

[49] Yuan, Z.Y.; Su, B.L.; *Colloids Surf A Physicochem Eng Aspects* 241, 2004, 173–183.

[50] Kung, H.H.; *Transition Metal Oxides: Surface Chemistry and Catalysis*, Elsevier Science Publishers B.V. 1989.

[51] IAPWS form release on the value of Temperature Pressure and density of ordinary heavy water substances and their respective Critical points, 1992.

[52] Jolivet, J.P.; Henry, M.; and Livage, J.; *Metal Oxide chemistry and Synthesis*, John Wiley & Sons Ltd, Baffins Lane, Chichester, West Sussex PO19 IUD, England 2000.

UNIVERSITY *of the*

WESTERN CAPE

CHAPTER FOUR:

GAS SENSING

4.1 Application as 1-D Nanobelts Room Temperature for High Hydrogen Gas Sensing.

4.1.1 Introduction

Metal oxide semiconductors based chemical sensors attract significant attention due to their simplicity, low cost, small size ability to be integrated in electronic devices. They can be defined as a device which can selectively respond to certain properties of the environment as temperature, pressure, magnetic field, and can transfer this response into the electrical/the optical signal by responding to concentrations of chemical species in the liquid or gas phases [1].They are currently several companies that market metal-oxide-based gas sensors such as Figaro [2], FIS [3], Microchemical Systems, MICS [4], City Technology [5], Applied Sensor [6], Umwelt sensortechnik GmbH, UST and Paragon [7]. Applications of metal oxides semiconductor are found in many areas such as coating technology, catalysts, gas sensors, photovoltaics, batteries, electronics, and cosmetics. See figure 4.1.
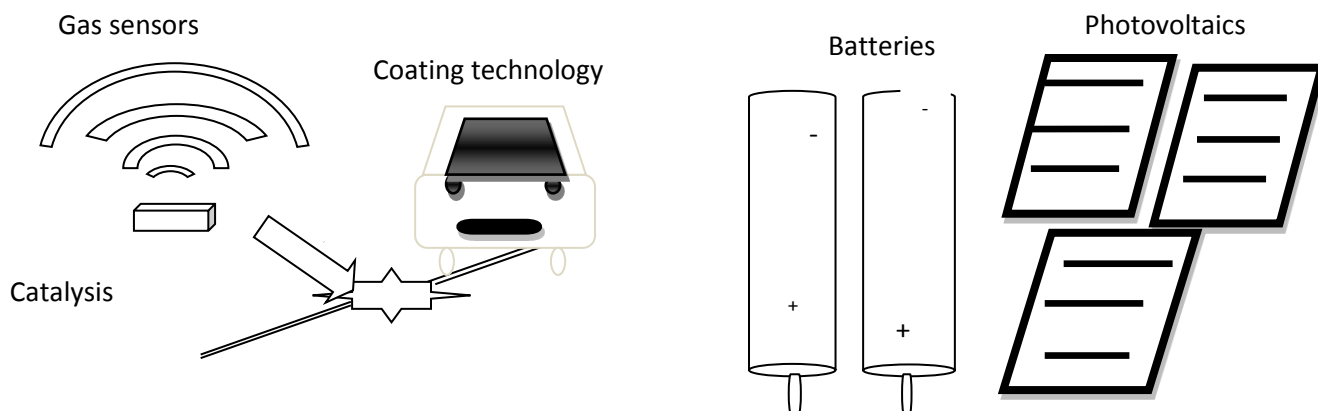
Figure 4.1: Potential applications of metal oxide sensors [2-7].

They can be used in industry, environment, home safety, monitor regulation, biomedicine, automotive, and security. However continuous improvements are required for sensors devices for implementation in constantly more demanding applications especially better sensitivity, selectivity, faster response with lower power consumption. A nanocrystalline semiconductor oxide gas sensor has shown outstanding sensing properties especially at low operating temperatures (200–300°C). Thus, an emerging field of research lies in the development of new scientific processes to produce nanocrystalline materials in the form of powders and thin films for gas-sensing applications.

4.1.2 Metal Sensor Device Principle

There are generally based on electrical transport properties of the metal oxide semiconductor of the sensing layer which is modified upon contact with reducing or oxidizing gases. What is important to note here is that the performance of the sensor material rely to the nature and the structure of the sensing material and to the nanoscale morphology of the layer and the grain size of the metal oxide where the overall conductivity is determined by nanocrystalline materials sensing. It has been demonstrated that the n-type materials sensors are the most extensively investigated due to their oxygen deficiency acting as electron donors [8]. In particular, many interesting results have been achieved and intensive efforts are still in progress in order to develop new materials and synthesis approaches. Nanocrystalline semiconductor oxide gas sensor show outstanding sensing properties at high temperature (200 °C-300° C)[9]. In brief, the response of an n-type metal oxide semiconductor (in our case Vanadium Dioxide) to the presence of an analyte gas relies on the surface reactions which occur between adsorbed oxygen species and the probed gas. Oxygen adsorbed on the surface traps free electrons because of its high electron affinity, forming a potential barrier at the grain boundaries. Comparatively to the p-type oxide, they are relatively unstable to the exchange of lattice oxygen with air. This potential barrier restricts the flow of electrons, causing the electric resistance to increase. This is true for

oxidizing gas such as CO_2, NO_2. In fact the gas sensing responses depend on many factors such as chemical (catalytic, acid-base properties of the surface) and microstructural (particle size, crystal structure) factors. See figure 4.2 and electronic transport properties. Additionally the morphology of the layer and the grain size of the metal oxides affect the conduction mechanism. Most modern gas sensors devices operate where the overall conductivity is determined by the nanocrystalline sensing materials.
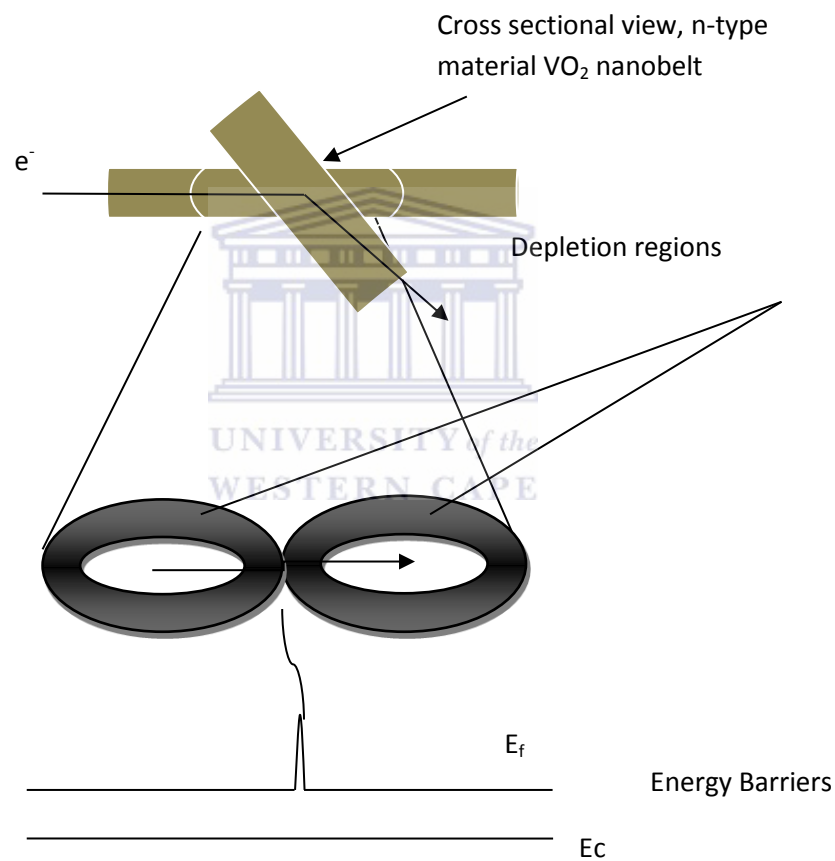
Figure 4.2 Cross section contact with energies barriers at the interface junction VO_2-VO_2 [9].

4.1.3 Experimental Setup

Gas sensing devices having sensing layers made of vanadium dioxide metal oxide semiconductor nanobelts have been pressed unto the glass substrate and then equipped

with a BeCu electric contact on the front and a heater on the back. The resistive sensing layer is thermally treated at constant environment room temperature.
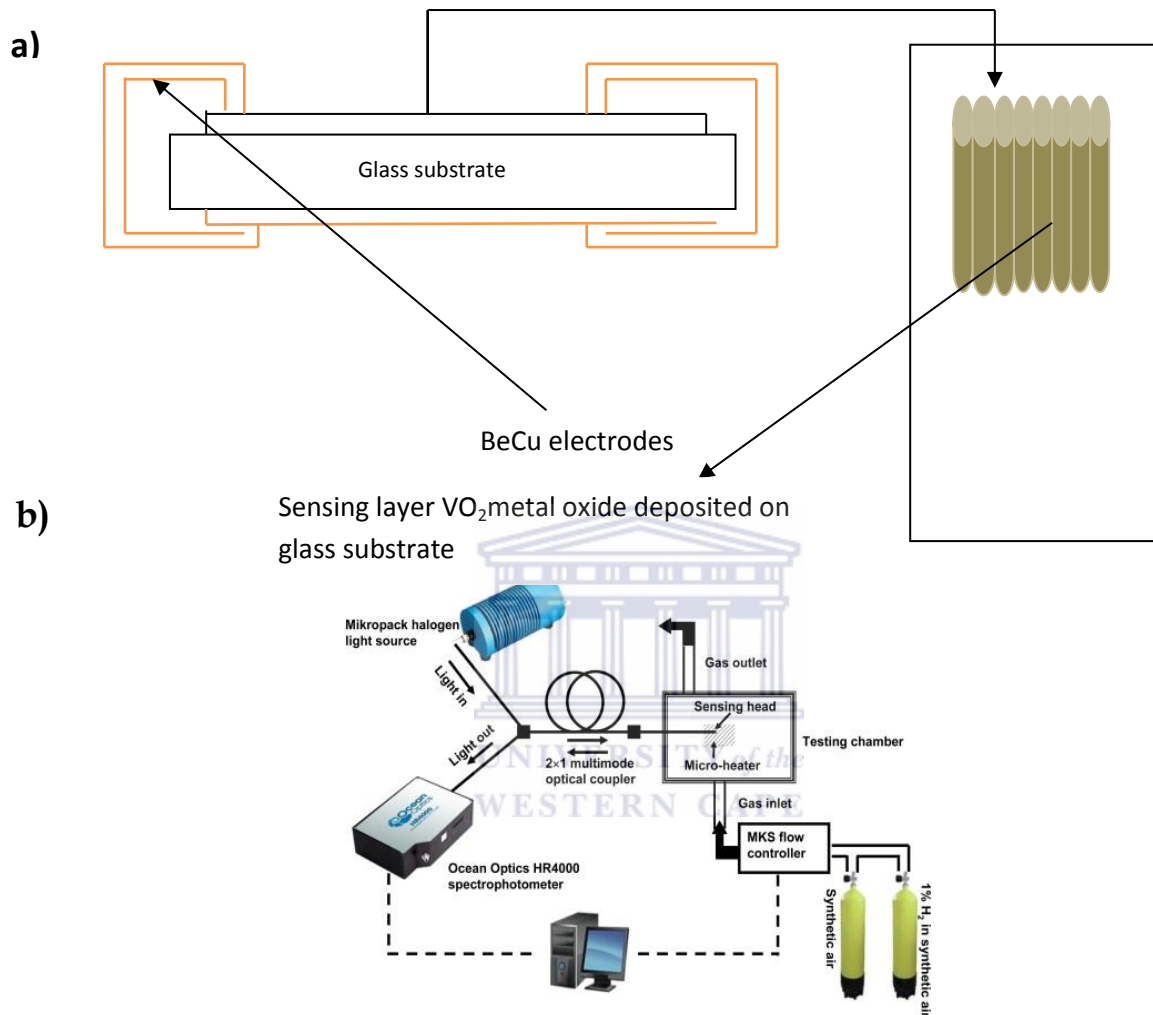
Figure 4.3: Sensing setup experiment with resistive sensing layer BeCu a) and PC for data recording b) Photograph of powdered samples placed between the AlCo contacts [10-11].

The resistance from the digital multimeter (DMM) is an analog-to-digital conversion ready to be processed by the computer via standard data logger software. Labeled on the schematics are as follows: (1) Al‑Co electrodes (2) Al foil (3) sample under test (4) insulating support such as glass c) The overall measurements were carried out in a testing chamber using a monitoring flow controller. The N_2 gas was used for the

removal of oxygen species present in the chamber facilitating the dryness and the purity of the chamber and the resistance changes were obtained through the monitoring of the gas flow of hydrogen at different concentrations, recording the data on a PC computer as seen figure 4.3) and b).The resistance of the sample was measured using a digital multimeter that was interfaced to a standard desktop PC via the universal line interface with a RS232 cable. The data logger software, named BsB-x421100, was used to record and store the resistance‑time data. For all materials investigated in the present trial, all H_2 gas flow rates were fixed to 200 ml/min in 5 l/min of N_2 gas [10]. According to [12], the effect of grain size on the sensitivity of nanocrystalline metal-oxide gas sensors present higher sensor performance signals and sensitivity responses as the grain size decreases. This is due to the enlarged active surface area of the sensing layer as the consequence of better surface to volume ratio so that the relative interactive surface area is larger and the density of charge carriers per volume is higher. The homostructures nanobelts VO_2 are presented as cross section contact with energies barriers at the interface junction VO_2-VO_2. See figure 4.2. The development for the first time of a metal oxide semiconductor chemiresistive sensor VO_2 highly selective of Hydrogen gas at room temperature, without addition of catalyst has been developped at iThemba LABS Cape Town.

4.1.4 Sensing mechanism

In general molecules gas and oxide layer interact in different ways:

- Molecular adsorption where the interaction is by σ donation and or π bonding interaction. This kind of interaction takes place on a single surface unsaturated ion.
- Dissociation into charge species of the molecule upon adsorption which require an anion-cation unsaturated pair site.
- Abstractive absorption where the absorbate abstracts a species from the surface which is a proton and the absorbate becomes cationic, it becomes held to the surface by electrostatic forces.

- In last reductive adsorption where an adsorbed molecule is oxidized while the surface is reduced. It is commonly observed on transition metal oxides which present cations with accessible multiple oxidation states. In this case the reduction of the vanadium dioxide by the molecules gas is accomplished by removal of lattice oxygen which is common to all oxides/ or dissolution of the reductant into the lattice. In the case of hydrogen molecules, the thermodynamic driving force is the formation of water which results in a hydrogenated surface or reduced oxide. The rates of reduction depend strongly on the presence of surfaces defects and bulk grain boundaries, orientation of the exposed surfaces planes, presence of hydroxyl groups, and the presence of other metals. The reduction process can be qualified as autocatalytic depending on the method of growth of the reduced portion of the oxide.

4.1.5 Surface Physics Description

The chemical composition and atomic arrangement at the surface of the solids and the theory and observations of their mechanical, electronic and chemical properties can be described by the surface physics. The ultimate objective is the establishment of understanding of the relationships between the properties, the composition and the structure. The surface material is generally determined as top 100 nm of the solid. For a minimum disturbance where the surface is decribed as a bulk exposed plane see figure 4.4 a, the formation of the surface inducing the loss of the periodicity in one dimension change the electronic state near and at the surface properties. The lacks of nearest neighbors on one side of the surface atoms make available dangling chemical bonds available for chemical reactions. The bonding cause by terminating the solid in a surface due to absence of nearest atoms on one side will cause a new equilibrium positions giving a relaxation illustrated in figure 4.4 b drawing the deviation in the bulk solid in decreasing magnitude. The surface region where the deviation from the bulk spacing operates is called the selvedge. A more extreme disturbance where the surface atoms

rearrange themselves in another symmetry altogether different from the bulk solid is called the reconstruction see figure 4.4 c) modifying the symmetry near the surface affecting structure sensitive properties–atomic vibrations, chemical optical and electronic behavior.

a)

Surface

b)

a_r= Selvedge

c)

Surface

Selvedge
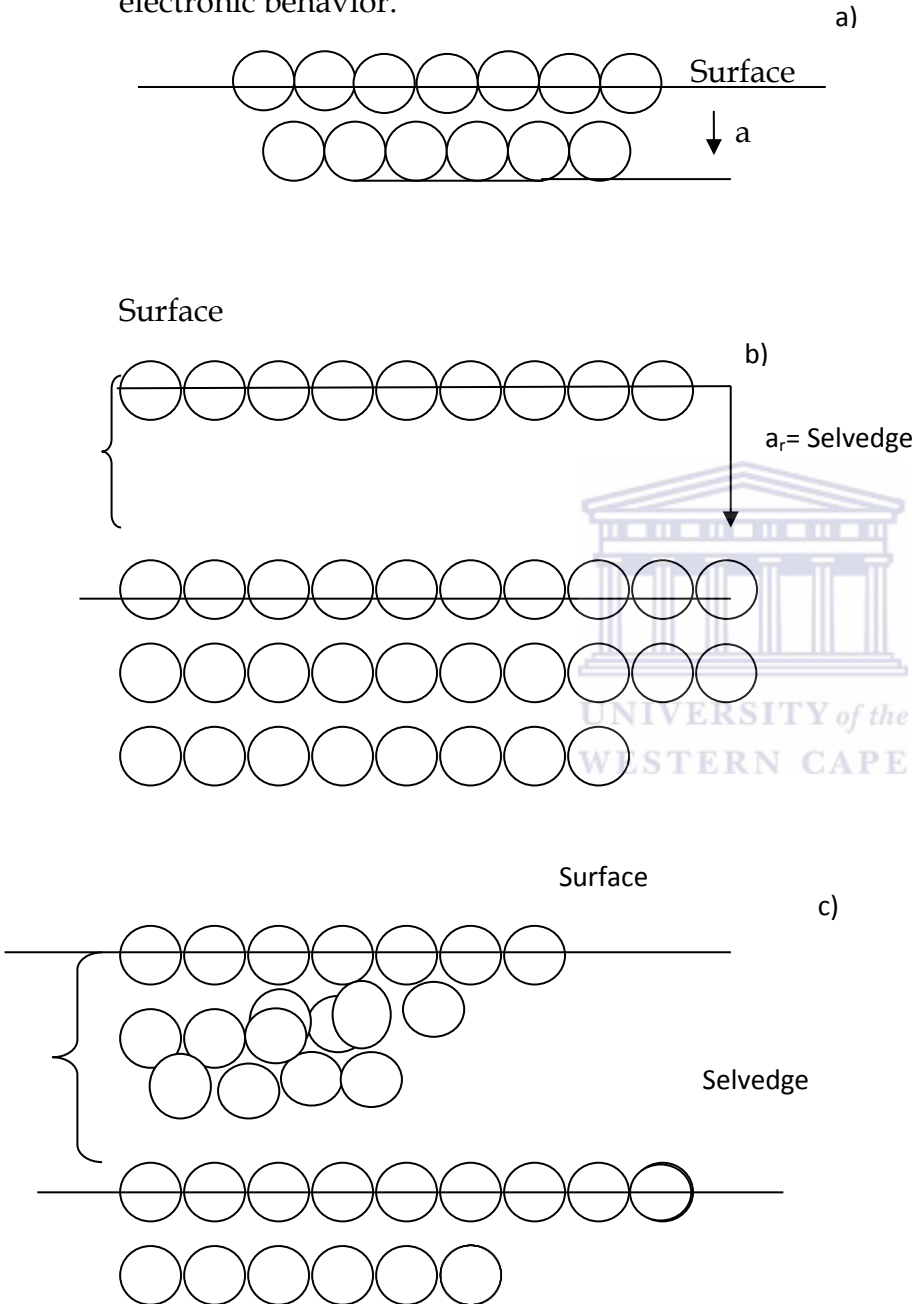
Figure 4.4: Rearrangements of atomic positions at a solid surface, Hexagonal close-packed atom. a) Bulk exposed plane, b) relaxation of the surface plane outwards, c) reconstruction of the outer four atomic planes. [13]

Processes occurring at the surface atoms can be listed in six ways:

- Thermionic emission important in many electronic devices as oscilloscopes tubes and electron microscope consist to impart sufficient energy at the top to the electrons in the conduction bands for them to be ejected from the surface to the vacuum

- Crystal growth : the process of crystal growth generally involves deposition of atoms upon single crystals surfaces where the arriving atoms can diffuse and build up three dimensional periodic array

- Chemical reactions involving interactions between different kinds of atoms across a surface or interface

- Catalysis the presence of surface atoms of a particular metal marked increase in the speed of the reaction

- Colloids : particles of a solid suspended in a liquid suspension

- Semiconductor interfaces involving the junction p-type and n-type material, a junction between metal oxide and a semiconductor with formation of a surface

- Brittle fracture due to the migration of impurity atoms to the grain boundaries in a solid which become weak regions under impact

The rise to the current level in surface physics is generally explained by three factors: the theory of the electronic structure and the chemical bonding in simple bulk solids explored in two directions [13]: properties of complicated ionic and molecular bulk solids and the properties of defects in solid-technological pressures –UHV in which the impingement upon the surface of molecules from the ambient atmosphere in the vaccum chamber is negligible in time with required for the observation. Here the kinetic theory of gases is given by:

$$N=2.89 \times 10^{22}\, p\, (MT)^{-1/2}\ \text{molecules cm}^{-2}\ \text{s}^{-1} \qquad\qquad Eq.4.1$$

$$N=2.24 \times 10^{24}\, p\, (MT)^{-1/2}\ \text{molecules m}^{-2}\ \text{s}^{-1}\ \text{with p in N\textbackslash m}^2,\ \text{T in K} \qquad Eq.4.2$$

4.1.6: Thermodynamics of reduction

The reduction between metal oxide and hydrogen (reducing gas) can be represented by the equation:

$$MO_n + H_2(g) \rightarrow MO_{n-1} + H_2O(g) \qquad\qquad Eq.\ 4.3$$

We define the free Gibbs energy change as:

$$\Delta G = \Delta G^0 + RTln\left(\frac{P_{H_2O}}{P_{H_2}}\right) \qquad\qquad Eq.\ 4.4$$

The stoichiometric ratio of the reaction above shows that the change of gas phase change molecules number between reactants and products is inexistent. Hence the entropy ΔS is very small. In general the nanosensor based vanadium dioxide exposed to hydrogen atmosphere undergo an adsorption –desorption sensing mechanism that we qualified as reversible gas chemisorption on surface on the VO$_2$. The electrons released to the conduction band follow the different reactions:

$$H_2 + \tfrac{1}{2}O_2^-(ads) \rightarrow H_2O + e^-(low\ temperature) \qquad\qquad Eq.4.5$$

$$H_2 + O^-(ads) \rightarrow H_2O + e^-(high\ temperature) \qquad\qquad Eq.4.6$$
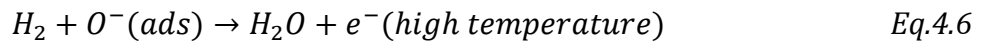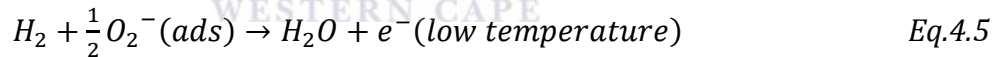
In this present work we are interested of chemisorption at low temperature. The hydrogen molecules react with adsorbed oxygen ions producing water molecules. The width of depletion region is hence reduced contributing to the increase of the current to the entire nanoplatelet. More effective interaction between H$_2$ and nanomaterial and high gas sensing response will be obtained from the high concentration of O_2^- ions on the surface. Additionally the presence of defects on the nanomaterial quantified through the lattice interspacing distance due to oxygen vacancies can act as adsorption sites for gas species which influence the electronic /chemical properties, adsorption behavior of metal-oxide surface and reversibility of sensor characteristics. The interaction of Hydrogen with surface defects can be modeled as [14]:

$$H_2 + \dot{O}_l \rightarrow H_2O + O_O^X + e' \qquad\qquad Eq.4.7$$

$$H_2 + \dot{V}_O + e' \rightarrow H_2O + O_O^X \qquad\qquad Eq.4.8$$

Where O_O^X neutral oxygen in an oxygen site is, $\dot{V}_O$ is a positive charged vacancy, e′ is a negatively charged electron according to Kröger-Vink notation. This shows that the hydrogen molecules are strongly correlated to the oxygen vacancies of the nanosensor material. According to V N Andreev et al [15], the Kröger Vink notation describing the reaction between hydrogen molecules and Vanadium Dioxide thin films is written in the form:

$$H + V_V^x + O_o^x \rightarrow (OH)_O^{\cdot} + V_V^{\cdot} \qquad\qquad Eq.4.9$$

Showing that the hydrogen radicals are donor to vanadium where the compound form as a direct hydrogenation of VO₂ with hydrogen at room temperature can be described by the formula:

$$VO_{2-x}(OH)_x \qquad\qquad Eq.4.10$$
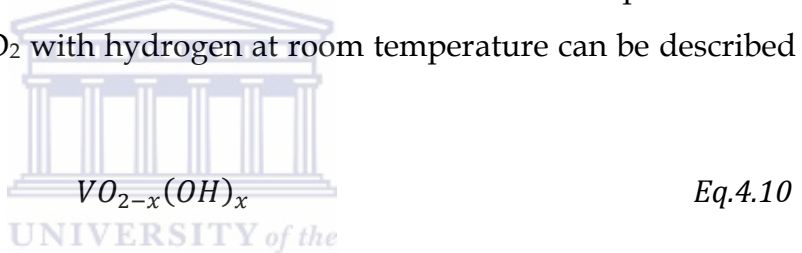
They observed a noticeable decrease of transition temperature dependence of the electrical conductivity relative to the amount of hydrogen inserted in the polycrystalline thin films. Which lead to the distortion of the lattice considering as the source of internal pressure that produce increase of the lattice strains responsible of the decrease of the transition temperature of the phase equilibrium Tc. Related to Vanadium Dioxide material, the phase transition is a martensitic transformation which is very sensitive to the elastic strains applied from the outside inducing misfit between the lattice parameters of the tetragonal and monoclinic phases. As we describe in the earlier subsection, we show the strong correlation between structural transition and strain-driven phase transition. In accordance with our first time VO₂ applicable as gas sensor at room temperature, the embedance of hydrogen onto VO₂ thin films in dry air with N₂ background is explained of the fact that hydrogen is a donor of electrons. They also suggested that the decrease in the electrical conductivity is associated to the decrease in

the gain of free energy of the crystal related to change in the electronic subsystem. During the transition from metallic state to less metallic or metastable to stable metallic state, σ bond are formed for every two neighboring vanadium ions approaching each other; splitting the $d_{//}$ conduction band in two identical bands: the lower turning into filled valence band while the upper band remains empty. The displacement of the V^{+4} atoms form the center leads to an increase in overlap π orbitals of vanadium and oxygen and accordingly an increase in the $π^*$ band which determine the conduction band. Due to the insertion of the hydrogen atoms, the electrons of H land in the $d_{//}$ conduction band, which contribute to the decrease of the energetically possibility to be splitted because extra electrons migrate into the $π^*$ band. Hence the complete phase transition is suppressed and the metallic state is stable over the whole working temperature. They show that the hydrogenation of polycrystalline vanadium dioxide lead to significant increase in the electrical conductivity. See figure 4.5.
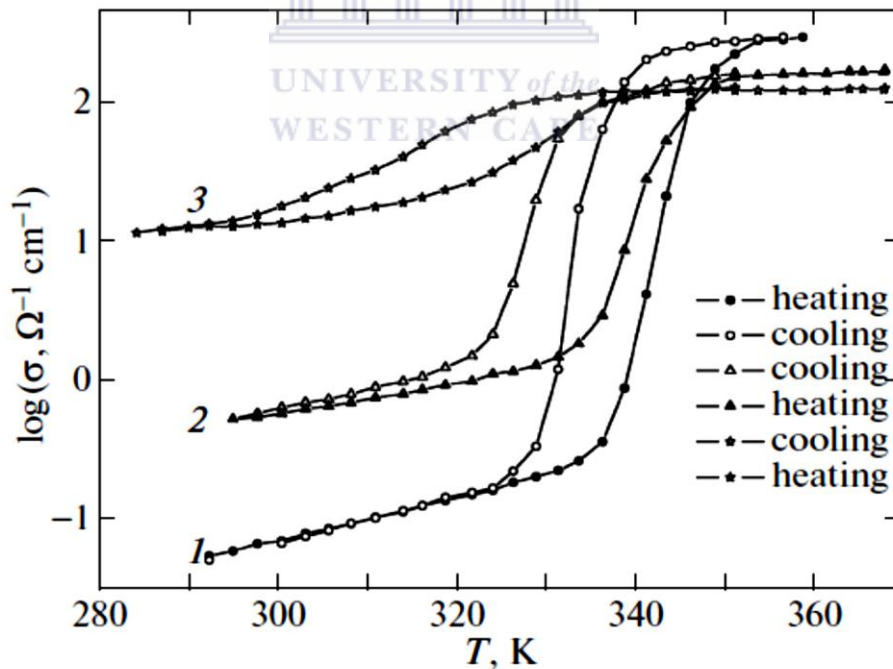
Figure 4.5: Temperature dependences of the electrical conductivity of H_xVO_2 thin films: (1) x=0, (2) ~0.012, and (3) x~0.02 [15].

4.1.7: Mathematical description

The reduction kinetics for metal oxides nanoparticles can be described with two models: the nucleation model and the contracting sphere model. Here we neglect all effect due to the support, impurities or anisotropy. In the nucleation model, the oxygen surface ions are removed from the lattice leaving behind an anion vacancy. When the concentrations of vacancies reach a critical value, they become annihilated by rearrangement of lattice with formation of smallest oxide grains with reduced metals ions and outward diffusion of the oxygen ions. These grains grow to the extent that their boundaries overlap which result in a particle of an oxide core with a shell reduced oxide. The time dependence of the degree of reduction α by the isothermal reduction in the nucleation model is given as:

$$\alpha = \frac{C_1 C_2}{V_{final}(p + q + 1)}(t - t_1)^{p+q+1} \qquad Eq.\,4.11$$

$$t = \left(\frac{\alpha V_{final}(p + q + 1)}{C_1 C_2}\right)^{\frac{1}{p+q+1}} + t_1, V_{final}(1 + p + q) \neq 0 \qquad Eq.\,4.12$$

V_{final} is the final volume of the grain of the reduced oxide, C_1, P are constants time dependent related to the volume of a grain, C_2, q are constants time dependent related to the number of the grains.
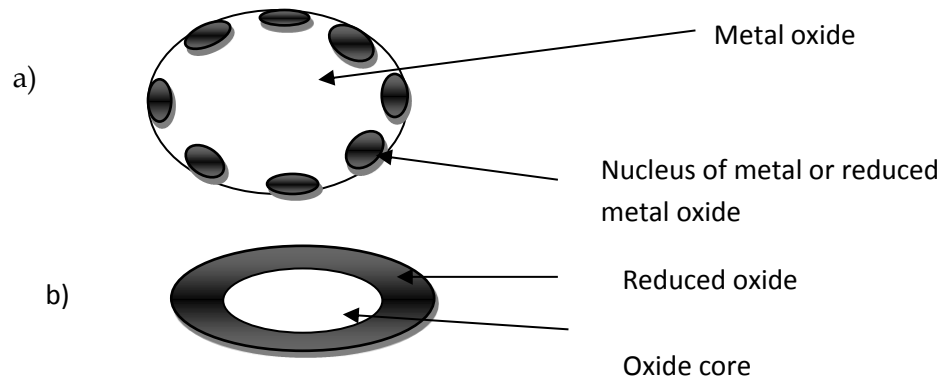
Figure 4.6: Initial stage of reduction of metal oxide by nucleation model a) and contracting sphere model b) [16].

These results shows that the interfacial grain areas increases with the size of the grain and the grain of the reduced oxide activates the reductant more than the fully oxide. When the grains of reduced oxide coalesce, the reduction follows the contracting sphere model and the rate of reduction decreases with time presenting a sigmoidal shape. The contracting sphere model is an extreme case of nucleation model where the number of reduced oxide grains formed on the surface of the sphere is so large that the boundaries of the grain overlap when the diameter of the grain is still small versus the radius of the sphere. See figure 4.6. This is accurately modeled as a rapid formation of a uniform layer of reduced oxide grains or metal formed on the sphere. The thickness of the layer grows uniformly resulting in a spherical core of oxide that shrinks with time. The distance of this interface and oxide increases with time and the rate of reduction decreases with time. The time dependence of isothermal reduction in the contracting sphere model is given as:

$$\frac{K_p}{r_0 d_0}(C_0 - C_{eq})t = \left[1 - (1 - \alpha)^{1/3}\right] + \frac{r_0 K_p}{K_d}\left[\frac{1}{2} - \frac{\alpha}{3} - (1 - \alpha)^{2/3}\right] \qquad Eq.\,4.13$$

K_p is the rate constant of reduction per unit area at the oxide reduced oxide interface, K_d is the diffusivity of the reductant through the reduced layer, r_0 is the radius of the entire sphere and C_0, C_{eq} are the reductant concentration at the outer surface of the sphere and equilibrium concentration. The chemical reaction is described as a first order chemical reaction. In the case between nucleation model and sphere model, small grains are first formed on the surface oxide, and the grains of reduced oxide are less active in activating the reductant molecules than the fully oxidized oxide. Hence they facilitate inhibition of the rate of reduction due to the decrease of the area exposed of the fully oxidized oxide. The grains grows as reduction continues, covering up the oxide particle. In this case the rate of reduction decreases continually with increase time. This process is accelerated in nanoparticles metal oxide. The kinetic model is generally divided in three groups: diffusion control group, boundary control group, random nucleation and subsequent growth of nuclei models.

The general method developed by the curve analysis give the rate laws for solid state reactions derived from the expressions:

$$\ln[-\ln(1-x)] = m\ln(t) + \ln(n) \qquad\qquad Eq.4.14$$

If the slope m is <1, the reaction is in favor of the diffusion; for 1<m<2, the phase boundary process is dominant. Table 4.1 gives some reactions mechanism with an explicit form of the kinetic rate reduction according to the dimension of the material.

Table 4.1: Reaction mechanisms and the algebraic expressions [16].

Reaction mechanism	f(X)	Integrated forms	m
One-dimensional diffusion	$(1/2)X$	$X^2 = kt$	0.62
Two-dimensional diffusion	$1/[-\ln(1-X)]$	$(1-X)\ln(1-X) = kt$	0.57
Three-dimensional diffusion (Jander eq.)	$3(1-X)^{2/3}/(2[1-(1-X)^{1/3}])$	$[1-(1-X)^{1/3}]^2 = kt$	0.54
Three-dimensional diffusion (Ginstein-Brounshtein eq.)	$(3/2)[(1-X)^{-1/3}-1]$	$1-2X/3-(1-X)^{2/3} = kt$	0.57
First-order reaction (unimolecular decay law)	$(1-X)$	$-\ln(1-X) = kt$	1.00
Phase-boundary controlled (contracting cylinder)	$(1-X)^{1/2}$	$1-(1-X)^{1/2} = kt$	1.11
Phase-boundary controlled (contracting sphere)	$(1-X)^{2/3}$	$1-(1-X)^{1/3} = kt$	1.07
Two-dimensional growth of nuclei	$2(1-X)[-\ln(1-X)]^{1/2}$	$[-\ln(1-X)]^{1/2} = kt$	2.00
Three-dimensional growth of nuclei	$3(1-X)[-\ln(1-X)]^{2/3}$	$[-\ln(1-X)]^{2/3} = kt$	3.00

Chwieroth et al. [14] developed an Integrated Reaction Conduction (IRC) model which integrates gas surface reactions with electrical conduction process in a weekly sintered porous metal oxide. They employ the effective medium approximation theory relating the mesoscopic structure and the carrier depletion at the granular surface to macroscopic electrical conduction. According to Bruggeman unsymmetrical effective medium theory, for a three dimensional system, the effective conductivity can be calculated as:

$$\frac{(\sigma_{eff}-\sigma_c)^3}{\sigma_{eff}} = (1-f_c)^3 \frac{(\sigma_i-\sigma_c)^3}{\sigma_i} \qquad\qquad Eq.\,4.15$$

σ_i and σ_c are conductivities of the insulating and conducting components. f_c is the volume fraction of high conductivity interior of the grain (non-depleted regions). See figure 4.7. The surface area to volume ratio considered in the IRC predicts a strong grain size dependence on the sensitivity. Depletion regions in nanocrystaline n-type materials extent throughout the entire composite in the presence of reducing gas. The total number of intrinsic electron Ni is given by: $2\rho x V_g$ where ρ is the number of molecular grain units per unit volume, and x is the intrinsic non stoichiometric. The number of surface ions N_d is proportional to the product of the surface grain area and the ion adsorption grain concentration. Hence the ratio N_d/N_i scales as a_0/xr_g, r_g is the grain radius and a_0 is the lattice. Nanocrystalline sensors have their depletion regions removed by the reducing gas and hence the density of electrons N_{lib} liberated by the oxidation reaction which return to the grain is proportional to the product Ag [So] where Ag represents the surface area of the grain and [So] is the concentration of O$^-$ion adsorption sites on the ceramic grain giving for ultrafine grains atoms N_{lib}/Ni scaling as ao/xr_g. As a result the volume fraction of the grain is the total volume fraction non pore f_{np} where the depletion layer is completely replenished in ultra-fine grained composites, unlike their coarsened counterparts. The response of a nanocrystalline sensor is thus characterized by a dramatically increased sensitivity enhancing response in nanocrystalline non-stoichiometric n-type ceramics, compared to the corresponding coarsened materials. The reduction by H_2 or CO present same low activation energy (20-100 kj/mol) due to the fact that they behave as reducing agent and so they are thermodynamically predominant for the reduction [17]. By analogy to CO reduction mechanism, H_2 reactions mechanisms can be similarly describe considering that ambient oxygen adsorbs on the surface of the grains and form negative oxygen ions with combination of intrinsic electrons from the n-type semiconductor. See figure 4.8. This give a dipole layer associated with charged surface and depletion region inside the surface of the grain which give highly resistive intergranular contact. The reaction energy model can be illustrated as below:

$$H_2(g) + \frac{1}{2}O_{2\ ads}^- \xleftrightarrow[k_{ads.r}]{} H_{2\ ads}.\frac{1}{2}O_{2\ ads}^- \xleftrightarrow[k_{ox.r}]{} H_2O_{,ads} + e^-\ libre \qquad Eq.4.16$$
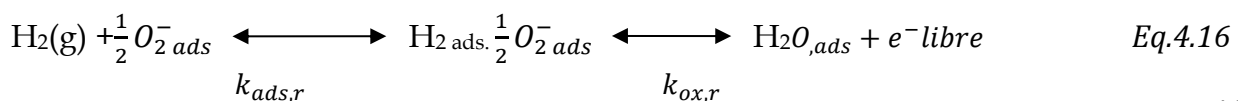
Where $k_{ads,f}$, $k_{ads,r}$, $k_{ox,f}$, $k_{ox,r}$ are the reaction rates adsorption and oxidation for the forward and reverse reactions. According to the sensing mechanism reaction rates, the changing reactant concentration due to the exposure of the oxide to the reducing gas is expressed as:

$$\frac{d[H_2(g)]}{dt} = k_{ads,r}\left[H_{2\,ads.}1/2\ O^-_{2\,ads}\right] - k_{ads,f}[H_2(g)].\left[\frac{1}{2}O^-_{2ads}\right] \qquad Eq.\,4.17$$

$$\frac{d\left[H_{2,ads.}1/2\ O^-_{2ads}\right]}{dt}$$
$$= k_{ads,f}[H_2(g)][1/2O^-_{2ads}] - k_{ads,r}\left[H_{2\,ads.}\cdot 1/2O^-_{2\,ads}\right]$$
$$- k_{ox,f}\left[\frac{H_{2ads}1}{2O^-_{2ads}}\right].+k_{ox,r}[H_2O_{,ads}] \qquad Eq.\,4.18$$

$$\frac{d[H_2O]}{dt} = k_{ads,r}\left[H_{2\,ads.}1/2O^-_{2ads}\right] - k_{ads,f}[H_2(g)].\left[\frac{1}{2}O^-_{2ads}\right] \qquad Eq.\,4.19$$

The ratio of forward and reverse reactions rates are given as:

$$\frac{k_f}{k_r} = \frac{Z_{product}}{Z_{reactant}}e^{-E/K_BT} \qquad Eq.\,4.20$$

E denotes the activation energy between the reactions. The functions ratio denotes the cubic power of the Debye wavelength for the corresponding analyte gas reductant, and unity of the oxidation reaction.
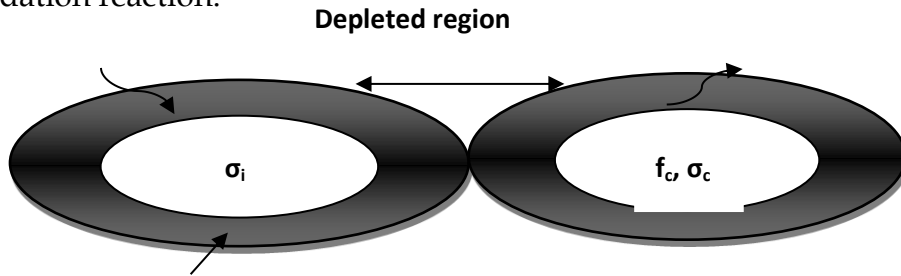
Figure 4.7: Physical sensing process between metal oxide and Hydrogen gas. The depletion layer has small conductivity σ_i compared to the large conductivity σ_c of the bulk interior region, volume fraction fc [16].

115
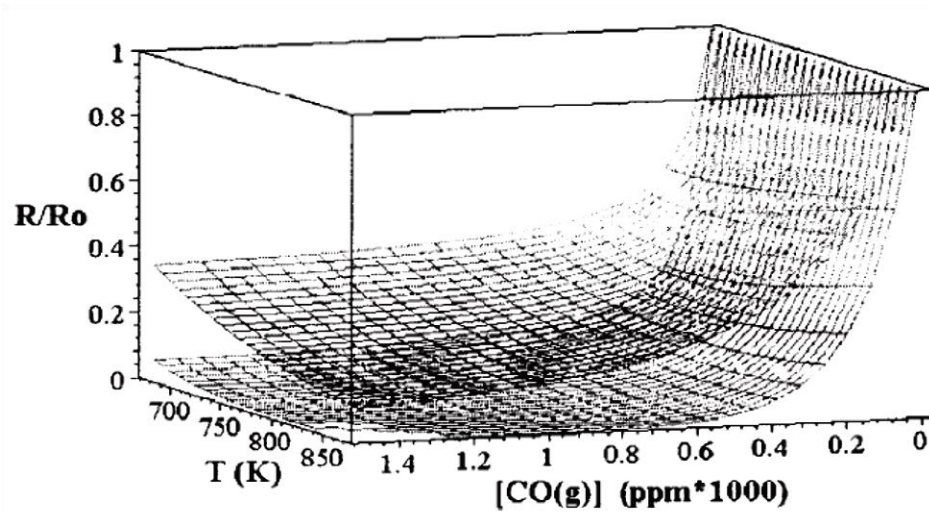
Figure 4.8: Sensor response characteristically more sensitive for smaller grain sizes (lower continuous grid) versus coarsened grains (upper continuous grid) with a ten times greater radius [17].

Barsan et al. [18] develop a general model applicable for real world gas sensor and on tin oxide in particular. They classified a sensor element as comprising sensitive layer deposited, substrate used and electrodes for the electrical measurements. Here the conductance is monitored as a function of the concentration of the target gas. It considered compact layers and porous layers geometry. The former can be completely or partly depleted depending on the ratio between layer thickness and Debye length λ_D. See figure 4.9 and figure 4.10. For a partly depletion layer, the conduction takes place in parallel to the surface while in the case of completely depleted layers, the conduction takes place due to the injection of additional free charge carriers.
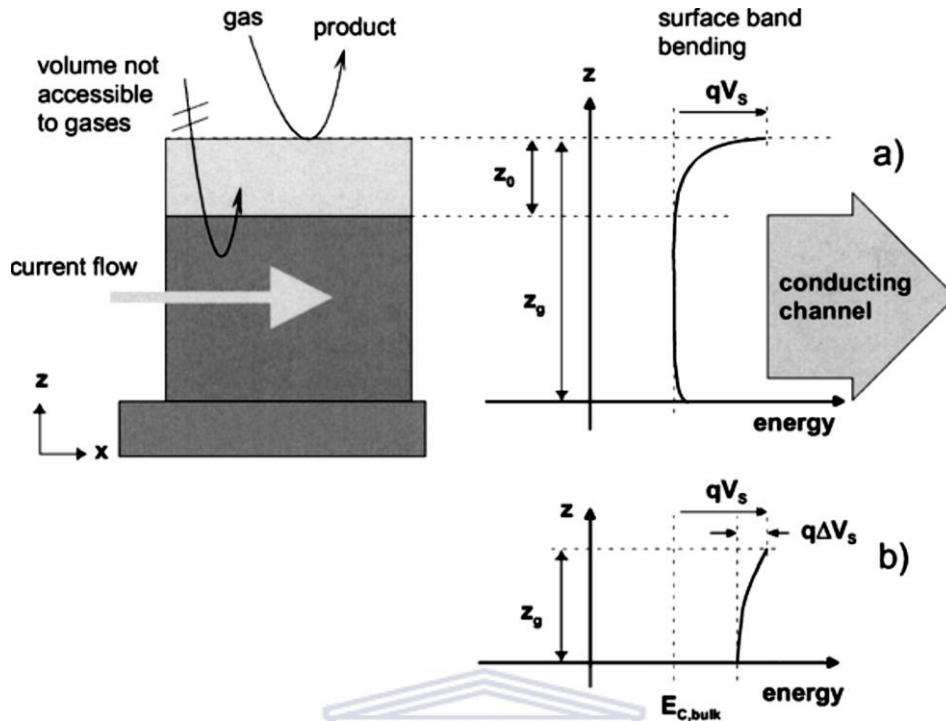
Figure 4.9: Compact sensing layer with geometry and energy band representations; z_0 is the thickness of the depleted surface layer; z_g is the layer thickness and qV_S the band bending. a) Represents a partly depleted compact layer ("thicker"), b) represents a completely depleted layer ("thinner")[18].
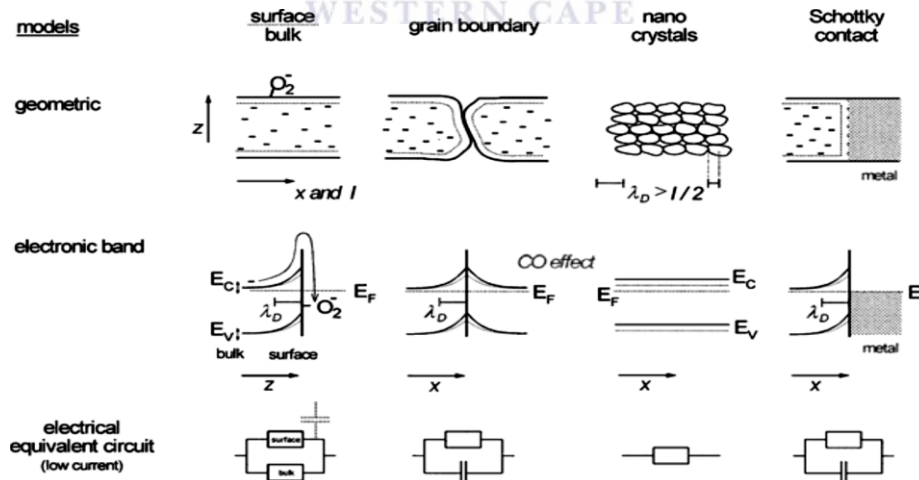
Figure 4.10: Different conduction mechanisms and changes upon O_2 and CO exposure to a sensing layer in overview: This survey shows geometries, electronic band pictures and equivalent circuits. EC minimum of the conduction band, EV maximum of the valence band, EF Fermi level, and λ_D Debye length [18].

At low temperature the molecular formed dominates and the ionosorbed oxygen induces a depletion layer of the material. The oxygen chemisorption is generally written as:

$$\frac{\beta}{2}O_2^{gas} + \alpha e^- + S \leftrightarrow O_{\beta S}^{-\alpha} \qquad Eq.\,4.21$$

S denotes the unoccupied oxygen site and vacancies oxygen or defects of the surface, $\alpha = 1/2$ for single or doubly ionized forms species; B is 1 for atomic or 2 for molecular species. The surface coverage θ with chemisorbed oxygen is given by:

$$\theta = \frac{[O]_{\beta S}^{-\alpha}}{[C_t]Eq} \qquad Eq.\,4.22$$

C_t represents the total concentration available on surface site for oxygen adsorption occupied or unoccupied. Using the conservation of surface sites and the mass action law we obtain:

$$(1-\theta)k_{ads}.\,n_s^\alpha.\,p_{O_2}^{\beta/2} = k_{des}.\,\theta \qquad Eq.\,4.23$$

Where n_S represents [e-]. This equation describes the surface coverage in connection with the concentration of electrons hopping from one grain to another controlling the electrical conduction in the layer. According to the limiting aspect of size thickness, where d<λ_D, the conduction is assume to take place in cylindrical filaments radius R by sintering of small grains. The combination of the equation of Poisson in cylindrical coordinate gives:

$$\left(\frac{1}{r}\frac{d}{dr} + \frac{d^2}{dr^2}\right)E(r) = \frac{q^2 n_b}{\varepsilon\varepsilon_0} \qquad Eq.\,4.24$$

The boundary conditions are expressed as:

$$E(r)/_{r=0} = E_0 \qquad Eq.\,4.25$$

$$\frac{dE(r)}{dr}/_{r=0} = 0, \qquad \Delta E = \frac{q^2 n_b}{4\varepsilon\varepsilon_0}R^2 \qquad Eq.\,4.26$$

And the Debye length in the Schottky approximation is given by:

$$\lambda_D = \sqrt{\frac{\varepsilon\varepsilon_0 K_B T}{q^2 n_b}} \qquad\qquad Eq. 4.27$$

$$\Delta E \sim K_B T \frac{R}{2\lambda_D} \qquad\qquad Eq. 4.28$$

In the case of small grains reacting with reducing gas H_2, the surface coverage is given as:

$$\theta = \frac{n_b . R}{2. \alpha[C_t]}\left(1 - \frac{n_S}{n_b}\right) \qquad\qquad Eq. 4.29$$

For large concentration or very sensitive reactors, we have:

$$n_S \sim P_{H_2}^{\frac{\beta}{\alpha+1}} \qquad\qquad Eq. 4.30$$

This model is analog to [19] who study the capacitance response of a sensitive layer under CO exposure showing that the resistance curve is function of the CO concentration with a power law such as:

$$R = R_0 P_{CO}^{-n} \qquad\qquad Eq. 4.31$$

The decrease of resistance was explained as the decrease of surface dipole concentration which is dominant for low CO concentration. The same decrease was observed in our experiment confirming the sensing response with consumption forming H_2O. The power law dependence is due to the transduction dominated by Schottky barriers with the existence of depleted or undepleted grains.

4.1.8 Physical Property Approach

The surface composition is generally given by anion to cation ratios which depend on the stoichiometry of the oxide and orientation of exposed crystal plane. Generally we faced several factors that cause a distorsion in the solid compound such as: surface

Nº	Vanadium Oxides	Synthesis Method	Grain shape	Temperature range	Gas tested	Best sensitivity	References
1	V_2O_5 coated with SnO_2, TiO_2 and FeO_3	Mild hydrothermal reaction	Nanobelts	180˚ C for 24hrs 100˚ C for 12hrs	-Air used as reference - ethanol at different concentrations	$S = \dfrac{R_a}{R_g}$ Limit of detection =5 ppm	20
2	VO_2 single crystal	Vapor solid method grown on SiO_2/Si substrate	Nanowires and mesoscopic ribbons	1000˚ C at 13 Torr and 3 sccm flux of Ar	Hydrogen helium, air, Ar : 1.5-560 Torr	$S\sim 10^{-3}$ V/pa	21
3	$V_2O_5.nH_2O$ +meso 3-and 4- pyridyl porphyrin cobalt (III) coordinated to four $[Ru(bipy)_2Cl]^+$ complexes	Sol gel method with cation exchange	Thin film prepared by drop coating on platinum electrode	Room temperature (25˚ C)	Nitrogen gas used as reference +ethanol /water vapor (0.1 L/min)	A good sensitivity was found up to 10% Of water : limiting concentration above which the resistance remains more or less constantwith a good sensitivity of Co3VXG sensor	22
4	Pd-nanoparticules decorated VO_2 single nanowires	Atmospheric pressure and physical vapor deposition to produce $VO_2 + e^-$ beam evaporation at a base pressure of 2.0×10^{-6} Torr	VO_2 nanowire single particle coated over by Pd well-spaced nanoparticles	650˚ C synthesis 200˚ C sensing	H_2 gas and air gas	H_2 exposure at 45-55˚C increase of 1000 fold- after 10 min or less 5 min when temperature 60˚ C	23
5	VO_2	Hydrothermal and heat transformation process	Nanoflowers	Room temperature	Relative humidity		24
6	V2O5	Sol-gel	Nanofibers onto silicon	Room temperature	1-butylamine Ammonia	10ppm 10	25

			substrates		1-propanol Toluene in 40% rh	1000 1000	
7	V2O5+addition of less electronegative cation (Ce,Zr, Mg) and electronegative cation (Al, Fe, Ni)	Precipitation method	Thick film	500	NH3, NO, CO, H2		26
8	Fe2O3 nanoparticules activated V2O5 nanotubes	Hydrolysis method	Fe2O3 nanoparticules of 15 nm dispersed on the surface of V2O5nanotubes	230˚ C	Ethanol	10ppm	27
9	VO2	RF reactive sputtering	VO2 nanowires thin film	35	H2		28
10	VO2(B) and VO2(M)	Hydrothermal method	Flowerlike and nanostructures	25	High and low humidity detection		29
11	VOx/CNFs	Atomic layer deposition	Commercial tubular carbon nanofibers uniformly coated with a 5 nm thick vanadium oxide layer	50-250	NO2 in air	80%	30
12	VSn	Co-precipitation method	Nanopowders	175	CO in air (50-500ppm)	50-500ppm	31
13	TiTaV	Screen printing technology	Thick film	380	CO Benzene Mixture of the two gases in dry air	100ppm 10ppm	32
14	Vanadium oxides: V2O5, V3O7, V4O9, VO2	Reactive RF sputtering	Thin film	200-250	NO2	100ppm	33
15	Vanadium oxides	RF reactive sputtering	Thin film	280-300	C2H5OH and NO2	300ppm 100ppm	34
16	V2O5-WO3/TiO2 on Al2O3 substrate	Screen printing	Thick film	500	NH3	80ppm	35
17	V2O5 coating of WO3	Sputtering of V2O5 on WO3 thin film	Thin film	250	NO2	6ppm	36
18	VPO Al-VPO	Wetness impregnation method	Nanopowders	200	Methanol and formaldehyde	100% selectivity	37
19	V-SnO2	Co-precipitation	Nanopowders	175	CO in air and	50ppm	38

		method			nitrogen		
20	FeVSn	Hydrolysis and coprecipitation method	Nanopowders 4.7 nm	200	CO	50-500ppm	39
21	Vanadium oxide nanotubes loaded with Fe2O3	Hydrothermolysis method	VONTs with Fe2O3 nanoparticules	230 270 330	Ethanol	330 at 1000 ppm C2H5OH	40
22	V2O5	Extrusion through a syringe within a PVA solution rotation beaker	Macroscopic fibers and hybrid PANI-V2O5	16-40 º C	ethanol	0.1ppm 12J.g-1	41
23	SnO2 with various promoters as V2O5, MoO3, Sb2O3, Al2O3, CeO2, MgO2	Precipitation method with calcinations in a furnance at 600º C for 1h	Thick films	300 350 450	SO2 gas	44% at 1 ppm	42
24	TiV1 and TiV2	Sol gel routes	Thick film samples fabricated by screen-printing fired for 1h at 650 and 850˚C	300 to 450	CO C6H6 C3H6	100ppm 10ppm 100ppm	43
25	V_2O_5/WO_3 mixed oxide	Ion exchange method by sol-gel	Membranes deposited on glassy carbones substrates		H+gas	68 mVpH-1	44
26	VO2 thin films coated on a Fe2O3 sub-layer	Thermal pyrolysis at 1700º C	Thin film on a mica substrate	18 to 60 º C	Light protective container		45
27	V_8C_7	MWCNTs produced by the arc-discharge method in a helium atmosphere V_2O_5 was dissolved in the prepared KOH solutions. Activation was conducted at 750◦C for 1 h in an argon atmosphere.	Multi-walled carbon nanotubes with appended vanadium	30º C	Hydrogen gas	Hydrogen storage of a capacity of 2.26wt%	46
28	V_2O_5-Sb_2O_3-TeO_2	Melt in air in a porcelain crucible in an electric furnace at 750°C for 1h and pellet of 1mm thick square plate of glass of area 4cm^2	N type semiconducting glass	303K-473K	O_2 and Ar gas with air	S=1.2 at 473K in O_2 gas	47

tension or surface Gibbs energy where the lower energy tends to be segregated to the surface; the bulk strain of the solid solution due to the mismatch of the ionic sizes or the coordination symmetry; the nature of the adsorbate and formation of the surface compound of a certain stoichiometry. The direct implication of the ionicity of metal oxide reaction with the molecules reductant is explained as the existence of a strong electric field pointing outward from the oxide surface. The separation of charges into cations and anions give strongly modulated electronic potential on the oxide surface. In the case of hydrogen, atoms are dissociatively adsorbed in opposite charges which represent differents reactivities. The ionic character increases the sticking probability of polar molecules. Their dipolar moments interact with the electric field at the surface which orients the molecule and enhance the probability of an attractive bonding interaction. The coulombic interaction is a long range process and the surface interaction is not only dependent on the cation /anion at the vicinity of the surface, but also on the ionicity of the matrix oxide of the solid solution which affects the activity energy of catalytic reactions where the rate involves the electron charge transfer between the oxide and surface intermediate.

4.1.9 Overview Gas sensors devices

There are four methods for monitoring gas material interactions which can be classified as electrochemical, optical, thermal and mass sensing techniques. In our case we used an electrochemical sensor relying on physical parameters which include potentiometric sensor, amperometric devices for current measurement over a potential and conductometric sensor for conductivity measurement at a fixed potential [48]. Several metal oxides semi-conductor had been investigated showing good sensing functionalities. Cheng et al. [49] developed SnO_2 nanobelt field effect transistor with low resistance, four ohmic terminal contacts and they applied them as gas sensor at room temperature and they correlated the channel conduction states with the level of oxygen deficiency or stoichiometry of the nanobelts [50]. This was possible with the corresponding threshold voltages and transconductance of the nanobelt FET device.

The behavior with a reducing gas is similar to sample where the hydrogen atoms release electrons to the conduction band by reacting with negatively oxygen charge ion on the surface according to the equations:

$$2H + O_2^- \leftrightarrow 2OH^- (molecular)$$
Eq. 4.32

Table 4.2 (above**)** gives an overview of vanadium gas sensors with their synthesis method and their gas sensitivity. It can be seen that there is no report regarding the obtention of nanobelts with direct application of low power hydrogen sensing.

$$H + OH^- \leftrightarrow H_2O\ (gas) + e^-$$
Eq. 4.33
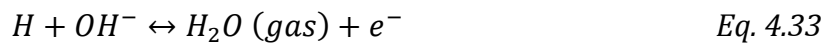
They attributed the fast response of the nanobelt to the large surface area to bulk volume ratio of the nanobelt [51] and to the small lateral dimensions and single crystalline morphology without grain boundary. Additionally, commercial hydrogen semiconductors sensors need substantial electric power to heat the working body of the sensor. Hence the decrease of operation temperature makes possible the decrease of Power consumption and possible to use the sensor device as portable battery supply. However sensor working at high temperature induces grain growth by coalescence and degradation of the materials. In a range of concentration from 1 to 50,000ppm, which were undertaken by applying a fixed bias voltage and monitoring the current over a period of time. It was observed that the material used very high concentrations of CO and CH$_4$ with no measurable effect even after prolonged periods of exposure. And also the device is not reversible when exposed to NOx gas. Adsorption and desorption of most of gas molecules on the surface of the metal oxide are generally thermally activated. However the need of room temperature gas sensors is highly demanded to obtained High Hydrogen gas sensing capabilities within the ppm level, simple system configuration, reduced explosion hazards and longer device lifetime [52]. It has been observed that the addition of catalysts as Pd on the metal oxide surface activate the processus of desorption and adsorption and reduce the working temperature of the

device. This is the case of WO_3 added to Pd at 10% gives a high sensitivity of 2.5×10^4 at room temperature [53].

Table 4.3: Summary of the effect of different gases on a spin–coated polyaniline chemiresistor at room temperature [48].

Gas	Concentration in N_2 (ppm)	Delay time τ_D (s)	Exposure time (min)	Recovery time τ_R(min)	Minimum detection level (ppm)	Normalised change per ppm $\frac{\Delta R}{R}$+gas concentration in ppm
NOx	10	48	36	100	4	-0.026 (10ppm)
H_2S	10	36	4	56	3	-0.033 (10ppm)
SO_2	10	12	6	100	2	-0.036 (10ppm)
CO	10000	No observed effect	25	N/A	N/A	N/A
CH_4	50000	No effect	25	N/A	N/A	N/A

4.2 References

[1] Vlasov, Y.; *Mikrochim.Acta*, II, 1991, 363-377.

[2] www.figarosensor.com

[3] www.fisinc.co.jp

[4] www.microchemical.com

[5] www.citytech.com

[6] www.appliedsensor.com

[7] www.paragononline1.de

[8] Graf, M.; Gurlo, A.; Barsan, N.; Weimar, U.; and Hierlemann, A.*; Journal of Nanoparticle Research,* 8, 2006, 823–839.

[9] Seal, S.; and Shukla, S.; *Nanomaterials Research Summary,* 2002.

[10] Mwakikunga, B.W; Motshekga, S.; Sikhwivhilu, L.; Moodley, M.; Scriba, M.; Malgas, G.; Simo, A.; Sone, B.; Maaza, M.; Ray,S.S.; *Sensors and Actuators B* 184, 2013, 170– 178.

[11] Sivapunniyam, A., Wiromrat, N.; Myint, M.T.Z.; Dutta, J.; *Sensors and Actuators B* 157, 2011, 232– 239.

[12] Rothschild, A.; & Komem, Y.; *J. Appl. Phys*. 95(11), 2004, 6374–6380.

[13] Prutton, M.; *Surface Physics,* Oxford Physics Series, Oxford University Press 1975.

[14] Lupan, O.; Ursaki, V.V.; Chai, G.; Chow, L.; Emelchenko, G.A.; Tiginyanu, I.M.; Gruzintsev, A.N.; Redkin, A.N.; *Sensors and Actuators B,* 144, 2010, 56–66.

[15] Andreev, V.N.; Klimov, V.A.; and Kompan, *Physics of the Solid State*, 54, (3), 2012, 601–606.

[16] Chwieroth B.; Patton, B.R.; and Wang, Y.; *Journal of Electroceramics* 6 (1), 2001, 27–41.

[17] Go, K.S.; Son, S.R.; Kim, S.D.; *International Journal of Hydrogen Energy* 33, 2008, 5986-5995.

[18] Barsan, N.; and Weimar, U.; *Journal of Electroceramics*, 7, 2001, 143–167.

[19] Bârsan, N.; and Weimar, U.; *J. Phys.: Condens Matter,* 15, 2003, R813-R839.

[20] Liu, J.; Wang, X.; Peng, Q.; Li, Y.; *Sensors and Actuators B* 115, 2006, 481-487.

[21] Strelcov, E.; Lilach, Y.; and Kolmakov, A.; *Nano letters,* 9 (6), 2009, 2322-2326.

[22] Timm, R.A.; Falla, M.P.H.; Huila, M.F.G.; Peres, H.E.M.; Fernandez, F.J.R.; Araki, K.; Toma, H.E.; *Sensors and Actuators B* ,146, 2010, 61-68.

[23] Baik, J.M.; Kim, M.H.; Larson, C.; Yavuz, C.T.; Stucky, G.D.; Wodtke, A.M.; and Moskovits, M.; *Nanoletters,*9(12), 2009, 3980-3984.

[24] Yin, H.; Ni, J.; Jiang, W.; Zhang, Z.; Yu, K.; *Physica E*, 43, 2011, 1720-1725.

[25] Raible, I.; Burghard, M.; Schlecht, U.; Yasuda, A.; Vossmeyer, T.; *Sensors and Actuators B*, 106, 2005, 730-735.

[26] Shimizu, K.I.; Chinzei, I.; Nishiyama, H.; Kakimoto, S.; Sugaya, S.; Matsutani, W.; Satsuma, A.; *Sensors and Actuators B* 141, 2009, 410-416.

[27] Jin, W.; Dong, B.; Chen, W.; Zhao, C.; Mai, L.; Dai, Y.; *Sensors and Actuators B* 145, 2010, 211-215.

[28] Byon, J.W.; Kim, M.B.; Kim, M.H.; Kim, S.Y.; Lee, S.H.; Lee, B.C.; and Jeong Min Baik, J.M.; *Journal of Physical Chemistry C* 116, 2012, 226-230.

[29] Yin, H.; Yu, K.; Zhang, Z.; Zeng, M.; Lou, L.; Zhu, Z.; *Electroanalysis 23*(7),2011, 1752-1758.

[30] Santagelo, S.; Messina, G.; Faggio, G.; Willinger, M. G.; Pinna, N.; Donato, A.; Arena, A.; Donato, N.; Neri, G.; *diamond and Related Materials* 19, 2010, 590-594.

[31] Wang, C.T.; Chen, M.T.; *Sensors and Actuators B* 150, 2010, 360-366.

[32] Carotta, M.C. ; Guidi, V. ; Malagu, C. ; Vendemiati, B. ; Zanni, A. ; Martinelli, G. ; Sacerdoti, M. ; Licoccia, S.; Vona, M.L.D. ; Traversa, E.; *Sensors and Actuators B* 108, 2005, 89-96.

[33] Manno, D.; Serra, A.; Giulio, M.D. ; Micocci, G. ; Taurino, A. ; Tepore, A. ; Berti, D. ; *J. Appl. Phys*. 81, 1997, 2709.

[34] Rella, Siciliano, R.P.; Cricenti, A.; Generosi, R.; Girasole, M.; Vanzetti, L.; Anderle, M.; Coluzza , C.; *Thin Solid Films* 349, 1999, 254-259.

[35] Shonauer, D.; Sichert, I.; Moos, R.; *Sensors and Actuators B* 155, 2011, 199-205.

[36] He, X.; Li, J.; Gao, X.; *Sensors and Actuators B* 108, 2005, 207-210.

[37] Behera, G.C.; Parida, K.; *Chemical Engineering Journal*, 180, 2012, 270-276.

[38] Wang, C.T.; Chen, M.T.; *Materials Letters* 63, 2009, 389-390.

[39] Wang, C.T.; Lai, D.L.; Chen, M.T.; *Materials Letters 64,* 2010, 65-67.

[40] Jin, W.; Chen, W.; Li, Y.; Zhao, C.; Dai, Y.; *Applied Surface Science* 257, 2011, 7071-7075.

[41] Brun, N. ; Leroy, C.M. ; Dexmer, J.; Serier, H. ; Carn, F. ; Biette, L.;Backov, R. ; *C.R.Chimie* 13, 2010, 154-166.

[42] Lee , S.C.; Hwang , B.W.; Lee , S.J.; Choi, H.Y.; Kim , S.Y.; Jung , S.Y.; Ragupathy, D.; Lee, D.D.; Kim, J.C.; *Sensors and Actuators B* 160, 2011, 1328-1334.

[43] Carotta, M.C. ; Ferroni, M. ; Gherardi, S. ; Guidi, V. ; Malagu, C. ; Martinelli, G. ; Sacerdoti, M. ; Vona, L.D. ; Licoccia, S.; Traversa, E.; *Journal of the European Ceramic Society*, 24, 2004, 1409-1413.

[44] Guidelli, E.J.; Guerra, E.M.; Mulato, M.; *Materials Chemistry and Physics* 125, 2011, 833-837.

[45] Verkelis, J.; Bliznikas, Z.; Breive, K.; Dikinis, V.; Sarmaitis, R.; *Sensors and Actuators A* 68, 1998, 338-343.

[46] Im, J.S.; Yun, J.; Kang, S.C.; Lee, S.K.; Lee, Y.S.; *Applied Surface Science* 258, 2012, 2749-2756.

[47] Mori, H.; Sakata, H.; *Materials Chemistry and Physics* 45, 1996, 211-215.

[48] Agbor, N.E.; *Gas sensors using thin films at room temperature*, Durham theses, Dhuram University Available at Dhuram E-theses online: http//etheses.dur.ac.uk/5694/1993.

[49] Cheng , Y.; Yang , R.; Zheng , J.P.; Wang, Z.L.; Xiong, P.; *Materials Chemistry and Physics* 137, 2012, 372e380.

[50] VanderWal, R.L.; Hunterb, G.W.; Xu, J.C.; Kulis, M.J.; Berger, G.M.; Ticich, T.M.; *Sensors and Actuators B* , 138, 2009, 113–119.

[51] Fields, L.L.; Zheng, J.P.; Cheng, Y.; and Xiong, P.; *Appl. Phys. Lett*. 88, 2006, 263102.

[52] Choi, K.J.; and Jang, H.W.; *Sensors*, *10*, 2010, 4083-4099.

[53] Fardindoost, S.; Zad, A.I.; Rahimi, F.; Ghasempour, R.; *International journal of hydrogen energy* 35, 2010, 854-860.

CHAPTER FIVE:

EXPERIMENTAL RESULTS AND DISCUSSIONS

5.1 Annealing Effect on Nanostructures VO₂ nanobelts

VO_2 (A) nanobelts were subjected to an annealing treatment in argon and nitrogen gas ambience at 500° C for 3hours giving an irreversible transition to VO_2 (M). This was done to study the effect of heat catalyst on the atomic structure and vibrational modes of the material. The composition and nanostructure were analysed using Raman spectroscopy. The differential scanning calorimetry analysis showed that the crystallization temperature of the annealed samples shifted to approximately 67 ˚C transition temperature of VO_2 (M) in proportion to the VO_2 grain size. The reduction of the sharpness and width of the hysteresis curve was found to be parallel to the nucleation, growth and aggregation of the VO_2 nanoplatelets.

5.1.1 Material Synthesis

VO_2 (A) nanobelts were synthesized using a hydrothermal procedure. The starting precursor V_2O_5 (2.25 g Alfa Aesar) was used as the source of vanadium and was completely hydrolysed and condensed upon addition of 50 ml of distilled water. Upon heating at 95 ᵒC and stirring thoroughly, 3.75 ml of sulphuric acid (H_2SO_4) was added into the aqueous suspension as an acid catalyst in order to convert the metalalkoxide V_2O_5 from the general dehydrating agent in its concentrated form. Then 1.25 ml of 98% of hydrazine hydrate ($N_2H_4 \cdot 2H_2O$) was added to the solution, as a foaming agent for the creation of a three dimensional network polymer with enhancement of the stability of the colloidal by its decomposition at high temperature. The surfactant not only allows the reduction of vanadium valence from +5 to +4 but also adsorbs in a reversibly manner to the surfaces of the growing nanoparticles providing a dynamic organic capping layer stabilizing the nanoparticles in solution and mediates their growth with selectivity towards specific crystal faces, and they are excellent control over crystal size, size distribution and morphology. Finally, we precipitated the nanoparticles by

addition of a strong chemical base Sodium Hydroxide NaOH diluted (5g/25 ml) and the nanoparticles were collected by filtration and washing with distilled water and ethanol. The final product was redispersed in suitable apolar solvent (water) forming stable colloidal suspensions. The hydrothermal synthesis was carried out in a Teflon-lined autoclave at ~230 °C for about 48h. Then the content was air-cooled to room temperature followed by a filtration step of the formed precipitates. The final black chemical product was washed extensively with water and ethanol and dried at about 60 °C for ~12 h and the supernatant liquid was discarded. To confirm the VO$_2$ (A) crystallographic nature of the synthesized nano-powder, High Resolution Electron Microscopy (HRTEM), X-Rays Diffraction (XRD) as well as transport (Resistance-Temperature) measurements were conducted. We can summarize our chemical reactions in the different process as shown below:

$$V_2O_5 + 2H_2SO_4 \rightarrow 2VOSO_4 + \frac{1}{2}O_2 + 2H_2O \text{ (orange colour)} \qquad Eq.5.1$$

$$2VOSO_4 + N_2H_2 2H_2O \rightarrow V_2O_3 + N_2 + 2SO_2 + O_2 + 3H_2O (green\ colour) \qquad Eq.5.2$$

$$V_2O_3 + N_2H_2 2H_2O + O_2 \rightarrow 2VO_2 + N_2 + 3H_2O (Blue\ colour) \qquad Eq.5.3$$

$$V_2O_5 + 2H_2SO_4 + 2N_2H_2 2H_2O \rightarrow 2VO_2 + 2N_2 + 2SO_2 + \frac{1}{2}O_2 + 8H_2O (green\ colour)$$
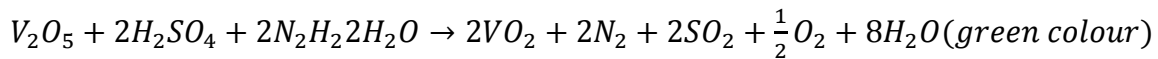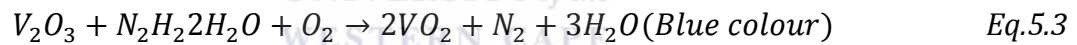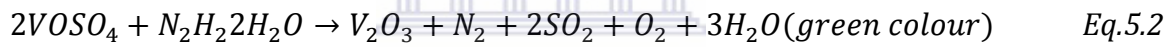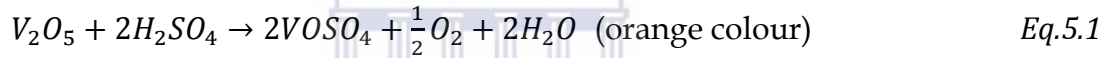
$$Eq.5.4$$

5.1.2 Morphological study and elemental analysis.

The morphology of the synthesized crystals was observed by A Tecnai G2 F20X-Twin MAT field emission high resolution transmission electron microscope (HRTEM) operated at 200 KV Field emission used to investigate the atomic structure and the presence of different oxidation state of the nanocrystals equipped with an elemental EDAX system. As typically reported on figure 5.1 a), the surface morphology of the samples exhibit one dimensional nanoplatelet structure. This was found to be correlated to the V$_2$O$_5$ initial concentration and the high surface-energy liable with chemical

reactions of the medium and becauseV$_2$O$_5$ crystallizes in an orthorhombic structure comprising   layers of [VO$_5$] square pyramids sharing edges and corners with a structure only weakly bound along the crystallographic b axis, which enables the facile intercalation of different molecular species within the interlayer sites [1]. The dimension of the crystallites is in the range of 20 nm to 150 nm for the as-prepared material and around 50-500 nm for the annealed sample. That means that annealing temperature induces significant grain growth promoting twin formation in larger grains. According to Razavi et al [2] surface topography of the films showed that for increase temperature, surface roughness, film porosity, and grain size increases. The increase grain size at higher deposition temperature is strongly correlated with the stoichiometry, grain development and stress. The elemental composition of the material acquired from the X-rays emitted as shown in figure 5.b) shows that the elemental composition is only constitute of vanadium atoms and oxygen with high intensity showing the nucleation of grains and crystallization of the particles. It was demonstrated that high temperature can stimulate the migration of grain boundaries and cause the coalescence of more grains during the annealing process. Additionally the grain growth can be explained as diffusion and occupation of the correct site in the crystal lattice where grains with low surface energies grow larger, which contributes to increase of the surface roughness and larger microcracks [3].

5.1.3 DSC analysis and structural study of as-synthesized material

The metal insulator phase transformation has been studied via DSC on cooling and on heating. See figure 5.2. The isotherms that occur during the thermal cycling explain the kinetics of the phase transformation of the system. In both samples (as-synthesized and annealed), two peaks were detected during the experiment from room temperature to 110°C at 10 °C/min with the presence of a flowing of nitrogen gas at 5 ml/min. The as prepared presents a big hysteresis in order of 9 °C comparing to the one anneal with 6.7 °C. This is due to the particle size of the material and the presence of strain in the material with grain boundaries. The as synthesized material peaks transition is due to

the presence of slightly metallic atoms inserted in the tetragonal metastable domains for the VO₂ (A). The insulator to metallic transition in the annealed sample occurs at 67.1°C with an enthalpy of -3.596 W/g related to the exothermic peak where the crystallization of the material occur and the metallic to insulator transition occurs at 60.4°C with an enthalpy of 3.1W/g transition, only 85.28 % recovery of the monoclinic phase. Changes in enthalpies of transformation are attributed to elastic stored energy and to some untransformed rutile phase [4-5] that we determine as percolative phenomena. Additionally, Lopez et al. [6] showed that there is a clear dependence between the transition temperature and the particle size where the decrease of the size produces higher transition temperature on heating and lower temperature on cooling leading to increasingly wider hysteresis loops as the particles become smaller. This is in accordance with our present work regarding the DSC results and structural morphology. Also Dai et al. [7] demonstrated that DSC indicates that the MST of VO₂ changes concurrently with size of the nanoparticles at different growth stages. We can hence correlate our results in the frame of classical nucleation theory. The change in free energy for spherical particles due to their formation consists of two terms such as:

$$\Delta G = -\frac{4\pi R^3 \Delta g_{ex}}{3} + 4\pi R^2 \gamma \ (3D) \qquad\qquad Eq.5.5$$

R represents the radius of the nucleus. In the case of 1D nucleus with diameter d and length L, the free energy is given as [8]:

$$\Delta G = -\frac{\pi d^2 L \, \Delta g_{ex}}{4} + 2\pi r L \gamma \qquad\qquad Eq.\,5.6$$

$$\Delta G = -\pi r^2 L \, \Delta g_{ex} + 2\pi r L \, \gamma \qquad\qquad Eq.\,5.7$$

Where Δg_{ex} is proportional to $|T - T_c|$ with proportionality constant determined by the entropy difference between the parent and the product phase. γ is the surface free energy increase per unit area which we assume to be 20mJ/m², r is the radius of the nanoplate. See figure 5.4.
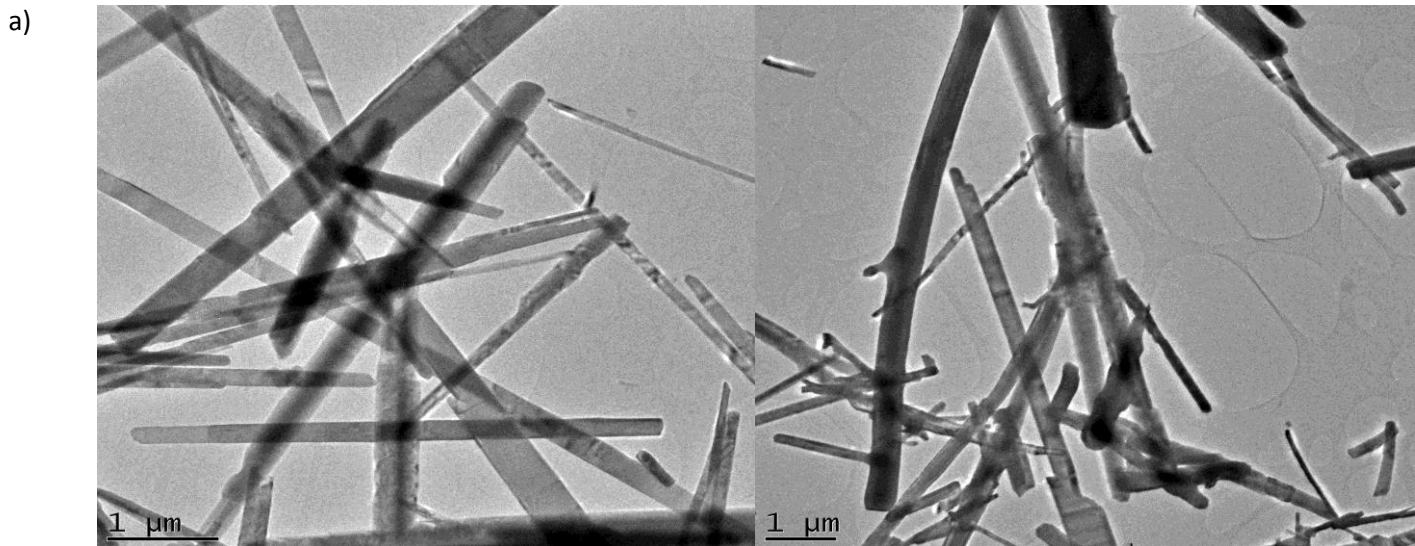
Figure 5.1.a) High magnification Transmission electron microscopy images of VO$_2$.
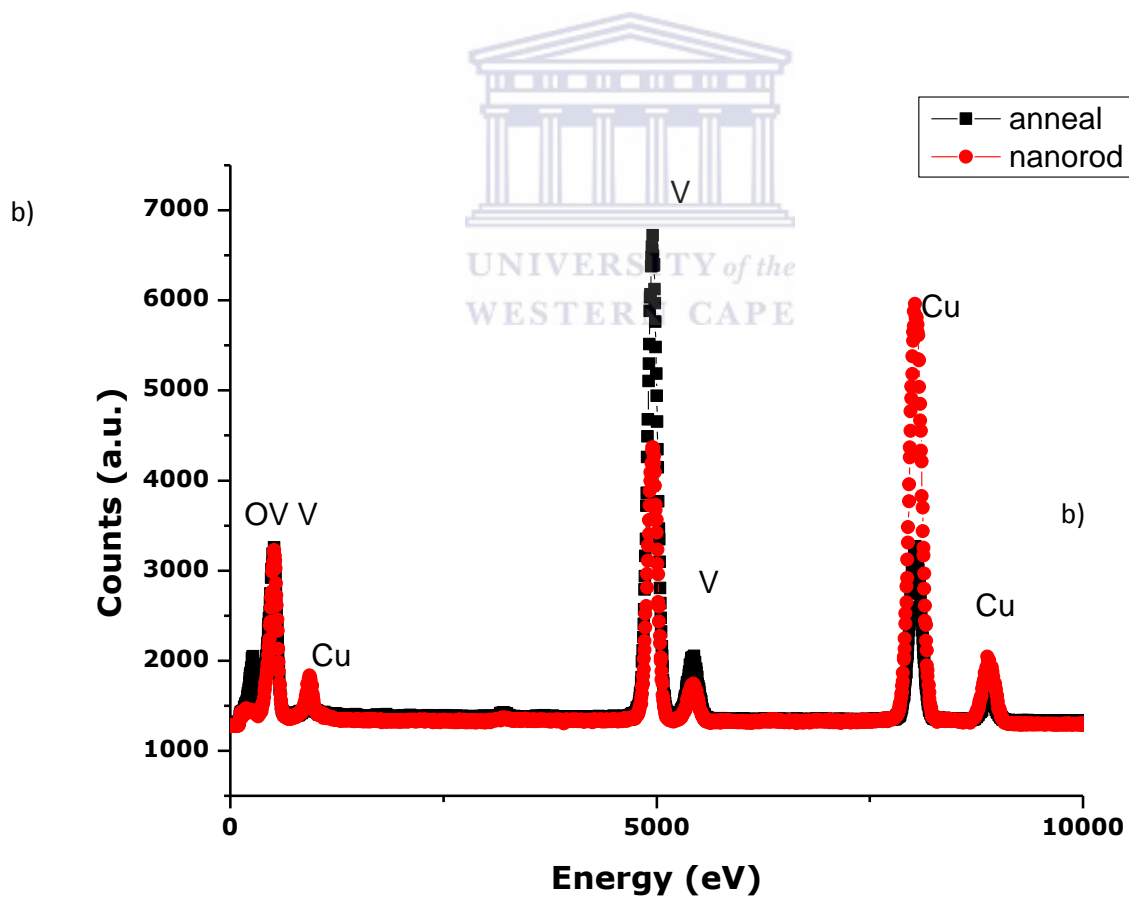
Figure 5.1.b): EDS spectra of VO$_2$ nanobelts as-synthesized and annealed.

The kinetics phenomena occur at different times. The well crystallized material after annealing present the transition temperature from $VO_2(M)$ to VO_2 (R) taking place after 10 min and stop after 18 min while in the as-synthesized sample only few metallic domain transit to VO_2 (R) just for 2 min approximately. Hence the ultrafast of the metal to insulator transition is proportional to the density of atoms intending to nucleate upon annealing temperature. Multiple physical phases or domains with dimensions of nanometres to micrometres can coexist in these materials at temperatures where a pure phase is expected. Due to the fact that the growth of the product is extremely fast, less than 500 fs, the control of transformation was proved to rely on thermal nucleation process rather than phase transformation as in the classical picture. The VO_2 semiconductor regarding as an n-type heterogeneous nucleation implies the existence of suitable nucleating defects sites in the sample space considered. The nature of these nucleation sites can range from simple vacancies, wall dislocations, untransformed embryonic regions, or electronic defects given all possible states valence of vanadium. R Lopez et al. described the nature of nucleation sites as extrinsic defects with high densities expected to be present during high temperature annealing and persistent in the whole process given the quenching process applied to the samples. The probability of a small volume ρdV to have a defect site can be expressed as:

$$F = 1 - exp[-C\Delta g_{ex}{}^y.V] \qquad\qquad Eq.5.9$$

Making use of the properties of correlated electron materials in device applications will require the ability to control domain structures and phase transitions in these materials [9]. Measures of the temperatures and heat flows associated with transitions in the material as a function of time and temperature in a controlled atmosphere (N_2) were obtained via Differential Scanning Calorimetry (DSC). The grain structure measured with the Software Image J presented in figure 5.3 shows that the grain size is smaller for high interspacing lattice for as-synthesized material approximately 0.400-0.600 nm ([110]) while for annealed sample the grain junction is shrinked and the interspacing

become smaller 0.300 nm reducing residual stresses and optimization of the uniformity of the sample.

5.1.4 X-Ray diffraction description

The determination of the material phase and crystallinity was done using XRD crystallography. The majority of the peaks are indexed as VO_2 (A) according to a JCPDS card 00-042-0876 at room temperature. The lattice parameters a and c are 8.45000 Å and 7.68600 Å respectively and Z=16. The space group is P42/nmc. Figure 5.5 reveals sharp peaks and intense diffraction with a preferential orientation along (110) which demonstrates that the sample is well crystallized without impurities and we note also the presence of some peaks belonging to VO_2 (M) with a weak intensity. It has been demonstrated that the distortion of the VO_6 octahedra in the low temperature VO_2 (A) phase is similar to the monoclinic VO_2 (M) phase [10]. After annealing at 500 °C, the (110) peak decreases in intensity when the material has been annealed under Nitrogen while it is completely vanished under Argon. The structure is monoclinic lattice with a= 5.75290 Å, b= 4.5263 Å, and c = 5.38250 Å with β= 122.60 showing a shrinkage of bond length and presence of two types of V-O with distorsion of the lattice. It has been shown that the strong anisotropy of the thermal expansion and the symmetrical orientation with respect to the lattice are related to structural changes with temperature where bond length distorsion and bond angle distorsion occured at high temperature [11]. The nanostructures exhibit two crystallographic structures: stable monoclinic and metastable tetragonal. Generally two main processes determined the phase transformation in annealing process: annealing temperature and time and interfacial stress. Here we see that the complete phase transformation is only possible with an annealing under Argon gas which is inert and act as gas purifier to prevent oxidation from the vanadium oxide, comparatively to the one under Nitrogen which interacts with the material and delays the metal insulator phase transition. The surface region appears as an imperfect region due to the presence of high surface region to volume ratio meaning that the number of atoms on the surface is comparable to the one inside

the particles where atoms relax inside the normal lattices sites. The surface structure of nanoplatelet as synthesized and annealed respectively presents highly surface active atoms with high surface energy where transition begins upon thermal treatment. We can see that the (110) of VO_2 (A) is the preferential orientation contrary to VO_2 (M) which presents a (011) preferential orientation. The trend in tetragonal peaks decrease while monoclinic peaks increase hence the application of heating temperature favours the structure achievement of monoclinic phase. This annealing effect was also similar to Wang et al. [12] who observed an irreversible transformation from VO_2 (B) to VO_2 (M) under vaccum annealing and suggested that the new birth structure is possible with diffusion of atoms and sufficient reaction at high annealing temperature of atoms of vanadium and oxygen. In another hand there is a recombination of VO_2 molecules that are taking place with increase thermal stress resulting in larger particles size and looser structure as the annealing time and temperature were prolonged.
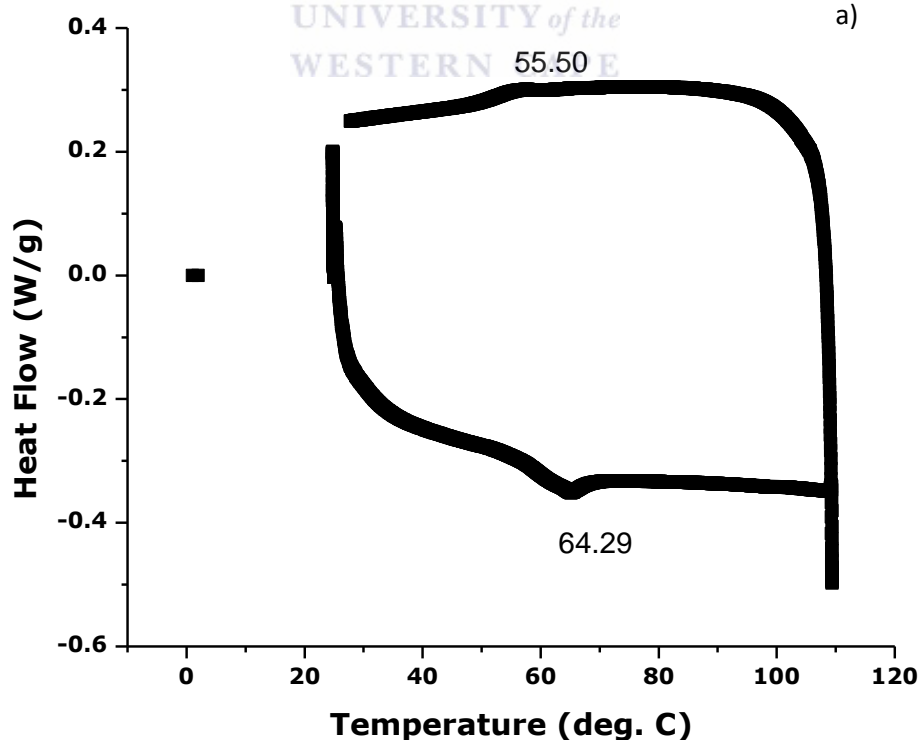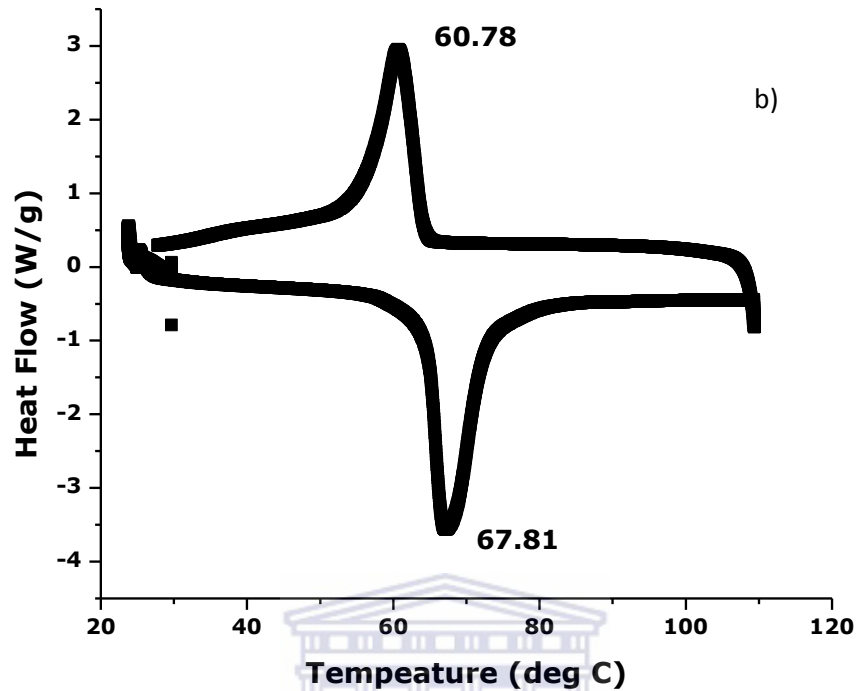
Figure 5.2 DSC curve showing the reversible phase transformation in the material during the thermal cycling in as synthesized material VO_2 (A) a) and VO_2 (M) b).

We observe a net increase of particles size with free energy until a critical point nucleation where ΔGc is approximately 12000 eV and then a sudden decrease of free energy occurs where the particles stabilize at around 60 nm and then aggregates with loss of energy up to -33805 eV. This was described as a heterogeneous nucleation fashion.
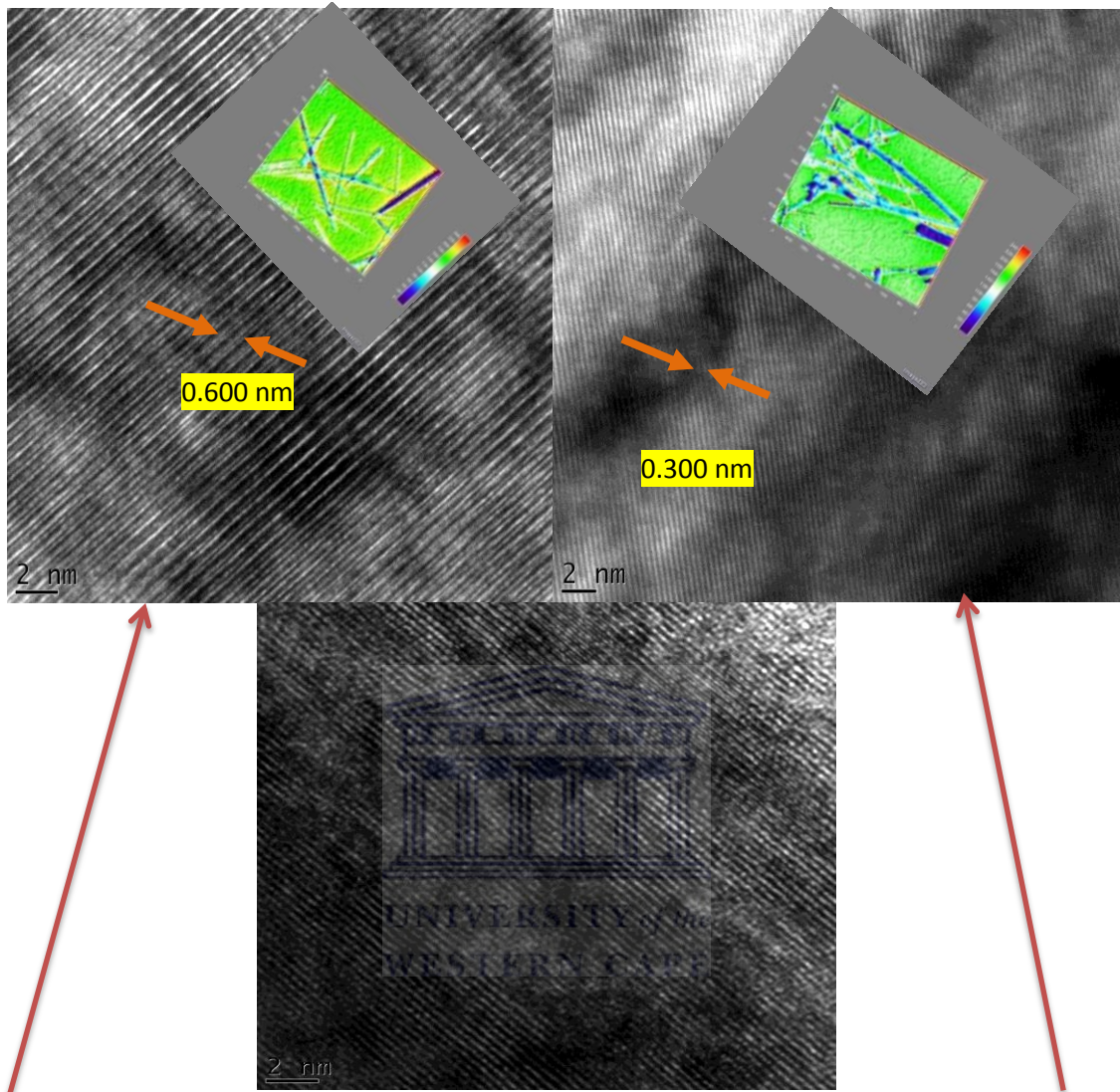
Figure 5.3 Grains structure observed at different annealing gas.
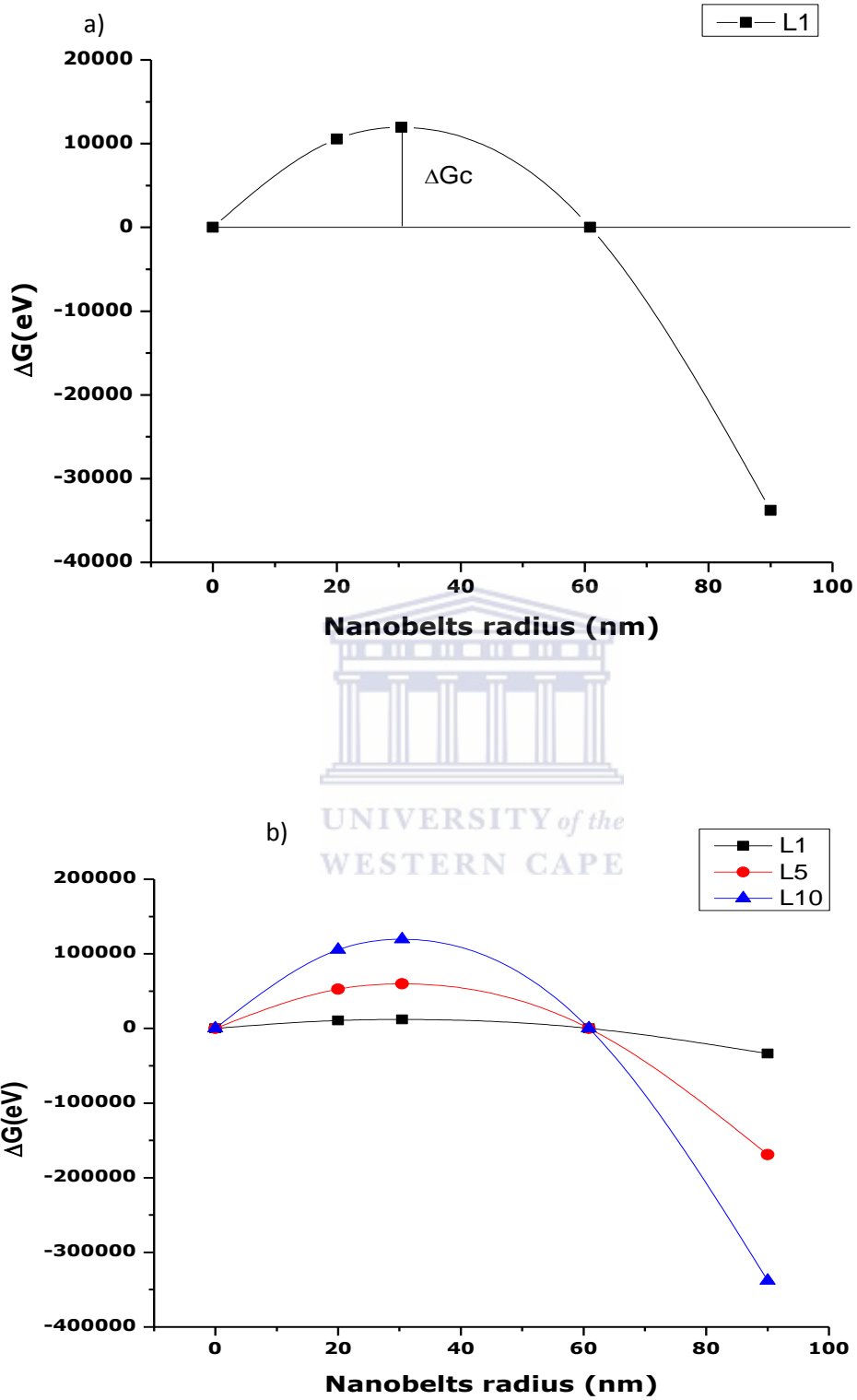
Figure 5.4: Free energy as function of the nucleating particle nanoplatelet during the phase transition at T=341K a) and function of the particle length L b).

In opposite with Suh et al., [13], they observed that as the grain grows in size with annealing time, the hysteresis gets wider. This can be described on the model of martensitic transformation in which the density of heterogeneous nucleation centers such as structural defects or oxygen vacancies. S.A Pauli et al. [14] studied the x-ray diffraction studies on the growth of vanadium dioxide nanoparticles and observed that the well below shift in the Bragg diffraction peak comparing to the resolution was explained as the fact that the highest oxidation state of vanadium V_2O_5 is formed under annealing treatment with monotonically way in intensity indicating that they form rapidly large in plane domains with associated diffraction widths that are narrower. They speculated the presence of a remainder of a reservoir of the amorphous material that was initially deposited at room temperature and has not been fully depleted before the V_2O_5 phase begins to form. Hence annealing results in small reduction in thickness although the layer still remains which may be due to the kinetic hindering of island ripening with increasing depletion. The VO_2 semi-conductor to metal phase transition proceeds in a heterogeneous fashion which rely on structural defects as source of nucleation sites. In accordance to this finding, Klimov et al. [15] showed that the hysteresis loop decreases with increasing particle size and is inversely proportional to the square root of grain size. This strong size dependence with heat flow hysteresis loops observed on our samples has been successfully modelled through the statistical nature of the activation sites. John Rozen et al. [16] showed an offset between the electrical and optical hysteresis measurements of the SMT of VO_2 in a two dimensional nanostructures. This is due to the relative fraction of nanoparticles in the semiconducting state (optical hysteresis) while in the electrical response the result is governed by the evolution of a continuous percolation path showing the current percolation through a network of nanometer scale grains of different sizes which undergo a SMT at distinct temperatures.
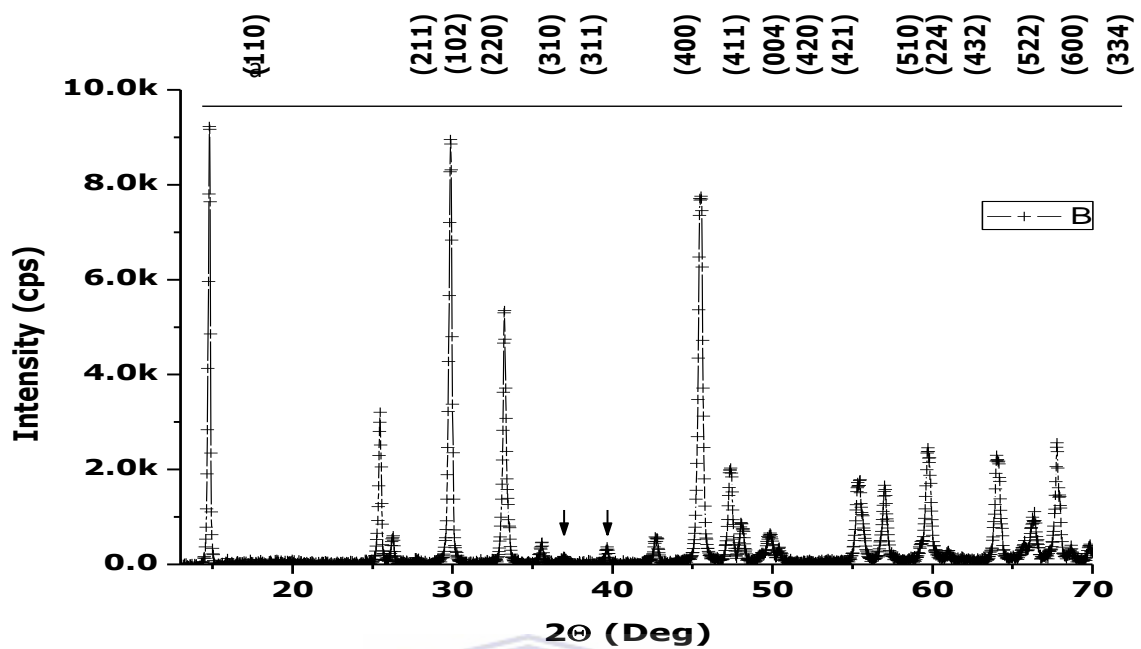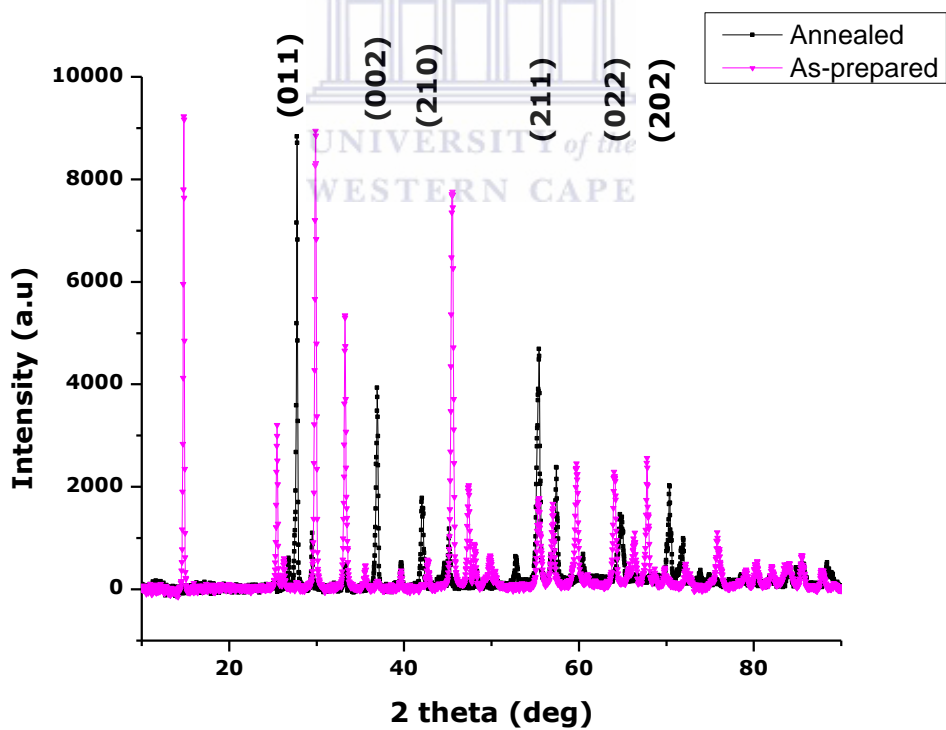
Figure 5.5: Typical room temperature indexed X-rays diffraction of the as-synthesized a) and annealed under Argon b).
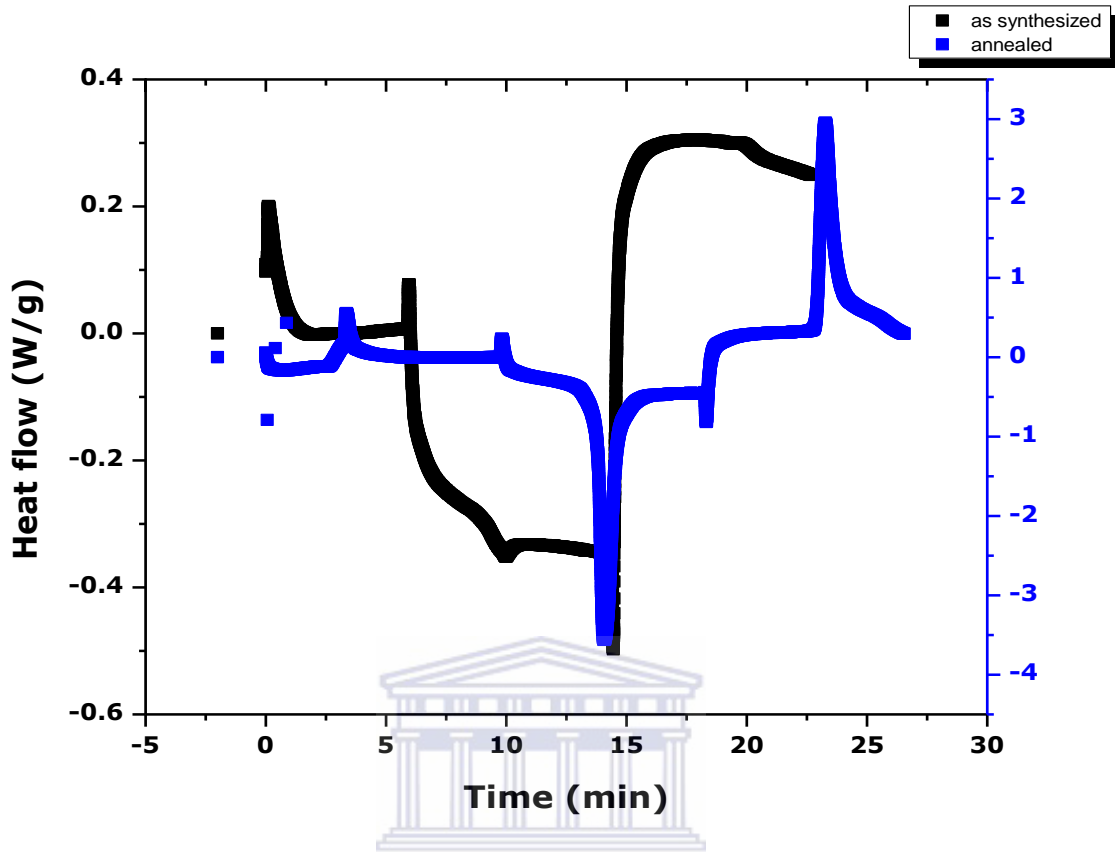
Figure 5.6: Heating flow versus time for as-synthesized and anneal samples.

5.1.5. Raman Spectroscopy

Nanoparticles have appreciable fraction of their atom at the surface as the data. A number of properties of materials composed of nanometer sized grains depend strongly on the surface area. The specific surface area of a catalyst is customarily reported in the units of the square meter per gram. ρ is the density expressed in g/cm^3, d is the diameter and V the volume. A cylinder of diameter d and length L has a Volume $\pi d^2 L/4$ and A=2 πrL. Hence the surface area is given by:

$$S = {A}/{\rho V} , S\left({m^2}/{g}\right) = {4 \times 10^3}/{\rho d} , d \ll L \qquad\qquad Eq.5.8$$

This relation is justified for nanowires, nanosheet or nanoplate and is assumed in our free energy calculation. Figure 5.7 presents Raman response of VO_2 (M) annealed under

143

N₂ at room temperature giving structural information of the material, obtained by excitation of continuous wave laser light with a 514.5 nm line from argon ion. It is possible to identify the in situ molecule and to determine the amount of the
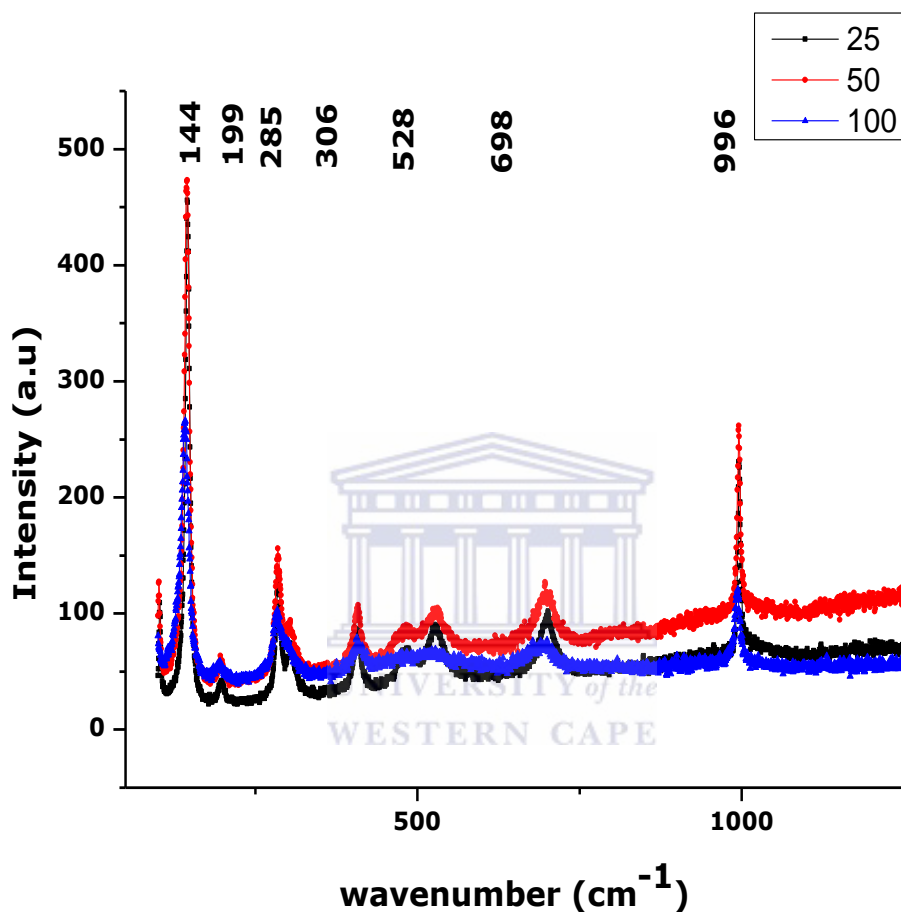
Figure 5.7:   Raman spectra collected for nanobelts VO₂ annealed at different output power 25mW, 50mW and 100mW.

molecule present in the sample. Most molecules at rest prior to interaction with the laser and at room temperature are likely to be in the ground vibrational state.

Therefore the majority of Raman scattering will be Stokes Raman scattering. The ratio of the intensities of the Stokes and anti-Stokes scattering is dependent on the number of molecules in the ground and excited vibrational levels. We notice that the output power

at 50 mW was the best choice providing the best spectral resolution of the full width at half maximum. The spectrum presents some raman lines of V_2O_5 which are very close to the lines of VO_2: 144cm^{-1}, 199 cm^{-1}, 306 cm^{-1}, 406 cm^{-1}. We note that the change of the surface stoichiometry oxidation induced by a local heating at 100 mW (lowering of the vibration modes) may be responsible for the change of Raman line position. Hence nanoscale interactions occur at the surface which present small amount of V_2O_5. Structural changes based on the ultrashort time scale was proposed [17] where the initiating pulse electron packet on the ultrashort time scale induces, by momentum conservation, a transient stress in the nanometer scale sample and as such leads to a nonequilibrium structure compatible with the insulator phase in its electronic configuration. The stress effects can be kinematical, by expansion, or possibly by Jan-Teller distortion. It is also possible that some stress be of acoustic wave generation by the photon.

5.1.6 Conclusion

In summary, nanoplatelets VO_2 (A) nano-crystals was well synthesized by hydrothermal process with a percentage of crystallinity of 89%, presenting high surface to volume ratio due to the smallest size of the particles. The annealing treatment under N_2 gas and Ar gas gives good insight of internal transformation taking place in the material. The annealing under Argon gas appears preferable due to the optimum crystallization and purity of the material comparatively to the one under Nitrogen which interacts with the material and delays the metal insulator phase transition. Additionally, the as-synthesized material was discovered for the first time to be applicable as gas sensing device at room temperature under H_2. See next section. As future work the optimization of the nanoscale structure of the material is required and the testing of the annealing sample under same conditions and operating at different temperatures to follow the effect of annealing time and annealing temperature on the electronically properties are highly demanded for the development of the semiconductor electronic device. It was also noted that the distribution of crystallite

sizes plays an important role, especially for thermal phase induced transition due to the fact that some crystallites completed the transition when others had not. This transition was qualified as latent heat transition and the equilibrium with the surroundings is not instantaneous.

5.2 First order solid-solid phase transition, Strain-thermal dependence on nanostructures VO$_2$ Monoclinic

In situ X-ray thermodiffraction of nanoplatelets VO$_2$ (M) was studied to characterize the dynamics of structural phase transition on (-211) Bragg peak monoclinic. The transition induced and controlled by using Peltier thermocouple shows intermediate phaseM2 due to the solid-solid phase transition with predominance of metallic domains rutile comparing to the M1 structure at around 61deg.Cdue to small perturbations and the percolative transition metal-insulator. The nucleation is referring to the kinetic processes that initiate the first-order phase transitions in the non-equilibrium VO$_2$. The present phonon study clearly demonstrates that the Coulomb correlation in M1-R at 65deg.Cfacilitates the Peierls-type structural transition. Hence the M1-R transition and the structural transition are facilitated by the mutual cooperation Coulomb correlation effect and the Peierls distortion.

Properties of Transition metal oxides (TmOx) can be engineered by the application of lattice strain as an external stimulus causing non-disruptive effects with profound influence on the structural properties through intrinsic coupling between charge, spin and orbital wave function of electrons. As a strongly correlated electron material TmOx, vanadium dioxide (VO$_2$) has been a model system of research for the Metal Insulator Transition (MIT). Applications such as thermo electrochromics, Mott transistors, strain sensors and thermal actuators have been proposed or realized by exploiting the MIT in VO$_2$ [18]. The MIT occurs with a dramatic change in resistivity accompanied by a ferroelastic, structural phase transition with an infrared reflecting state to a relative transparent state change [19]. Here, Vanadium dioxide (VO$_2$) hydrothermally synthesized at low temperature exhibits an insulator-to-metal transition (IMT) at 65 deg. C with abrupt changes in structural and mechanical properties and coupled to a structural phase transition (SPT) from monoclinic to tetragonal tracking the nucleation to stabilization of an intermediate new phase. We have successfully measured independently the IMT and SPT nanoplatelets VO$_2$ structures by in-situ x-ray

diffraction, and shown that both phenomena are congruent. Strained structure of the VO_2 could be a mechanism for the formation of such intermediate phase [20] known as monoclinic M2 phase which represent the nucleation reaction based on temperature fluctuations. Considering previous reports on intermediate monoclinic phase which is caused by stress, we discuss the mechanism of the intermediate phase formation in our powders. The existence of M2 intermediate crystalline phase with room temperature insulator phase and high temperature metallic phase across MIT in VO_2 nanostructures could be of relevance to understand structural contributions to the phase transition dynamics [21]. The insulating, monoclinic M1 phase, which is the stable phase for undoped, strain-free VO_2 at room temperature, turns into the metallic, rutile R phase at approximately 65 ^{o} C that can be further complicated by factors such as doping and strain, resulting in another insulating, monoclinic phase, M2, which is metastable phase for VO_2. In practice, although the M1 phase is always the energetically favorable phase in freestanding VO_2 samples, small domains of M2 phase ratio 2:1 can exist when the sample is strained by the temperature which results in an insulator (M1)insulator (M2) phase transition before the MIT (M2 to R). As a result, the intermediate phase M2 transitional phase between the M1 and the R phase may play a critical role in the physics phenomena of the thermodynamics in our nanosystems [18]. Figure 5.8 shows the M2 structure where one-half of the V chains of the R phase pairs but does not twist and the other half twists but does not pair and the M1 phase of VO_2 can be viewed as a simple superposition of two lattice distortions of the M2 type (Mott-Hubbard insulator) which present V chains Heisenberg with s=1/2 [22-23].
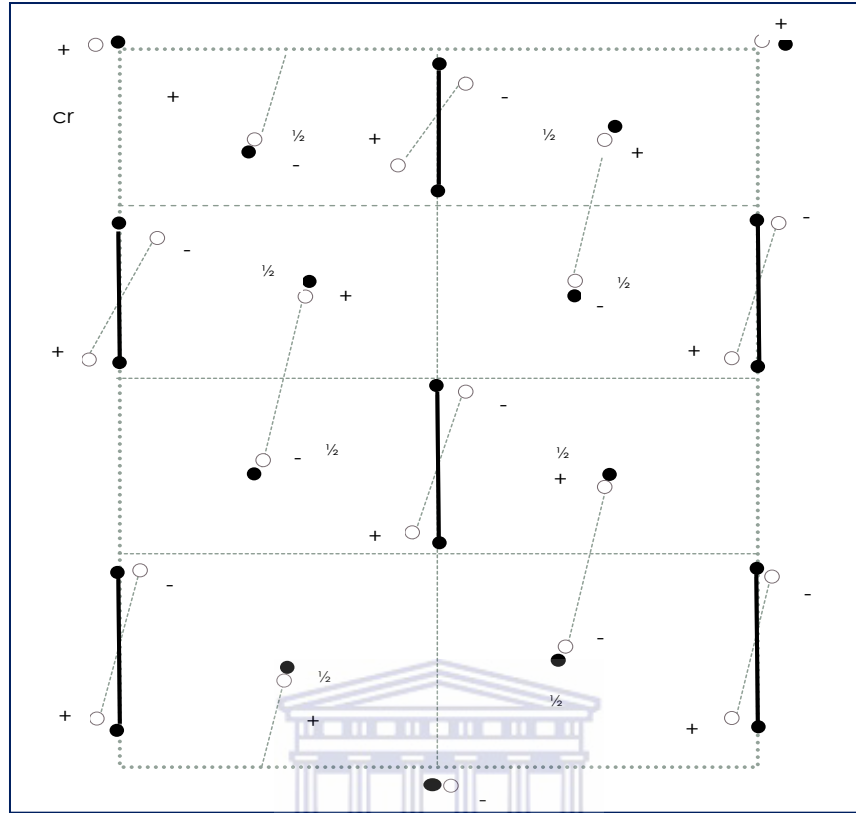
Figure 5.8: Comparison of V-V pairing in the three phases (R, M1, and M2). In M1, (open circles) all the vanadium atoms both pair and twist from the rutile positions. In M2 (filled circles) one-half of the vanadium atoms pairs but does not twist and the other half forms unpaired zigzag chains. (The distortions are exaggerated by a factor of 2 for clarity. [24]

For XRD measurements we followed the change of (-211) m diffraction in XRD against temperature for the VO_2 sample. The sample was insitu heated from 323 to over 343 K. The thermodynamics mechanism studied in this paper is an important key to control and manipulate the MIT in our system.

Figure 5.9.a) reveals sharp peaks and intense diffraction which demonstrate that the sample is well crystallized with strong constructive interference. All peaks are indexed as VO_2 (M) according to a JCPDS card 00-043-1051 with the lattice constants a, b and c are of 5.75170 Å, 4.53780 Å and 5.38250 Å respectively, β=122.64˚C. XRD analysis shows that VO_2 (M) with a space group of $P2_1/c$ has a strong preferential reflection along

(011). The other peaks are indexed as (200) the 2nd main Bragg peak series, (002), (012), (210), (-302), (102), (211) the 3rd main Bragg peak series. But as the reflection Bragg angle becomes high the probability to obtain constructive interference is weak. See figure 5.9 a) and 5.9 b).
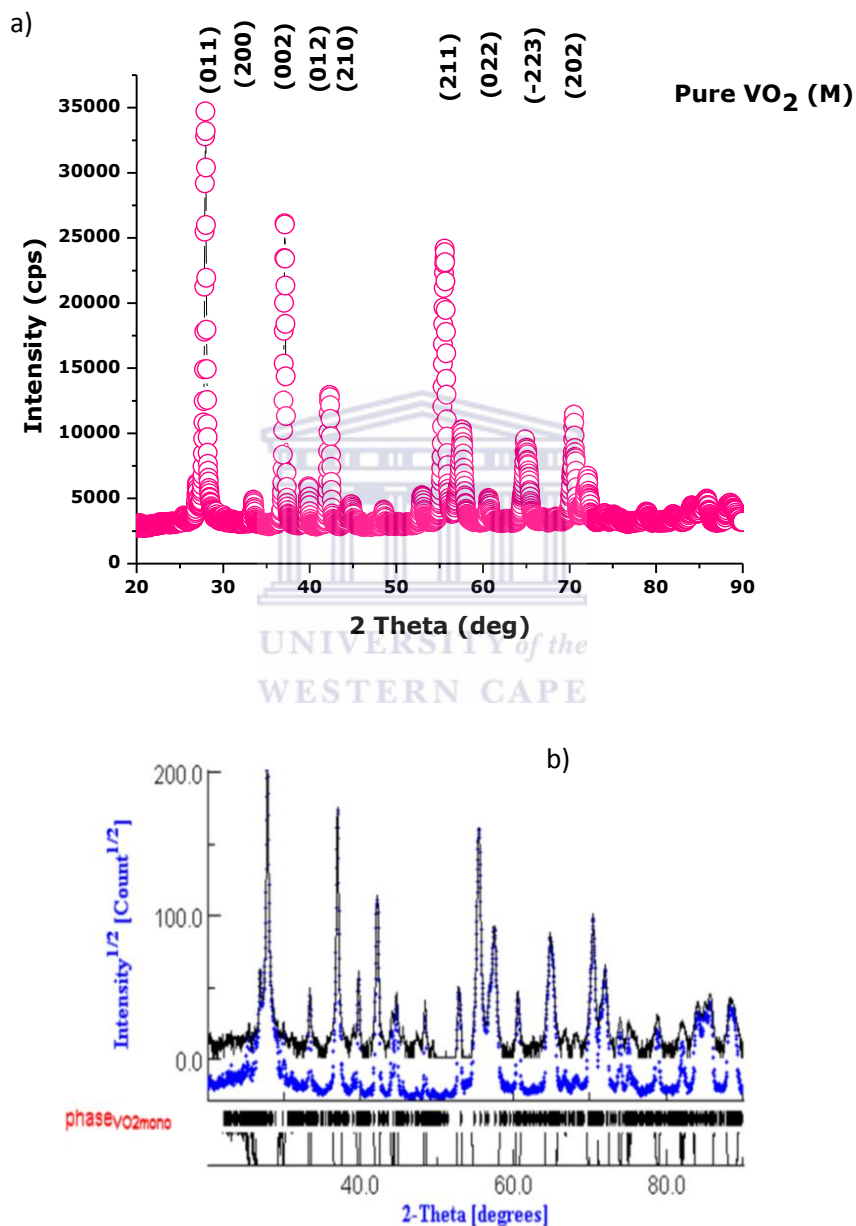
Figure 5.9: X-rays diffraction pattern of the snow-flake like synthesized nano-crystalsVO$_2$ (M) b) fitting of the x-Ray Bragg diffraction with MAUD software analysis showing good concordance of experiment and theory.

The elemental composition of the material acquired from the X-rays emitted is shown in figure 5.10. The snow-flake crystals consist of ~35.24 and ~63.40 wt% of oxygen and vanadium respectively demonstrating that the stoichiometry of the compound is almost VO_2. See table 5.1.
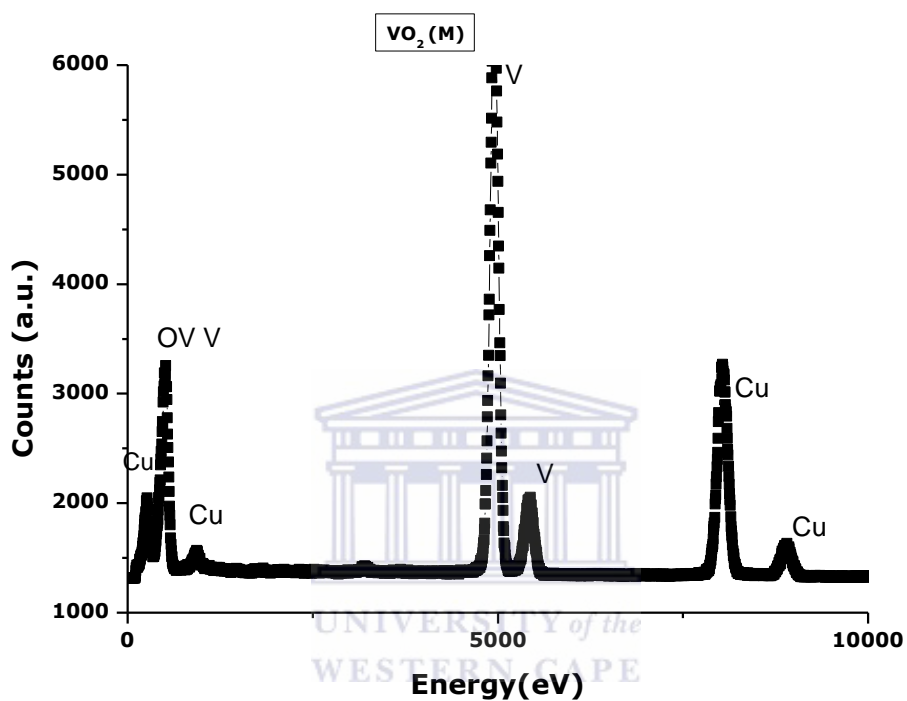
Figure 5.10: Elemental composition of VO_2

Table 5.1: Elemental composition of VO_2

Elements	Atomic% Weight %
OK	35.24
OK	63.40
VK	64.76
VK	36.60
Totals	100.00

The metal insulator phase transformation has been also studied via DSC on cooling and on heating. See figure 5.11c) and d). The isotherms that occur during the thermal cycling explain the kinetics of the phase transformation of the system. Two exothermic peaks were detected during the experiment from room temperature to 110°C at 10 °C/min with the presence of a flowing of nitrogen gas at 5 ml/min to maintain appropriate pressures quotients. The reversible process has been observed after cooling back to room temperature due to the slightly change of the crystallographic structure of VO_2 (R) to VO_2 (M). The insulator to metallic transition occurs at 65.3°C with an enthalpy of -6.796 J/g related to the exothermic peak where the crystallization of the material occur with an intermediate weak transition at around 61° C and the metallic to insulator transition occurs at 57.5°C with an enthalpy of -5.33 J/g transition, only 88.05 % recovery of the monoclinic phase with a giving hysteresis of almost 8 °C in peaks temperature between heating and cooling which can be assigned to the stress in the sample. According to J. Cao et al [9] multiple physical phases or domains with dimensions of nanometres to micrometres can coexist in these materials at temperatures where a pure phase is expected. Making use of the properties of correlated electron materials in device applications will require the ability to control domain structures and phase transitions in these materials. The High Resolution Transmission Microscopy shows that the material consists of two phases at room temperature that we can differentiate through the colour of the image. Information about the surface structure see figure 5.11 composition, chemistry, topology, and possible surface reconstructions is a prerequisite to understand recent findings that quasicrystalline surfaces and coatings exhibit low surface friction and high oxidation resistance, properties important to many technological applications [25]. The layer with more dense atoms is dark in high resolution while the less dense M2 is light. See figure 5.12 a). This is in accordance with our in situ thermodiffraction result. The electron diffraction on a single crystal of VO_2 presents constructive interference of regular array of scattered intensities which carry information about the position of the atoms in the crystal figure 5.12 b). The indexation of planes in the low symmetry structure is obtained. The diffraction pattern of a single

crystal exhibits a quasi P2$_1$/c symmetry. Surface sensitive measurements as low energy electron diffraction have become possible through advances of the metallurgy the growth of very sizable, high quality, single grain samples structure of quasicrystals, determining their surface structure presents new and important challenges.
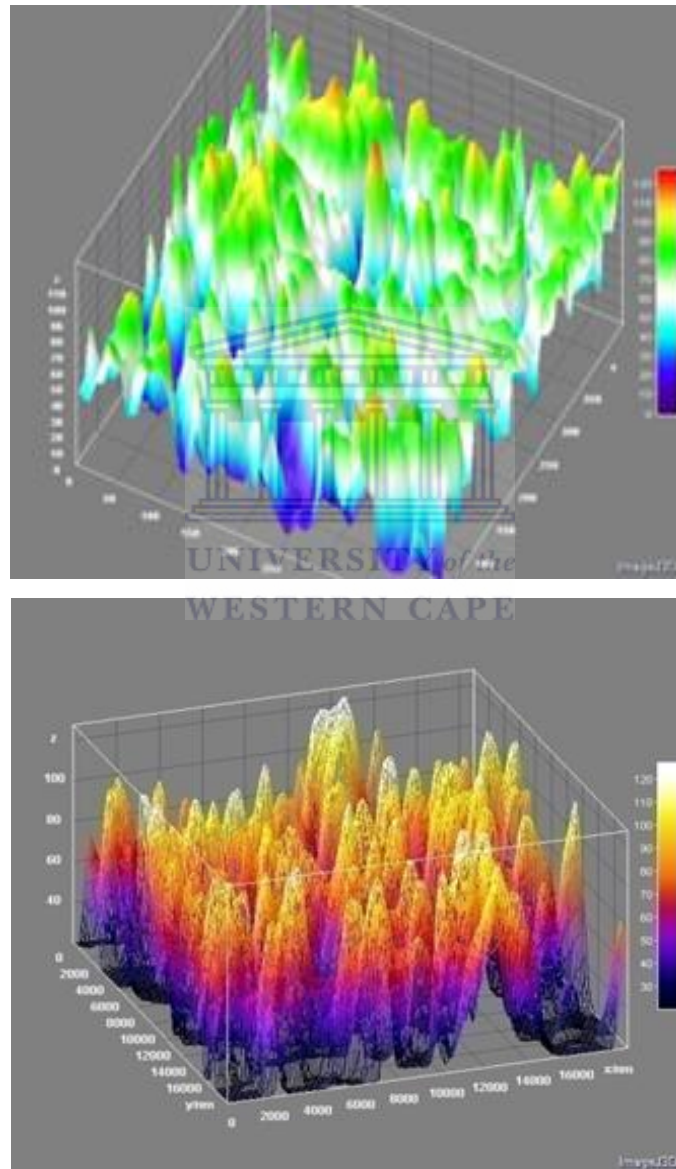
Figure 5.11: Surface profile of nanocrystals VO$_2$

c)
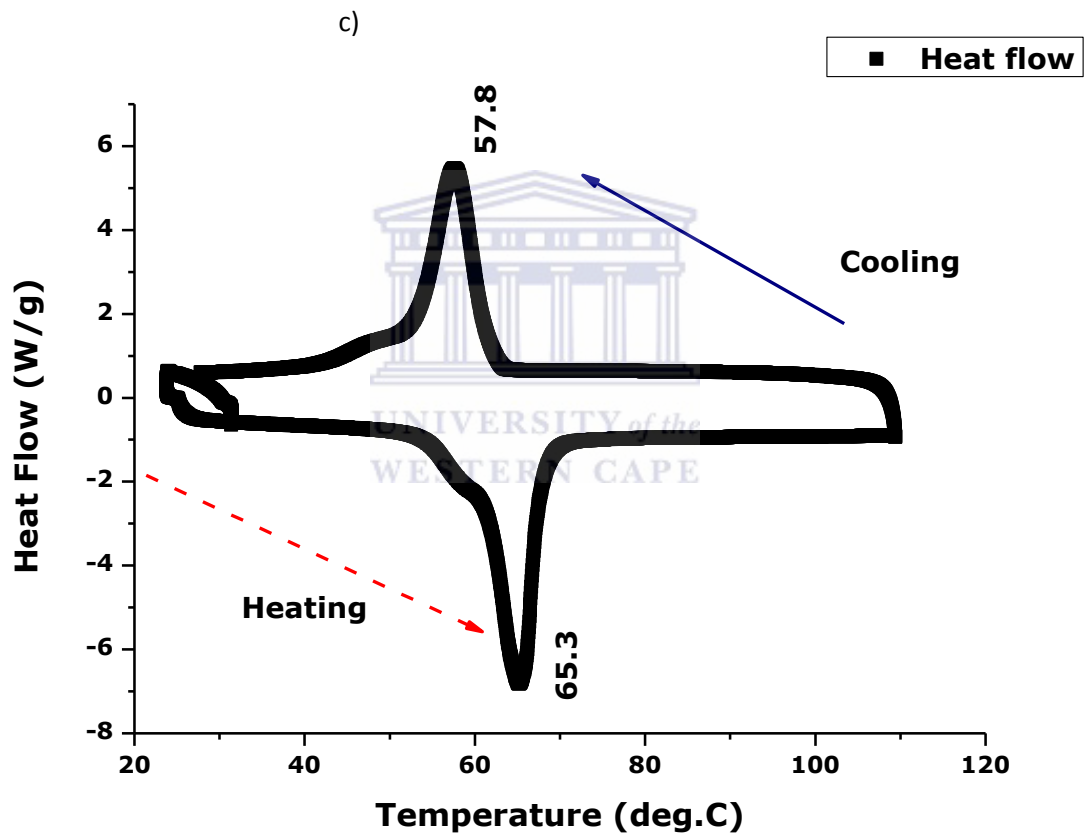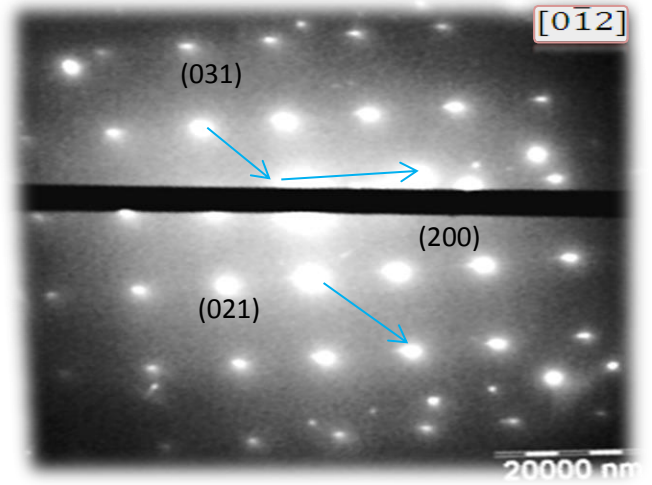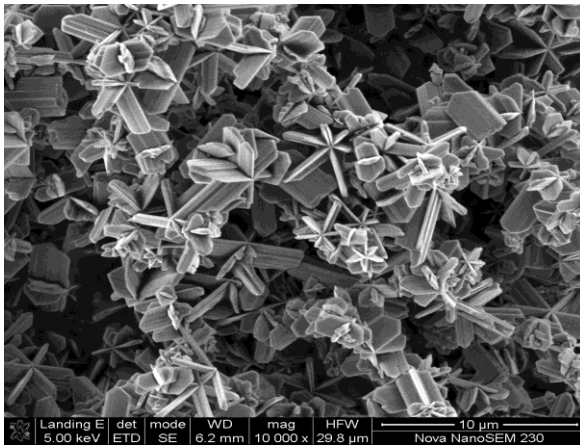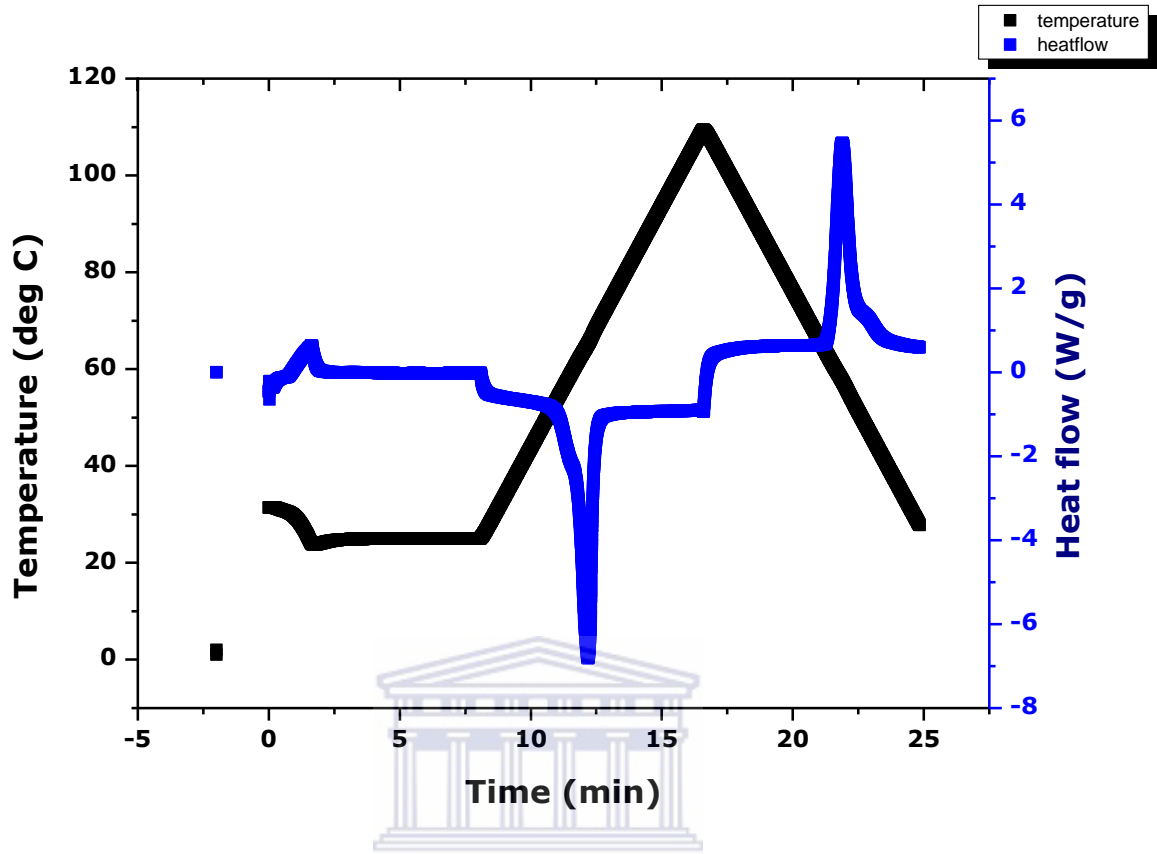
Figure 5.12: HRTEM for a single nanoplate and identification of two phases probably M1 and M2 low temperature a)Electron diffraction pattern in VO$_2$(M) with a zone of reflecting planes of [0$\bar{1}$2]. b)DSC curves ofVO$_2$ monoclinic nanomaterials versus time c) and temperature d)

The mechanical strength and ductility of structural materials is controlled by defects that determine dislocation migration.
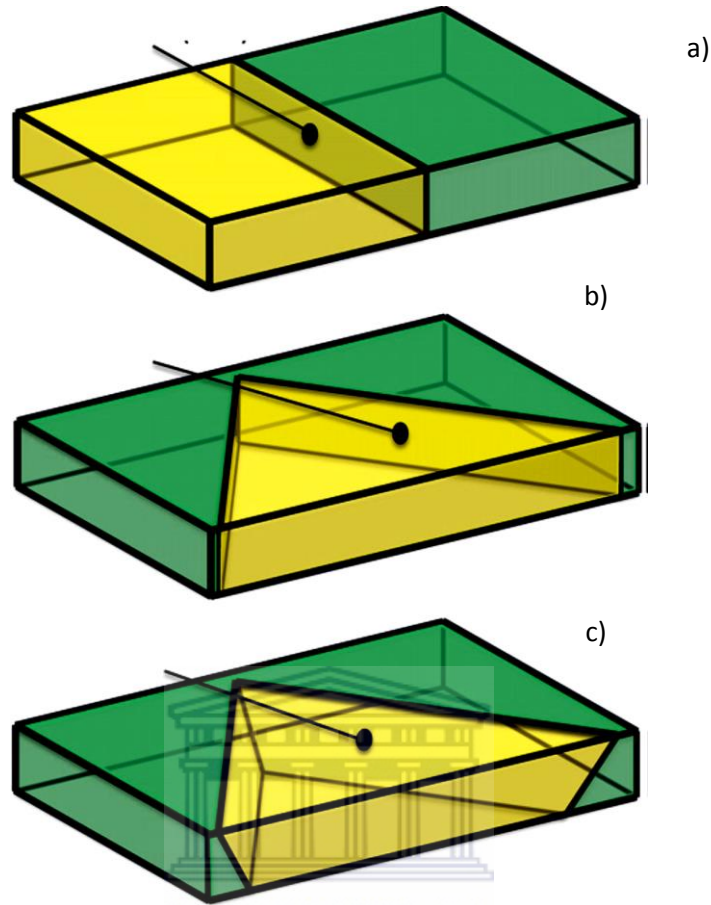
Figure 5.13: Possible geometries for VO_2 domains and interfaces during phase coexistence of metal and insulating M2 phases a) Bamboo morphology b) triangular domains with interface perpendicular to the surface, c) triangular domains with interface planes tilted at an oblique angle. [27]

Advances semiconductors devices enhance their carrier mobility through nanoscale strain gradients. In strongly electrons system such as VO_2, local phase coexistence and competition give rise to exotic macroscopic electronic properties such as colossal magnetoresistance, or multiferroic domains. Budai et al [26] shows that for the common materials, inhomogenous local interactions give fundamental intriguing and technologically useful physical phenomena. Hence high resolution material characterization tools are increasingly needed to explore and understand issues related to synthesis and processing, structure property relations and testing theoretical models

for nanoscale and nanostructured materials. Figure 5.13 present different types of morphology of VO_2 that we can found in the literature but the most abundant was found to be the bamboo morphology with the interface boundaries perpendicular to the c-axis of the material and presents the highest mismatch between atomic planes which is opposite in triangular shapes associated with the lattice strain energy. It was hypothesized that nanowires with small cross section present minimal interfacial energy by small area interfaces perpendicular to the nanowire axis. Also the large sample cross section favor the bamboo structure R//M1 or M2 which is consistent with a preference for stable interfaces with small lattice distortions as well a preference for minimum boundary area. By Hu et al. [27], the coexistence of M1, M2 and R while heating is the result of minimizing the system energy when subjected to external strain.

Table 5.2 Enthalpy of crystallization and fusion for VO_2 calculated by determining the area under Gauss fitting plot.

	Area	Enthalpy J/g	Peak Positions	Width	Height
Cooldown	-82.59391	82.59=1636cal/mol	57.60343	-5.77087	5.46528
Heating up	-104.31404	104.31= 2066 cal/mol	65.19992	4.83106	-6.81642

Considerable challenges exist in engineering the MIT of VO_2 bulk or thin films for different applications. It was demonstrated quantitatively that the strain stabilize the coexistence of both structures due to small perturbation which is the local minimum for VO_2 whose free energy is slightly higher than that of M1 at room temperature and pressure. Lattice strain, if tuned continuously, would be a sensitive means to shed light on the origin of the phase inhomogeneity. In contrast to conventional materials, where elastic deformation causes continuous, minor variations in material properties, lattice strain has profound influence on the electrical, optical, and magnetic properties of correlated electron materials (CEMs) through coupling between the charge, spin, and

orbital degrees of freedom of electrons. If phase inhomogeneity is absent in strain-free, single-crystal specimens, but can be introduced and modulated by external strain, it would then be possible to eliminate or strain engineer the inhomogeneity and domains in CEMs for nanoscale device applications. Fitting the experimental data we obtain the stress and plot the limit boundaries separating the monoclinic and insulator phase in the 6-T_c phase diagram through the equation. In the stress–temperature phase diagram, the rate at which the transition temperature T_C is modified by the uniaxial stress can be given by the Clausius–Clapeyron equation as:

$$\frac{dT_c}{d6} = \frac{\varepsilon_o T_c^o}{\Delta H}$$

$Eq.\,5.9$

Where the new transformation temperature $T`_c$ under uniaxial stress is given by:

$$T`_c = T_c^0\left(1 + \frac{6\varepsilon_o}{\Delta H}\right)$$

$Eq.\,5.10$

Where ΔH *is* the latent heat of transition, ε_o is the strain expansion along the $c-$ axis, T_c^o corresponds to the transition temperature of the sample ($T_c^0 = 341K$.) the latent heat has been determined as 2000 cal/mol and 1600 cal/mol upon heating and cooling respectively which is consistent with the literature data obtained 1025cal/mol-1200 cal/mol. If we consider the minimum strain to induce the M2 phase is 0.01GPa [19] where the elastic energy of internal stresses arises in the formation of a macroscopic equilibrium inclusion. The necessary condition for the transformation from one phase to another with coherent phases with presence of external field is generally given by:

$$\Delta\emptyset + e(\widehat{\varepsilon(\sigma)}, \widehat{S_1 S_2}) \le 0$$

$Eq.\,5.11$

Where $\Delta\emptyset$ the Gibbs is free energy of phases 1 and 2 and $\widehat{S_1 S_2}$ is the compliances of the initial and product phases respectively. The phase transformation temperature of the high-temperature phase lies below the phase equilibrium temperature; while that of the

158

low-temperature phase lies above it [28]. In reality the transformation from one phase to another usually proceeds in reaching some deviation from the phase equilibrium. This deviation determines a line of onset of transformation, or a transformation line which corresponds to the limit of stability of the initial phase with respect to the formation of the first fraction of the product phase. For each phase the latent heat transformation is different. Assuming the latent heat of transformation R →M1 is different with the one R →M2 and M2→M1 and the different stress value obtained according to Aizu are given. See figure 5.14 a) and 5.14 b).

$$e_{11} = -0.00543 = e_{22};$$ *Eq.5.12*

$$e_{33} = 0.0019.$$ *Eq.5 .13*

a)

b)
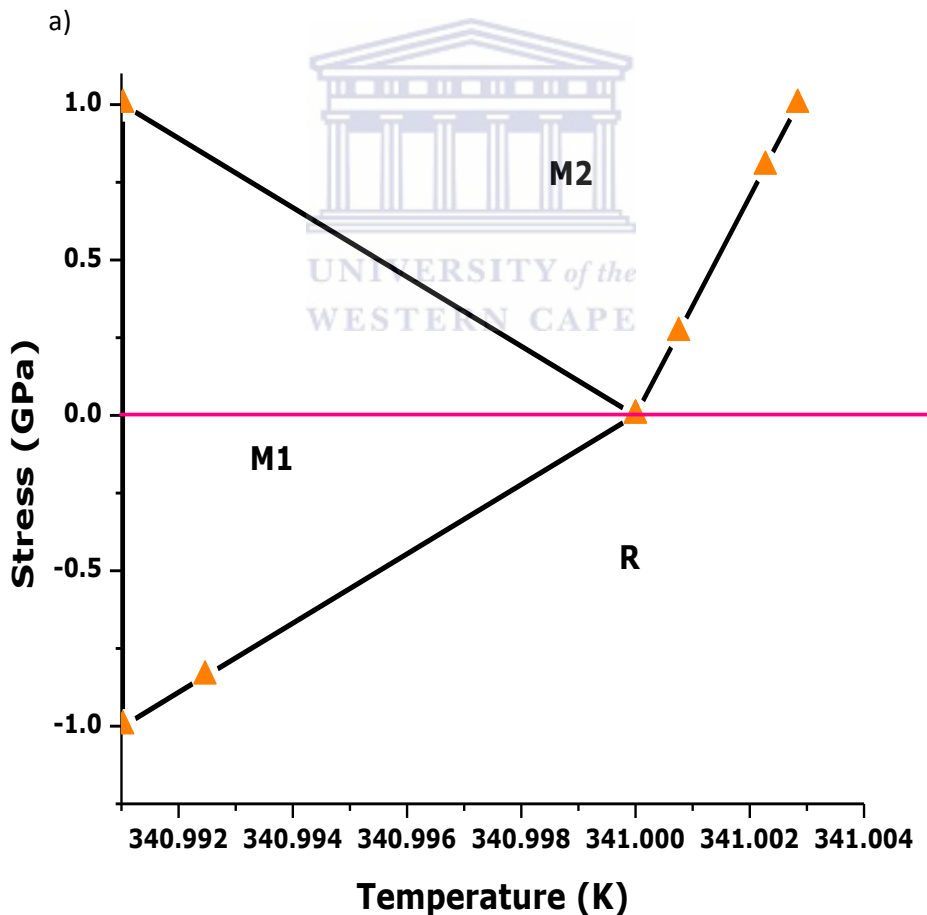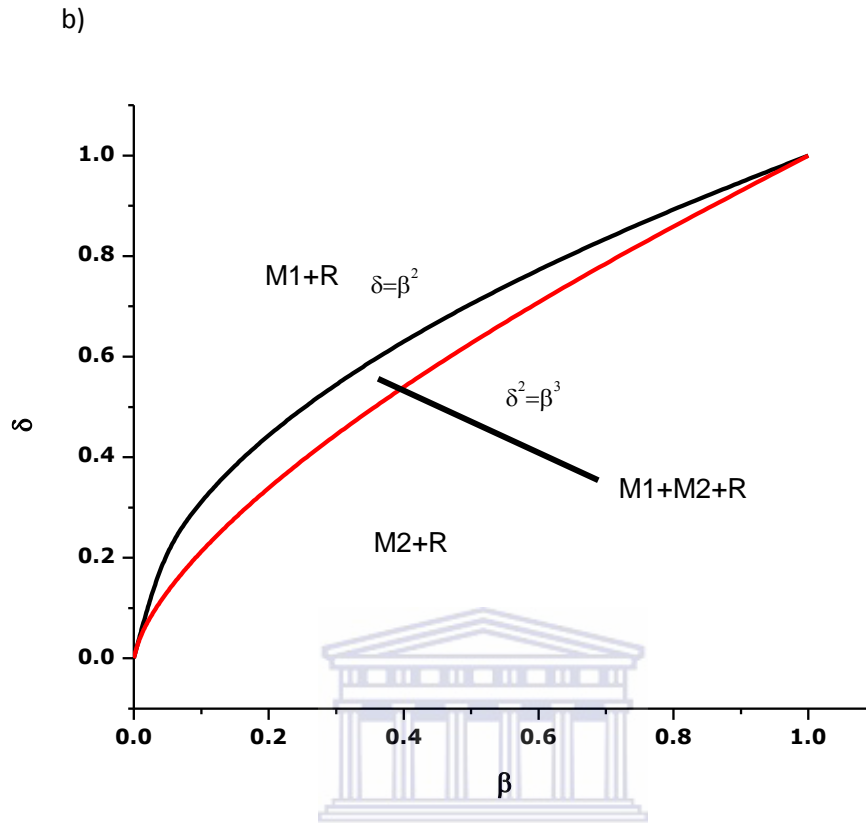
Figure 5.14: x_3 uniaxial stress versus transformation temperature in VO_2 single crystal.a) and b).

For a large range of applied stresses, from $\sigma_c = 0$ to $\sigma < 0$ the first order line transition phase separates the Rutile phase from the M1 phase with disappearance of the M2 phase. For $\sigma = 0.01$ down to 0, a first order line separates M1 phase to M2 phase. The phase diagram is easily interpreted as a competition between natural ordering along [110]. For $\sigma < 0$ the stress is too small to compete and only perturbs the normal ordering slightly. For $\sigma > 0$ the stress wins over the natural ordering.The point $\sigma = 0$ terminates the line of continuous phase transition and is known as a tricritical point. Rice at al. [24] presented the origin of M2 phase as due to the symmetry-breaking uniaxial stress applied in the $[110]_R$ direction. Zhang S et al. further showed that the M2 phase was observed competing with M1 in the VO_2 nanobeams as part of the heterophase domain

structure [29]. This phenomenon was ascribed to the surface stress effects. This is in accordance with our finding. In a ferroelectric transformation the S1 and S2 states can be seen as a small distortion caused by slight displacements of the atoms of the parent phase. The spontaneous strain characterizes the distortion of each orientation state relative to the prototype structure. The second rank strain tensor for monoclinic symmetry for a single orientation state (S1) is given by:

$$e_{ij}(S_1) = \begin{pmatrix} \epsilon_{11} & \epsilon_{12} & 0 \\ \epsilon_{21} & \epsilon_{22} & 0 \\ 0 & 0 & \epsilon_{33} \end{pmatrix} \qquad Eq.5.13$$

$e_{ij}S(2)$ is related to $e_{ij}S(1)$ by $e_{ij}S(2)$ by $e_{ij}S(2) = Re_{ij}S(1) \ R^T$, where R and RT are the 90°rotation matrix around the b axis of the monoclinic structure and its transpose. Following Schlenker [30] the strain components can be calculated as follows according to the basis Bi, i = 0, 1 before and after the deformation:

$$e_1 = e_{11} = \left(\frac{a_0 sin\beta_0 \sin \gamma *_0}{a_1 \sin \beta_1 \sin \gamma *_1}\right) - 1 \qquad Eq.\,5.14$$

$$e_2 = e_{22} = \left(\frac{b_0 \sin \alpha_0}{b_1 \sin \alpha_1}\right) - 1 \qquad Eq.\,5.15$$

$$e_3 = e_{33} = \left(\frac{c_0}{c_1}\right) - 1 \qquad Eq.\,5.16$$

$$e_{12} = e_{21} = \frac{1}{2\left(\frac{a_0 sin\beta_0 \cos \gamma *_0}{a_1 \sin \beta_1 \sin \gamma *_1} - \frac{b_0 sin\alpha_0 \cos \gamma *_1}{b_1 \sin \alpha_1 \sin \gamma *_1}\right) Eq} \qquad Eq.\,5.17$$

$$e_{13} = e_{31} = 1/2\left[\left(\frac{c_0 \cos \beta_1}{c_1 \sin \beta_1 \sin \gamma *_1} + \frac{\cos \gamma *_1}{\sin \gamma *_1}\right) \times \left(\frac{c_0 cos\alpha_1}{c_1 \sin \alpha_1} - \frac{b_0 cos\alpha_0}{b_1 \sin \alpha_1}\right) - \left(\frac{a_0 cos\beta_0}{a_1 \sin \beta_1 \sin \gamma *_1}\right)\right] \qquad Eq.5.18$$

$$e_{23} = e_{32} = \frac{1}{2\left(\frac{c_0 \cos \alpha_1}{c_1 \sin \alpha_1} - \frac{b_0 cos\alpha_0}{b_1 \sin \alpha_1}\right) Eq} \qquad Eq.\,5.19$$

The transition from the high-temperature space group P4/mmm to the low-symmetry subgroup P2/c involves no loss of translational symmetry and is due solely to the critical behavior of phonons associated with the centre (Γpoint) of the Brillouin zone. The spontaneous strain tensor can be expressed with no effect of shear compression we have [31].

$$e_s = \sqrt{1/2}(|e_{22} - e_{11}|) \qquad\qquad Eq.5.20$$

X-ray diffraction peaks are broadened by small grain-size and by lattice distortions caused by lattice defects. Some typical lattice defects are: i) dislocations, ii) unrelaxed misfits between coherent phases, iii) severely distorted grain boundaries in nanocrystalline materials, iv) strains between coherent sheets, especially in strained layer structures, v) point defects, vi) second phase particles or inclusions, vii) concentration gradients in non-equilibrium multiphase materials or viii) stacking faults, etc. Stacking faults are a peculiar kind of lattice defect acting as boundaries in certain crystallographic directions, thus creating smaller 'particle size' in these directions. This part of these defects, if separable at all, causes 'size broadening' without 'strain broadening'. The bounding partial dislocations, especially if they are in the interior of the crystallite, however, correspond to the first class of defects causing 'strain broadening [32]. We can see that strained regions are present. During heating heat monoclinic, domains started to nucleate where the stress was most compressive. These domains continue to grow and expand with increasing temperature. Uniaxial external stress was used to engineer MIT domains along nanoplatelets of VO_2, and to observe the Mott MIT at room temperature. The ability to engineer phase inhomogeneity and phase transitions with strain opens opportunities for designing and controlling functional domains of VO_2 for device and sensor applications. The latent heat obtained via DSC experiment on cooling and heating cycle allows us to deduce that the phase transition is of first order according to the equation:

$$L = T \, \Delta S \qquad\qquad Eq.5.21$$

The interfacial effect was explored through the oxygen vacancies in nucleating the observed phase transformation by performing the first principles density functional calculations by Kannatassen et al. [33]. He presented the origin of phase transition of nanoparticles VO_2 as the nucleation of specific point defects of oxygen vacancy present at grain boundaries. This is in accordance with our material where the metallic domains nucleate at specific points defects of the insulator material. The in situ temperature controlled XRD measurements on VO_2 nanoparticules prepared by hydrothermolysis method were studied. Appearance of an intermediate insulator phase was observed across MIT. Considering previous reports on monoclinic M2 phase which is caused by stress, we discuss the mechanism of the intermediate phase formation in our material. The existence of an intermediate crystalline phase with room temperature insulator phase and high temperature metallic phase across MIT in VO_2 could be of relevance to understand structural contributions to the phase transition dynamics. We observe that all VO_2 crystals are stabilized in either the M1 or M2 insulating phase at around 65 deg C which appears to be a consequence of different strain related to variations in growth conditions. Insulating domains in crystals initially in the M1 phase at room temperature are found to convert to the M2 phase during the MIT prior to the formation of the fully metallic state. Crystals initially in the M2 phase convert directly via the formation and growth of periodic R domains in a similar fashion but at slightly higher temperatures compared to the M1 case. See figure 5.13. Budai et al. [26] shows that epitaxial VO_2 films incorporate a wide range of inhomogeneous domain sizes and strain distributions that give rise to broad transitions where the material consist of complex mixture of distorted rutile, M1 and M2 domains and twins with a variety of orientations. Confirmed by Qazilbash et al. [34], nanoscale metallic puddles are local rutile domains created by strain interactions with surrounding distorted monoclinic domains. At the MIT the rutile lattice instability leads to distortions associated to zone boundary rutile point in the primitive tetragonal Brillouin zone. Short and long wavelength distortions reduce the point symmetry of the lattice and at the Brillouin zone center respectively. The strong coupling between zone center and zone boundary distortions are restricted by

external stresses which influence how exactly the transformation will occur at the zone-boundary and the resulting value of the zone parameter. Zhao et al. [35] consider that the material VO_2 during the θ-2θ scan of the sample for two closest Bragg peaks presents twinning domains formation in the sample. This latter is expected if a structure phase transition take place from a space group to another less symmetric space group. This was explained as the removal of the degeneracy between the equivalent directions in tetragonal by the monoclinic structure.
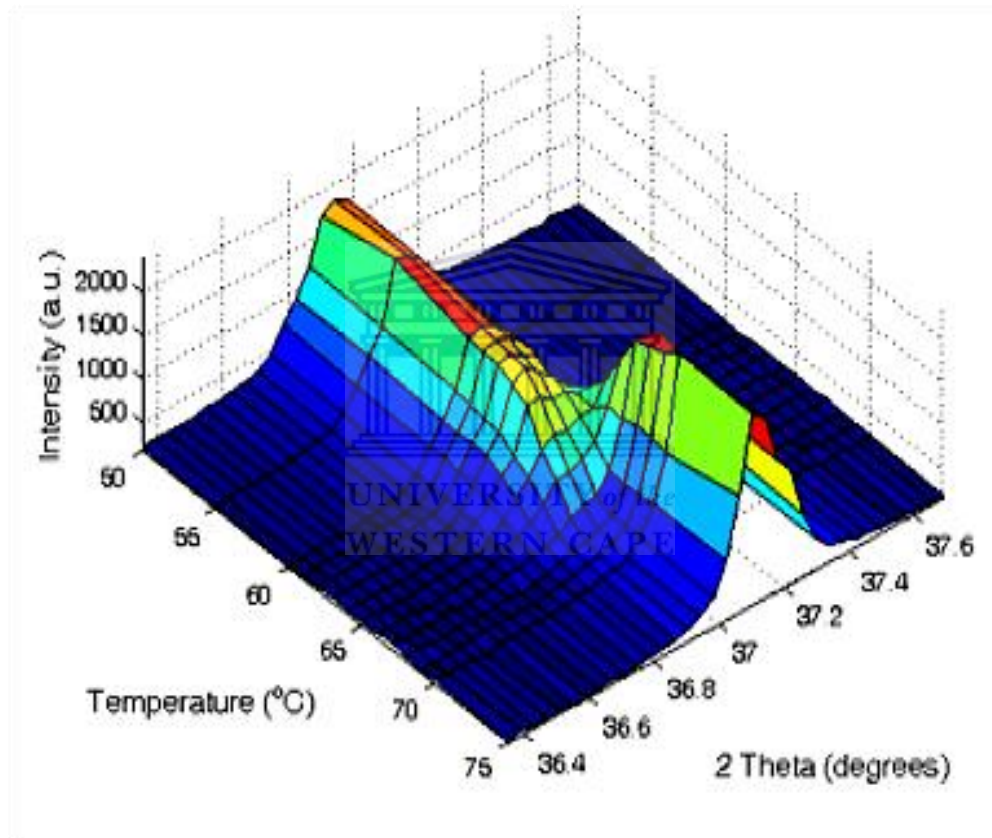
Figure 5.15: Evolution of monoclinic Bragg peak (-211) versus temperature in the range of 50˚ C to 75˚ C with presence of nucleation, coexistence phases and complete structure apparition at high temperature.

It is known that the M2 phase, which in the unstrained material has a free energy very close to that of M1, can be stabilized by doping or compressive uniaxial stress. The relationship between the crystal lattices of the different phases of VO_2 can be understood in terms of the displacement and pairing of two interpenetrating

sublattices, each composed of chains of V atoms oriented along the crystallographic. High resolution X-ray diffraction experiments have shown that peak profiles corresponding to plane surfaces either perpendicular or parallel to the tensile or compressive axis of plastically deformed metals or alloys reveal characteristically asymmetric shapes. In the case of tensile deformation the intensity of the diffraction peaks decreases at a slower or faster rate on the smaller or larger diffraction angle side of profiles corresponding to surfaces perpendicular (axial case) or parallel (side case) to the tensile direction, respectively. Two alternative interpretations have been suggested such as heterogeneous dislocation distributions and dislocation manifold that can have a net dipole polarization.
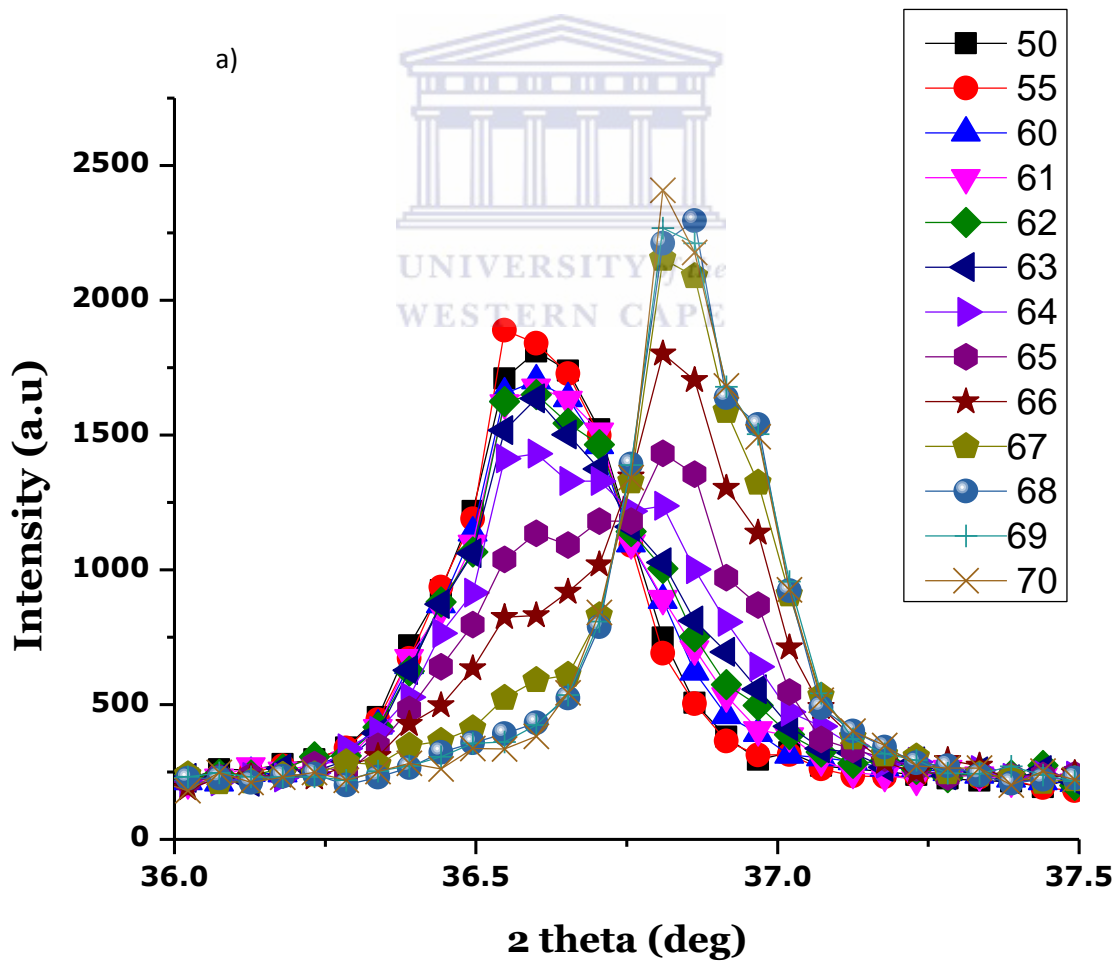
b)
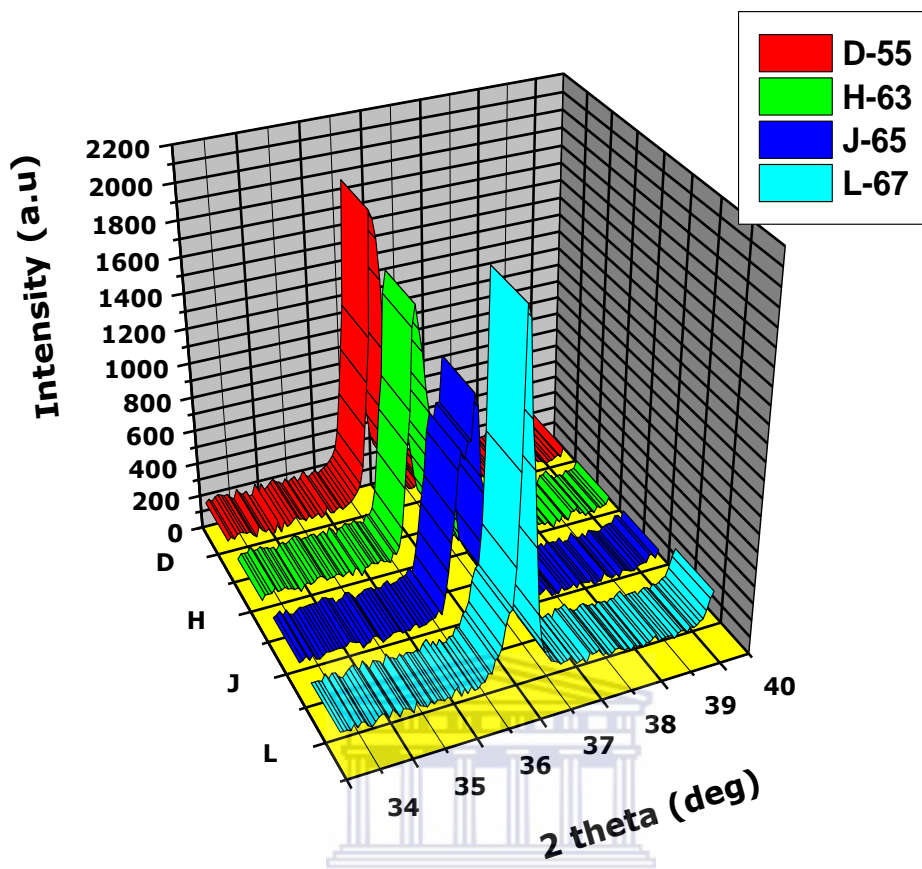
Figure 5.16: Changes in XRD monoclinic (200) pattern of the VO$_2$ monoclinic platelet from 50deg C towards 70 deg C a) and b).

The heating of the samples during the x-ray measurement were performed using a Peltier thermoelectric heat pump with a regulation module of ~0.1°C. The ability to automate the scattering intensity and particle size trend measurements is a major advantage in many applications in this set up. Processes as aggregation, solubilisation, sedimentation and change in molecular conformation can be followed by the scattering of the intensity of the samples as a function of temperature. Figure 5.15 a) depicts the evolution of the major Bragg peaks versus temperature. Monoclinic Bragg peaks (D, H) convertto tetragonal (L) through the intermediate phase (J). See figure 5.15 b). More accurately, and in the range of 50 °C to 75 °C , the intensity of two different diffraction

peaks at 36.89 ° corresponding to (-211) monoclinic and his equivalent at ≈ 37.06° (101) were followed. The X-ray spectrum shows the shifting of the entire transition monoclinic-tetragonal with temperature. The evolution is continuous at the operational time scale. While there is net decrease of the monoclinic Bragg peak intensity (situated at about 36.89deg) with a steady increase of the intensity of the Bragg peak corresponding to the tetragonal peak located at about 37.06 deg. This trend concurs with Joyeeta et al's predictions [36]. The area under the monoclinic peak decreases as the tetragonal fraction grows. Both phases coexist in quasi equal fractions at around 65°C as substantiated by Figure 5.16. The VO_2 (M) nano-crystals are entirely tetragonal at 70°C. Naturally, the Bragg peak shift during the transition is attributed to thermal expansion and VO_2 lattice. It was observed that the shortening of one of the lattice parameter in the monoclinic phase bm indicates in-plane tensile strain for keeping unit cell volume constant [37]. Hence the lattice transformation started before the rapid decrease in resistance. This was attributed to the inhomogeneity of the material due to the presence of both non crystalline and non-stoichiometric phases in addition to the grain boundaries between VO_2 crystal grains confirmed with [38] who proves the nature of metallic phase transition by performing optical experiments with 15fs resolution and report an evidence of a limiting structural time scale for the formation of the metallic phase. Hence the evidence for a structurally mediated transition is suggestive of important band insulating character of monoclinic of VO_2 despite much faster hole doping into the correlated band. This suggests that VO_2 is more bandlike character. A Tselev et al. [39] show that the competition of two monoclinic phases M1 and M2 is purely lattice symmetry driven where M1 is due to pairing of vanadium atoms which contribute to the formation of band gap through a Peierls mechanism and M2 phase is a pure Mott insulator structure.
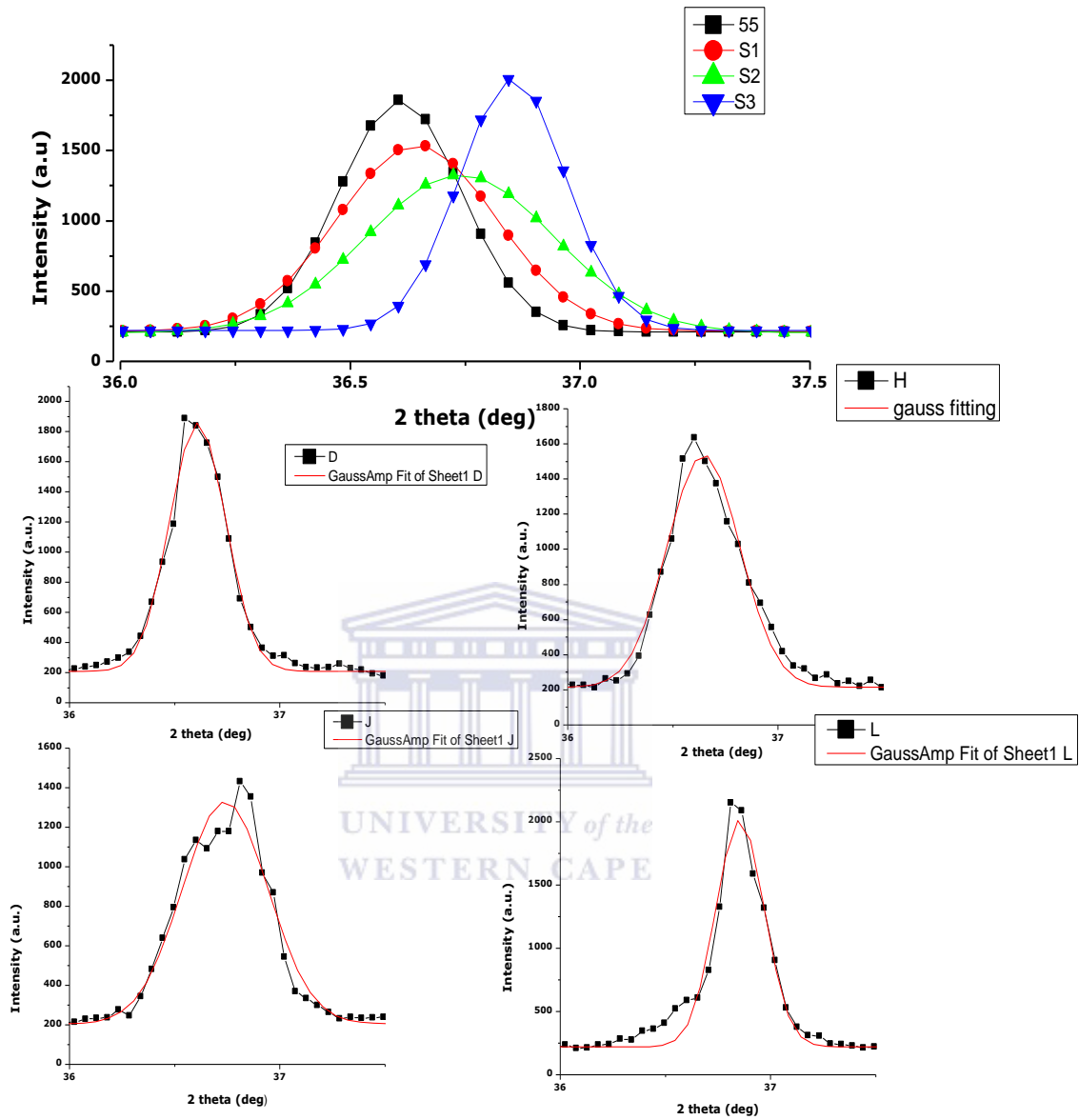
Figure 5.17: Gaussian fit plot at different temperature of the evolution of different reflections Bragg peaks angles it is clearly shown that the coexistence phase is maximized at 65 deg C. (J)

According to Tsung-Han et al. [40] the monoclinic to tetragonal phase transformation is a diffusionless first-order phase transformation where it is assumed that the nucleation rather than the propagation controls the overall kinetics of phase transformation control by grain boundary nucleation effect. The grain boundary energy is function of the

misorientation between the grains which are nucleation sites due to their high energy related to the grain boundary angle. We labeled three curves S1, S2 and S3 corresponding for each phase M1, M2 and R respectively at 36.64 º C, 36.74 º C and 36.85 ºC. In addition, the Gaussian curve fittings performed here indicates the presence of an intermediate phase different from M1 and R phases across MIT. S3 increased rapidly from room temperature and became dominant at a temperature of 340 K, while S1 decreased gradually until 340K, with rapid decrease in the range 336K-340K. At temperature of 343 K, S1 disappeared and S2 remains constant. On the other hand, S3 revealed apparent increase from 334 K and became dominant after 340 K, where metallic phase appears to be dominant than insulating phase and is more dominant comparatively to the intermediate phase M2.The changes in the phase ratio of S1 and S3 show validity of assignments of them as insulating monoclinic M1phase and metallic rutile phase R, respectively. Since the intermediate S2 is dominant phase in the temperature range from 334–340 K with insulator property, we speculate that this phase can be assigned to monoclinic M2 phase shown in Figure 5.18 which has insulating property basically.
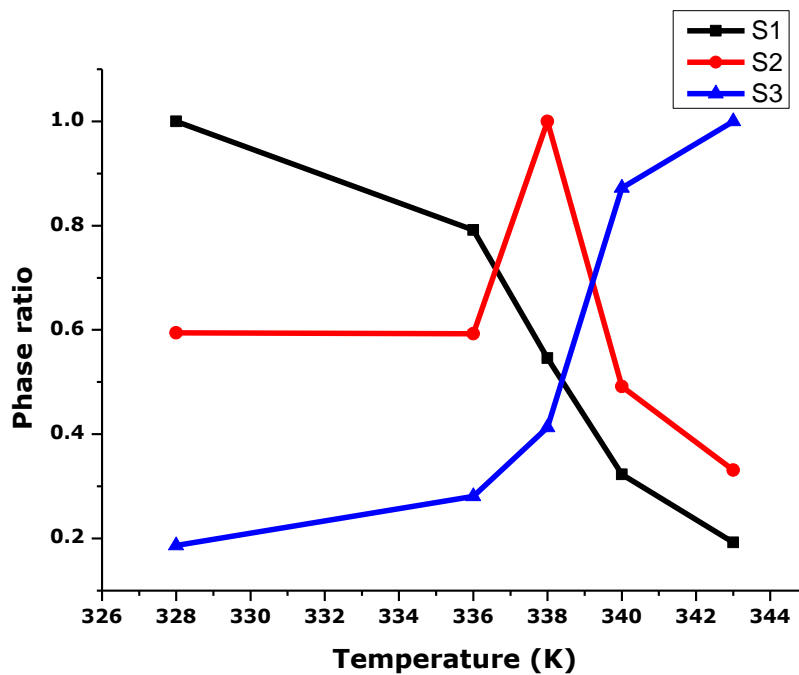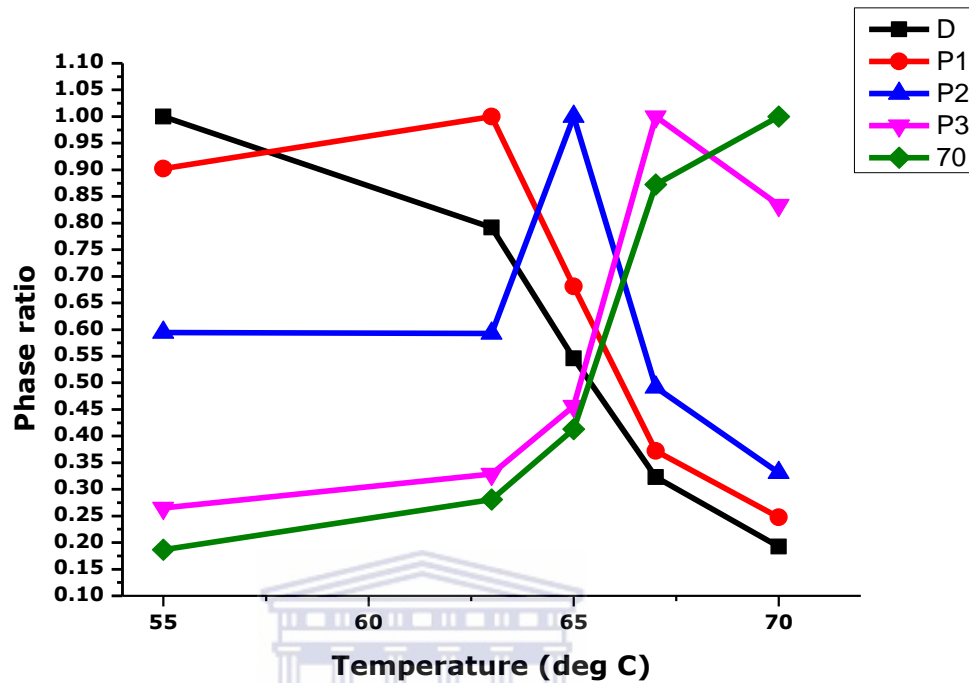
Figure 5.18: Composition ratios of S1, S2, and S3 against temperature. Each ratio is calculated by Gaussian curve area.

It is noted that M2 remained even at temperature higher than 340K. Recently, the intermediate phase has been noted by authors in relation with discussion on the MIT of VO_2 films. HuaGuo et al.[18] studied in situ VO_2 nanowires by push-to-pull microelectromechanical device to realize quantitative tensile analysis in a transmission electron microscope and a synchrotron X-ray microdiffraction beamline. They observed single pinning and depinning events of M1-M2 domain walls in the superelastic regime, allowing for evaluation of the domain wall pinning potential energy. Also Jones et al. [41] studied the MIT and associated nanodomain formation in individual VO_2 microcrystals subject to substrate stress. They deduce that the MIT is influenced by the competition between the R, M1, and M2 crystal phases with their different lattice constants subjected to the external substrate-induced stress. They employ symmetry-selective polarization Raman spectroscopy to identify crystals that are strain-stabilized

170

in either the monoclinic M1 or M2 insulating phase at room-temperature. But in their case the percolative model did not exist. In accordance with Sooran Kim et al, they explore the driving mechanisms of the metal-insulator transition (MIT) and the structural transition in VO$_2$ and investigated phonon dispersions of rutile VO$_2$ (R-VO$_2$) in the DFT and the DFT+U (U: Coulomb correlation) band calculations and found that Coulomb correlation effect plays an essential role of assisting the Peierls transition in R-VO$_2$ predicting a new phase Mx monoclinic structure but with metallic nature [42]. Fan and al. [43] measure the force displacement of the VO$_2$nanobeams showing nonlinearity that signifies activation and expansion of domains of a new phase out of the old one describing the first-order phase transition. X-ray microdiffraction measurements from individual VO$_2$ microcrystals reveal a strong link between external strain and local phase stability, domain orientations and interfaces. Recently Bongjin et al. [44] shows that the MIT in a macroscopic VO$_2$ crystal occurs due to the Joule heating effect with self-switching effect cause by large asymmetry in heating power just before and after the MIT maintaining the crystal temperature at MIT temperature. They assume that the heat obtained in the overall VO$_2$ crystals is mainly due to the balance between resistive Joule heat and heat loss from the crystals to the environment via heat conduction expressed as a simple heat conduction as:

$$\frac{dQ}{dt} = \frac{V^2{}_C}{R_C} - k(T_C - T_A) \qquad\qquad Eq.\,5.22$$

Where the crystal temperature Tc is expressed as:

$$T_C = T_A + \frac{V^2{}_C}{kR_C} \qquad\qquad Eq.\,5.23$$

And they demonstrate that the conducting path for electrons is dominated by the bulk material while there is a coexistence of insulator and metallic phases with a partially insulating surface skin layer and they attributed the shift of the phase boundary as evidence of thermal fluctuations between surface skin layer and bulk layer.

5.2.1 Theory of Landau

The displacements of the atoms which are associated with the breaking of the symmetry are characteristic of the distorted phase, and, furthermore, at a continuous phase transition decrease continuously to zero as the high-symmetry phase are approached. In a single domain of the distorted phase, the displacements in any one unit cell have a definite relationship to those occurring in any other unit cell [45]. The simplest example of a structural phase transition occurs when the distortions may be described by a single normal mode; the amplitude of the distortion is then given by the order parameter:

$$Qo = N^{-\frac{1}{2}}\langle Q(q_s j)\rangle \qquad\qquad Eq.5.24$$

Where $(q_s j)$ is the particular normal mode which describes the atomic displacementsin the distorted phase, and the factor of $N^{-\frac{1}{2}}$ is introduced so that Q_0 is independent of the crystal size. If the phase transition is continuous, the order parameter will approach zero as T~Tc and is assumed to be given by a power law:

$$Q_0 \sim (Tc - T)^\beta \qquad\qquad Eq.5.25$$

Where β is known as the critical exponent for the order parameter. In classical theories of phase transitions, such as those discussed and the exponent β=0.5, while in practice it varies between 0.25 and 0.5. Evidence in the tricritical behavior of the material is shown by the linearity temperature dependence of integrated intensities of elastic scattering. See figure 4.19. Landau assumes that the free energy of one unit cell of the crystal may be expanded in a power series in the order parameter:

$$G = G_o + \frac{1}{2}rQ^2 + dQ^3 + uQ^4 \qquad\qquad Eq.5.26$$

Where the coefficients may be function of the temperature. The continuous phase transition and first order transitions are mainly described by the equation:

$$G = G_o + \frac{1}{2}a(T - Tc)Q^2 + uQ^4 + hQ^6 + \cdots \qquad\qquad Eq.5.27$$

G_o describes the free energy for the disordered state. A second order phase transition is obtained for temperature below Tc this is due to a non- zero equilibrium value of the order parameter that minimizes the free energy. The free energy of the ordered phase

decreases below that of the disordered phase. The Landau theory describes also the first order transition at temperature Tc where the order parameter appears discontinuous describing the association of a latent heat with the phase transition. This is due to the quartic of the parameter. These results are in agreement with the DSC experiment and diagram phase of the material obtained. The landau expansion at this point is obtained so that the order parameter is given by:

$$Q_0^4 = \frac{a}{6h}(T_c - T) \qquad\qquad Eq.\,5.28$$

The possible atomic displacements are generally expressed in terms of linear combinations of n normal modes coordinates where n represents the number of components of the order parameter (order parameter dimensionality). In the high symmetry phase all the normal modes have the same frequency while in the distorted phase, the order parameter is expressed as:

$$Q_i = Q_0 \xi_i, \text{ Where } \sum_i \xi_i^2 = 1. \qquad\qquad Eq.5.29$$

c)
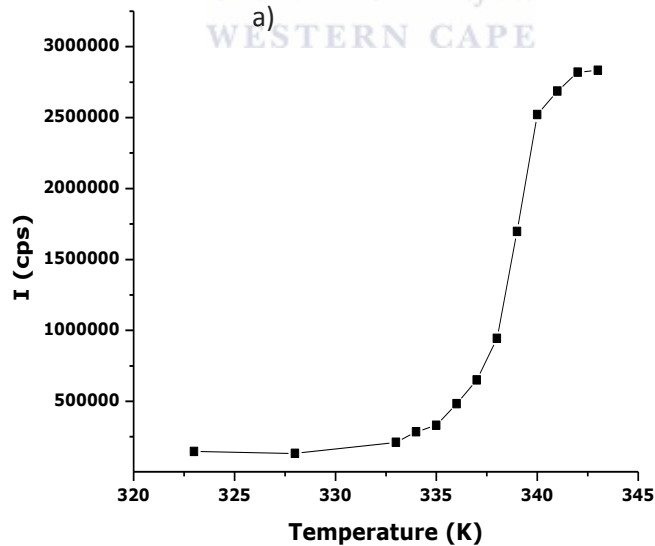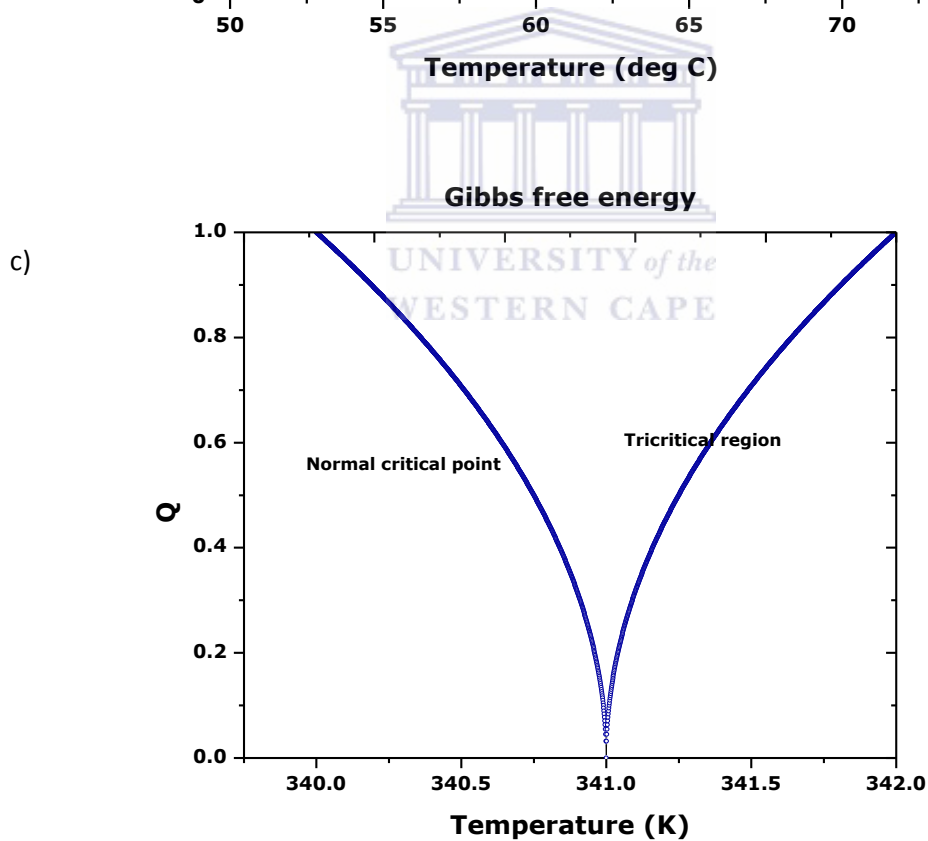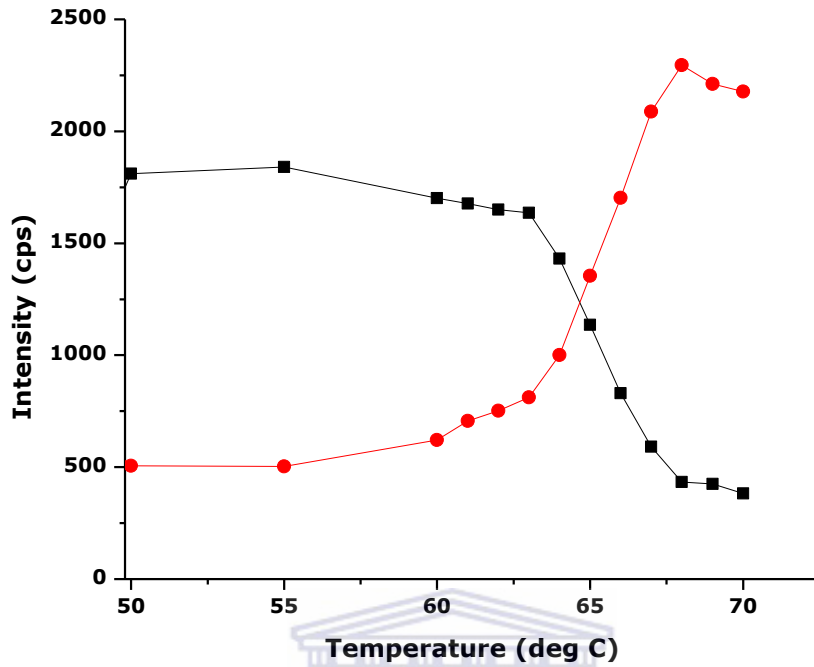
Figure 5.19: a) Temperature variation of the square of the intensity of elastic scattering of the (-211) reflection, tetragonal and monoclinic Bragg evolution b) and c) order parameter versus temperature.

Low temperature of M1 and M2 with predominance of M1 phase can also be explored via Raman spectroscopy. Structural information of the material was obtained by excitation of continuous wave laser light with a 514.5 nm line from argon ion. It is possible to identify the in situ molecule and to determine the amount of the molecule present in the sample. Most molecules at rest prior to interaction with the laser and at room temperature are likely to be in the ground vibrational state (lowest energy). Since the virtual states are not real states of the molecule but are created when the laser interacts with the electrons and causes polarization, the energy of these states is determined by the frequency of the light source used. The Rayleigh process will be the most intense process since most photons scatter this way. It does not involve any energy change and consequently the light returns to the same energy state. The Raman scattering process from the ground vibrational state m leads to absorption of energy by the molecule and its promotion to a higher energy excited vibrational state (n). This called Stokes vibration. The power of the laser was about 100mW. The T64000 was operated in single spectrograph mode with the 1800 lines/mm grating and a 100x objective on the microscope. $VO_2(M)$ raman results has prominent phonons peaks at 144 cm^{-1}, 194 cm^{-1}, 225 cm^{-1}, 387cm^{-1} and 617 cm^{-1}. Our nanoplateletsVO_2 (M) isolated in KBr present two prominent phonons peaks at around 196 cm^{-1} and 617cm^{-1} characteristics of M1 phase. We can see that the intermediate phase is completely diminished with the presence of KBr which has been used as host materials for infrared emission due to its lower maximum phonon energy 168 cm^{-1} favoring the suppression of nonradioactive losses improving the luminescence of optically active dopants by making the sample homogenous. In addition, KBr has been considered as a potential material for infrared emission due to its unique properties, which include being easy to crystallize, wide IR transparency and high refractive indexes [46].
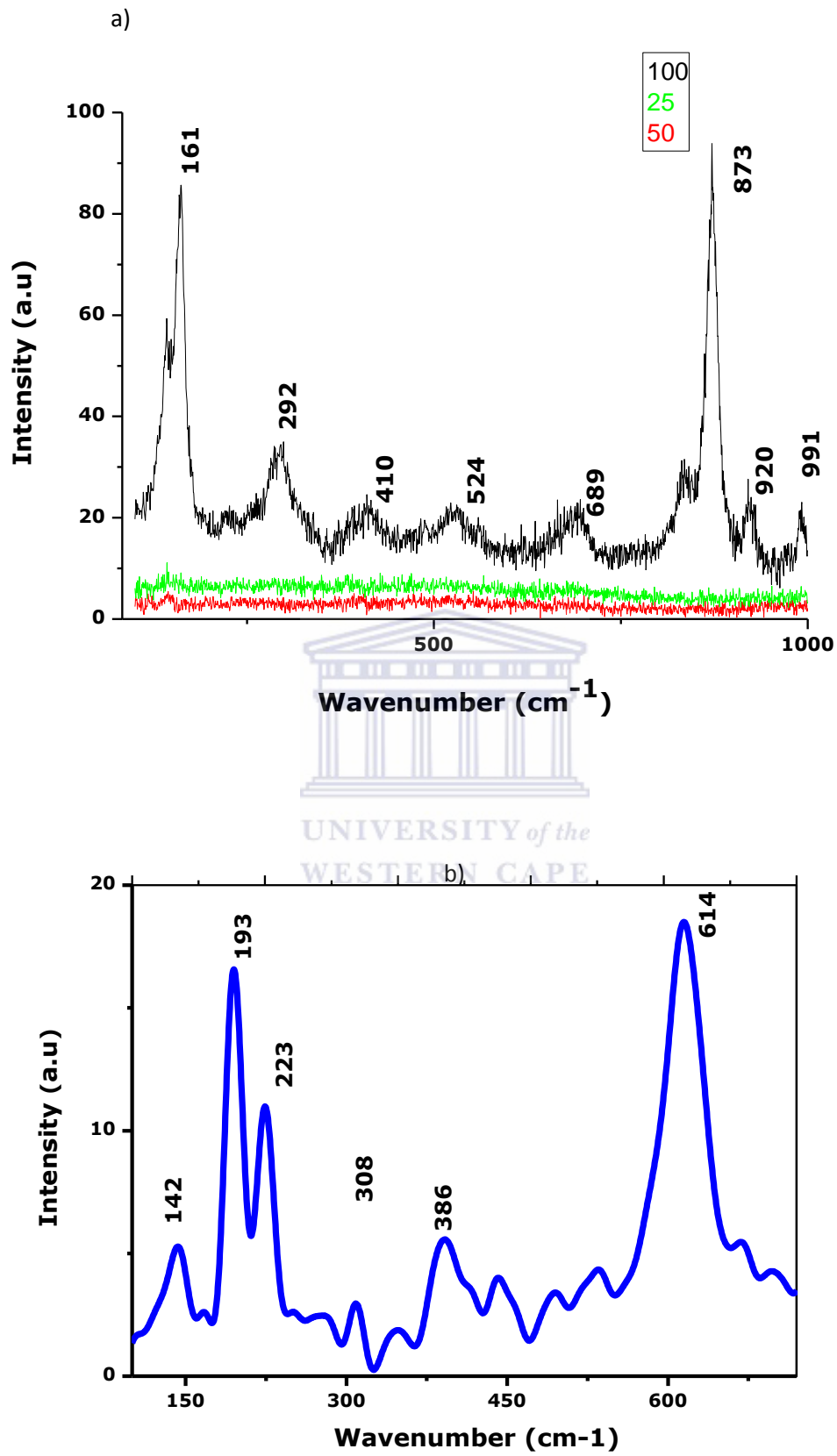
Figure 5.20: Raman spectra collected for VO$_2$ as synthesized a) and dispersed in KBr b).

Also, we notice that due to some inhomogeneities of the nanostructure, which remain strong, there is some presence of vanadium pentoxide(V_2O_5) raman line shown in the figure 4.20 a) with specific peaks at 991cm^{-1} [47-48] 690 cm^{-1},527 cm^{-1}, 409 cm^{-1} and 294 cm^{-1}. Although the stoichiometry was found to be pure VO_2 (M), high resolution transmission electron microscopy and ED shows that it possess a metastable monoclinic structure that we assigned the two pronounced peaks at 873 and 162 cm^{-1}. The 144cm^{-1} and 194cm^{-1} are assigned to the bending vibration modes of (V_2O_2) chains. They arise from the deformation of the bond between different molecular units in the layer planes and strongly associated with the oxide layered structure. The peaks located at 293cm^{-1} and at 411cm^{-1} are due to the bending vibrations of the V=O bonds and those located at 306 cm^{-1} and 487cm^{-1}are bending modes of the triply coordinated oxygen bonds and bridging V-O-V respectively peculiar to VO_2. The 529cm^{-1}-531cm^{-1} is the stretching modes of the triply coordinated oxygen involve in the O edge share atoms in common to three pyramids. The 693 cm^{-1} originated in the stretching vibration of the doubly coordinated oxygen involve in corner share atom to two pyramids. The 993 cm^{-1}-997 cm^{-1} is the stretching mode of the terminal unshared oxygen V=O. Recent experiments have shown that the Raman spectrum of an oxide material can be greatly affected by deviations in oxygen stoichiometry. It is evident that the results presented here and those of Parker [49] are substantially different from the results of Chase and Srivastava. See table 5.3 and perhaps the differences may be attributed to an oxygen deficiency in the VO_2crystals which favour the presence of M2 phase coexisting with M1 insulator phase. The x-ray and raman measurements performed on our VO_2 single crystals indicate that the samples are stoichiometric VO_2 with presence of M2 domains. Therefore, we can conclude that the spectrum obtained in this work would be the identifiable spectrum of stoichiometric VO_2 and M2 structure. Significant intensity variations for the high energy sharp peaks at different output power laser are obtained. The peaks are prominent for the highest power 100mW while it is very weak at 25mW and 50mW. The sample measured at low power excitation is very feeble (25mW and 50mW). This shows that strong resonance effects are taking place at 100mW excitation.

Table 5.3: Comparison of Raman peak positions measured in this work and the results of previous studies. The data in the columns labelled present work and other peaks V_2O_5 positions are determined from Figure 5.20 b) [49].

Raman modes of VO₂.	Assignment Raman frequency cm⁻¹	Present work		Srivastava and Chase	Aronov et al.
		VO_2	Other peaks cm⁻¹ V_2O_5		
–	142	144	158-162*		142
Ag	191	194	291-293	208	191
Ag	221	225	409-411	236	222
Ag	258		529-531		259
Ag	308		692-693		308
Ag	335		871-873*		335
Ag	392	387	923-925		389
Ag	497		993-997	450	497
Bg	594			655	
Ag	612	617		850	611

High-resolution XPS measurements were performed with a PHI 5000 Versaprobe – Scanning ESCA Microprobe spectrometer employing 100 µm 25 W 15 kV Al monochromatic x-ray beam. The resolution of this instrument has been determined to be 0.1eV after 30 cycles. The specimens were nanostructures VO_2 single crystals sputter for 2 min under Ar ion gun in the spectrometer vacuum of 10^{-7} Torr. It is well known that under typical XPS measuring conditions insulating and semiconducting samples become charged and the resulting peaks are shifted and broadened. Two phenomena can be observed during the experiment: absolute peaks positions and peak splitting. Charging effects broadened the spectra to such an extent that no direct evidence of

multiplet splitting could be obtained. The $2P_{1/2}$ and $2P_{3/2}$ peaks are separated by $3/2\ \xi_{2p}$ where ξ_{2p} is the spin-orbit coupling constant given by:

$$\xi_{2p} = \frac{-e}{2m^2c^2}\frac{1}{r}\frac{\partial V}{\partial r} \qquad\qquad Eq.5.30$$

The anomalous behavior of (2p) for the transition-series metals is very obvious for compounds which have been explained as exchange coupling between the unpaired 3d spin S and the $2P_{3/2}$ and $2P_{1/2}$ holes, with the highest-spin state in each case being pushed to the extremes of the multiplet pattern [50]. XPS binding energy difference, E $(2P_{1/2}) - E\ (2P_{3/2}) = \Delta E\ (2P)$ can be plotted against Z (atomic number) as:

$$\Delta Er\ (2p) = \ \Delta E\frac{(2p)z}{\Delta E}(2p)A_l\left(\frac{(Z-2)^4}{Z}\right) \qquad\qquad Eq.\,5.31$$

The sample under study is subjected to irradiation by a high energy X-ray source. The X-rays penetrate only 5 – 20 Å into the sample [51] allowing for surface analysis. As an atom absorbs the X-rays, the energy of the X-ray will cause a K-shell electron to be ejected. The ejected electron has a kinetic energy (KE) that is related to the energy of the incident beam (hv), the electron binding energy (BE), and the work function of the spectrometer (φ). The binding energy is calculated as:

$$BE = h\nu - KE - \varphi_{spec} \qquad\qquad Eq.\,5.32$$

BE is the electron binding energy. KE is the electron kinetic energy and φ_{spec} is the spectrometer work function. It was observed according to [52-53] that the material is composed of vanadium valence V+4 and V+5 states respectively at 515.15 eV (2p 3/2), 522.64 (2p 1/2) and 516.74 (2p 3/2), 524.92 (2p 1/2). See figure 5.21 and 5.22.
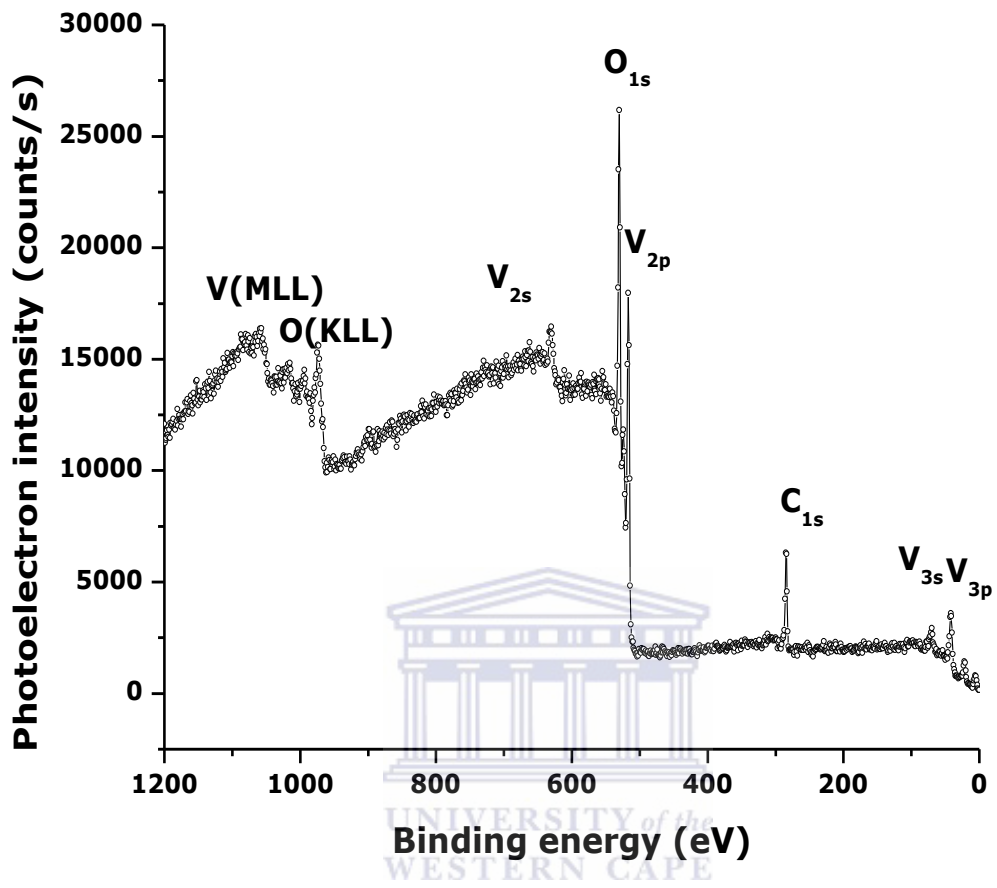
Figure 5.21: Wide scan spectra of VO_2 nanocrystals
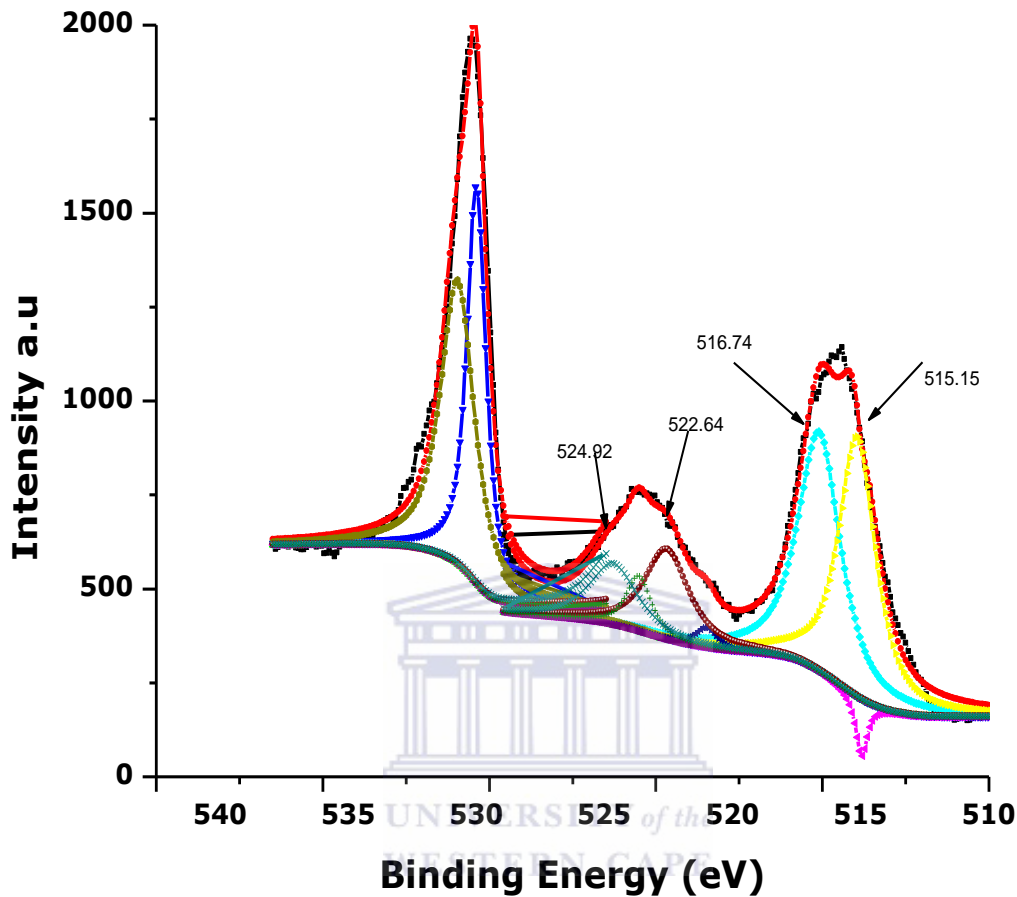
Figure 5.22: XPS measurements on VO_2 nanoparticles.

5.2.2 Conclusion

Taking advantage of the spontaneous strain associated with the structural change of the phase transition, a colossal thermal mechanical actuation in VO_2 nanoplatelet was reported, making them suitable for thermal sensors, energy transducers and actuators with unprecedented sensitivities.VO_2nanoplatelets`Structural Phase Transition was investigated by temperature-controlled XRD across MIT. We observed coexistence of an intermediate crystalline phase with room temperature insulator phase and high temperature metallic phase in nanostructures VO_2platelets. Gaussian curve fittings for measured XRD patterns revealed a significant contribution of the intermediate phase

covering wide temperature across MIT around 65deg C. Strained–thermal effect was suggested to be responsible for the formation of a monoclinic M2 phase which was assigned and belongs to a monoclinic phase remaining at higher temperature with weak proportion. Hence the study of the coexistence of M2 phase with R will be of great interest to investigate and fabricate the ultrasensitive transition edge-sensors, and fast optical shutters. The transition between M1 and M2 insulator can be used in developing fast and reproducible strain sensors or logic switches.

5.3 VO₂ Nanostructures based chemiresistors for High Hydrogen Gas Sensing capabilities within ppm level.

In relation to the hydrogen economy in general and hydrogen gas sensing in particular, an extensive set of 1-D nano-scaled oxide materials such as nanowires, nanotubes, nanorods, and nanobelts based systems, in addition to standard nano-powders/thin films structures are being investigated as ideal candidates for potential gas sensing applications. This is correlated to their set of singular surface characteristics; shape anisotropy and readiness for integrated devicesMott-type VO_2 oxide nanobelts are demonstrated to be effective hydrogen gas sensors at room temperature. These nanobelts synthesized by hydrothermal process and exhibiting the $VO_2(A)$ crystallographic phase in our work, display sound room temperature H_2 sensitivity as low as 0.17 ppm.

Whilst many aspects of hydrogen are well known, knowledge gaps have existed for several decades, as conditions for ignition, flame acceleration, detonation of heterogeneous mixtures, structural protection and other mitigation strategies such as ventilation. Therefore, it is necessary to build trust by demonstrating safety not only in the large demonstration projects but also by the way in which this vital topic is addressed. Understanding hydrogen and hydrogen system safety needs is critical for local government officials, fire officers, and the general public. Emergency personnel must be informed of the special properties of hydrogen and trained in the methods used to respond to accidents involving its use. Public perception and confidence in hydrogen relies on credibility, transparency and individual [54]. A comparative safety relevant property of four gases is given below. Serious considerations in South Africa are considered to develop hydrogen economy such as safety, cleaning and reliable alternative energy source to fossil fuels to produce electricity. Another driving force behind this technology is the prevalence of platinum reserves found in South Africa. Platinum materials used in most fuel cells, and with more than 75% of the world's

known platinum reserves found within South African borders, there is great potential for socio-economic benefits to be obtained from these natural resources. Although hydrogen and fuel cell technology falls squarely under the energy security grand challenge, it also has implications for global-change science with the potential to help mitigate the effects of climate change through reduced emissions and improved adaptation through use of cleaner energy technologies. The safe handling and use of hydrogen requires an appreciation of its physical properties in each of the forms in which its use as a fuel is considered (gas, liquid, adsorbed to another material, etc.). The properties of hydrogen are different from those of today's conventional fuels such as methane or gasoline. Hydrogen generally exhibits wider limits of flammability, a high detonation sensitivity, and relative low ignition energy if mixed stoichiometrically with air, in comparison to conventional fuels. See figure 5.23.
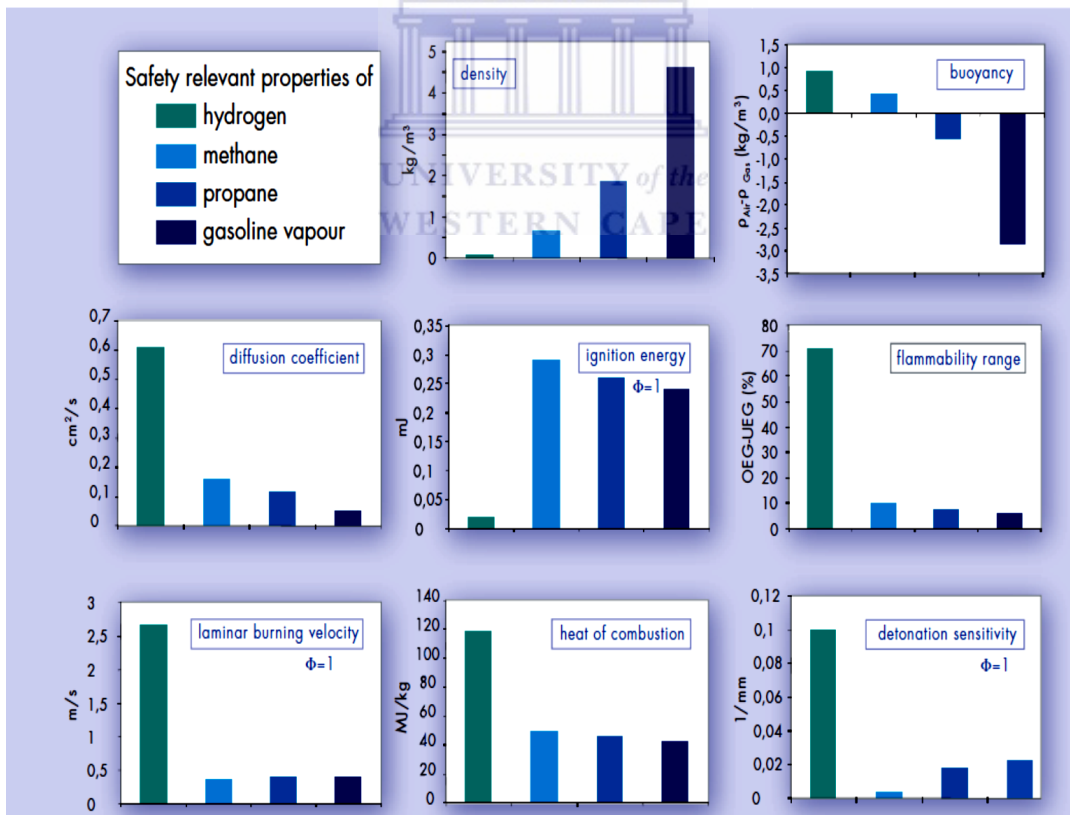
Figure 5.23: Hydrogen properties [54].

However, hydrogen may be responsible for stronger pressure effects if released and ignited in a confined space. To be a successful energy carrier, hydrogen must be economically competitive, and the individual technological components must be connected via an infrastructure that provides a safe and environmentally acceptable energy system throughout the whole production, distribution and end-use chain. The Sensor Performance Testing Facility Hydrogen leaks can be a serious hazard if not detected reliably and rapidly. Appropriate detection systems need to be tested, and their performance validated so that they can be deployed in hydrogen applications to ensure high safety of hydrogen-powered vehicles, stationary fuel cells for power generation, hydrogen filling stations, hydrogen pipelines, etc. The Sensor Performance Testing Facility, SenTeF, at the JRC's Institute for Energy, (JRC-IE) located in Petten, the Netherlands, has been designed and built for this purpose. The accuracy of a hydrogen sensor, the rapidity of its response, the reproducibility of its signal upon changes of temperature, humidity and altitude, the ability to ignore interfering gases and prevent false alarms are some of the elements that make a system reliable. At JRC-IE, a sophisticated gas-handling and temperature control system allows all these parameters to be controlled, simulating real ambient conditions, and submitting the sensors to a severe test. In collaboration with other European partners, such as Hysafe and StorHy, the JRC-IE will use SenTeF in experimental programmes aimed at the preparation of guidelines for testing the reliability of hydrogen detectors, both for automotive and stationary applications. See figure 5.24.

Figure 5.24: Gas handling and temperature control system at JRC-IE [54].

In relation to the hydrogen economy in general and hydrogen gas sensing in particular, an extensive set of 1-D nano-scaled oxide materials such as nanowires, nanotubes, nanorods, and nanobelts based systems, in addition to standard nano-powders/thin films structures are being investigated as ideal candidates for potential gas sensing applications. This is correlated to their set of singular surface characteristics, shape anisotropy and readiness for integrated devices [55-59]. Their shape anisotropy at the sub-micron scale induces their large surface/volume ratio, and hence a significant increase in surface chemical active sites [60-61]. The nanostructures of well-established gas sensing materials such as SnO_2 [62-66], In_2O_3 [67-68], and WO_3 [69-70] have shown higher sensitivity and selectivity, quicker response and faster time recovery, as well as an enhanced capability to detect gases at low concentrations compared with the corresponding thin film materials [70-71]. While the overall sensing characteristics of these so called 1-D nanomaterials are optimal, they are efficient at high temperature; generally above 200 °C, resulting in significant power consumption, in addition to

complexities in device integration, which limits their technological applications. Consequentially, there is still space and need to develop 1-D nanomaterials for gas sensors that have very good sensing performance but at room-temperature. Unfortunately, for room temperature applications, there is a necessity to dope the above mentioned nano-scaled oxides with non-cost effective noble metals such as Pt, Pd, Au, and Ru. Indeed, as demonstrated by Tien et al. and Wang et al. [72-73], ZnO nanorod sensors showed higher H_2 sensitivity and quicker response at room temperature for ZnO nanorods surface-modified by sputter-deposited clusters of Pd or Pt when compared with the undoped and corresponding thin film sensors. Ramgir et al. [74] reported that 0.48 wt% Ru-doped SnO_2 nanowires exhibited the highest sensitivity towards NO_2 gas at room temperature while Neri et al. [75] reported that Pt-doped In_2O_3 nanopowders showed better gas sensing performances to oxygen at room temperature compared with the undoped samples. To single out the reported experimental large room-temperature H_2 gas sensing of the specific phase of VO_2 (A) nanobelts, one should position this work relatively to the reported studies on an ensemble of vanadium oxides nano-systems. Oxide systems of vanadium present a wide range of ordered and disordered structures due to the presence of multivalent vanadium ion from V_2O_5 to VO_2 whose structures and stoichiometry satisfy the general formula V_nO_{2n+1} (3<n<8). Raible et al. [76] showed high sensitivity and selectivity in nanofibers of V_2O_5 based sensors capable of detecting organic amines at room temperature. Baik et al. [77] produced Pd nanoparticles-decorated single VO_2 nanowires and studied the sensitivity under H_2 close to the metal insulator transition temperature which is about 70 $^\circ$C. They showed that the material undergoes a large downward shift in the insulator to metal transition temperature >10 $^\circ$C following the adsorption and incorporation of atomic hydrogen produced by the dissociative chemisorption of H_2 on Pd in VO_2. Manno et al. [78] investigated the influence of the NO_2 gas on the conductance of vanadium oxides films sputtered at different concentrations of O_2. They realized that pure stoichiometric VO_2 and V_2O_5 have lowest response between 200 to 300 $^\circ$C while V_3O_7 and V_4O_9 had the best sensitivity to 100 ppm NO_2. Hence the

crystallographic phases play an important if not a critical role in gas sensing at least in such a system. Strelcov et al. [79] studied VO_2 nanowires thermistor based gas sensor with variation of the temperature close to the transition temperature edge which can be lowered to room temperature by appropriate doping or by axial stress. Recently Yin et al. [80] studied the sensitivity of VO_2 (B) and VO_2 (M) in moisture environment demonstrating that they exhibit good stability, fast response and good recovery detection in low relative humidity (11.5% RH) and high relative humidity (97.2% RH) respectively. However, and to the best of our knowledge, no report has been published on room temperature sensitivity to H_2 gas of synthesized VO_2 (A) nanostructures in general and their nanobelt form especially. VO_2 (A) phase is a singular V-O system oxide. More accurately, it is based on an oxygen bcc lattice with vanadium in the octahedral where the oxygen atoms are mainly aligned along one direction [81] (Figure 5.25). It possesses a tetragonal structure with space group P42/nmc and can be directly transformed to VO_2 (M/R) under annealing treatment. VO_2 (A) shows a thermal stability at 162 ˚C with a reversible change from tetragonal VO_2 (A) to body-center tetragonal VO_2 (A_H) (Figure 5.25). It has been shown that, according to the density functional theory (DFT) and crystallographic topology analysis, VO_2(A) is the thermodynamically stable phase compared with VO_2 (B) and is much more stable than VO_2 (R) based on calculations principles using the hybrid function as highlighted in Table 5.4. Due to such stability, Li et al [82] studied the field emission and electric properties of such a metastable phase VO_2 (A) in their ultra-long nanobelt form. This latter set of VO_2(A) nanobelts were found to exhibit a colossal field performance factor of about 1739 in the field emission measurement and a significant time stability of the current density, indicating the potentiality of VO_2 (A) to be applied as an electron emission nano-material. As mentioned previously, this paper reports for the first time the H_2 gas sensing properties at room temperature of VO_2 (A) nanobelts. The exhibited large H_2 sensitivity at room temperature of the synthesized VO_2 (A) nanobelts can easily reach values smaller than 0.17 ppm concentration.

TABLE 5.4:   Specific parameters of some phases of VO_2 [83].

Phases	Density (g/cm³)	Band gap (eV)	Formation energy (eV)
VO_2 (R)	4.67	Metal	-6.93
VO_2 (M)	4.67	0.84	-7.18
VO_2 (B)	4.031	0.65	-6.66
VO_2 (A)	4.035	0.21	-7.14
VO_2 (A_H)	4.035	Metal	-6.97
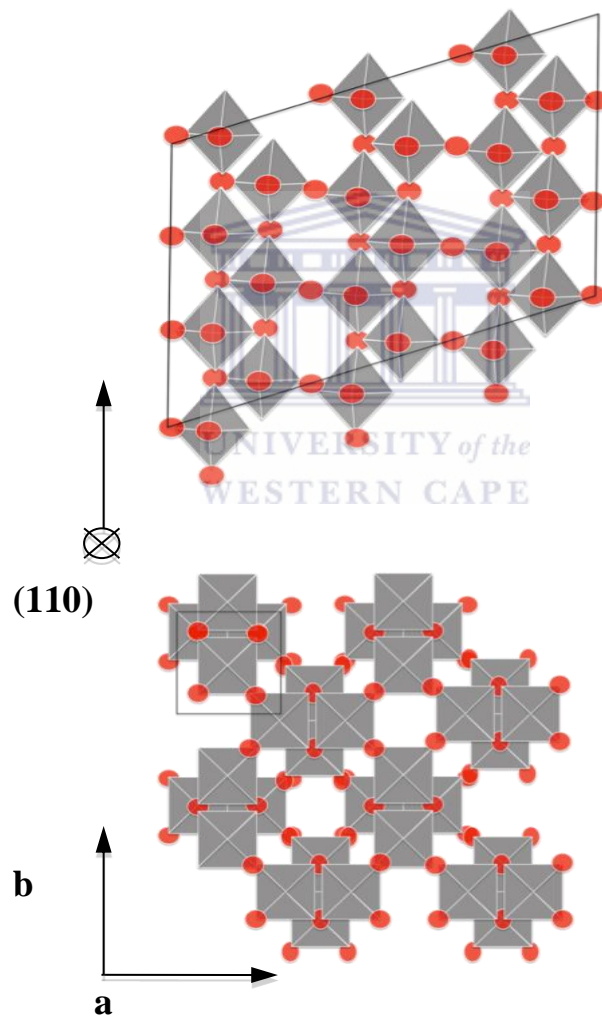
Figure 5.25: Tetragonal structure of VO_2 (A) [83].

VO_2 (A) nanobelts were synthesized using a hydrothermal procedure [84]. In a typical

synthesis, 0.75ml of sulphuric acid H_2SO_4 followed by $N_2H_4 \cdot 2H_2O$ was added into an aqueous suspension of V_2O_5. After stirring thoroughly, the solution's color changed from yellow (V^{5+} valence state) to blue, characteristic of the presence of V^{+4} ions in the solution. Following an optimization study, it was found that the concentration of NaOH determines the shape of the final product. The hydrothermal synthesis was carried out in a Teflon-lined autoclave at ~230°C for about 48h. Then the content was air-cooled to room temperature followed by a filtration step of the formed precipitates. The final black chemical product was washed extensively with water and ethanol and dried at about 60 °C for 12h. To confirm the VO_2 (A) crystallographic nature of the synthesized nano-powder, High Resolution Electron Microscopy (HRTEM), X-Ray Diffraction (XRD) as well as transport (Resistance-Temperature) measurements were conducted. The HRTEM and the XRD measurements were carried out on a TECNAI G2-F20 and a Bruker unit in a θ-2θ mode with CuKa 1(AXS Bruker, λ=1.54056Å) respectively while the resistance-temperature cycling R(T) were measured with a standard two probe system. Figure 5.26 shows a typical electron transmission micrograph of the filtered synthesized powder. The nano-particles exhibit crystal-clear shape anisotropy: a nanobelt-like morphology. Statistical imaging studies show that they have an average size of 20-150 nm in the transverse direction and a length ≥ 20 μm with a thickness less than 10 nm. The high resolution electron microscopy analysis of the bulk of individual nanobelts indicates a significant crystallinity of the VO_2 (A) with an interspacing $d_{(hkl)}$ ~ 0.600 nm corresponding to the (011) reticular plane orientation. To find out if the surface of the nanobelts is different from the bulk in terms of elemental distribution, Energy Dispersion Analysis (EDAX) investigations were carried out on the same high resolution electron microscopy unit. The 200 KeV accelerated beam was set to impinge the nanobelts surface at an inclination angle of 15.02 ° C. The corrected V/O ratio was found to be identical (about 0.48) both at the interface and the volume part of the nanobelts indicating therefore the identical degree of chemical homogeneity within the nanobelts at least from chemical point of view.
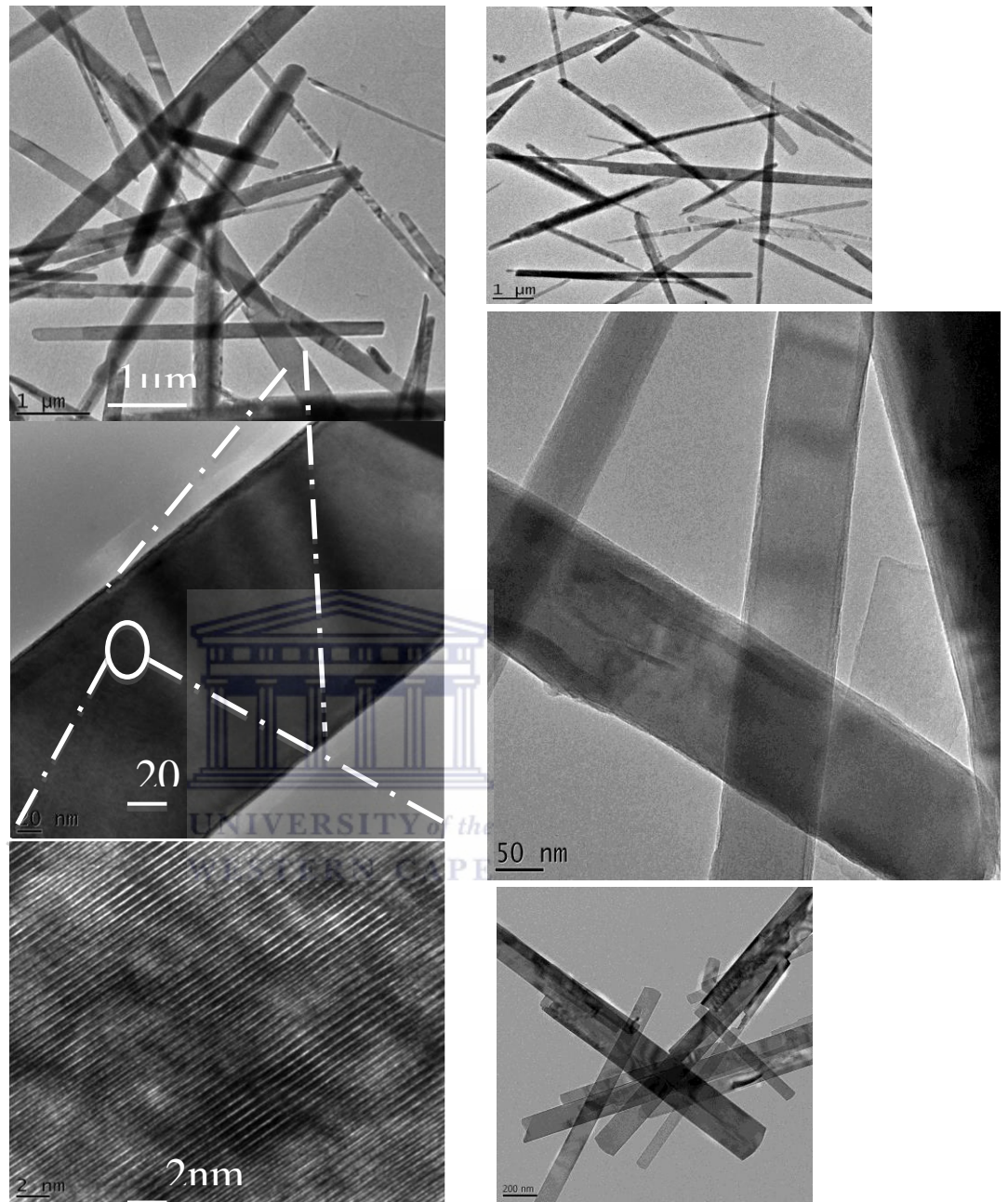
Figure 5.26: Electron transmission micrograph of synthesized powder.

From a crystallographic point of view as well established, VO_2 has several kinds of crystalline structures [83-87]. One is the tetragonal rutile-type VO_2 with lattice constants of a ~ 0.455 nm and c ~ 0.285 nm and that shows metallic feature. A second is monoclinic VO_2 with a ~ 0.5753 nm, b ~ 0.4526 nm and c ~ 0.5383 nm, which has an

insulator behavior at room temperature. It is widely accepted that the formation of an electron pair in the monoclinic crystalline structure results in the insulator phase. This monoclinic VO_2 can inversely transit to tetragonal rutile and conducting VO_2 phase. A third structure is also monoclinic VO_2, but with a ~ 1.209 nm, b ~ 0.3702 nm and c ~ 0.6433 nm. This type of VO_2, however, does not show the highly attractive Metal-Insulator Transition (MIT) characteristic. The 3 phases mentioned previously are known as VO_2 (T) for the tetragonal type, VO_2 (M) for the monoclinic type with the phase transition, and VO_2 (M-II) for the non-transition monoclinic type. In addition to this set of stable phases, VO_2 (A) phase shows a thermal stability at 162 ˚C with a reversible change from tetragonal VO_2 (A) to body-center tetragonal VO_2 (A_H) as highlighted in Figure 5.25. Figure 5.27 reports a typical room temperature X-ray diffraction of the filtered powder. The majority of the peaks are indexed as VO_2(A) according to the JCPDS card referenced as 00-042-0876 with a preferential orientation along (110) yet there is a slight angular shift of many Bragg peaks. The derived lattice parameters via a Rietveld treatment gives the average values of <a> and <c> of 8.451 Å and 7.697 Å respectively and a space group of P42/nmc. The lattice values are slightly different from the bulk parameters: <a>= 8.450 Å and <c>= 7.686 Å of the VO_2(A) phase suggesting that there is a slight inter-plane strain (Δ<c>/<c> ~ 1.5%. Likewise, one could observe the presence of little low intensity Bragg peaks belonging to VO_2(M) phase. Such bi-phase coexistence could be due to stress-strain phenomena at the crystallites' interface. Indeed, it has been demonstrated that the distortion of the VO_6 octahedra in the low temperature VO_2 (A) phase is similar to the monoclinic VO_2 (M) phase. Hence monoclinic domains could be found in the low temperature VO_2 (A) nanostructures. As confirmed by the preceding high resolution electron microscopy as well as the X-rays diffraction investigations, the VO_2(A) phase has been substantiated by additional transport measurements via resistance-temperature (R(T)) profiles within the temperature range of 25-100 °C. Before presenting the R(T) experimental results, it is worth describing the characteristics of the VO_2(A) phase specifically and VO_2 in general which is gaining momentum in interest within the global scientific community

[88-92]. VO_2 exhibits an ultrafast femtosecond 1st order metal–insulator/semiconductor (MIT) Mott's type phase transition at around ~ 67.8 °C with large orders of change in the electrical resistivity due to its strong electrons correlation [93-95]. More precisely, above the transition temperature T_c~ 67.8 °C, VO_2 is metallic and adopts the tetragonal rutile (P42/mnm) structure with chains of edge-sharing VO_6 octahedra along the c-axis; the V-V distances along the chain are 0.2851 nm. Below T_c, i.e. in the semiconducting/insulator monoclinic (P21/c) crystal structure, the dimerized vanadium atoms have alternate V-V distances of 0.2619 and 0.312 nm. Such an ability to undergo a reversible structural distortion as a function of temperature is accompanied by a reversible semiconductor/insulator-to-metal transition. From theoretical point of view, this phase transition has been, initially, interpreted in terms of Mott-Hubbard like transition [96] or electron trapping in a homopolar bond. The very recent ultrafast spectroscopy investigations shed-lighted, on how fast is such a phase transition as well as on the electronic band structure changes. Indeed, using a femtosecond laser excitation, the relaxation processes in VO_2 were studied by optical pump-probe spectroscopy highlighting that the light-induced phase transition was as fast as the laser pulse duration of 100 fs itself [97-99]. As a consequence of such a femtosecond and reversible electric phase transition, the optical dielectric constant and thus the refractive index of VO_2 exhibit a temperature modulation which translates in a large reversible optical modulation in the infrared spectral region. This singular property of VO_2 make it an optical coating candidate of choice for smart windows applications [100], thermal sensors [101], optical switching devices [102], field effect transistors and electro-optical gates [103] as well as ultrafast tunable nano-plasmonics among others [104-105]. Figure 5.27 b) presents the diffraction pattern observed on the screen as a series of aperiodic sequence of diffraction spots which is produced by nano-size dimension of the nanobelts in combination with double diffraction due to twinning. The nanometric size of the nanobelt along its cross section produces the enlargement of reciprocal spots [106]. Hence the combination of spots obtained is both the zero order Laue zone and

first order Laue zone. For a [001] beam direction, the reciprocal lattice point contributes to the diffraction pattern if it satisfies:

$$[001].(uvw) = 0 \qquad \textit{Eq. 5.33}$$

The smallest vectors satisfying this equation and that also satisfying the condition that all of the indices are even or all of them are odd are (200) and (020). So the diffraction pattern will consist of all the integer combinations of these vectors such as: (010), (100), (110), (200), and (020).
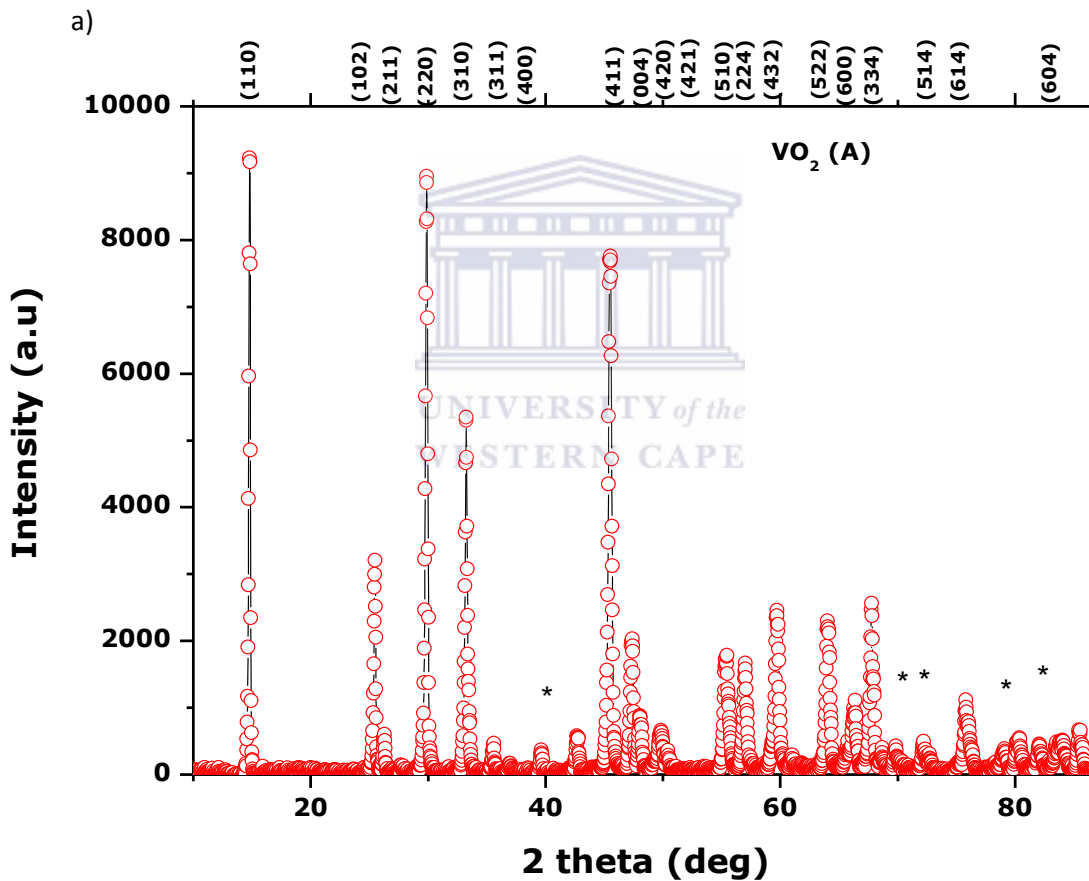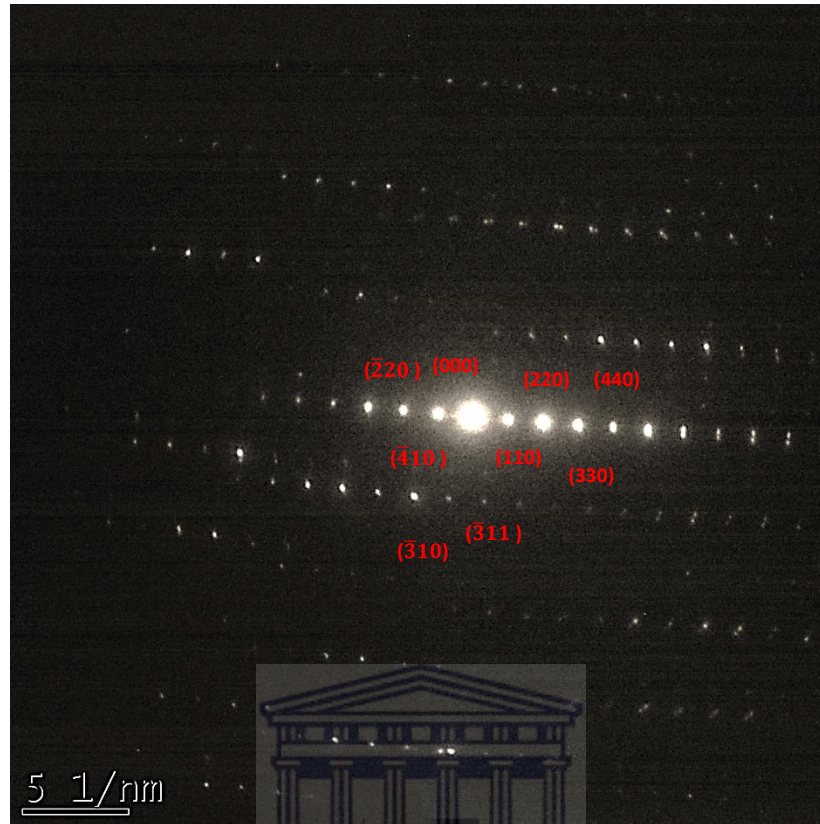
Figure 5.27: Crystallographic structure of VO_2 a) and diffraction pattern of VO_2 b).

Figure 5.28 reports the variation of the electrical resistance/cm^2 versus temperature of a typical cold pressed pellet of the VO_2 (A) nanobelts. The measurements were conducted within the temperature range of 25-100°C both in the cooling and heating cyclings. As one could notice, the electrical variation within the 55-72°C is approximately over 4 decades with a hysteresis type evolution upon heating/cooling, characteristic of VO_2 (A). The average value of the electric resistance is 10^8 Ω and 10^4 Ω at 50 and 72°C respectively. Though the variation of the electrical resistance is of the order of 4 magnitudes, its value above the bulk critical temperature of 68°C is still high. This could be caused by the porosity of the pressed VO_2 (A) nanobelts powder and could be explained in terms of percolation phenomena. Taking into account both the values of the average hysteresis as well as the change in the magnitude of the electrical resistance/cm^2, the average transition temperature, T_c can be estimated to ~62°C. Relative to the bulk T_c, this smaller value could be due to a strain-stress phenomenon as

195

suggested in the case of previous electron transmission and X-ray diffraction experiments.
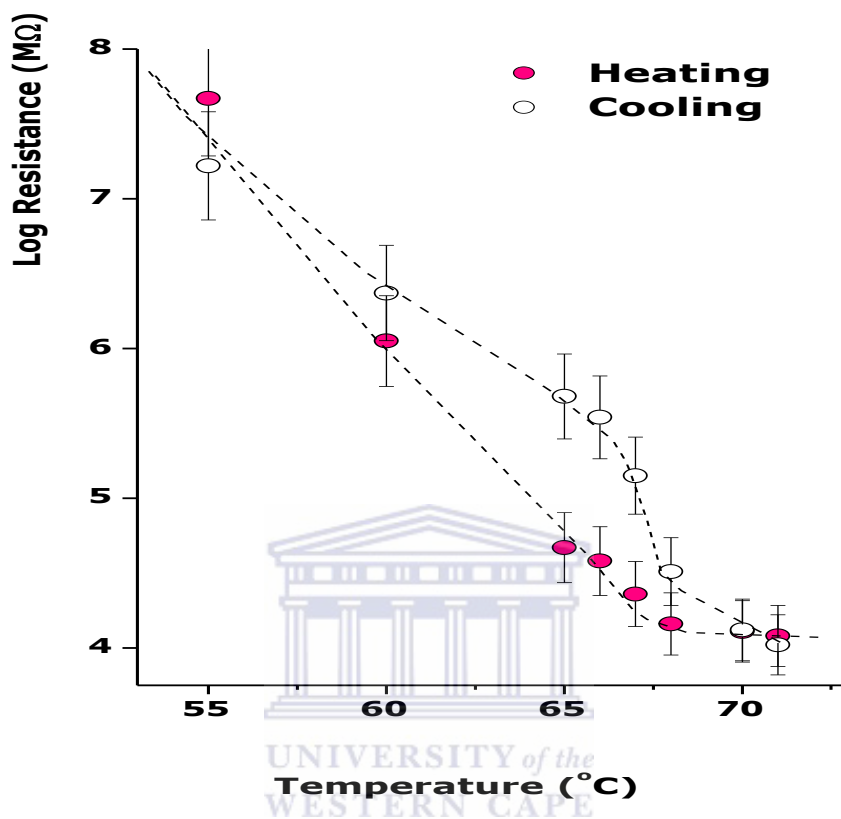
Figure 5.28: electrical resistance measurement of VO$_2$ (A).

For the H$_2$ gas sensing experiments, a standard in-situ 2 point probe system was used. The cold pressed VO$_2$ (A) nanobelt pellet was squeezed between two Al electrodes and a Si substrate wafer while the whole was interfaced to a heating stage (25 ^{o}C– 300°C). The isothermal responses of the resistance of the pressed VO$_2$ (A) nanobelts powder at different concentrations of H$_2$ fluxes were measured upon injection of H$_2$ N$_2$ mixture as a carrier gas and refluxing with pure N$_2$. The reproducible experiments were conducted with different H$_2$ partial pressures equivalent to 140, 90, 50, 14 and 0.17 ppm of H$_2$ carried by N$_2$. Before any H$_2$ sensing experiment, the chamber was refluxed to minimize any contamination effect. Figure 5.29 at room temperature and close to 50 deg. C reports a typical variation of the conductometric sensing signal for the above H$_2$ concentrations

i.e. 140, 90, 50, 14 and 0.17 ppm of H_2. The initial electrical resistance which is about 1.2×10^7 Ω decreases to 0.18×10^7 Ω upon initial refluxing. Upon injection of 140 ppm H_2, it increases to reach a plateau-like steady-state. As in the case of effective sensing oxide based nano-systems, the electrical resistance decreases once H_2 gas flow is cut off. To estimate the H_2 detection limit, the room temperature conductometric measurements were performed at the various H_2 flow concentrations of 90, 50, 14 and 0.17ppm as reported in figures 5.29 a) and figure 5.29 b). It can be observed that, the resistance variation, which is reproducible with a small bar error, is still sensitive up to 0.17ppm H_2. See figure 5.30 a) and b). Compared to the various oxides studied earlier, as well as the 1-D reported nanosystems, this detection limit at room temperature is, indeed, significant if not unique.
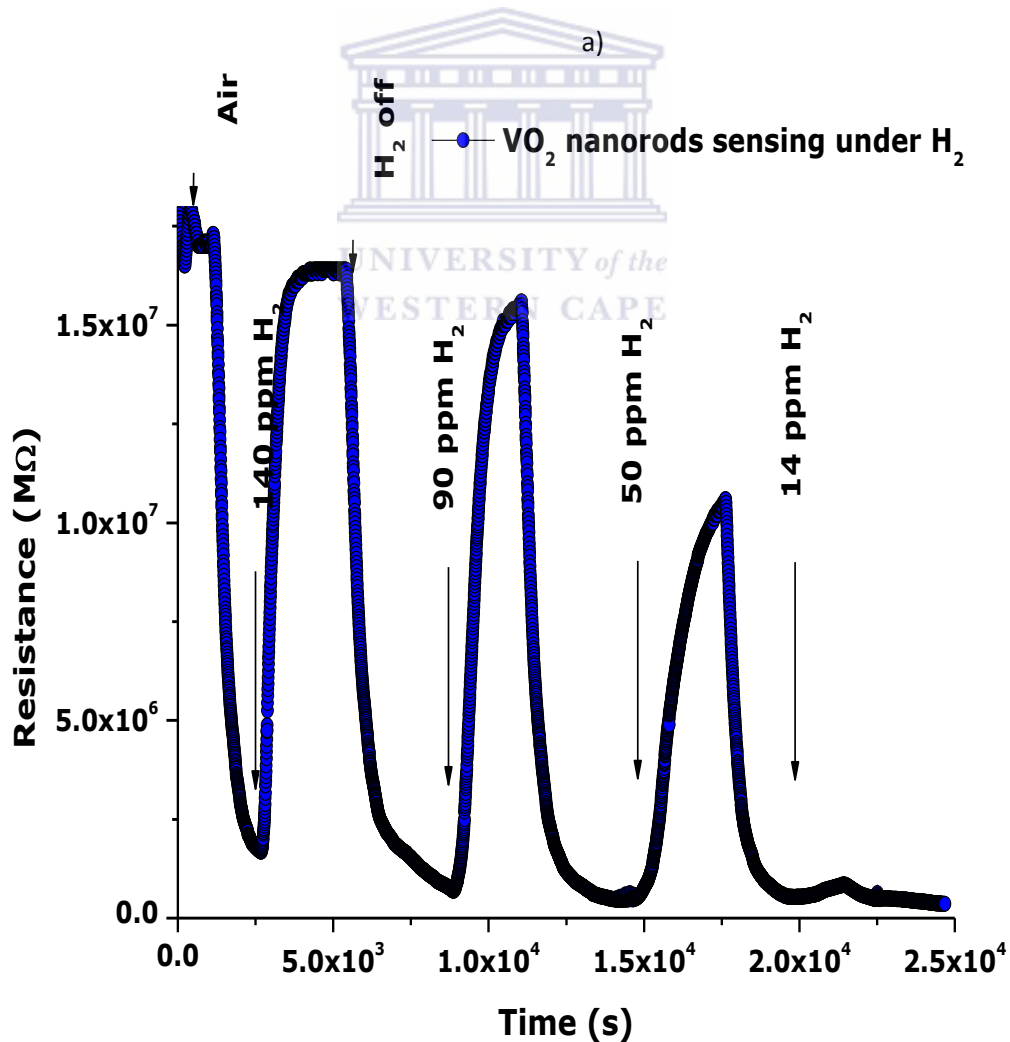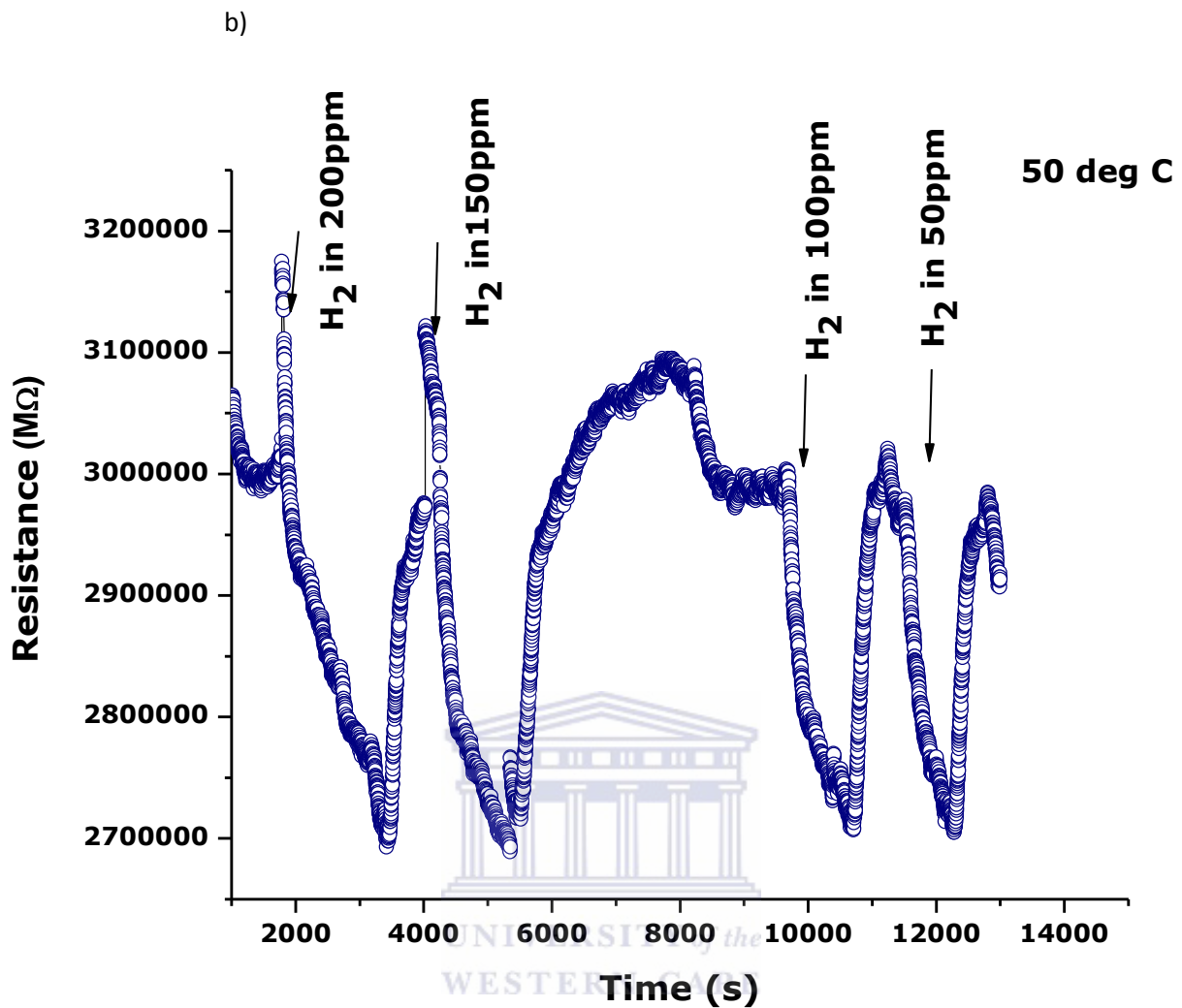
Figure 5.29: Conductometric sensing signal of powder VO_2 at room temperature and close to the transition temperature.

The gas sensing properties of VO_2 nano-platelets has been investigated at room temperature and 50 °C in N_2 dry air at different pressures of H_2 gas using the conductometric sensor signal. The decrease in the resistivity is due to the injection of the H_2 gas describing the charge transfer with the material and because the low temperature favors the adsorption of negatively-charged hydroxyl species. Intrinsic oxygen atoms trap the electron in the n-type VO_2 (A) metal reducing the charge carrier density in a depletion region close to the surface due to the band bending at the surface [107]. Depletion regions occur between grains giving higher resistance. A wide variety

of events occur when a molecule impinges upon a surface. It may be reflected with no loss of energy or it may suffer a redistribution of momentum and be diffracted by the surface again with no loss of energy. In the case where the hydrogen molecules lose sufficient quantity of energy they become effectively bound to the surface with strength depending on the kinds of atoms involved. The resistance underwent a drastic drop when the gas is open exhibiting n-type semiconductor characteristic of VO_2 (A). This whole process responsive behavior has been qualified as conduction type inversion n-to-p of the sensing material whose conduction is surface trap limited owing to the high surface to volume ratio of this material [108]. Therefore, this detection limit is low enough for potential commercialization if the recovery and response times would be optimal. Concerning the response and the recovery time, the VO_2(A) nanobelts exhibit comparable values relatively to standard doped sensing nano-scaled oxides at room temperature and comparable H_2 concentration. More precisely, the average response times are ~840, ~890, ~1080, ~1020, and ~1050 seconds for 140, 90, 50, 14 and 0.17 ppm of H_2 respectively. Likewise, the corresponding average recovery times are: ~455, ~870, ~1020, ~1037, and ~2080 seconds for 140, 90, 50, 14and 0.17 ppm of H_2 respectively. In comparison, the H_2 sensing of the equivalent oxide system i.e. ZnO nanorods [108-109], records at room temperature response times in the order of 600 seconds for 500ppm H_2. In addition to such a substantial characteristic, and as reported in Figure 5.31 a), the sensitivity of the nanobelts S (S= $(R_{H2}-R_0)/R_0$, R_{H2} and R_0 are the sample resistance with and without H_2 gas respectively) is in the range of the values exhibited by standard 1-D oxides [62, 110]. In this case, the VO_2 (A) nanobelts seem to present a better H_2 sensing sensitivity in the range of 90 ppm H_2 at room temperature.
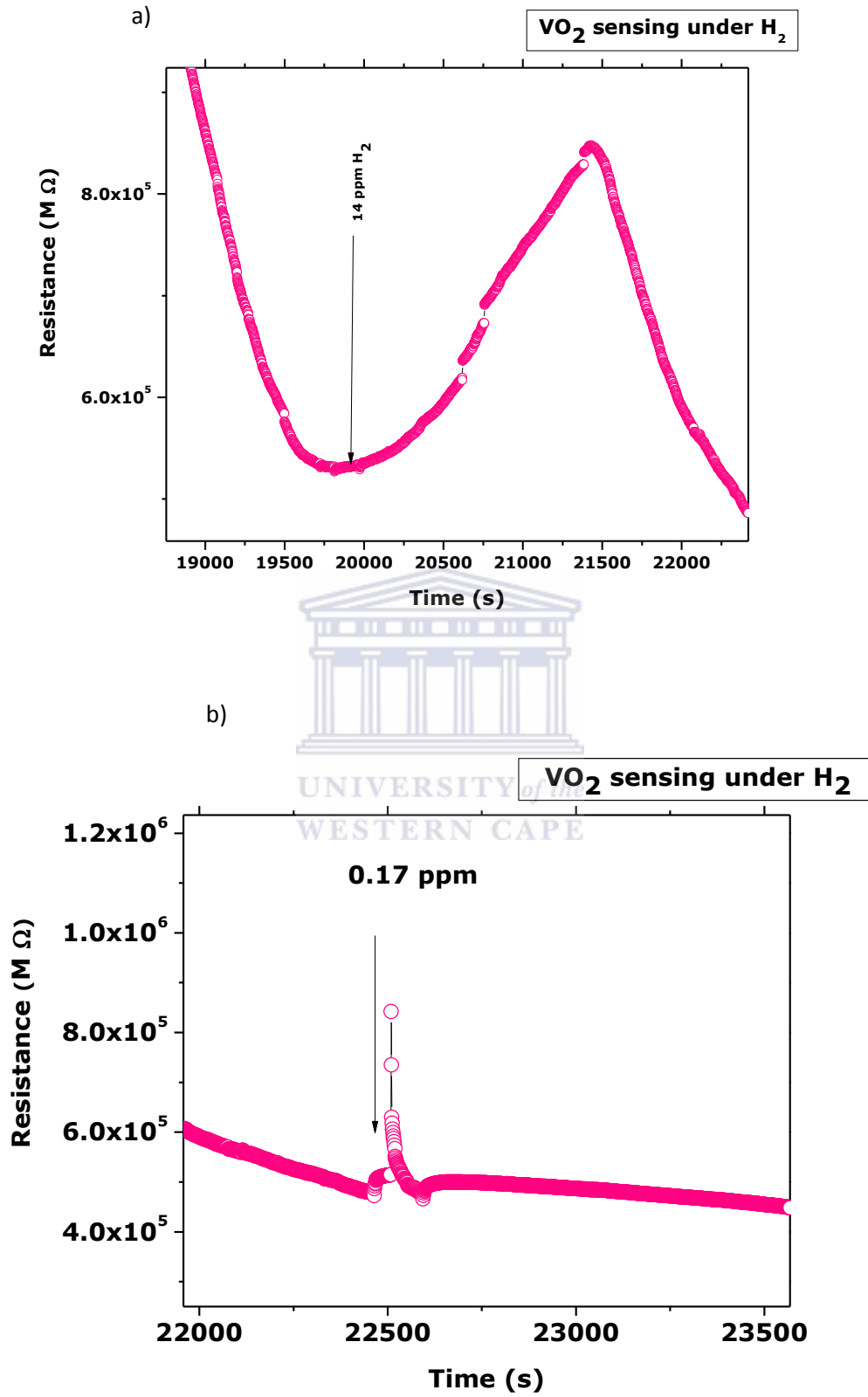
Figure 5.30: Detection limit H_2 sensing at 14 ppm a) and 0.17 ppm b)
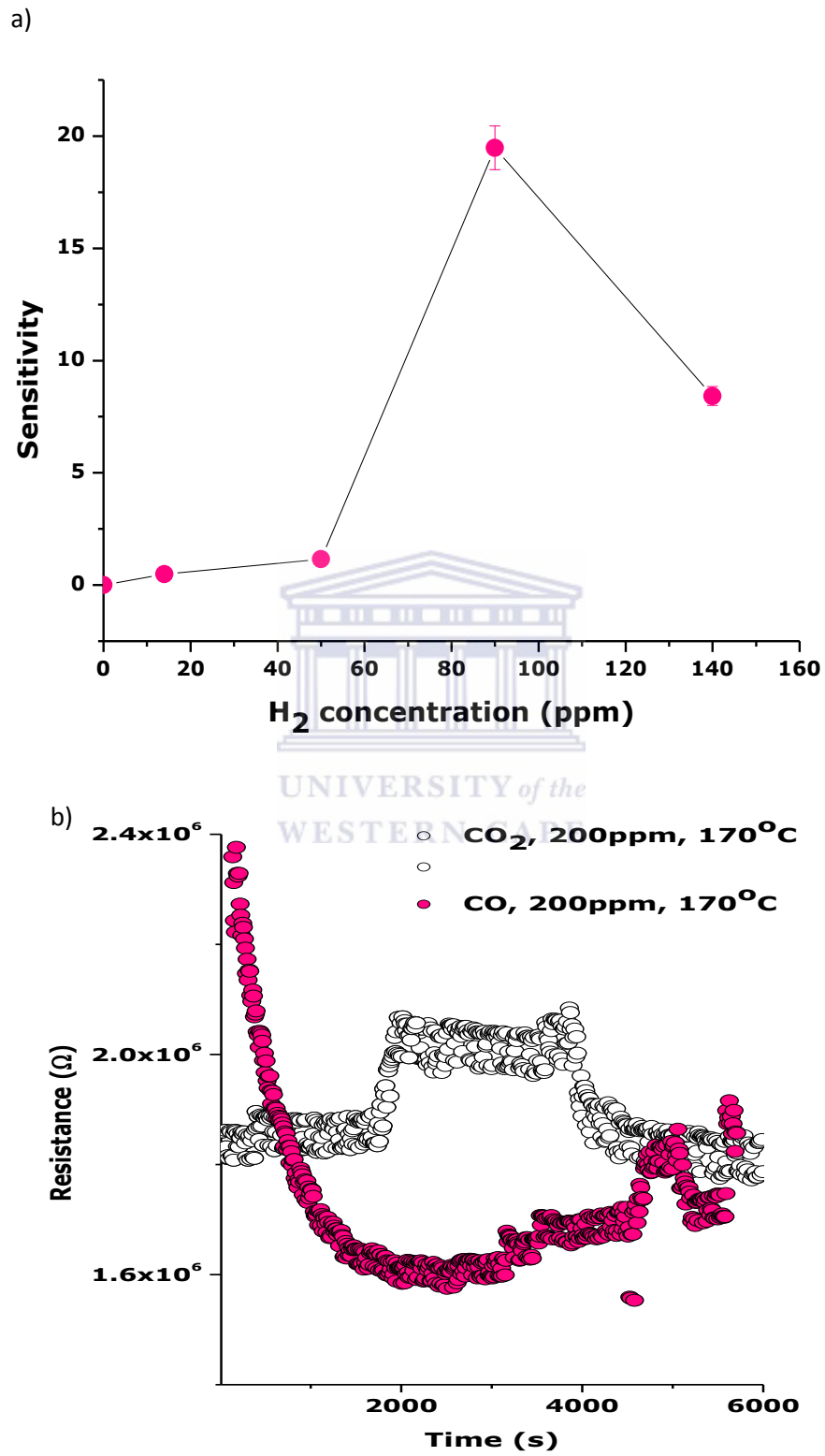
Figure 5.31: Nanobelts sensitivity a) and selectivity b) comparing to CO and CO₂.

Finally, to shed light on the sensing selectivity of the VO_2 (A) nanobelts, further experiments were carried with other standard gases such as CO and CO_2. As their corresponding sensing characteristics seemed to be very weak at room temperature under identical sensing conditions, threshold type experiments were conducted. Figure 5.31 b) shows one cycle conductometric sensor signal for CO and CO_2 gases. At it can be noticed, the sensing signal is at the background level yet at a temperature of 170 °C and concentrations of 200 ppm CO and CO_2. Consequentially, it could be deduced that the VO_2 (A) nanobelts seem to exhibit a noteworthy gas sensing selectivity towards H_2.

5.3.1 Conclusion

This research section reported, for the first time, unexpected room temperature enhanced hydrogen sensing properties of a specific phase of vanadium dioxide (VO_2:phase A) in their nanobelt form. The relatively large H_2 room temperature sensing in this Mott type specific oxide seems to have a limit below 0.17 ppm H_2. If this contribution demonstrated the H_2 sensing efficiency of VO_2 (A) nanobelts at room temperature relative to corresponding 1-D oxides in general, various issues are still to be addressed amongst which, one should mention the following:

(i) Sensitivity to humidity which is well known for semiconducting gas sensors should be addressed through the selection of a high operating temperature which is naturally smaller than T_c and (ii) The sensor's selectivity for H_2S, NH_3, and C_2H_5OH gases should be investigated and enhanced. Follow up investigations would address all these issues by combining selected laser spectroscopy and synchrotron surface-interface characterization techniques.

5.4 Transport Measurement on a Single Nanograin

Being a Mott type oxide, at a temperature of TC~ 340.8K and ambient pressure, stoichiometric VO₂ undergoes a reversible 1st order semiconductor-metal transition, which is accompanied by a reversible abrupt change in the band gap opening. The variation of the bandgap Eg versus the external thermal stimulus on a single VO₂ nanoparticle is reported for the first time using scanning tunneling spectroscopy in the temperature range of 293.5-361.0 K.

Carriers of electrical current in semiconductor are much more dilute than in metals and they are thermally activated out of filled band, or injected by light, charged particles or through tunnel barriers or produced by intentional doping [111]. Generally the main differences from the metals are the strong correlation between theory and devices applications; metal-insulator phase transition at low temperature and alternate mechanism to band transport due to the hopping process. Regarding the electrical transport, the tunneling effect is generally studied due to the quantum confinement of the electrons. This plays an important role in many semiconductor devices. Esaki discovered in 1958 [112] the diode tunneling through a forward biased heavily doped junction in germanium. This diode exhibits negative differential resistance (NDR) which makes possible the semi-conductor to be used as high frequency oscillator (microwave).The tunnel current is expressed as [113]:

$$I_t = I_{C \to V} - I_{V \to C} \qquad Eq. 5.34$$

$$I_t$$

$$= A \int_{E_{C0}}^{E_{V0}} \{f_C(E)C(E)\}W\{[1 - f_V(E)V(E)]\}dE$$

$$- A \int_{E_{C0}}^{E_{V0}} \{f_V(E)V(E)\}W\{[1 - f_C(E)C(E)]\}dE \qquad Eq. 5.35$$

Where W represents the quantum mechanical transition probability, C(E) and V (E) are the density of states in conduction and valence bands, $f_V(E)$ and $f_C(E)$ are the occupations functions. In the case of temperature not very low,

$$\frac{eV_n}{kT} = \frac{E_F - E_{C0}}{kT} \ll 1 \qquad\qquad Eq.\,5.36$$

And

$$\frac{eV_p}{kT} = \frac{E_{V0} - E_F}{kT} \ll 1 \qquad\qquad Eq.\,5.37$$

Hence

$$f_V(E) \approx \frac{1}{2} - \frac{E - E_F}{kT} = f_C(E) \qquad\qquad Eq.\,5.38$$

For parabolic bands:

$$C(E) \propto (E - E_{C0})^{\frac{1}{2}}, \quad V(E) \propto (E_{V0} - E)^{\frac{1}{2}} \qquad Eq.\,5.39$$

This gives:
$$I_t \propto W \frac{eV}{kT} \left(V_p + V_n - V\right)^2 \qquad\qquad Eq.\,5.40$$

Junction field effect transistor was first time analysed by Shockley in 1952 which basically consists to a voltage controlled resistor involving predominantly one kind of carrier which is qualified as unipolar transistor [114]. Field effects transistors present many attractive features for applications in analog switching, high input impedance amplifiers, and integrated circuits. At high current level, the device presents a negative coefficient temperature. Hence the current decreases as the temperature increases. This property leads to a uniform distribution temperature over the device area and prevents the device from thermal runaway and breakdown. The FETS do not suffer from minority carrier storage effects and consequently present high switching speed and higher cutoff frequencies. VO_2 exhibits an ultrafast femtosecond 1st order metal/semiconductor (MS) Mott's type phase transition at about TC~ 340.8K with a consequential change in the electrical resistivity (larger than 104 in bulk) due to its strong electrons correlation structure [115] and a bandgap Eg about ~0.70 eV far below TC.

VO$_2$ possesses several kinds of crystalline stable structures [116]; one is the tetragonal rutile-type VO$_2$ with lattice constants of a~ 0.455 nm and c~ 0.285 nm exhibiting a metallic feature above T$_C$. A second, at a lower value, is monoclinic VO$_2$ with a~0.5753 nm, b~ 0.4526 nm and c~ 0.5383 nm, has an insulator behavior at room temperature. It is widely accepted that the formation of an electron pair in the monoclinic crystalline structure results in the insulator phase. This monoclinic VO$_2$ can inversely and reversibly transit to the tetragonal rutile conducting VO$_2$ phase. A third monoclinic VO$_2$ structure does exist too, but with a~ 1.209 nm, b~ 0.3702 nm and c~ 0.6433 nm. However, this later VO$_2$ phase, however, does not show the so attractive MS transition characteristics. The 3 phases mentioned above are known as VO$_2$ (T) for the tetragonal type, VO$_2$ (M1) for the monoclinic type with the Mott phase transition, and VO$_2$ (M2) for the non transiting monoclinic type. More precisely, above the transition temperature T$_C$~ 340.8K, VO$_2$ adopts the tetragonal rutile (P42 /mnm) structure with chains of edge-shared VO$_6$ octahedral along the c-axis; the V– V distances along the chain are 0.2851 nm. Below T$_C$, i.e. in the semiconducting monoclinic (P21/c) crystal structure, the dimerized vanadium atoms have alternate V–V distances of 0.2619 and 0.312 nm. While extensive studies were conducted on VO$_2$ in terms of synthesis and investigations of its physical properties as well as its potential optoelectronic technological applications, a limited set of studies were carried out on the variation of its electronic bandgap Eg(T) in its nanostructured form [117] yet an extensive experimental and theoretical research were performed on its bulk. Relatively to the bulk, and due to the 3-D symmetry breaking and coordination effects in addition to strain surface effects, the nano-structured form should exhibit a different behavior than bulk. For our best knowledge, relatively to published literature and the recent work of Yin et al [118], this contribution reports the first experimental results of the thermal variation of the Eg(T) on a unique and single VO$_2$ nanocrystal. Hence, The I-V and transport measurements on VO$_2$ nanoparticles which will be carried out in view of investigating the targeted temperature bandgap dependence Eg(T) in this paper, will be performed on this discontinuous film mainly as it is below the percolation threshold. Nonetheless, probing

the transport properties of the thick VO_2 films by scanning tunnelling spectroscopy (STS) is worth to check the phase transition process below and above T_C of ~340.8K. For the STS experiments, the transport I-V measurements versus temperature were conducted on the various films with the F: SnO_2 coating onto the glass substrates and the STM tip as the electrodes. See figure 5.32 a). The advanced Brucker scanning tunneling spectroscopy unit was equipped with an in-situ heating stage allowing a heating/cooling temperature range of 298.5-573.5K with a step temperature increase of 0.1K. Figure 5.32a) illustrates representative STS 1µm x1µm scans just at the vicinity and far above T_C for the thickest VO_2 film (~1218±5 nm); more precisely at 338.7K and 361.0K respectively. The transformation of the VO_2 surface can already be observed in the STS surface topography images. As in the case of Yin et al work on thick VO_2 films [119], the thermal drift during the heating of the sample was corrected regularly in order to image the same group of nanocrystals repeatedly. The surface density of states and their spatial distribution was studied by measuring the I-V characteristics in the voltage interval from -1 to 1 V by single point STS averaging over ~15 times of I-V scans in each spot and grid measurements. See figure 5.32 b). The grid measurement consisted of a matrix of 445 x 445 pixels and I-V curves were taken at each pixel. This time consuming STS measurements illustrated in Figure 4.33 with a pixel size of 1.5x1.5 nm2 were required to have, indirectly, more accurate bandgap maps. The images were recorded with a bias voltage of ~0.207 V and the electronic states close to the Fermi energy dominate the tunneling current. The metallic regions of the surface, where the local density of states (LDOS) close to the Fermi energy, EF, dominate, appear darker (brownish) in the STS topography images, and the progression from a predominantly insulating to a metallic surface is clearly seen in the evolution of the images of Figure 5.32.a). The changes in the STS topography images, as see in figure 5.33 which were recorded as a function of temperature with a bias voltage of 1.1 V are significant yet the small differences in LDOS between metallic and insulating regions deeper in the band. These voltage dependent surface electronic topography images gave the first impression of the insulator-metal transition at the surface as observed and reported by

Qazilbash et al [34]. The white areas correspond to the insulating/ semiconducting phases while the brown regions match up with metallic VO_2 phases. As it can be observed, the cover surface of the brown regions is somehow equivalent to the white ones at 338.7K indicating that the Mott phase transition, yet incomplete, takes place at slightly lower temperatures than the bulk value of T_C ~341.5K. Above T_C i.e. 361K, while almost the entire scanned surface is conducting (brownish area), one could notice that there is, notwithstanding, insulating/semiconducting domains (white regions). This difference could be due, either to the amorphous nature of the surface layer surrounding the investigated VO_2 nano-particle, its oxygen sub-stoichiometry or to the strain/stress on the corresponding nanocrystals. In all three cases, this surface layer would act as a resistive component and hence would affect the value of the bandgap $Eg(T)$ of the single VO_2 nanocrystals. In view of the recent converging studies on VO_2, the surface strain hypothesis should be favored. Indeed, as it was evidenced by Wei et al [46], the surface strain phenomenon affects significantly the metal-semiconductor phase transition of VO_2 nanobeams. This was sustained theoretically by Tselev et al. [4] while investigating the origin of ferroelastic domains in free-standing single crystal ferroelectric films. However, at room temperature only two oxide phases, VO_2 and VO_X (x~1), are insulating. All other oxide phases have already undergone the phase transition and are metallic. In terms of the bandgap Eg of single VO_2 (M1) nanocrystals and their temperature dependence, which is the cornerstone of this research paper, more quantitative assessments by STS are required via I-V single point measurements in the discontinuous thinnest VO_2 film. Indeed the bandgap Eg is determined from the extension of the flat section at the center of the dI/dV STS characteristics, while the spatial distribution of bandgaps can be visualized by setting a threshold tunneling current at a set voltage in the dI/dV curves from the grid measurement. As well established and reported by Yin et al [118], Eg values determined from the flat section are less prone to measurement errors in noisy data sets but are also systematically smaller by 0.1–0.3 eV than if one uses the inflection point method. The tunneling threshold current at a set voltage is uniquely linked to Eg, which has been confirmed in

a large number of I-V characteristics. Above T_C and as depicted by the curve at 358.5K, the I-V variation is nearly fully linear of an ohmic i.e. metallic type. At temperatures lower than T_C, the behavior is an obvious semiconductor type with a typical quasi-flat step I-V profiles. By correlating our result with the one of Kuchibhatla et al [117] who measures the conductivity of iodine doped polyaniline nanofibers, we observed a room temperature dependence temperature with enhancement of the current at negative gate voltage and suppressed at positive gate voltage. This is taken as a proof of charge carrier being the hole in the vanadium dioxide. The nonlinear trends in the I-V curve see figure 5.32 b), obtained is originated from the soliton tunneling conductivity in the material, which was found to be exponentially dependent on the potential barrier width. These step voltages are temperature dependent; hence confirming the expected variation of the bandgap of the single VO_2 nanocrystal with temperature Eg (T). Eg(T) which is approximately half of the flat step-voltage and is very large at lower temperature while decreasing rapidly at the vicinity of 343.5K. This temperature variation of the bandgap Eg(T), derived from the standard derivative dI/dV for various temperatures, is distinctly illustrated in figure 5.34. The junction field effect transistor consists of a conductive channel provided with two ohmic contacts one acting the source and the other one as the drain. When a positive voltage is applied to drain with respect to the source, the current flow from source to drain. The third electrode forms a rectifying junction with channel. The differences between the 25 °C and 50 °C curves, which present a distinct region of NDR, and the one at 65 °C is slightly different because the magnitude of peak to valley current ratio is determined by the scattering of the tunneling electrons within the well by phonons, interface roughness and other defects. The scattering of the phonons become important as the degradation of the peak to valley ratio degrade when the temperature increases. This is completely obtained at 85 °C where the material is fully metallic. This is what we call resonant tunneling devices. The temperature effect is used to distinguish the avalanche mechanism which has a positive temperature coefficient and the tunneling effect. Eg(T) temperature evolution can be splitted in 3 different regions. In region I, it decreases almost linearly while in

region III, its evolution in nearly exponential with temperature reaching zero value close to 358.5K. In region II (T range of 330-340K) i.e. in the vicinity of T_C, it decreases with a sharp decay. This type of temperature variation is certainly correlated to the singular 1st order phase transition of VO_2. However, one should point out 2 major concerns: (i) the value of Eg(T) in the room temperature range and, (ii) the observed temperature variation of Eg(T) itself. First, concerning the values of Eg(T) within room temperature range, even with the experimental bar-error of ±10%, the experimentally derived values of Eg(298.5K) and 323.5K are about ~0.93 and ~0.81 eV. Both are higher than the bulk value of ~0.7 eV. This difference could be due to the STS approach itself or/and either to other 3 major causes. As it was mentioned previously, the bandgap value Eg deduced from the I-V flat section are analytically different by 0.1–0.3 eV than if one uses the inflection point method. The tunneling threshold current at a set voltage is uniquely linked to the band gap. They correlated the asymmetry of the dI/dV curves to the defect doping of the VO_2 contributions from a tip induced band bending which can be the origin for this asymmetry. They attributed the prevalence of the regions with a band gap < 0.4eV to reduced oxides which are formed due to the loss of oxygen from the surface and a buildup of a large concentration of oxygen vacancies. They present also a variation in the local electronic structure of V_2O_3 which show that the electronic characteristics of a material are not always reflected in surface properties but the local defects can play a critical role. It was observed that the driving force of oxygen diffusion was linked to the chemical potential due to the coexistence of a wide range of oxide phases and also the presence of local strain fields which play a substantial role in phase separation. This first source of error has been minimized as the deduced Eg(T) values were averaged using in fact both I-V and dI/dV derived values. The 3 additional causes are: (i) the amorphous nature of the surface layer surrounding the investigated VO_2 single investigated nanoparticle, (ii) its oxygen substoichiometry due to surface effects such as breakdown of the 3-D symmetry and atomic coordination or to (iii) the strain/stress on it. In all three cases, this surface layer would act as a resistive component and hence would affect the effective value of the bandgap of the single VO_2

nanoparticle. This surface layer seems to exist in view of the inset zoom of the I-V curve at 358.5K. Indeed, this zoom shows clearly that the I-V evolution is not a complete ohmic type. The temperature dependance of I-V curve measured on nanograins VO$_2$ deposited on tin oxide substrate shows that with increasing temperature the MIT voltage decreases while the MIT current increases as indicated by the transition line. The right panel shows an excitation of holes with increasing temperature, which confirms the excitation nature of electrons due to thermal excitations. Near the transition temperature, the ohmic behavior is observed without any current jump at 85 ^{o} C comparatively to 65 ^{o} C which presents slightly current jump. This latter explains the existence of the nonmetallic phase or insulator with the monoclinic structure. According to Hyun-Tak Kim et al. [119] they observed an abrupt current jump without the structural phase transition at a given electric field for VO$_2$ films. The abrupt jump current was correlated to the abrupt Mott insulator without structural phase transition. This was observed by inducing internal holes charges of about 0.018% in the holes levels into conduction band with a source drain field or gate field. Yang et al. [120] develop vertical VO$_2$ on Ge substrates which have high mobility semiconductor. They show that the voltage triggered the MIT phase transition in VO$_2$ with a threshold voltage of 2.1V. They observed staircases discontinuity shapes due to grain boundary or domain related contributions to MIT with step-like shape emergence with critical voltage needed to initiate transition. Hence the Poole-Frenkel model (Ln I/V versus Sqrt V) show metallic behavior at large voltage ~3.1V. At intermediate bias voltage below the MIT temperature, the PF mechanism dominates the conduction with a linear dependence according to Yang. [120] Ohmic conduction was observed at low bias voltage with low temperature. Non stoichiometry defects present in VO$_2$ such as oxygen vacancies serve as localized traps required for the PF emission. K Martens et al [121] shows that the magnitude of the transition decreases for higher voltage and for thicker insulators VO$_2$ thin films with no abrupt transitions indicating absence of abrupt field. They observed a larger transition for a 2 nm 300 ^{o}C ALD HfO$_2$ insulator than the 200 ^{o}C ALD Al$_2$O$_3$ insulator and pointed transition degradation due to the influence of

the used of the insulator deposition on the underlying VO₂. The tunneling current allowed by the band gap insulator is modified by the MIT in VO₂ through a barrier which gives rise to a MIT tunnel junction disregarding the electron correlation at interface. In addition, in regard of the recent converging studies on VO₂, the surface strain hypothesis should be considered too. The first order Mott transition then leads to the sudden disappearance of the bandgap at 340K. These results are consistent with the crystalline distorsion model of Adler [122], which predicts a 4% decrease in zero temperature gap by Tc/2, and approximately a ~20% decrease just below Tc, if the bands are extremely narrow. The decrease of the bandgap which begins to become important at about 300K, should lead to an increase in the activation energy from the intrinsic value of ~0.39 eV to approximately ~0.47 eV In view of the slope of the electric conductivity lnσ as a function of $1/k_BT$ increases just below Tc. It was pointed out by Adler that if the crystalline distorsion model is correct, the decrease of the energy gap with increasing free carrier concentration begins to become significant just below Tc. Consequentially, the bandgap would be decreasing quadratically with T in the form of $Eg(T) \sim E_0 - A (k_BT)^2$. As reported in figure 5.34, the variation of Eg(T) seems to agree with such a temperature quadratic evolution(semi-dashed curve) in region II yet it is necessary to carry out more measurements at the vicinity of T_C to ensure a better statistics.
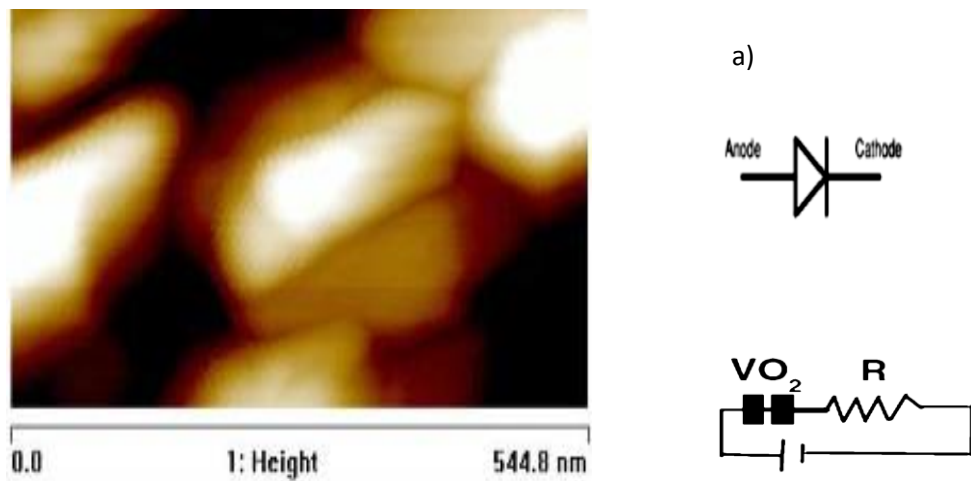
Figure 5.32: F: SnO₂ coating onto the glass substrates &the STM tip as the electrodes. a)
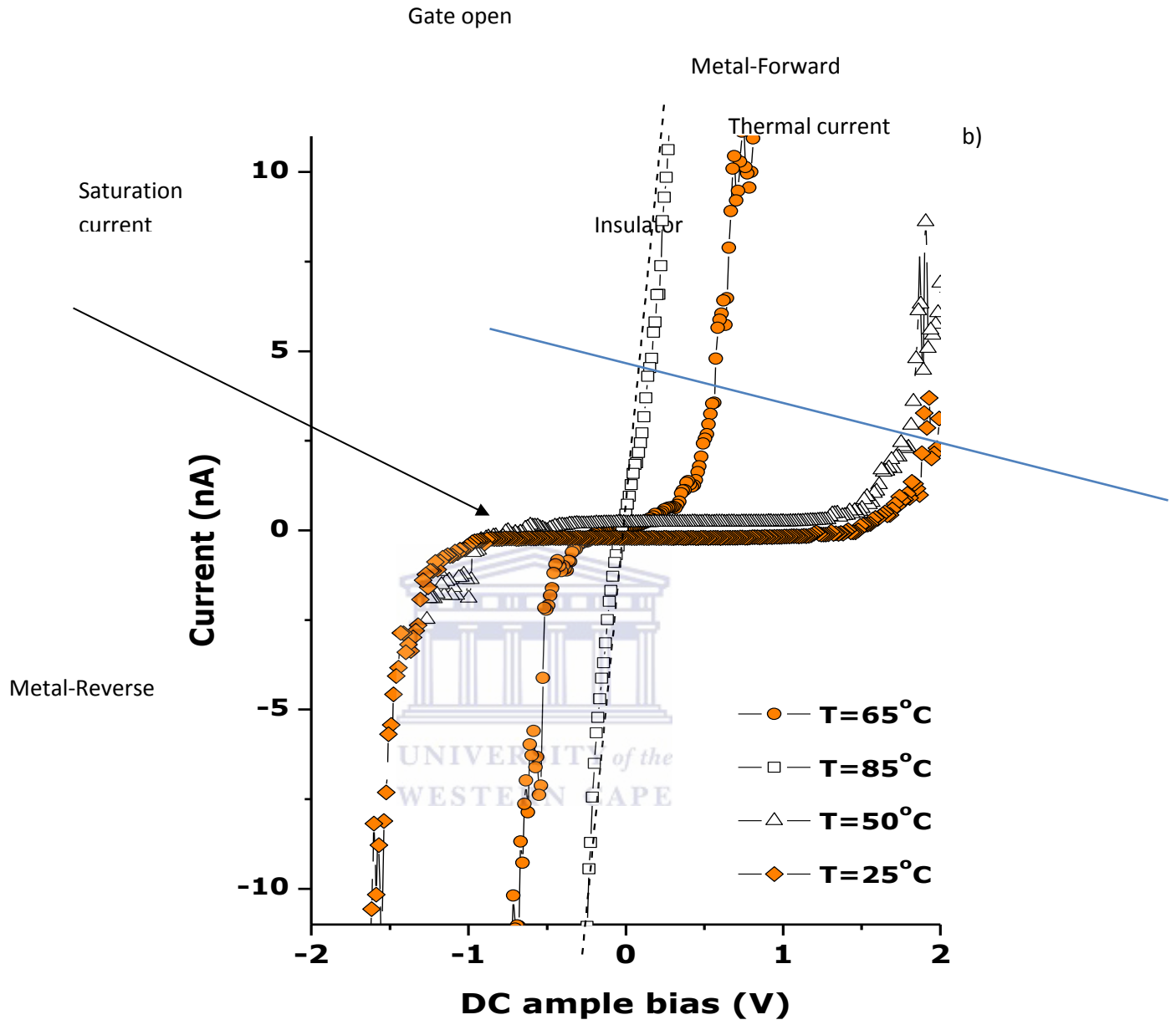
Figure 5.32: Shockley`s model of the junction field effect transistor b).
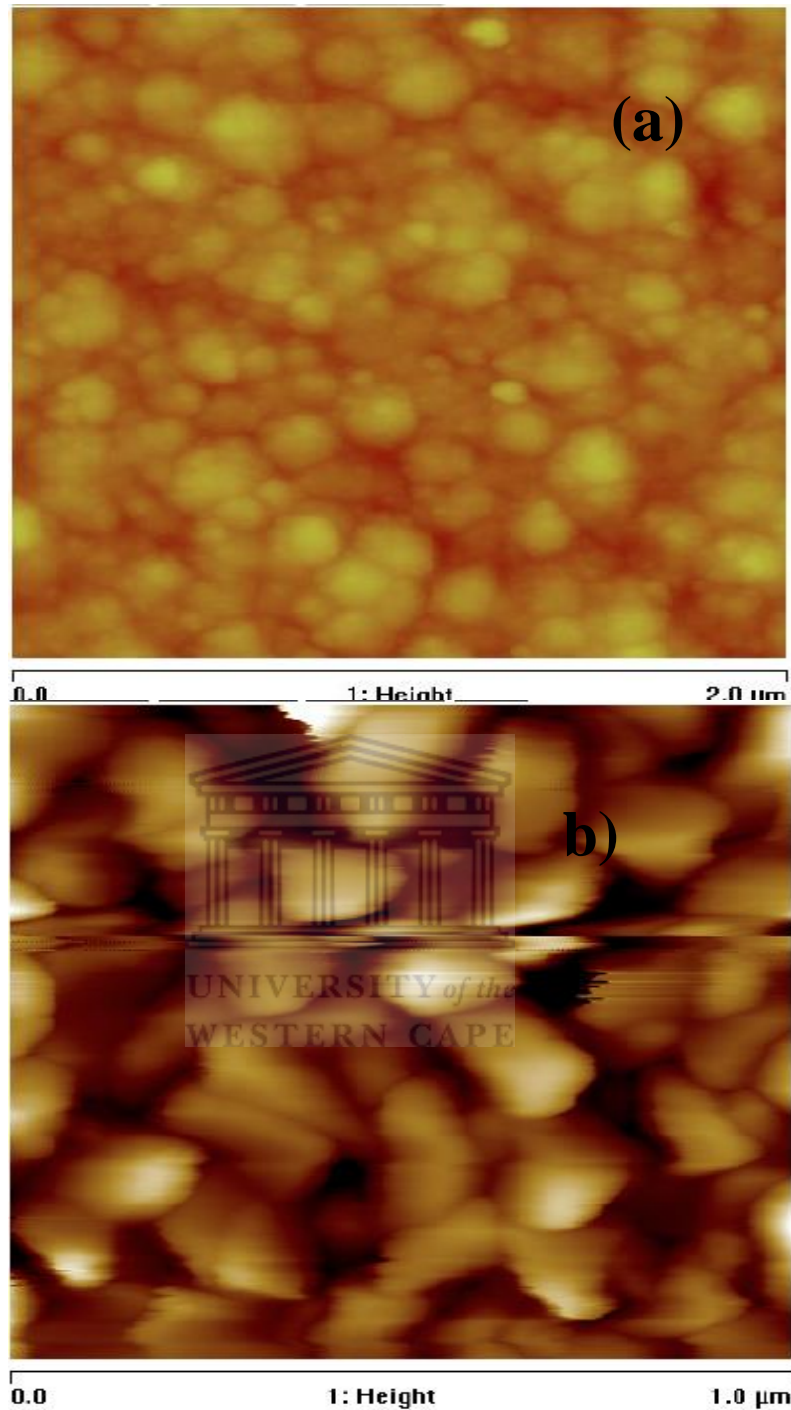
Figure 5.33: Scanning tunneling spectroscopy of the percolated VO_2 film (here the thickest film, 1218 nm±2 nm in size: (a) just below T_C (338.5K) and (b) above T_C (358.5K).

The energy band gap, contraily to the superconductor which is far smaller and result from an attractive force between the electrons in the lattice, is tied to the Brillouin zone. For a high field applied to p-n junction, a breakdown junction occurs conducting a very

large current. We have basically thermal instability, tunneling effect and avalanche multiplication.
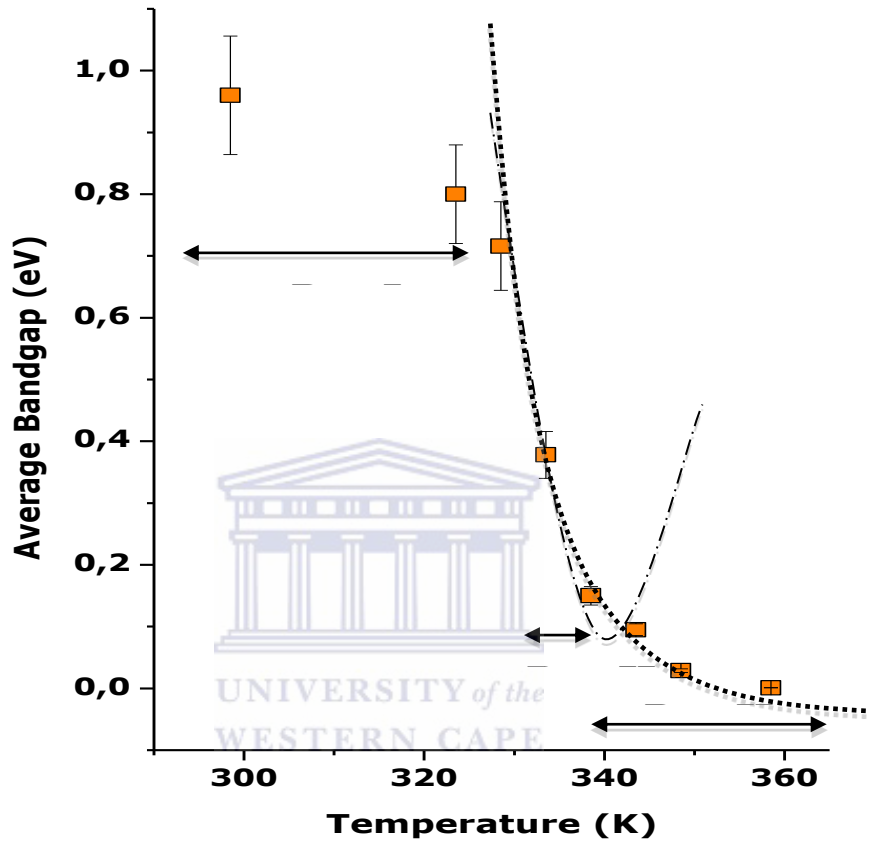
Figure 5.34: Band gap energy of VO₂ single nanograin.

5.4.1 Conclusion

The I-V behavior obtained in the single nanograin VO₂ describes the charge carrier originating from the soliton tunneling conductivity of the material with abrupt jump current correlated to the abrupt Mott insulator without structural phase transition. This was observed by inducing internal holes charges of about 0.018% in the holes levels into conduction band with a source drain field or gate field which make possible the semi-conductor to be used as high frequency oscillator (microwave).

5.4.2 References

[1] Whittaker, L.; Zhang, H.; and Banerjee, S.; *J. Mater. Chem.* 19, 2009, 2968

[2] Razavi, A.; Hughes, T.; Antinovitch, J.N.; and Hoffman, J.; *J. Vac. Sci. Technol. A,* 7(3) 1989

[3] Sendi, R.K.; Mahmud, S.; *Applied Surface Science* 258, 2012, 9954– 9960

[4] Tselev, A.; Strelcov, E.; Luk'yanchuk, I.; Budai, J.; Tischler, J.; Ivanov, I.; Jones, K.; Kalinin, P.; and Kolmakov, S.A.; *Nano Lett* 10, 2009, 2003-2011

[5] Bai, H.; Berkhan, M., and Cortie, M. B.; *Proceedings-31st Annual Condensed Matter and Materials Meeting*, 2007

[6] Lopez, R.; Haynes, T.E.; Boatner, L.A.; Feldman, L.C.; Haglund, R.F.; Jr; *Physical Review B,* 65, 2002, 224113

[7] Dai, L.; Cao, C.; Gao, Y.; Luo, H.; *Solar Energy & Solar Cells* 95, 2011, 712-715

[8] Jr, C.P.P.; Owens, F.J.; *Introduction to Nanotechnology*, Wiley- Interscience Publication, ISBN 0-471-07935-9 (cloth)

[9] Cao, J.; Ertekin, E.; Srinivasan, V.; Fan, W.; Huang, S.; Zheng, H.; Yim, J.W.L.; Khanal, D.R.; Ogletree, D.F.; Grossman, J.C.; and Wu, J.; *Nnano*, 4, 2009, 266

[10] Zhang, S; Shang, B.; Yan, J.; Yan, W.; Wei, S.; and Xie, Y.; *Phys.Chem.Chem.Phys.* 13, 2011, 15873- 15881

[11] Catti, M.; Ferraris, G.; Ivaldi, G.; *American Mineralogist*, 73, 1988, 1370-1376

[12] Wang, Y.L.; Li, M.C.; Zhao, L.C.; *Surface & Coatings Technology* 201, 2007, 6772– 6776

[13] Suh, J.Y.; Lopez, R.; Feldman, L.C.; and Haglund, R.F.; Jr; *Applied Physics*, 96(2), 2004

[14] Pauli, S.A.; Herger, R.; Willmott, P.R.; Donev, E.U.; Suh, J.Y.; and Haglund, R.F.; Jr; *Journal of Applied Physics* 102, 2007, 073527

[15] Klimov, V.A.; Timofeeva, I.O.; Khanin, S.D.; Shadrin, E.B.; Ilinski, A.V.; and Andrade, S.F.; *Tech. Phys.* 47, 2002, 1134

[16] Rozen, J.; Lopez, R.; Haglund, R.F.; Jr; and Feldman, L.C.; *Applied Physics Letters* 88, 2006, 081902

[17] Grinolds, M.S.; Lobastov, V.A.; Weissenrieder, J.; and Zewail, A.H.; *PNAS*, 103 (49), 2006, 18427-18431

[18] Guo, H.; Chen, K.; Oh, Y.; Wang, K.; Dejoie, C.; Asif, S.A.S.; Warren, O.L.; Shan, Z.W.; Wu, J.; and Minor, A.M.; *Nano let.* 11, 2011, 3207-3213

[19] Gu, Y.; Cao, J.; Wu, J.; and Chen, L.Q.; *Journal of Applied Physics* 108, 2010, 083517

[20] Wang, C.X.; Yang, G.W.; *Materials Science and Engineering* R 49, 2005, 157–202

[21] Okimora, K.; Sakai, J.; and Ramanathan, S.; *J. Appl. Phys.* 107, 2010, 063503

[22] Eguchi, R.; Taguchi, M.; Matsunami, M.; Horiba, K.; Yamamoto, K.; Chainani, A.; Takata, Y.; Yabashi, M.; Miwa , D.; Nishino , Y.; Tamasaku , K.; Ishikawa, T.; Senba , Y.; Ohashi , H.; Inoue, I.H.; Muraoka, Y.; Hiroi ,Z.; Shin, S.; *Journal of Electron Spectroscopy and Related Phenomena* 156–158, 2007, 421–425

[23] Pouget, J.P.; and H. Launois, H.; *Colloque C4, supplement* 10 (37), 1976, page C4-49

[24] Rice, T.M.; Launois, H.; Pouget, J.P.; *Phys. Rev. Lett.* 22 (1), 1994, 3042

[25] Gierer, M.; and Van Hove, M.A.; Goldman, A.I.; Z. Shen, Z.; Chang, S.L.; Jenks, C.J.; Zhang, C.M.; and Thiel, P.A.; *Phys.Reviews Letters* 78(3),1997

[26] Budai, J.D.; Tselev, A.; Tischler, J.Z.; Strelcov, E.; Kolmakov , A.; Liu , W.J.; Gupta, A.; Narayan, J.; *j.actamat.*, 074, 2012, 09

[27] Hu, B.B.; Ding, Y.; Chen, W.; Kulkarni, D.; Shen, Y.; Tsukruk, V.V.; and Wang, Z.L.; *Adv. Mater.* 2010, XX, 1–6

[28] Roytburd, A.; Slutsker, J.; *Physica B* 233, 1997, 390-396

[29] Zhang, S.; Chou, J.Y.; Lauhon, L.J.; *Nano Lett,* 9, 2009, 4527

[30] John, L.; Schlenker, G.V.; Gibbs; Boisen, M.B.; Jr; *Acta Cryst.*, A 34, 1978, 52-54

[31] Redfern, S.; and Saljie, E.; *J. Phys. C: Solid State Phys.* 21, 1988, 277-285

[32] Ungar, T.; Institute for General Physics, Eotvos University Budapest H-1445 Muzeumkrt. 6-8, Budapest VIII, P.O.B. 323, Hungary

[33] Appavoo, K.; Lei, D.Y.; Sonnefraud, Y.; Wang, B.; Pantelides, S.T.; Maier, S.A.; and Haglund, R.F.; Jr; *Nano Letters* 2011

[34] Qazilbash, M.M.; Brehm, M.; Chae, B.G.; Ho, P.C.; Andreev, G.O.; Kim, B.J.; Yun, S.J.; Balatsky, A.V.; Maple, M.B.; Keilmann, F.; Kim, H.T.; Basov, D.N.; *Science* 318,2007, 1750-1753

[35] Zhao, Y.; Lee, J.H.; Zhu, Y.; Nazari, M.; Chen, C.; Wang, H.; Bernussi, A.; Holtz, M.; and Zhaoyang, F.; *Journal of Applied Physics* 111,2012, 053533

[36] Nag, J.; Haglund, R.F.; Payzant, E.; and More, K.; *Cond-Mat1*, 3876, 2010,

[37] Okimura, K.; and Sakai, J.; *Japanese Journal of Applied Physics* 48, 2009,045504

[38] Cavalleri, A.; Dekorsy, T.; Chong, HHW. ; Kieffer, J.C.; and Schoenlein, R.W.; *Physical Review B* 70, 2004, 161102 (R)

[39] Tselev, A.; Luk`yanchuk, I.A.; Ivanov, I.N.; Budai, J.D.; Tischler, J.Z.; Strelcov, E.; Kolmakov, A.; and Kalinin, S.V.; *Nano Lett.*, 10, 2010, 4409-4416

[40] Han, T.; Aggarwal, R.; Gupta, A.; Zhou, H.; Narayan R.J.; and Narayan, J.; *Journal of Applied Physics* 107, 2010, 053514

[41] Jones, A.C.; Berweger, S.; Wei, J.; Cobden, D.; and Raschke, M.B.; *Nano Lett.* 10, 2010, 1574–1581

[42] Kim, S.; Kim, K.; Kang, C.J.; and Min, B.I.; *cond-mat.str-el* 2012, 1207

[43] Fan, W.; Huang, S.; Cao, J.; Ertekin, E.; Barrett, C.; Khana, D.R. Grossman, J.C.; and J. Wu, J.; *Physical Review, B* 80, 2009, 241105 (R)

[44] Mun, B.S.; Yoon, J.; Mo, S.K.; Chen, K.; Tamura, N.; Dejoie, C.; Kunz, M.; Liu, Z.; Park, C.; Moon, K.; and Ju, H.Y.; *Applied Physics Letters* 103, 2013, 061902

[45] Cowley, R.A.; *Advances in Physics*, 29 (1), 1980, 1-110

[46] Wei, W.F.; -Song, Z.X.; LiLan; Ping, X.J.; -Liang, Z.Y.; Liu Pei, L.; *Chin. Phys. Lett.* 28 (7), 2011, 077803

[47] Wang X.J.; Li, H.D.; Fei, Y.J.; Wang, X.; Xiong, Y.Y.; Nie, Y.X.; Feng, K.A.; *Applied Surface Science*, 177, 2001, 8-14

[48] Santagelo, S.; Messina, G.; Faggio, G.; Willinger, M.G.; Pinna, N.; Donato, A.; Arena, A.; Donato, N.; Neri, G.; *Diamond and Related Materials* 19, 2010, 590-594

[49] Parker J.C.; et al., *Phys. Rev., B Condens. Matter* 42 (5), 1990, 3164-3166

[50] Gweon, G.H.; Park, J.G.; and Oh, S.J.; *Phys. Rev. B*, 48, 1993, 7825

[51] Olovsson, W.; *Department of Materials Science and Engineering, Kyoto University, Sakyo, Kyoto* 606-8501,Japan, C. Goransson, T.Marten, and I.A. Abrikosov Department of Physics, Chemistry and Biology, Link• oping University, SE-581 83 Linkoping,Sweden-9 Scientific highlight of the month"*Core-Level Shifts in Complex Metallic Systems from First Principles*.

[52] Silversmit, G.; Depla, D.; Poelman, H.; Marin, G.B.; Gryse, R.D.; *Journal of Electron Spectroscopy and Related Phenomena* 135, 2004,167–175

[53] Kurmaev, E.Z.; Cherkashenko,V.M.; Yarmoshenko, Y.M.; Bartkowski, S.; Postnikov, A.V.; Neumann, M.; Duda, L.C.; Guo, J.H.; Nordgren, J.; Perelyaev, V.A.; and Reichelt, W.; *cond-mat.mtrl-sci*, 1998

[54] http://ec.europa.eu/research/energy/2013].

[55] Ramirez, H.F.; Prades , J.D.; Diaz , R.J.; Fischer , T.; Rodriguez, A.R.; Mathur, S.; and Morante, J.R.; *Phys. Chem. Chem. Phys.*,11, 2009, 7105-7110

[56] Yamazoe, N.; *Sensors and Actuators B* 108, 2005, 2–14

[57] Kiriakidis, G.; Moschovis, K.; and Sadale, S.B.; *Sensors for environment, health and security*, M.I. Baraton Editor, NATO Science for Peace and Security Series C: Environmental Security, I, 2009, 159-178

[58] Kim, W.S.; Kim, H.C.; and Hong, S.H.; *J. Nanoparticles Research*, 12(5), 2010, 1889-1896

[59] Joshi, R.K.; Kruis, F.E.; and O. Dmitrieva, O.; *J. Nanoparticles Research*, 8(6), 2006, 797-808

[60] Pan, Z.W.; Dai, Z.R.; Wang, Z.L.; *Science* 291, 2001, 1947–1949

[61] Cui, Y.; C.M. Lieber, *Science* 291, 2001, 851–853

[62] Comini, E.; Faglia, G.; Sberveglieri, G.; Calestani, D.; Zanotti, L.; Zha, M.; *Sens. Actuat. B* , 111–112, 2005, 2–6

[63] Comini, E.; Faglia, G.; Sberveglieri, G.; Pan, Z.W.; Wang, Z.L.; *Appl. Phys. Lett.*, 81 2002, 1869–1871

[64] Kolmakov, A.; Klenov, D.O.; Lilach, Y.; Stemmer, S.; Moskovits, S.; *Nano Lett.*, 5 2005, 667–673.

[65] Tien, L.C.; Wang, H.T.; Kang, B.S.; Ren, F.; Sadik, P.W.; Norton, D.P.; Pearton, S.J.; *J. Lin, Electrochem. Solid State* 8, 2005, G230–G232

[66] Lv, Y.Z.; Guo, L.; Xu, H.B.; Chu, F.; *Physica E* 36, 2007, 102–105

[67] Sberveglieri, G.; Baratto, C.; Comini, E.; Faglia, G.; Ferroni, M.; Ponzoni, A.; Vomiero, A.; *Sens. Actuat. B* 121, 2007, 208–213

[68] Röhlig,C.; Cimalla, V.; Stauden, T.; Ambacher, O.; *Sens. Actuat. B* 130, 2008,589–593

[69] Rout, C.S.; Hegde, M. ; Rao, C.N.R. ; *Sens. Actuat. B* 128, 2008, 488–493

[70] Rout, C.S. ; Govindaraj, A. ; Rao, C.N.R. ; *J. Mater. Chem.* 16, 2006, 3936–3941

[71] Liu, Z.F.; Yamazaki, T.; Shen, Y.B.; Kikuta, T.; Nakatani, N.; Li, Y.X.; *Sens. Actuat. B* 129, 2008, 666–670

[72] L.C. Tien, L.C.; P.W. Sadik, P.W.; D.P. Norton, D.P.; L.F. Voss; L.F.; S.J. Pearton, S.J.; H.T. Wang, H.T.; B.S. Kang, B.S.; F. Ren, F.; J.Jun, J.; J. Lin, *Appl. Phys. Lett.*, 87, 2005, 222106

[73] Wang, H.T.; Kang, B.S.; Ren, F.; Tien, L.C.; Sadik, P.W.; Norton, D.P.; Pearton, S.J.; Lin; *Appl. Phys. Lett.,* 86, 2005, 243503

[74] Ramgir, N.S; Mulla, I.S.; Vijayamohanan, K.P.; *Sens. Actuat. B*, 107, 2005, 708–715

[75] Neri, G.; Bonavita, A.; Micali, G.; Rizzo, G.; Pinna, N.; Niederberger,M.; *Sens. Actuat. B*, 127, 2007, 455–462

[76] Raible, I.; Burghard, M.; Schlecht, U.; Yasuda, A.; Vossmeyer, T.; *Sensors and Actuators B* 106, 2005, 730-735

[77] Baik, J.M.; Kim, M.H.; Larson, C.; Yavuz, C.T.; Stucky, G.D.; Wodtke, A.M.; and Moskovits, M.; *Nano Letters*, 9, 2009, 3980-3984

[78] Manno, D.; Serra, A.; Giulio, M.D. ; Micocci, G. ; Taurino, A. ; Tepore, A. ; Berti, D. ; *J. Appl. Phys.*, 81(6), 1997, 2709

[79] Strelcov, E.; Lilach, Y.; and Kolmakov, A.; *Nano letters,* 9 (6), 2009, 2322-2326

[80] Yin, H.; Yu, K.; Zhang, Z.; Zeng, M.; Lou, L.; Zhu, Z.; *Electroanalysis*, 23 (7), 2011, 1752-1758

[81] Leroux, C.; Nihoul, G.; Tendeloo, G.V.; *Physica Review B*, 57, 1998, 9.

[82] Li, M.; Kong, F.; Li, L.; Zhang, Y.; Chen, L.; Yan, W.; and Li, G.; *Dalton Trans.*, 40, 2011, 10961

[83] Zhang, S.; Shang, B.; Yan, J.; Yan, W.; Wei, S.; and Xie, Y.; *Phys.Chem.Chem.Phys.* 13, 2011, 15873-15881.

[84] Simo, A.; Madjoe, R.; Otu, L.E.; Maaza, M.; *Mater. Res. Soc. Symp. Proc.*, 1406 © 2012 Materials Research SocietyDOI: 10.1557/opl.2012.192

[85] Okimura, K.; and Kubo, N.; *Japanesse J. Appl. Phys.*, 44, 2005, 1150

[86] Eyert, V.; *Europhys. Lett* 58, 2002, 851.

[87] Maaza, M.; Bouziane, K.; & Maritz, J.; *Optical Materials*, 15, 2000, 41.

[88] Takahashi, I.; Hibino, M.; Kudo, T.; *Japanese J. Applied Physics,* 40 (3), 2001, 1391–1395.

[89] Kana Kana, J.B.; Ndjaka, J.M.; Vignaud,G.; Gibaud, A.; M. Maaza, M.; *Optics Comms*, 284, 2011, 807-812.

[90] Lysenko, S.; Vikhnin, V.; Fernandez, F.; Rua, A.; and Liu, H.; *Phys. Rev. B*, 75, 2007, 075109.

[91] Wang, H.; Yi, X.; Chen, S.; Fu, X.; *Sensors and Actuators A*, 122, 2005, 108–112.

[92] Wang, H.; X. Yi, X.; Chen, S.; *Infrared Physics & Technology*, 47, 2006, 273–277.

[93] Morin, F.J.; *Phys. Rev. Lett.,* 3, 1959, 34.

[94] Goodenough, J.B.; *Phys. Rev.,* 117 1960, 1442.

[95] Goodenough, J.B.; *Metallic Oxides*, Ed. H. Reiss, Pergamon Press, Oxford, 1971, 145

[96] Zylbersztejn A.; and Mott, N.F.; *Phys. Rev.B*. 11, 1975, 4383.

[97] Cavalleri, A.; Toth, C.; Siders, C.W.; Squier, J.; Raski, F.; Kieffer, J.; *Phys. Rev. Lett.* 87, 2001, 237401.

[98] Cavalleri, A.; Dekorsy, T.; Chong, H.; Kieffer, J.C.; Schoenlein, R.W.; *Phys Rev. B 70*, 2004, 161102.

[99] Lysenko, S.; Rua, A.J.; Vikhnin, V.; Jimenez, J.; Fernandez, F.; Liu, H.; *App. Surf. Sci.* 252, 2006, 5512.

[100] Sella, C.; Maaza, M.; Nemraoui, O.; and Lafait, J.; *Surface & Coating Technology.*98, 1998, 1477.

[101] Chen, S.; Ma, H.; Yi, X.; Wang, H.; Tao, X.; Chen, M.; Li, X.; Ke, C.; *Infrared Phys. & Tech.* 45, 2004, 239.

[102] Maaza, M.; Hamidi, D.; Simo, A.; Kerdja, T.; Chaudhary, A.K.; J.B. Kana Kana, J.B.; *Optics Comms.,* 285, 2012, 1190-1193.

[103] Balberbg, I.; Trokman, S.; *J. Appl. Phys.,* 4, 1975, 2111.

[104] Maaza, M.; Sella, C.; Baruch-Barak, B.; Ouassini, N.; and Beye, A.; *Optics Comms.,* 254 ,2005, 188.

[105] Maaza, M.; Ouassini, N.; Sella, C.; & A.C.Beye, A.C.; *Gold Bulletin*, 38, 2005, 3.

[106] Romeu, D.; Gomez, A.; and Gasga, J.R.; *Electron Diffraction and HRTEM Structure Analysis of Nanowires, Nanowires* - Fundamental Research, Dr. Abbass Hashim (Ed.), ISBN: 978-953-307-327-9, 2011.

[107] Bochenkov,V.V.E.; Sergeev, G.B.; *Metal Oxide Nanostructures and their Applications,* 2010, 31-52.

[108] Huang, J.; and Wan, Q.; *Review Sensors,* 2009, 9903-9924.

[109] Tien, L.C.; Wang, H.T.; Kang, B.S.; Ren, F.; Sadik, P.W.; Norton, D.P.; Pearton, S.J.; Lin, J.; *Electrochem. Solid State*, 8, 2005, G230–G232.

[110] Lev, Y.Z.; Guo, L.; Xu, H.B.; Chu, X.F.; *Physica E*, 36, 2007,102–105.

[111] Allen, P.B.; *Contemporary Concepts of Condensed Matter Science*, Conceptual Foundations of Materials: A Standard Model for Ground- and Excited-State Properties Copyright © Published by Elsevier B.V., 2006.

[112] Esaki, L.; *Phys. Rev.* 109, 1958, 603.

[113] Frova, A.; *Physics of Modern Materials*, *Lectures presented at International Course Trieste,* 29 March-24 June 1978, IAEA Vienna March 1980.

[114] Sze, S.M.; *Physics of semiconductor device*, A Wiley-Interscience Publication." Includes index, I. Semiconductors. I. Title. Copyright, 1981 by John Wiley &Sons, Inc 1936.

[115] Zylberstejn, A.; Mott, N.F.; *Phys. Rev. B*, 11, 1975, 4383.

[116] Felde, B.; Niessner, W.; Schalch, D.; Scharmalm, A.; Werling, M.; *Thin Solid Films*, 305, 1997, 61-65.

[117] Kuchibhatla, S.V.N.T.; Karakoti, A. S.; Bera, D.; Seal, S.;   *Progress in Materials Science* 52, 2007, 699–913.

[118] Yin, W.; Wolf, S.; Ko, C.; Ramanathan, S.; and Reinke, P.; *Jounal of Applied Physics* 109, 2011, 024311.

[119] Kim, H.T.; Chae, B.-G.; Youn, D.H.; Maeng, S.L.; Kim, G.; Kang, K.Y.; and Lim, Y.S.; *New Journal of Physics* 6, 2004, 52.

[120] Yang, Z.; Ko, C.; and Ramanathan, S.; *Journal of Applied Physics*, 108, 2010, 073708.

[121] Martens, K.; Radu, I.P.; Mertens, S.; Shi, X.; Nyns, L.; Cosemans, S.; Favia, P.; Bender, H.; Conard, T.; Schaekers, M.; Gendt, S. D.; Afanas'ev, V.; Kittl, J.A.; Heyns, M.; and Jurczak, M.; *Journal of Applied Physics* 112, 2012, 124501.

[122]   Adler, D.; *Solid State Physics, Advances in Research and Applications Series*, Eds. F. Seitz, D. Turnbull & H. Ehrenreich, 21, 1968,1.

CHAPTER SIX:

GENERAL CONCLUSIONS & OUTLOOK

The findings obtained within this thesis contribute primarily in the understanding of the metal insulator phase mechanism with coexistence of differents crystallographic change present in our material which shows the presence of the intermediate phase M2 coexisting between M1 and R. This was proved through the thermodynamic of stress-Temperature fitted with the Clausius-Claperyon equation giving the new transformation temperature under uniaxial stress. This latter was confirmed with the theory of Landau describing structural phase transition as the presence of distortions given by a single normal mode order of parameter. The mechanism confirms the association of latent heat with the phase transition. Hence the study proves our material to be used directly as ultrasensitive transition edge-sensors and fast optical shutters. Additionally, the strong size effect dependence was studied which affects the thermal calorimetric heating and cooling cycles of the system, that we study with the influence of the free energy, the strong correlation between the energy band gap associated to the working temperature. It was observed that the Metal Insulator transition phase transformation is a diffusionless first-order phase where the nucleation rather than the propagation controls the overall kinetics of the phase transformation due to the grain boundary angle. Also, we explore the strong size effect on the thermal calorimetry cooling and heating cycles with 60.4 $^{\circ}$C comparing to 67.1 $^{\circ}$C which was attributed to elastic stored energy and some untransformed metallic phase. It was observed that smaller particles have low probability to contain nucleation site. Hence they need great thermal driving force to become activated. This phenomenon was confirmed through thermodynamic of nucleation in the case where our material is 2D dimension. Then , by means of synthesis techniques, we were able to reproduce nanobelts VO_2 with planar surface through sol-gel technique method at low working temperature with high surface to volume ratio and we discovered the unexpected room temperature enhanced hydrogen sensing properties of vanadium dioxide VO_2 tetragonal (n type

semiconductor) in their nanobelt form. This latter present a relatively limit detection of about 0.17ppm, which is good enough for potential commercialization and an optimum sensitivity at 90 ppm comparing to 140, 50, 0.17 ppm due to the variation of the resistance of our sample and it presents good gas selectivity and sensitivity relatively to CO and CO_2 gas. Response Times obtained are ~840, ~890, ~1080, ~1020, and ~1050 seconds for 140, 90, 50, 14 and 0.17 ppm of H_2 respectively. Likewise, the corresponding average recovery times are: ~455, ~870, ~1020, ~1037, and ~2080 seconds for 140, 90, 50, 14 and 0.17 ppm of H_2 respectively. By comparison, the H_2 sensing of the equivalent oxide system i.e. ZnO nanorods, these latter possess a room temperature response time of the order of 600 seconds for 500 ppm H_2. This induces a direct application as gas sensor device at High hydrogen gas sensing capabilities within the ppm level for the first time. Finally, we studied the energy band gap models associated to the different phases of our sample with the electronic transport on single nanocrystals of VO_2. The abrupt jump current observed was strongly correlated to the internal holes charges in the holes level of the conduction band through source drain field. The Mott transition associated to the electronical changes is consistent with the crystalline distorsion model of Adler which states that the decrease of energy band gap with increasing free carrier concentration is significant below the transition temperature Tc. These latter shows that it would be possible to make a single nanocrystal as a H_2 gas sensing device. It is true that the outcome of this research has bring important results if not novelty in the nanotechnology field of science regarding our contribution of potential application of VO_2 (A) as gas sensor and with any exploratory endeavor, the work is not final. Further work needs to be done regarding potential new set of size effects giving quantum confinement issues and develop different sensors devices with optimization of sensing response at low temperature. If this contribution demonstrated the H_2 sensing efficiency of VO_2 (A) nanobelts at room temperature relatively to corresponding 1-D oxides in general, various issues are still to be addressed. Among these, one should mention the following:

(i)   The sensing properties below and at the vicinity of the semiconductor-metal transition as the $VO_2(A)$ is a Mott oxide with a MIT temperature above 69 °C,

(ii)   Sensitivity to humidity which is well known to influence the performance of semiconducting gas sensors should be investigated. This would be addressed through the selection of a high operating temperature that is naturally smaller than Tc and

(iii)   The need to enlarge the sensor's selectivity for H_2S, NH_3, and C_2H_5OH gases. Follow up investigations would address all these issues by combining selected laser spectroscopy and synchrotron surface-interface characterization techniques.

APPENDIX

In general, characterizations techniques are used to establish a correlation between the structure, shape and chemical composition of nanomaterial which have been obtained in processing with their properties.

1) Scanning Electron Microscopy

Electron microscope uses a beam of highly energetic electron which is produced to examine objects on a very fine scale. The electron beam strikes the sample and causes both electron and photons to be emitted which for example give topographical, composition, electrical information about the sample. Among second electrons which are generated some of them escape the surface of the specimen. They are detected by an electron detector. The outgoing signals from the electron detector are proportional to the number of detected electron and give the intensity of the electron beam in the picture tube and topographic picture of the object.
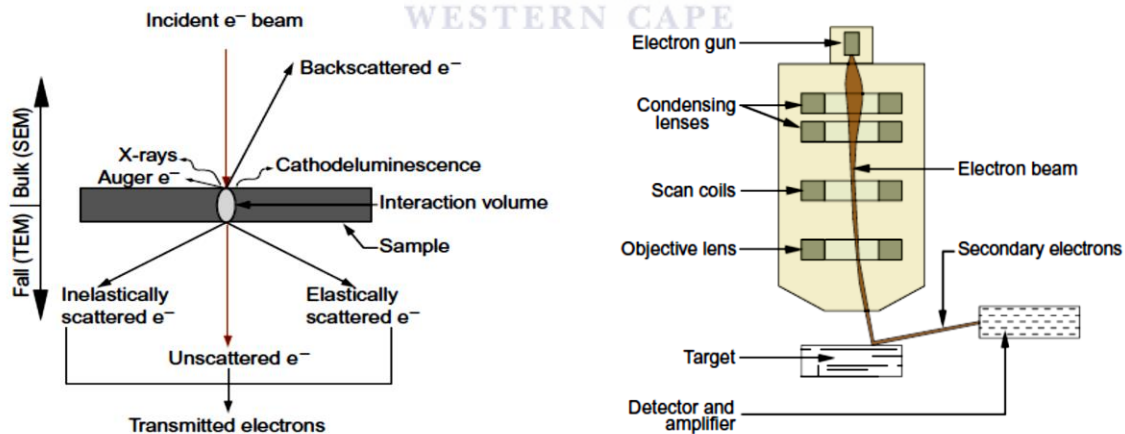
Figure 1: Various specimen-beams electrons interactions and schematic diagram of an operation of SEM [1].

Signals emitted from the sample as result of specimen-primary electron beam interaction include backscattered electrons and x-rays. The brightness is proportional to the average atomic number Z of a phase [2].

2) Differential Scanning Calorimetry

DSC is a thermal analysis instrument which determines the temperature and heat flow associated with the material transitions as a function of time and temperature in a controlled atmosphere giving quantitative and qualitative information about chemical and physical changes involving endothermic and exothermic processes or changes in heat capacity. The DSC technique presents many types of applications such as thermosetting materials, pore size distribution, chemical reactions [3] and production of controlled transformation [4]. 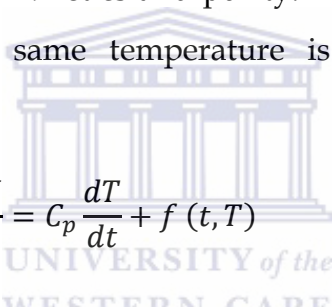It gives accurate information concerning the glass transitions, melting and boiling points, crystallization time and temperature, percent crystallinity, heats of fusion and reactions, Specific heat, oxides and thermal stability, rate and degree of cure, reaction kinetics and purity. The difference in heat flow to the sample and reference at the same temperature is recorded as function of the temperature.

$$\frac{dH}{dt} = C_p \frac{dT}{dt} + f(t,T) \qquad\qquad Eq.1$$

Where $\frac{dH}{dt}$ represents the heat flow measured by the calorimeter, Cp is the specific heat capacity, $\frac{dT}{dt}$ is the underlying heating rate, f (T,t) is the kinetic response of the sample. The crystallization in the material is generally a two steps process: nucleation and growth where the onset temperature is the nucleation temperature and the maximum peak is the crystallization temperature. The crystallization can be treated using the Johnson-Mehl Avrami equation:

$$f = 1 - exp[-(kt)^n] \qquad\qquad Eq.2$$

F is the crystalline fraction after an annealing time t and k is a rate coefficient. N is function of the nuclei growing dimension. The percentage of crystallinity is generally given:

$$\% \, crystallinity = 100 \, \Delta H_m / \Delta H_{lit} \qquad\qquad Eq.3$$

ΔH_m is the enthalpy of melting for 100% crystalline material.
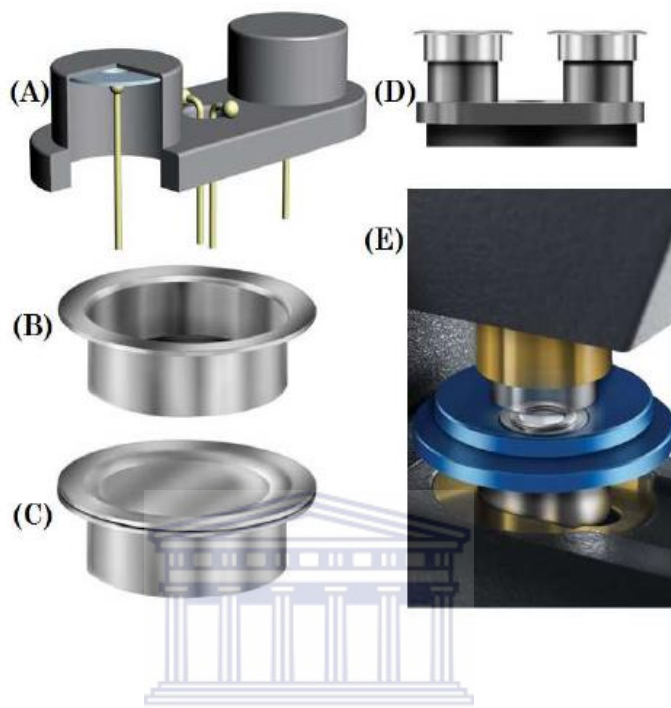
Figure 2: A) DSC sample stage connected with the water, B) Hermetic pan and C) Hermetic pan attached with lead, D) Pans on the sample stage shown on A) one is the sample pan and the other is the reference pan E) DSC T zero press which takes sample encapsulation to a new level of performance and convenience in crimp and hermetic sealing of a wide variety of material [5].

3) X-Ray Photoelectron Spectroscopy

Probe of the interactions between electrons in atoms, molecules, and solids and as a diagnostic way for acquiring information about unpaired spin in chemical systems are possible through multiplet splitting of core-level peaks in x-ray photoemission (XPS) spectra [6]. XPS is a widely used technique to investigate the chemical composition of surfaces and make use of the electronic photoemission. It consists of an adsorption of an

X ray photon by the core electron of an atom. With sufficient photon energy, the core electron escapes from the atom and emit out of the surface [7-12]. See figure 3.
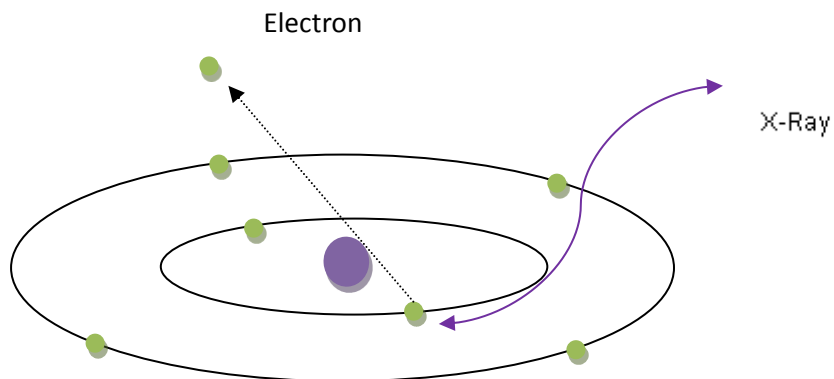
Figure 3: XPS scheme interaction [10].

In XPS, the sample is irradiated with low-energy (~1.5 keV) X-rays, in order to provoke the photoelectric effect. The energy spectrum of the emitted photoelectrons is determined by means of a high-resolution electron spectrometer. The sample analysis is conducted in a vacuum chamber, under the best vacuum conditions achievable, typically ~10^{-7} torr. This facilitates the transmission of the photoelectrons to the analyzer but more importantly minimizes the re-contamination rate of a freshly cleaned sample. This is crucial because XPS is very surface-sensitive, with a typical "sampling depth" of only a few nanometers. Multiplet splitting is expected to be observed in an XPS spectrum if the specimen possesses unpaired electrons in its outer valence shells. The splitting arises upon ejection of the core electron which can couple with the open valence shell forming multiplet of different energy (possible angular momentum configurations) given by Van Vleck's theorem:

$$\Delta E_{n,s} = \frac{2S + 1}{2l + 1} G^l(ns, n`l) \qquad Eq. 4$$

S is the initial state-spin formed by coupling n`l electrons, $G^1$ is the atomic exchange integral, the principal quantum numbers can be equal (n and n`).

However other considerations are required to describe completely the photoemission experiment such as intrashell correlation and charge transfer splitting. Bagus et al. [13] introduce intrashell correlation to resolve forth discrepancies in the energy separation and intensity ratio of peaks in spin orbit splitting. They focused on the final state excitation $3s3d^n \rightarrow 3p^23d^{n+1}$ and $3s3d^n \rightarrow 3s3p^23d^{n+2}$. Charge transfer splitting result from the Coulomb interaction between the core hole and ligand. Core electrons refer to electron which is tightly bound to the atomic nucleus characterized by the binding energy E_B. They are sensitive to the atomic species of the chemical environment and give an idea to the physical properties of the electronic structure and bonding of the system (structural determination) and the effect of disorder broadening of the core spectral lines (differences in binding energies due to local environment). Transition metals compounds (TMC) have been a subject of study for many years because of their diverse physical properties. In spite of their apparently similar electronic structures, having unfilled 3d shells, their electrical conductivities vary widely from metallic to insulating behavior, and they show besides diverse magnetic properties. According to independent electron band theory most of TMCs should be metallic because of their unfilled 3d shells. Some of them are indeed metals, but many compounds are insulators (CuO, NiF_2, NiO, and $CrCl3$) or subject to metal-to-nonmetal transitions (NiS, V_2O_3, Ti_2O_3) depending on temperature or pressure.

4) Transmission Electron Microscopy

The electron beam which is irradiating the sample is manipulated through magnetic lenses and solenoids where the electrons travel along the symmetry axis. The circular motion of the electrons around the axis and the transversal component of the magnetic field are responsible of the pointing force towards the center of the lens. The capacity to control the point focus through the electric current represents the key to electron microscopy. The objective lens just below the specimen forms an intermediate image with 20 to 50 times in its image plane. The rays that leave the specimen are collected in the back focal plane of the objective lens. The viewing of the planes can be projected on

the screen by a second lens. The diffraction pattern is observed through the projection of the back focal plane where the objective aperture is located, allowing single spots for image formation. According to the scattering of the electrons, two types of image are obtained: bright field image due to the unscattered electrons beam and dark field image due to the scattered electrons [14]. Due to the truncation of the Fourier coefficients due to the smallest aperture used in DF and BF, high resolution is required HRTEM. This latter gives plane spacing on an atomic scale where lattice fringes appear in one or more directions. At the nanoscale level, the fringes represent tunnels between column of atoms and atoms in the DF and BF respectively. Orientation contrast in a bright field or dark field micrographs yields only a qualitative representation of the true grain structure. Grains of same orientation have different intensity due to local variations in thickness while those of different orientations have same intensity. TEM provide dislocation density which measure the stored deformation energy in a grain [15].
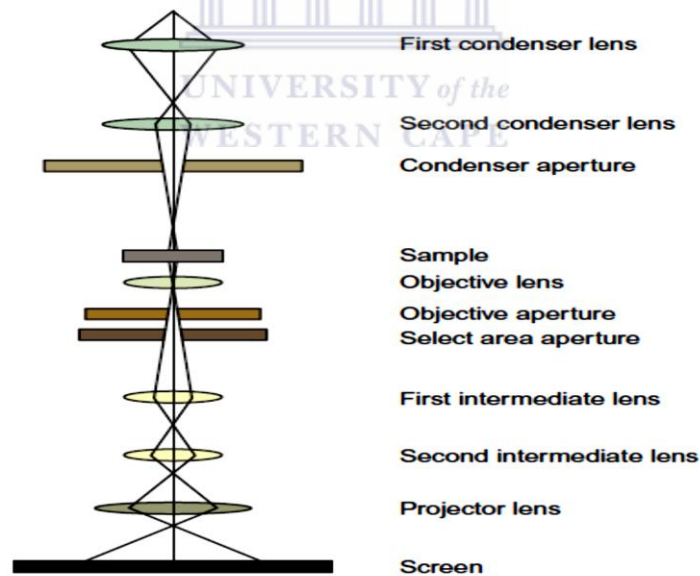
Figure 4: Diagram operation of a TEM [1].

In the case of thick sample, bright and dark fields are interchanged. HRTEM images can be simulated by the Gauss profiles at positions given by 2D Bravais lattice. In the

absence of deficiencies from the microscope, the brightness at a position x/y in the micrograph due to the tunnel at a position p/q is therefore given as:

$$exp\left(-c((x-p)^2 + (y-q)^2)\right) \qquad Eq.5$$

5) Fourier Transform Infrared Spectroscopy (FTIR-ATR)

Infrared spectrum is considered as a fingerprint to identify by the comparison to an unknown reference spectra. Infrared spectrum is generally formed due to the absorption of electromagnetic radiation at frequencies which correlate to the vibration of specific sets of chemical bonds from within the molecule. The sum of the contributing energy terms possessed by a molecule at any given moment is:

$$E_{total} = E_{electronique} + E_{vibrational} + E_{rotational} + E_{translational} \qquad Eq.6$$

The vibrational energy component is a higher energy term and corresponds to the absorption of energy by a molecule as the components atoms vibrate about the mean center of their chemical bonds [16]. The vibrational energy is given on the basis of simple harmonic oscillator and its modification to account for anharmonicity which suffice to explain the origin of many of characteristic frequencies that are assigned to particular combinations of atoms within the molecule. According to Hooke`s law:

$$v = \frac{1}{2\pi c}\sqrt{\frac{\kappa}{\mu}} \qquad Eq.7$$

v is the fumdamental vibration frequency, κ force constant and μ is the reduced mass. All the possible variants of the vibrational motions of the molecule can be reduced to the number of normal modes of vibration determined by:

$$number\ of\ normal\ modes = 3N - 6\ for\ nonlinear\ molecule \qquad Eq.8$$

$$number\ of\ normal\ modes = 3N - 5\ for\ linear\ molecule \qquad Eq.9$$

N is the number of components atoms in the molecule.

The FT-IR spectrum is an application of Fourier`s integral theorems in which a complex wave functions (interferograms) is transformed into an optical spectrum [17]. The most commonly used is the Michelson interferometer (see figure 5) which consists of a fixed mirror Mf, and a movable mirror Mm. A beam splitter Bs bisects the two mirrors at an angle 45 º which ideally transmits half and reflects half of the incoming radiation. The two beams are then reflected where the amplitudes are combined and exit from the interferometer to the detector. In the case of polychromatic light source is used, the output is a cosine function due to the interference caused by all simultaneous frequencies.

$$I(v) = \int_{-\infty}^{+\infty} \cos(2\pi v) I(x) . dx \qquad Eq. 10$$

$I(x)$ is the interferogram function of the mirror displacement x and $I(v)$ is the intensity of the source of the spectrum frequency v .
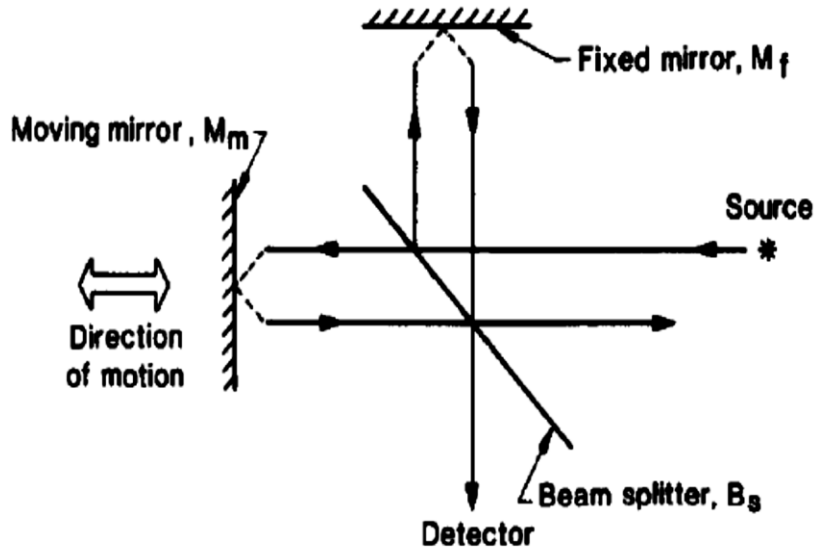

Figure 5: Diagram of Michelson interferometer [18].

The composition of the crystal state is given. We have absorption bands of silicon crystal with optical and acoustical vibrational modes at 610 cm^{-1} and 739 cm^{-1}. The presence of impurity of carbon and oxygen are present at 1106 cm^{-1} for Si-O-Si and 604.9 cm^{-1} for carbon. Weak absorption bands of vanadium oxides near 400 cm^{-1} (V-O) bond 440 cm^{-1}. 690 cm^{-1} appears for VO_2 (M). 717 cm^{-1} is characteristic of first rutile packing of octahedral which is the band of VO_2; 490 and 840 cm^{-1} band correspond to V^{+5}. The complete decomposition of the precursor is identified by the increase of the surface V=O bond and decrease of the oxidation state at the surface. Chemical and kinetic information related to band absorption for multiple internal reflections have been performed by attenuated IR total reflection spectroscopy using a Perkin Elmer Spectrum 1000 FTIR-ATR spectrometer. Initially and as a reference, V_2O_5 powder was investigated. Its IR spectrum exhibited the 1000.703 cm^{-1} and 782.392 cm^{-1} bands, characteristic of the intermediate oxidation state V^{+5} to V^{+4} of V=O bond. The snow-flake synthesized nano-crystals exhibited four bands; at 840.65 cm^{-1} describing the coupled vibration V=O and V-O-V (figure 6). This concurs with the transition from VO_2 (amorphous) to VO_2 (M). The 420 cm^{-1} band is a weak vibration of the absorption band of V-O bond while 544.5 cm^{-1} is assigned to the V-O-V octahedron bending modes. In accordance to the previous IR studies of Sorapong et al [19], such a spectrum is a characteristic of pure VO_2(M) phase.
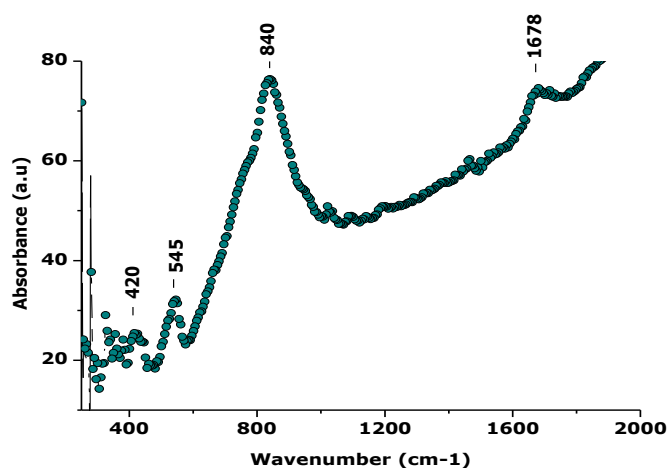
Figure 6: Typical room temperature ATR-FTIR of the snow-flake VO_2.

The reason of the remarkable change of infrared absorption spectra in the tetragonal rutile VO_2 structure, rv_{06} belongs to the highly symmetrical O h group. Simplified vibration modes of octahedral molecule XY_6 of Oh group are given in Figure 7 [20]. In this case symmetrical stretching vibration modes $V_1(A_{1g})$, $v_2(E_g)$, $v_5(F_{2g})$ and $v_6(F_{2u})$ would not give rise to a dipole moment change of full octahedron and therefore these vibrations are infrared-inactive and have no absorption peaks in the infrared spectrum. However, vibration modes $v_3(F_{x9})$ and $v_4(F_b)$ give rise to a dipole moment change and have absorption peaks in the infrared spectrum. This is the reason why some absorption peaks disappear in the infrared spectra of VO_2 powders above Tt.
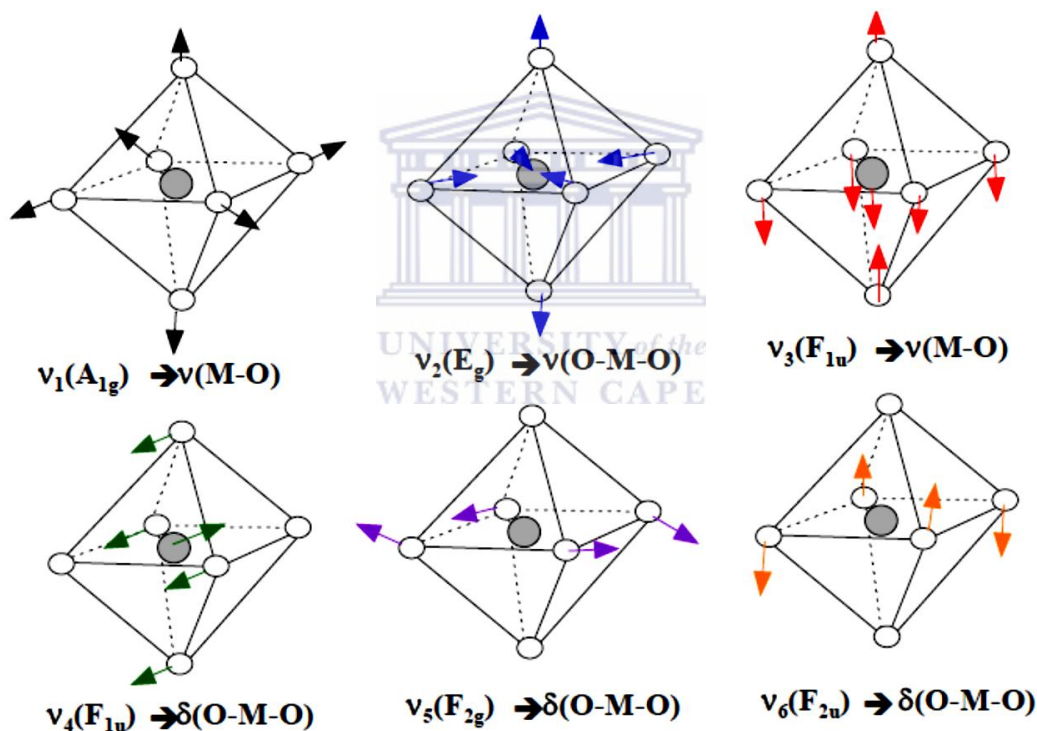
Figure 7: Vibration modes of octahedral molecule VO_6 of O_h group (O) O and (●) V [20]

As the oxidation state of the central atom becomes higher, the stretching frequencies force increase across the periodic table. Hence the higher the oxidation, the higher the frequency. The normal modes of octahedral XY6 molecule in the O_h symmetry are given. See table 1.

Table 1: Activity of the normal modes of XY_6 molecule in the O_h symmetry [20].

MODES	SYMMETRY	ACTIVITY
v_1	A_{1g}	R(stretching)
v_2	E_g	R (stretching)
v_3	F_{1u}	IR (stretching)
v_4	F_{1u}	IR (bending)
v_5	F_{2g}	R (bending)
v_6	F_{2u}	Inactive

6) X-ray Diffraction

Diffraction effects are observed due to the impingement of electromagnetic radiation on periodic structures with geometrical variations on the length scale of the wavelength of the radiation. The diffraction spectrum consists of a plot of reflected intensities versus the detector angle depending on the goniometer configuration [21]. In the case of non-random distribution of the crystallites the material is referred to as preferred orientation. X-ray diffraction is generally used for chemical analysis including phase identification, investigation of the high/low temperature phases and cell parameter determination. The crystallinity of the material is given through sharp narrow diffraction peaks. The condition for constructive interference is given by Bragg`s law according to the equation:

$$\lambda = 2d \sin \theta \qquad\qquad Eq.\,11$$

d is the interplanar spacing perpendicular to the between the planes [22]. The crystalline material diffract the electron beam x-rays strongly through well-defined directions dependent on electron wavelength and crystal lattice spacing. There is reinforcement of

reflections form successive parallel planes when the angles of incidence and reflection satisfy Bragg`s law. See figure 8. X-Ray diffraction investigation is extensively used to study grain sizes, crystalline lattice faults, texture and residual stress. The x-ray radiation emitted from a laboratory is of random polarization where the scattering through a sample is decomposed in σ and π components. In the case where the intensity of σ and π bonds is equal, the polarization factor is given as:

$$\bar{C} = \frac{1 + \cos^2 2\theta}{2} \qquad Eq.\,12$$

The polarization factor determines the scale of the detector. Additionally the x-rays are attenuated during their transit into the matter described via the Lambert-Beer law absorption given by:

$$I_0 exp(-2\mu l) \qquad Eq.\,13$$

Where Io is the intensity entering the sample after a path 2l and μ depend of the wavelength of the radiation, chemical composition of the sample and its density. See figure 9.
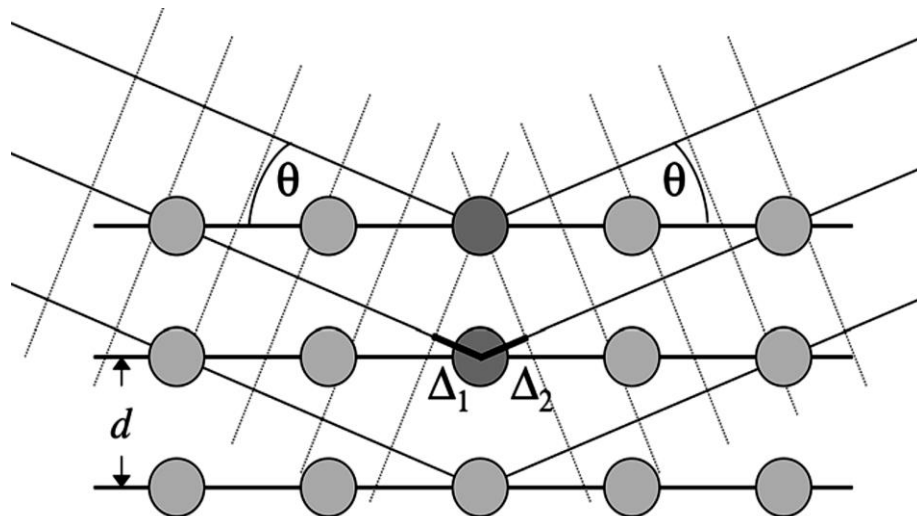
$$\Delta_1 + \Delta_2 = 2d\cos(90° - \theta) = 2d\sin\theta$$

Figure 8 Diagram showing the concept of the Bragg`s law [23].
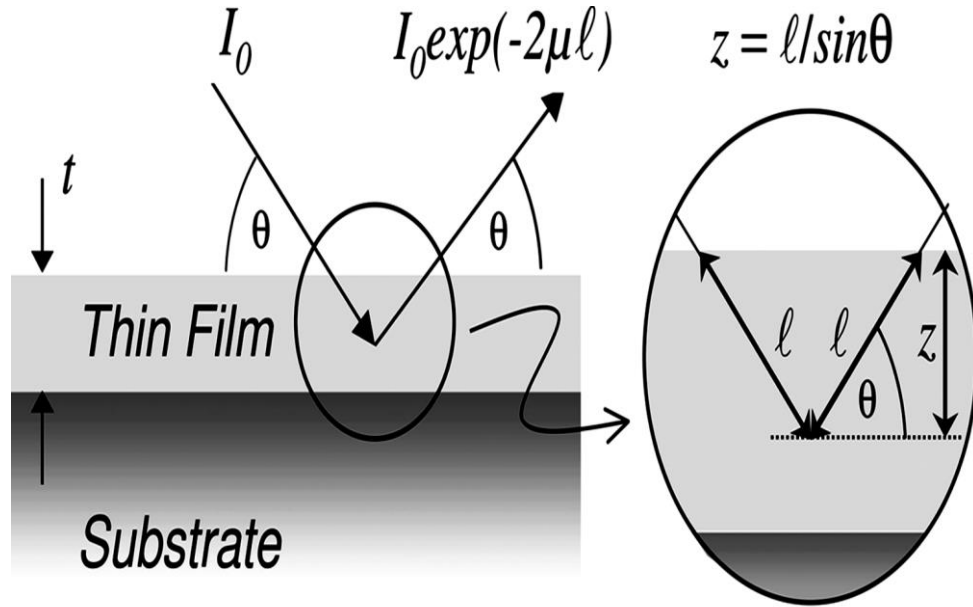
Figure 9: Schematic representation of the absorption effect for a thin film sample in a θ/2θ scan [23].

7) Raman Spectroscopy

Raman Spectroscopy was discovered in 1928 and the first Raman microscopes were described in 1974 and it has been proved to be a powerful technique to investigate vibrational excitations in superlattices. Figure 10 presents the different scattering events observed in Raman spectroscopy with the light absorption in Infrared spectroscopy. Here an intense monochromatic laser radiation excites a molecule to a virtual state; the excited molecule relaxes to a higher vibrational level and the emitted photon has lower energy comparing to the excited laser light. This event is called inelastic Stokes Raman scattering. The ratio of Stokes and anti-Stokes Raman scattering is dependent of the number of molecules in the ground and excited vibrational levels. This is described according to the Boltzmann equation: [24]

$$\frac{N_n}{N_m} = \frac{g_n}{g_m} exp\left[\frac{-(E_n - E_m)}{kT}\right] \qquad\qquad Eq.\,14$$

Nn is the number of molecules in the excited vibrational energy levels n.

Nm number of molecules in the ground vibrational energy levels m, g is the degeneracy of the levels n and m, En-Em is the difference energy between vibrational energy levels

$$K = 1.3807 \times 10^{-23} \, JK^{-1} \qquad\qquad Eq.\,15$$
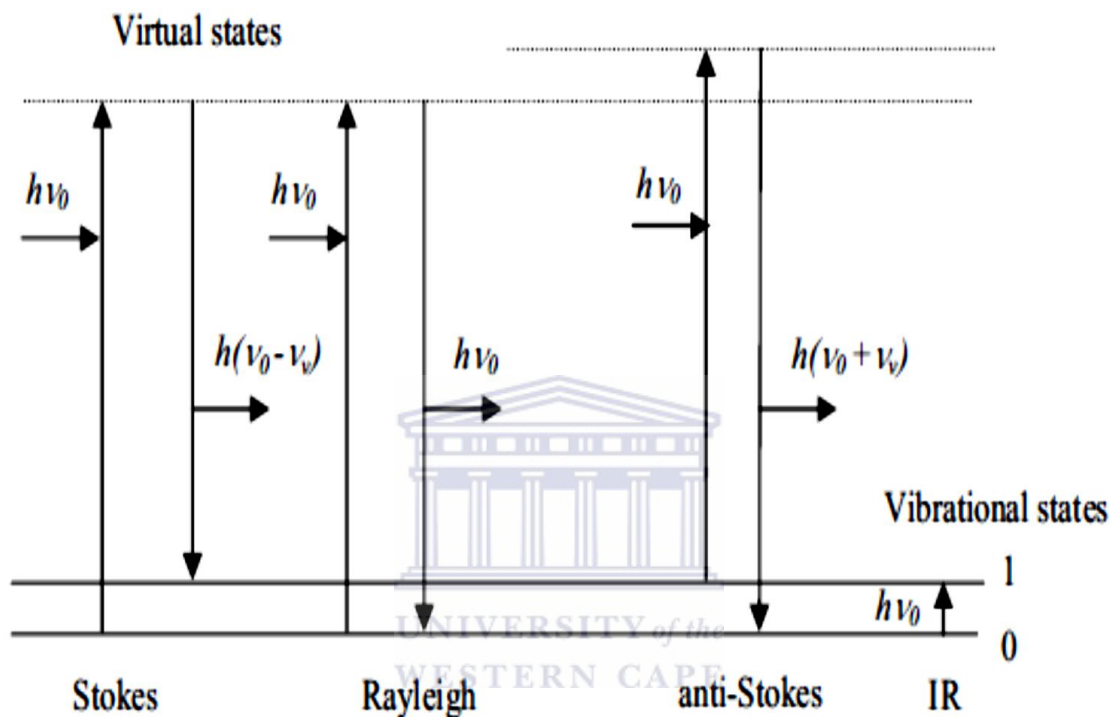
Figure 10: Schematic drawing of vibrational energy states and light energies involved in Raman and IR spectroscopies. v_0 is frequency of incident light, v_v vibrational frequency, h is Planck `s constant [25].

The intensity of Raman Spectroscopy is generally given by:

$$I \approx N.I_0.\left(\frac{d\sigma}{d\Omega}\right) \qquad\qquad Eq.\,16$$

N is the number of scattering molecules per unit of volume, I_o is the intensity of the incident laser beam, $\frac{d\sigma}{d\Omega}$ is the differential scattering cross-section. The Raman spectrum of the overall sample relies on a linear superposition. The depth profile resolution is

determined by the laser wavelength, the objective and the pinhole size that restricts the Raman scattering from out of focus zones. The physical limit is exprimed as:

$$\Delta Z \geq \left| \frac{4.4\, n\lambda}{2\pi (NA)^2} \right| \qquad\qquad Eq.\,17$$

n is the refractive index of the sample, λ is the laser wavelength, and NA is the numerical aperture of the objective. Raman Spectroscopy is a very good tool to characterize and identify elements and molecules for inorganic components, chronological establishment of dyes, resins, and pigments; color probes with a great advantage to be used as largely nondestructive in situ sampling technique, electronic devices applications reflecting the behavior of phonons and the electronic characterization where bound and free charges contribute to the Raman scattering through collective and single particle excitation processes.

8) Electron Diffraction

Diffraction results in various phenomena associated with the bending of waves when they interact with obstacles in their path. De DE Broglie describes the electrons as a wave having the wavelength λ given as:

$$\lambda = \frac{h}{p} \qquad\qquad Eq.\,18$$

By considering non relativistic electrons, their momentum such that:

$$\lambda = \frac{h}{\sqrt{2meV}} \qquad\qquad Eq.\,19$$

Where e is the charge of the electron, V is the electric potential and m is the electron rest mass. Since the wavelength is in the order of lattice spacing in crystals, a diffraction pattern is expected to appear for electrons in the energy range of few KeV scattered by a crystalline lattice. The electron diffraction pattern obtained is dependent of the solid matter: single crystals, polycrystals and amorphous materials. Diffraction patterns give

information about the type of material, defects presence, cell parameter, symmetry specification, atom configuration in the unit cell [26]. The diffraction of fast electrons Bragg angles are very small about 1º:

$$d = \lambda L/R \qquad\qquad Eq.\,20$$

Where λ L is the camera constant depend on the magnification of a diffraction pattern; R is the measured of diffraction pattern between spot coming from the lattice plane diffracting the beam.
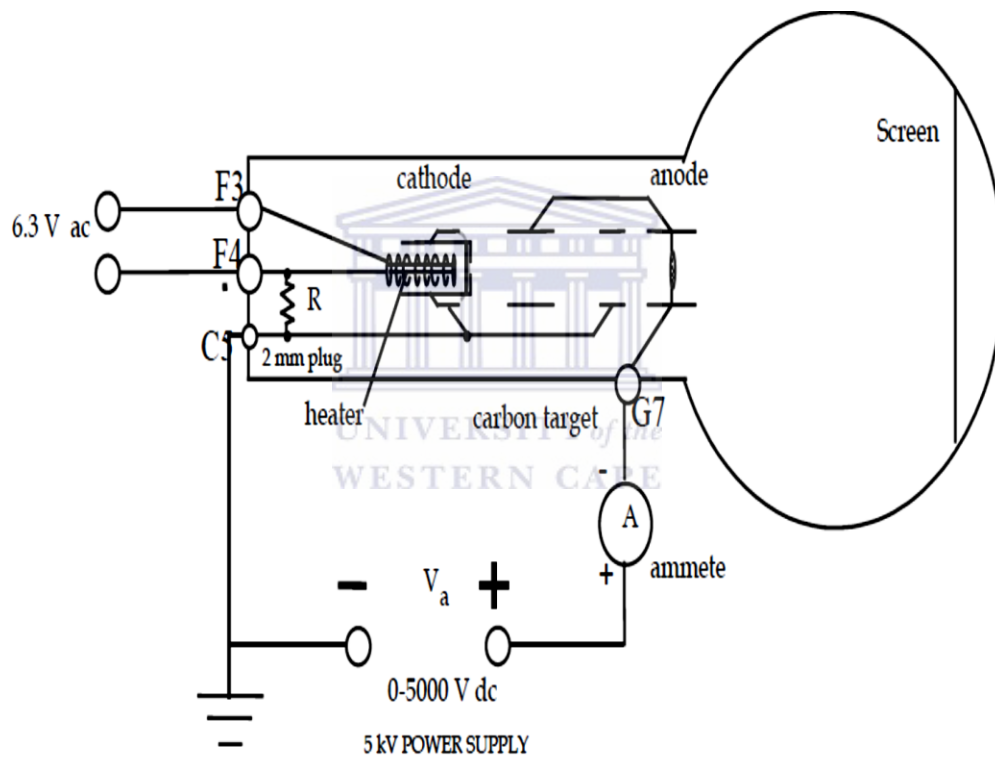
Figure 11: Electron diffraction Experiment Diagram [27].

The electron gun is made up of heater, cathode and anode. Ejection of the electrons is obtained by thermionic emission from the heated piece of metal which is located inside the cathode. The emitted electrons are accelerated by two pairs of anode rings under acceleration potential V ~2000-4000 V dc giving an electron beam.

9) Crystallography

According to the ab initio calculations the structural data of different phases, formula space group lattice parameters and fractional atomic coordinates are given:

Table 2: VO cell description [28].

Formula	VO	
Space group	$Fm\bar{3}m$ (hexagonal axes)	
a (Å)	4.186	
V(Å^3 atoms^{-1})	9.169	
Z	4	
Atoms	V	O
Site	4b	4a
X	0.0	0.5
Y	0.0	0.5
Z	0.0	0.5

Table 3: V$_2$O$_3$ cell description with hexagonal axes [28].

Formula	V$_2$O$_3$	
Space group	$R\bar{3}c$ (hexagonal axes)	
a (Å)	4.925	
C (Å)	13.834	
V(Å^3 atoms^{-1})	9.687	
Z	6	
Atoms	V	O

Site	12c	18e
X	0.0	0.329
Y	0.0	0.0
Z	0.341	0.25

Table 4: VO_2 cell description [28].

Formula	VO_2	
Space group	$P4_2/mnm$	
a (Å)	4.558	
C (Å)	2.858	
V(Å³ atoms⁻¹)	9.897	
Z	2	
Atoms	V	O
Site	2a	4f
X	0.0	0.300
Y	0.0	0.300
Z	0.0	0.0

Table 5: V_6O_{13} cell description [28].

Formula	V_6O_{13}
Space group	Cmma
a (Å)	11.935
b (Å)	19.940
C (Å)	3.687

V(Å^3 atoms^{-1})	11.545						
Z	4						
Atoms	V	V	O	O	O	O	O
Site	16o	8n	16o	16o	8n	8m	4g
X	0.147	0.148	0.174	0.151	0.177	0.0	0.0
Y	0.069	0.25	0.049	0.153	0.25	0.056	0.25
Z	0.75	0.75	0.25	0.75	0.25	0.75	0.75

Table 6: V_4O_9 cell description [28].

Formula	V_4O_9			
Space group	Pnma			
a (Å)	17.910			
b (Å)	3.642			
C (Å)	9.452			
V(Å^3 atoms^{-1})	11.858			
Z	4			
atoms	Site	x	Y	Z
V	4c	0.491	0.25	0.274
V	4c	0.080	0.25	0.543
V	4c	0.163	0.25	0.205
V	4c	0.313	0.25	0.449
O	4c	0.024	0.25	0.727

O	4c	0.449	0.25	0.049
O	4c	0.339	0.25	0.654
O	4c	0.198	0.25	0.005
O	4c	0.088	0.25	0.341
O	4c	0.047	0.25	0.088
O	4c	0.392	0.25	0.357
O	4c	0.167	0.25	0.584
O	4c	0.240	0.25	0.316

Table 7: V_3O_7 cell description [28].

Formula	V_3O_7							
Space group	I4/mmm							
a (Å)	13.986							
C (Å)	3.631							
V(Å^3 atoms^{-1})	11.838							
Z	6							
Atoms	V	V	V	O	O	O	O	O
Site	2a	8h	8i	2b	8h	8h	8j	16l
X	0.0	0.184	0.366	0.0	0.099	0.294	0.094	0.29
Y	0.0	0.184	0.00	0.00	0.099	0.294	0.5	0.093
Z	0.0	0.0	0.0	0.5	0.0	0.0	0.0	0.0

Table 8: V_2O_5 cell description [28].

Formula	V_2O_5			
Space group	Pmmn			
a (Å)	11.532			
b (Å)	3.600			
C (Å)	4.401			
V(Å^3 atoms^{-1})	13.051			
Z	2			
Atoms	V	O	O	O
Site	4f	4f	4f	2a
X	0.102	0.106	0.931	0.25
Y	0.25	0.25	0.25	0.25
Z	0.890	0.523	0.003	0.004

10) References

[1] Ashby, F.M.; Ferreira, P.J.; Schodeck, D.L.; *Nanomaterials, Nanotechnologies and Design, An Introduction for Engineers and Architects*, Elsevier Ltd. ISBN: 978-0-7506-8149-0, 2009.

[2] Bentz, D. P. and Stutzman, P. E., "*SEM Anslysis and Computer Modelling of Hydration of Portland Cement Particles*", Petrography of Cementitious Materials, ASTM STP 1215, Sharon M. DeHayes and David Stark, Eds., American Society for Testing and Materials, Philadelphia, 1994.

[3] Widmann, J.; Toledo, M.; GmbH, Analytical Sonnenbergstrasse 74, CH-8603 Schwerzenbach, Schweiz, Usercom 2/2000.

[4] Mikhail, S.A.; and Webster, A.H.; *Handbook of thermal analysis and calorimetry. Applications to organic and miscellaneous materials*, M.E. Brown and P.K. Gallagher, editors, 2, 2003.

[5] Pradhan, N.R.; Ph.D. Thesis, Worcester Polytechnic Institute, Department of Physics April 2010.

[6] Kowalczyk, S.P.; Ley, L.; McFeely F.R.; and Shirley, D.A.; *Phys. Review B,* (11) 4, 1975.

[7] Pollini, I.; A. Mosser, A.; Parlebas, J.C.; *Physics Reports* 355, 2001, 1–72.

[8] Hyland, G.J.; *Journal of Solid State Chemistry* 2, 1970, 318-331.

[9] Pintchovski, F.; Glausinger, W.S.; and Navrotsky, A.; *J.Phys Chem.Solids Phys.* 39 pp, 941-949.

[10] Barron, A.R., Harrison, L.; *Physical Methods in Chemistry and Nano Science: XPS Analysis of Modified Surfaces*. http://cnx.org read on the 12 September 2012

[11] Shirley, D.A.; LBL-2936, *Invited talk presented at the International Conference on Hyperfine Interactions Studied in Nuclear Reactions and Decay,* Uppsala, Sweden, June 10-14, 1974.

[12] Silverman, I. M.; Ph.D. Thesis, *Modeling Spin Transitions in LACOO3, Applied Physics*, 10 June 2010.

[13] Bagus, P.S.; Freeman, A.J.; and Sasaki, F.; *Phys. Rev. Lett*. 30, 1973, 850.

[14] Rose, M.; Ph.D. *Thesis Spacing measurements of lattice fringes in HRTEM images using digital dark field decomposition,* Missouri - St. Louis, July 2006.

[15] Schwarzer, R. A.; *Ultramicroscopy 67*, 1997, 19-24.

[16] Coates, J.; *Interpretation of infrared Spectra, A Practical Approach*" Encyclopedia of Analytical Chemistry R.A. Meyers (Ed.) pp. 10815-10837 © John Wiley & Sons Ltd, Chichester, 2000.

[17] Nguyen, T.; *Progress in Organic Coatings,* 13, 1985, 1-34.

[18] http://www.chem.ufl.edu.

[19] Sorapong, P.; Yoshikazu, S., Athapol, K.; Sommai, P.; and Susumu, Y.; *J Solid State Chem.* 178, 2005, 2152-2158.

[20] Julien, C.M.; *Proceedings of the International Workshop: Advanced Techniques for Energy Sources Investigation and Testing*, Sofia, Bulgaria 4 – 9 Sept. 2004.

[21] www.scintag.com

[22] Midgley, P.; *Materials Science*, Course A: *Atomic Structure of Material*, University of Cambridge, Michaelmas Term 2011-12.

[23] Birkholz, M.; *Thin film Analysis by X-Ray Scattering*, Copyright © Wiley-Vch Verlag GmbH & Co. KGa A, Weinheim, 2006.

[24] Smith, E.; Dent, G.; *Modern Raman Spectroscopy-A Practical Approach,* Copyright © John Wiley & Sons Ltd, the Atrium, Southern Gate, Chichester, West Sussex PO19 8SQ, England, 2005.

[25] Vyörykkä, J.; *Confocal Raman Microscopy in Chemical and Physical Characterization of Coated and Printed Papers*, Helsinki University of Technology Laboratory of Forest Products Chemistry, Reports Espoo 2004.

[26] Sarakinou, E.; -Koziorowska, J.S.; *Physics of Advanced Materials Winter School* "From Electron Diffraction to Electron Crytallography" 2008.

[27] http://physics.bu.edu/ulab/modern/Electron_Diffraction.pdf.

[28] Reeswinkel, T.; *Self-lubricious tool coatings for ecological metal cutting*. Materials Chemistry Dissertation, 16, 2012.

Scientific Production

<div align="center">

List of publication of Ms. Aline Simo

</div>

Monograph:

0

Further publications:

A) Publications with peer review process

1. M. Maaza, D. Hamidi, A. Simo, T Kerdja, A.K Chaudhary, J.B. Kana Kana, *Optics Communication*, 285, 2012, 1190-1193

2. A.Simo , R Madjoe, L.Edomwonyi-Otu, A. Gibaud, et M.Maaza, *SA Institute of Physics* 2011 ISBN: 978-1-86888-688-3

3. A. Simo, L.C. Edomwonyi-Otu, R. Madjoe and M. Maaza (2012*), MRS Proceedings,* 1406 , mrsf11-1406-z05-36 doi:10.1557/opl.2012.192

4. L.C. Edomwonyi-Otu, B.O. Aderemi O. Edomwonyi-Otu A. Simo and M. Maaza, *International Journal of Engineering Research in Africa*, 7, 2012, pp 13-19

5. Bonex W. Mwakikunga , Sarah Motshekga, Lucky Sikhwivhilu , Mathew Moodley, Manfred Scriba, Gerald Malgas, A. Simo, B. Sone, M Maaza, Suprakas Sinha-Ray, *Sens. Actuators B: Chem*. 184, 2013, 170-178
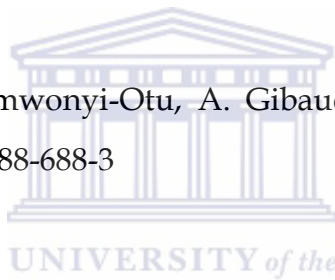
6. A. Simo, R. Madjoe, B.T. Sone, L. Kotsedi, Bonex W. Mwakikunga, M. Maaza`` Proceeding of SAIP 2012`` Annealing effect on Nanostructures VO_2 and Potential Application as Gas sensor device.Accepted for publication.

B) Submitted publications with peer review process:

1. A. Simo, J. M. Ndjaka, R. Madjoe,G. Vignaut, O. Nemraoui, M. Maaza ``First order solid-solid phase transition Strain-thermal dependence on nanostructures $VO_2$ monoclinic`` (under correction)

2. M. Maaza, A. Simo, B.M. Itani, J.B. Kana Kana, S. El Harthi, K. Bouziane, M.L. Saboungi, I. Luk'yanchuk Nanotechnology 2012

3. A. Simo et al. Room temperature elevated H_2 sensing in Mott-Type VO_2 Nanobelts (Accepted manuscript)

4. Hybrid VO_2-PVP submicronic composites coatings for IR solar radiations modulation, Surface Coating and Technology. (under review)

C) Publications without peer review process

1. A. Simo, R. Madjoe, A. Gibaud and Malik Maaza, AIP Conf. Proc. 1517, 223-234 (2013); doi: 10.1063/1.4795256. ISBN: 978-0-7354-1139-5

The following above mentioned publications have evolved from my doctoral dissertation: A1, A2, A3, A5, B1, B2, and B3.

Direct Synthesis of Pure Radiative Vo₂ (M) Plate Like Structures Via Hydrothermolysis at Low Temperature

A.Simo[1,3], L.C. Edomwonyi-Otu[1,2,4], R.Madjoe[3], M. Maaza[1]

1   Nanoscience Laboratories, Materials Physics Dept., iThemba LABS-National Research Foundation, P O Box 722, Somerset West 7129, Faure, South Africa
2   Chemical Engineering Dept, Ahmadu Bello University, Zaria, Nigeria. 870001
3   Physics Dept., University of Western Cape, Belleville, South Africa
4   Chemical Engineering Department, University College London, WC1E 7JE, UK

ABSTRACT

Facile and direct synthesis of radiative VO_2 (M) plate-like is reported. The snowflake material presents superstructures plate-like aggregate with an anisotropic orientation in shape governed by V_2O_5 and NaOH concentration giving high surface energy liable for chemical reactions with the medium. Pure crystalline VO_2 (M) has been obtained with a complete hydrothermolysis of the precursor. The morphological, structural, elemental composition, crystallinity and vibrational bands of the powders were characterized by Powder X-ray Diffraction (XRD), Scanning Electron Microscopy (SEM), Selected Area Electron Diffraction (SAED) and Fourier Transform-Attenuated Total Reflection (FTIR-ATR) infrared spectroscopy.

INTRODUCTION

The unusual properties of the metallic state near the insulating transition have been most extensively studied in d-electron systems. Among these materials, the Vanadium dioxide (VO_2) has intrigued researchers for five decades since its discovery by Morin in 1959 with regards to its thermochromic properties [1]. This behavior determines its ability to regulate the infrared radiations at high temperature and so acts as an intelligent window filter. In addition, it has great applications in thermal sensing and switching devices [2], cell electrodes batteries [3] etc. It is accompanied by structural change from monoclinic phase at low temperature (below 68^0C) with a space group P21/c to tetragonal rutile phase (more stable P4/mmm) due to a single coordinate jump of the V cations[4 -7].

Semi conductor to metal transition has been recently investigated by the femtosecond laser excitation by time resolved-measurements of the characteristic x-rays and optical signatures [8]. Various micro/nanostructures of VO_2 such as nanoribbonds, nanobelts, nanorods, nanowires, hollow microspheres by facile template-free process [9] have been prepared. Few reports are available to date on direct synthesis without post heat treatment of pure VO_2 (M). Recently Shidong et al [10] prepared VO_2 (R) single crystal nanorods by hydrothermal method with a reversible change of surface charge associated with the semiconductor –metal phase transition of the material while Xin-Ping et al [9] reported the synthesis of pure VO_2 (M) after annealing at 500°C for 5h. In our present work, we report for the first time the direct synthesis of pure radiative VO_2 (M) plate-like via hydrothermolysis at low temperature without post-annealing. The products were characterized via XRD, SEM, EDX, SAED and FTIR-ATR.

Optical limiting in pulsed laser deposited VO$_2$ nanostructures

M. Maaza [a,b,c,d,*], D. Hamidi [a], A. Simo [a], T. Kerdja [a,c], A.K. Chaudhary [a,e], J.B. Kana Kana [a,f]

[a] NANOAFNET, MRD-iThemba LABS, National Research Foundation, 1 Old Faure road, Somerset West, South Africa
[b] Faculty of Sciences, Pretoria-Tshwane University of Technology, Private Bag X 680, Pretoria, South Africa
[c] African Laser Centre, CSIR campus, P.O. Box 395, Pretoria, South Africa
[d] Centre de Development des Technologies Avancees, Baba Hassen, Algiers, Algeria
[e] Nonlinear Optics Group, Advanced Centre of Research in High Energy Materials, University of Hyderabad, India
[f] Dept. of Materials Science & Engineering, University of Arizona, Tucson, AZ 85721, USA

ARTICLE INFO

ABSTRACT

Being a Mott type oxide, at a temperature of ~68 °C and ambient pressure, stoichiometric VO$_2$ undergoes a first order metal-insulator transition, which is accompanied by a reversible abrupt change in the band gap opening. From an optical point of view, this metal-insulator transition manifests itself by a significant and reversible variation of the refractive index under either a thermal stimuli or by photo-induction. This contribution reports on the ultrafast optical limiting in the IR regime of pulse laser deposited VO$_2$ nanostructures.

© 2011 Elsevier B.V. All rights reserved.

Letter

Within the thermochromic vanadium based family there are several optically active vanadium oxides among which VO, V$_2$O$_3$ and VO$_2$. These later oxides are known for their metal/insulator–semiconductor (M/I–S) phase transition characteristics and hence exhibiting effective changes in their electrical resistivity at specific temperatures [1–7] which make them optically active under temperature/photo external stimuli. One should single out vanadium dioxide "VO$_2$" which exhibits a singular ultrafast 1st order type phase transition at the vicinity of ~67.8 °C with several orders of change in the electrical resistivity due to its strong electron correlation. Such a large electrical resistivity modulation as a function of temperature is accompanied by a reversible semiconductor–insulator to metal transition. This latter behavior causes noteworthy reversible changes in the optical response, specifically in the infrared region.

From a theoretical point of view, this phase transition has been, initially, interpreted in terms of Mott–Hubbard like transition [8] or electron trapping in homopolar bonds. The very recent ultrafast spectroscopy investigations shed-lighted, on how fast is such a phase

transition as well as on the electronic band structure changes [9–10]. Using a femtosecond laser pump-probe geometry, the relaxation processes in VO$_2$ substantiated that the light-induced phase transition was as fast as the laser pulse duration of 100 fs itself. As reported in Fig. 1, possible mechanism in relation to the phase transition may be due to changes in the 3d band structure associated with crystal structure changes. More precisely, the upper d||—an unoccupied in conduction band of semiconductor phase is within the broad π*-band which is empty, but more strongly hybridized with oxygen 2p-orbitals and lies above the Fermi level E$_F$. In the metallic phase, however, all 3 d-bands are close to Fermi-level. Upon the laser excitation, the main transitions related to ultrafast light-induced phase transition are from occupied d||–valence band to unoccupied d||–π* mixed conduction band followed by resonant transitions to unoccupied excited states of metallic phase. As a result the screening of the charge transfer by conduction electrons in metallic phase takes place by ultrafast laser excitation. The additional complementary recent work of Lysenko et al. [11] indicated that upon a laser excitation, an instantaneous response in the transient reflectivity and transmission was observed followed by a relatively longer relaxation process. The observed phase transition has been then associated with the optical interband transition in VO$_2$. This singular phase transition characteristic of VO$_2$ at about 68 °C, makes it an optical coating candidate of choice for smart windows applications [12–13], thermal sensors [14], optical switching devices [2], field effect transistors and

* Corresponding author at: NANOAFNET, MRD- iThemba LABS, National Research Foundation, 1 Old Faure road, Somerset West, South Africa. Tel.: +27 21 843 1149; fax: +27 21 843 3543.
E-mail address: Maaza@tlabs.ac.za (M. Maaza).

Title: VO2 NANOSTRUCTURES BASED CHEMIRESISTORS FOR LOW POWER ENERGY CONSUMPTION HYDROGEN SENSING
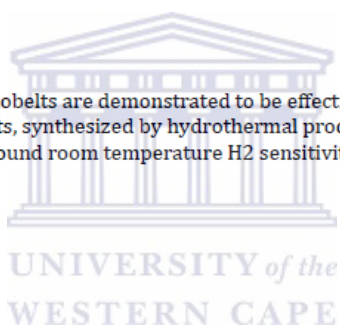
Corresponding Author: Ms. Aline Simo,

Corresponding Author's Institution:

First Author: Aline Simo

Order of Authors: Aline Simo

Abstract: Mott-type VO2 oxide nanobelts are demonstrated to be effective hydrogen gas sensors at room temperature. These nanobelts, synthesized by hydrothermal process and exhibiting the VO2 (A) crystallographic phase, display a sound room temperature H2 sensitivity as low as 0.17 ppm.

UNIVERSITY *of the*
WESTERN CAPE

254

VO₂ NANOSTRUCTURES BASED CHEMIRESISTORS FOR LOW POWER ENERGY CONSUMPTION HYDROGEN SENSING

Aline Simo[1, 2, 4], Bonex Mwakikunga[3], Bertrand T. Sone[1], Serge Zekeng[4], Reginald Madjoe[1-2], Malik Maaza[1,5]

[1]Nanosciences African Network (NANOAFNET), Materials Research Department, iThemba LABS-National Research Foundation, 1 Old Faure road, Somerset West 7129, POBox 722, Somerset West, Western Cape Province, South Africa

[2]Physics Dept., University of Western Cape, Bellville-South Africa.

[3]National Centre for Nanostructured Materials, Council for Scientific and Industrial Research, P O Box 395, Pretoria 0001, South Africa

[4] University of Yaounde I, Cameroon cuti[at]uy1.uninet.cm, +(237) 222 13 20, BP 337

[5]College of Graduate Studies, University of South Africa (UNISA), Muckleneuk ridge, PO Box 392, Pretoria, South Africa,

Corresponding author: simo@tlabs.ac.za

Abstract

Mott-type VO_2 oxide nanobelts are demonstrated to be effective hydrogen gas sensors at room temperature. These nanobelts, synthesized by hydrothermal process and exhibiting the VO_2 (A) crystallographic phase, display a sound room temperature H_2 sensitivity as low as 0.17 ppm.

Keywords:

Gas sensing, hydrogen sensing, vanadium dioxide nanobelts, Mott type oxides, size effects, surface-interface, low power consumption.

Phase transition in hydrothermal synthesized VO$_2$(M) nano-crystals: an X-ray diffraction study

A Simo[1,2], R Madjoe[2], L Edomwonyi-Otu[1,3] , A Gibaud[4] and M Maaza[1,5]

[1] Nanosciences African Network, Nanoscience Laboratories, Materials Research Dept., iThemba LABS-National Research Foundation, Po Box 722, Somerset West 7129, South Africa

[2] Physics Dept., University of Western Cape, Belleville, South Africa

[3] Chemical Engineering Dept, Ahmadu Bello University, Zaria, Nigeria. 870001

[4] Laboratoire de Physique de l'Etat Condense, Dept. De Physique, Universite du Maine, UMR CNRS 6087, Le Mans- France

[5] Faculty of Sciences, Pretoria-Tshwane University of Technology, Private Bag X 680, Pretoria, South Africa.

E-mail: simo@tlabs.ac.za

Abstract. We report on the phase transition of VO$_2$(M) nano-particles synthesized by hydrothermal processing. The study was carried out by X-ray diffraction with a focus on the major Bragg peaks located at 37.1 and 36.9°. The reversible crystallographic transition from monoclinic to tetragonal phase at about 67°C is close to the bulk value. It was observed that the dynamic of the tetragonal and monoclinic one are complementary. This structural phase transition studies were complemented by elemental composition, selected area electron diffraction and Fourier transform attenuated total reflection infrared spectroscopy.

1. Introduction

The unusual properties of the metallic state near the insulating transition have been most extensively studied in d-electron systems. Among these materials, the Vanadium dioxide (VO$_2$) has intrigued researchers for five decades since its discovery by Morin in 1959, especially with regard to its thermochromic properties in the Infrared spectral range [1]. This latter peculiar behaviour determines the ability of VO$_2$ based coatings to regulate the infrared radiations and so acting as an intelligent reversible window filter. In addition, it has potential applications in thermal sensing and switching devices [2]. VO$_2$ is considered as an archetypical system with a conductivity change of several orders at the critical temperature T$_c$ (341.1 K) accompanied by a transition in lattice structure from a monoclinic to a tetragonal phase and a dramatic increase of the infrared modulation [3]. Various micro/nanostructures of VO$_2$ such as nanoribbons, nanobelts, nanorods, nanowires, hollow microspheres by facile template-free process have been prepared [4]. Few reports are available to date on direct synthesis of pure VO$_2$ (M) micro-nano radiative platelets with high crystallinity without thermal annealing due to the abscence of propagation of the transition across the grain boundaries and the dissipation of the intrinsic stress. Grain size is widely believed to determine the structure-dependent hysteresis curve in the phase transition [5]. Figure 1 presents structural information during VO$_2$ metal insulator transition (MIT) with an increase in symmetry both in the VO$_6$ octahedron and in the V atomic chains where the V-V pairs undergo the elongation, shortening and twist from the

zigzag-type to a linear chain. Different techniques have been used to investigate the kinetics of the transition via electron –correlation-driven Mott transition, structure-driven Peierls transition or the cooperation of the two mechanisms [3] and synchrotron X-ray scattering in conjunction with real space analysis showing that the transition from low temperature monoclinic to high temperature tetragonal phase occurs in a first order manner with coexistence of the two phases [6]. It has been shown that the phase of electronic property occur simultaneously suggesting for the MIT of VO_2 the existence of a cooperative mechanism of a structural driven and electron correlation mechanisms.
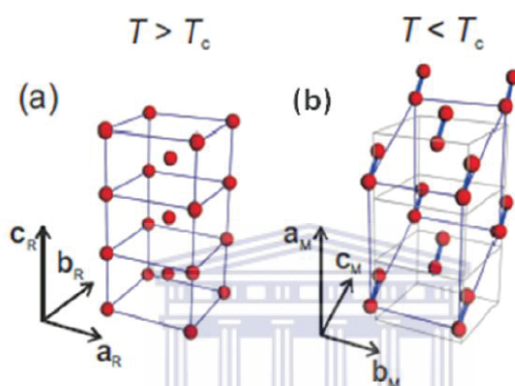
Figure 1: (a) the metallic high temperature tetragonal rutile form of VO_2 with a single V-V distance and (b) the insulating low-temperature monoclinic form showing dimerized chains of alternating short and long V-V distances along the c-axis [6].

This contribution is highlighted in the present study via in-situ x-ray diffraction versus temperature within a thermal range of 25-110°C on highly crystalline VO_2(M) nano-crystals. It has been reproducibly observed that such hydrothermal synthesized nano-crystals exhibit an average transition temperature at around ~67°C equivalent to the bulk value pointing out that the investigated snow-flake type nano-crystals could be stress/strain free.

2. Experimental techniques
All the reagents were of analytical grade and used without further purification. 0.75ml of Sulfuric acid H_2SO_4 (Kimix, 98%) followed by the drop-wise addition of 0.25ml of $N_2H_2 \cdot 2H_2O$ (Merck) were added into an aqueous suspension (10 mL) containing 0.45g of V_2O_5 (Alfa Aesar). After being warmed at 95˚C while stirring, the solution changes from yellow to green, then green to blue, characteristic of the presence of V^{+4} ions in the solution, finally blue to gray depending on the concentration of NaOH used to stabilize the dissolved precipitates. Hydrothermal synthesis was carried out in a Teflon-lined autoclave at ~230˚C for ~48h. Then the content was air-cooled at room temperature followed by the filtration of the formed precipitates. The final black product was washed thorougthly with water and ethanol for the exfoliation of bulk layered V_2O_5 and then dried at about 60˚C for 12h in an oven.

3. Results and discussion
3.1 Morphological studies and elemental analysis
The morphology of the synthesized crystals was observed by a scanning electron microscopy Nova NanoSEM 230 equipped with an elemental EDAX system. As typically reported on figure 1, the surface morphology of the samples exhibit snowflake radiative platelike aggregates in 3-D structures,

A classification and ranking system on the H_2 gas sensing capabilities of nanomaterials based on proposed coefficients of sensor performance and sensor efficiency equations

Bonex W. Mwakikunga [a,b,*], Sarah Motshekga [a], Lucky Sikhwivhilu [a,c], Mathew Moodley [a], Manfred Scriba [a], Gerald Malgas [a], A. Simo [d], B. Sone [d], M. Maaza [d,e], Suprakas Sinha Ray [a,f,*]

[a] DST/CSIR National Centre for Nano-Structured Materials, Pretoria 0001, South Africa
[b] Department of Physics, University of Malawi – The Polytechnic, Blantyre 0003, Malawi
[c] DST/Mintek Nanotechnology Innovation Centre, Advanced Materials Division, Mintek, Johannesburg 2125, South Africa
[d] Nanosciences African Network, iThemba LABS, Somerset West 7129, South Africa
[e] College of Graduate Studies, University of South Africa, Pretoria 001, South Africa
[f] Department of Chemistry, King Abdulaziz University, Jeddah 21589, Kingdom of Saudi Arabia

ARTICLE INFO

ABSTRACT

A coefficient of performance is defined based on the traditional definitions of response, S, of a chemoresistive sensing material to a specific gas from resistance–time data. The new definition not only considers the $S_{response}$ and $S_{recovery}$ but also the temperature, T, and the relative humidity, H, at which the sensor operates and the response time, τ_{res}, and recovery time, τ_{rec}. Resistance–time data at various temperatures in a H_2 atmosphere for six samples of different materials, including WO_3 nanoparticles, SnO_2 nanoparticles, SnO_2 nanoparticles mixed with carbon nanotubes, TiO_2 nanorods, TiO_2 nanotubes and VO_2 nanobelts, are presented in this report. The VO_2 nanobelts were the best sensing materials when these materials were ranked according to the temperatures at which they operate; however, the SnO_2 nanoparticles are the superior sensing materials when they are ranked by the defined coefficient of performance.

© 2013 Elsevier B.V. All rights reserved.

1. Introduction

As the world faces a critical energy demand that currently arises largely from the use of CO_x-emitting petroleum, there is a compelling need to turn to renewable energy sources. Among the renewable energy resources, the highly explosive reaction of hydrogen and oxygen gases, whose emission is water vapor, has considerable potential to be a near future fuel if the reaction is properly controlled. This fuel source is to cater to vehicles, space and other modes of transportation as well as the power industry. In this hydrogen economy in which global warming is expected to be alleviated, hydrogen sensors are to be employed in such pertinent devices, such as fuel gauges, meters and various types of indicators and alarms in safety electronics.

Materials that sense hydrogen are therefore sought. These materials have been developed based on different sensing materials and various transduction platforms. The primary classes of gas sensing materials include metal oxide semiconductors, intrinsically conducting polymer composites, metal oxide/polymer composites and other novel materials. Among these materials, the chemoresistive semiconducting metal oxides have the most potential due to their very low-cost, high response, rapid response and recovery time, simple electronic interface, ease of use, low maintenance and ability to detect a large variety of gases [1]. Tiny changes in the molecular composition, pressure of the ambient gas environment and the functionalization of the surface with metal nanoparticles improve the selectivity and high response of one-dimensional nanostructures of metal-oxides semiconductor-based gas sensors [2]. The sensitivity of the sensors can be enhanced when the materials are at the nanoscale. Therefore, a high surface-to-volume ratio, which is available in nanomaterials, is suitable for this purpose. However, selectivity becomes a major setback as nano-sensors are known to possess a gas specificity weakness. Semiconducting oxides are known to present a response to various gases at elevated temperatures that are typically >200 °C.

When deciding what materials are to be employed as sensors for a particular gas, it is important to assess the range of materials based on a valid yardstick. The following figures of merit have been extensively used to assess sensors:

* Corresponding authors at: DST/CSIR National Centre for Nano-Structured Materials, Pretoria 0001, South Africa. Fax: +27 12 841 2229.
E-mail addresses: bmwakikunga@csir.co.za (B.W. Mwakikunga), rsuprakas@csir.co.za (S. Sinha Ray).

Alum Production From Some Nigerian Kaolinite Deposits

L.C. Edomwonyi-Otu[1,a], B.O. Aderemi[2], O. Edomwonyi-Otu[3], A. Simo[4]
and M. Maaza[5]

[1,2]Chemical Engineering Department, Ahmadu Bello University, Zaria, Nigeria. 870001
[3]Economics Department, Ahmadu Bello University, Zaria, Nigeria. 870001
[1,4,5]Materials Research Department, iThemba LABS – NRF, BOX 722, Somerset West 7129,
South Africa
[a]uceclce@ucl.ac.uk , osas1law@yahoo.com

Abstract: The development of sustainable processing technologies for the vast mineral resources available in Nigeria and their varied applications is a major pursuit by the Federal Ministry of Science and Technology. In this work, alum was produced from three different kaolin deposits in Nigeria namely Kankara brown, Bauchi and Kankara white by acid dealumination of the metakaolin obtained by calcination of the beneficiated kaolinites and the yields were measured to ascertain the process repeatability. The reproducibility studies carried out on samples from each deposit showed a mean yield of 80 %, 92 % and 87 % and standard deviation of 2.50 %, 1.063 % and 1.296 %, for Kankara brown, Bauchi and Kankara white respectively. The values from the three deposits fall within 3 standard deviations of the mean in accordance with the 68-95-99.7/three-sigma rule. The alum quality also compares well with available commercial alums in the market. BET analysis, of the alumina obtained by calcination of the alum (Kankara white), gave a surface area of $192.2441m^2/g$ comparable to commercial alumina. These results suggest/establishes the huge possibility of commercial alum production, including alumina, using kaolinite clay from these deposits as starting materials.

Nomenclature

X_i = i[th] weighted sample
$\bar{\bar{X}}$ = mean of weighted samples
$\%$ = percentage
σ = standard deviation of the weighted samples
Σ = summation
N = total number of weighted samples

Introduction

Nigeria as a nation is faced with the challenge of harnessing her abundant natural resources to meet the needs of her teeming population. The current effort by the Federal Government to be one of the twenty most developed economies by year 2020 can only be achieved under a diversified economic system, which underscores the need to develop the solid minerals sector for national development [1]. The recently created Ministry of Solid Mineral Development has been a major stimulus to the Nigerian mining industry. It offers a viable alternative to petroleum for foreign exchange earnings. Globally, the mining industry has been a close rival to the petroleum industry, although Nigeria earns currently a paltry $89 million per annum from it [1].